

Meerlaagse optische verbindingen
geïntegreerd op een gedrukte schakeling

Multilayer Optical Interconnections
Integrated on a Printed Circuit Board

Nina Hendrickx

Promotor: prof. dr. ir. P. Van Daele
Proefschrift ingediend tot het behalen van de graad van
Doctor in de Ingenieurswetenschappen: Elektrotechniek

Vakgroep Informatietechnologie
Voorzitter: prof. dr. ir. D. De Zutter
Faculteit Ingenieurswetenschappen
Academiejaar 2008 - 2009



ISBN 978-90-8578-250-6
NUR 959
Wettelijk depot: D/2009/10.500/8

Samenvatting

In de huidige en de toekomstige breedband netwerken zal multi-gigabit transmissie over langere afstanden alleen mogelijk zijn door gebruik te maken van optische verbindingen, die het hart van het netwerk vormen. Wereldwijd wordt er onderzoek verricht naar de uitbreiding van optische verbindingen naar bord- en schakel-niveau. Optische verbindingen, die typisch afstanden van een paar centimeter tot een meter overbruggen, zijn een aantrekkelijke oplossing voor de bandbreedte limitatie van elektrische transmissielijnen. Echter, de integratie van een optische verbinding in een commerciële gedrukte schakeling legt strenge beperkingen op aan de gebruikte materialen en processen. De belangrijkste vereisten aan het lichtgeleidende medium zijn een laag propagatie verlies, een hoge thermische stabiliteit, een kost-effectief fabricage proces en compatibiliteit met de bestaande processen die gebruikt worden voor de fabricage van gedrukte schakelingen en met soldeer processen.

De integratie van optische verbindingen naar het bord-niveau kan worden gedaan met behulp van een polymere optische laag, die multimodale golfgeleiders bevat om het licht in het vlak van de optische laag te geleiden. Polymere materialen bieden een aantal voordelen ten opzichte van alternatieve geleidingsmaterialen zoals dunne glaslagen en optische vezels zoals een potentieel lage kost, de grote variëteit aan potentiële technieken die kunnen worden gebruikt om de lagen vorm te geven and de mogelijkheid om eigenschappen zoals de brekingsindex en de mechanische en thermische stabiliteit naar wens aan te passen. Optische polymeren zijn gedurende de laatste jaren ontwikkeld door laboratoria wereldwijd en sommige daarvan hebben uitstekende optisch en thermische eigenschappen.

De belangrijkste doeleinden binnen dit onderzoekswerk is de ontwikkeling van een optische link die op bord-niveau is geïntegreerd en de uitbreiding van een eenlaagse optische structuur naar een meerlaagse optische structuur. De uitbreiding naar meerlaagse optische structuren is interessant omdat op deze manier hogere interconnectie dichtheden kunnen worden bekomen en het feit dat het mogelijk is om minder ingewikkelde routing schema's te gebruiken. Meerlaagse optische structuren kunnen bovendien ook volledig gebruik maken van de eigenschappen van 2D opto-electronische elementen zoals VCSEL en fotodetector rijen.

Laser ablatie wordt onderzocht als een alternatieve micro-structureringstechnologie die kan gebruikt worden voor het vormen van de belangrijkste bouwblokken van een optische verbinding in de polymere optische laag. Laser ablatie is een flexibele, maskerloze technologie die kan gebruikt worden voor het vormen van patronen in een groot aantal materialen, afhankelijk van de gebruikte laser bron. Ze kan gebruikt worden voor snelle prototyping, dit in contrast tot masker-gebaseerde aanpakken waar er eerst een

masker moet worden ontworpen en gemaakt. Aanpassingen en correcties kunnen worden aangebracht in een zeer late fase van het proces. Laser ablatie is compatibel met de bestaande fabricage methodes die worden gebruikt voor de fabricage van gedrukte schakelingen en wordt momenteel reeds gebruikt voor het drillen van micro-via's in hoge dichtheid elektrische borden.

De belangrijkste nadruk binnen dit onderzoek ligt op het gebruik van Truemode Backplane™ Polymer (Truemode) voor de optische laag. Dit materiaal heeft een propagatieverlies van 0.04dB/cm bij 850 nm, uitstekende thermische eigenschappen, is compatibel met standaard processen die gebruikt worden voor de fabricage van gedrukte schakelingen, en is UV-gevoelig waardoor er patronen in kunnen worden gevormd met behulp van UV-lithografie. Het materiaal toont een uitstekende respons naar KrF excimer laser ablatie toe, waarbij er structuren met een lage ruwheid kunnen worden gevormd. Het gebruik van drie alternatieve polymeren (Ormocer®, Epocore/clad en SU8) is ook kort besproken. Alle drie deze materialen zijn UV-gevoelig en hebben uitstekende thermische eigenschappen. Het optisch verlies bij 850 nm is echter hoger dan voor het Truemode materiaal (0.06dB/cm voor Ormocer, 0.2dB/cm voor Epocore/clad en 0.55dB/cm voor SU-8).

Truemode bestaat in twee verschillende formulaties: een natte film, die van bij de aanvang van dit onderzoek beschikbaar was, en een droge film, die in een latere fase beschikbaar is gekomen. Voor de natte film formulatie moet de UV-belichting gebeuren in een stikstofomgeving waardoor de beschikbare mask aligner niet kan worden gebruikt. Zoals reeds werd vermeld, vertoont Truemode een uitstekende respons naar KrF excimer laser ablatie toe. Golfgeleiders met een cross-sectie van $50 \mu\text{m} \times 50 \mu\text{m}$ op een pitch van $125 \mu\text{m}$ werden geableerd in de optische laag en nadien geëvalueerd. The golfgeleider kernen hebben een lage ruwheid (35 nm RMS op een scan gebied van $46 \mu\text{m} \times 60 \mu\text{m}$) en een propagatie verlies van 0.13dB/cm bij 850 nm, wat aanvaardbaar is voor korte interconnectie lengtes. Een tweelaagse optische structuur die geableerde golfgeleiders bevat werd gepresenteerd. De realiseerbare alignatie nauwkeurigheid is $\leq 5 \mu\text{m}$, wat binnen het tolerantie interval ligt voor een extra verlies van 0.2dB.

De vereiste compatibiliteit met de bestaande fabricage processen voor gedrukte schakelingen impliceren dat het materiaal bestand moet zijn tegen de hoge temperaturen en drukken die optreden gedurende een laminatie cyclus. Metingen tonen aan dat de performantie van de geableerde golfgeleiders niet beïnvloed wordt door de hoge temperaturen en drukken die optreden gedurende een laminatie cyclus, waarbij het materiaal tussen twee gedrukte schakelingen wordt ingebed. De golfgeleiders zijn ook bestand tegen twee verschillende versnelde verouderingstesten: een versnelde vochtigheidsverouderingstest en een thermische cyclus test. Deze tests zijn gebaseerd op Telcordia 1209-CORE, welke goed aanvaarde standaarden zijn voor passieve optische componenten, en worden gebruikt om de performantie van de componenten te testen over de verwachte levensduur. Thermografische analyse (TGA) resultaten tonen aan dat Truemode thermisch stabiel is tot temperaturen boven 300°C . Uit de bovenstaande vermelde resultaten kunnen we besluiten dat Truemode een geschikt materiaal is om als optische laag te gebruiken.

De droge film formulatie mag UV-belicht worden in standaard omgeving met het masker geplaatst in fysisch contact met de optische laag, waardoor de beschikbare maskaligner kan worden gebruikt. De doorvoersnelheid kan hierdoor gevoelig opgedreven worden omwille van het parallel karakter van het proces, wat wil zeggen dat meerdere

golfsgeleiders of rijen van golfsgeleiders op hetzelfde moment kunnen worden gevormd, in overeenstemming met het patroon op het masker. Dit in tegenstelling tot laser ablatie, dat een serieel proces is, wat wil zeggen dat de golfsgeleider een voor een gevormd wordt. Bovendien is het propagatie verlies bij 850 nm van de UV-gedefinieerde golfsgeleiders lager dan dat van de geableerde (0.05dB/cm versus 0.13dB/cm). Omwille van deze redenen draagt voor praktische toepassingen het gebruik van UV-gedefinieerde golfsgeleiders de voorkeur.

Naast de problemen die verband houden met het integreren van de optische laag in of op de gedrukte schakeling, is de lichtsignalen in en uit de optische laag brengen een van de grootste problemen. Vertikaal emitterende lichtbronnen (VCSELs) dragen de voorkeur omwille van hun prestatie, kost en fabricage voordelen. Het is duidelijk dat efficiënte koppelstructuren, die de lichtbundel over 90° deflecteren, vereist zijn om deze VCSELs te kunnen gebruiken. 45° micro-spiegels zijn de meest evidente keuze omwille van het feit dat ze golflengte onafhankelijk zijn, een hoge reproduceerbaarheid hebben en kunnen gemaakt worden met een grote variëteit aan technologieën. De KrF excimeer laser bundel kan onder een hoek worden geplaatst, wat het vormen van gehelde structuren zoals 45° facetten vergemakkelijkt. De spiegels zijn op deze manier direct geïntegreerd in de optische laag waardoor hoge alignatie nauwkeurigheden mogelijk zijn.

Twee verschillende spiegel configuraties werden geëvalueerd: een gemetaliseerde spiegel en een totale interne reflectie (TIR) spiegel. De gemetaliseerde spiegel is ingebed in de optische laag en op deze manier beschermd van externe invloed zoals stof en vocht. Ze kunnen bovendien in een meerlaagse structuur gebruikt worden om het licht uit het vlak van de optische laag en tussen verschillende optische lagen te koppelen. Het koppelverlies dat de gemetaliseerde spiegels teweeg brengen is echter onaanvaardbaar hoog. Dit is waarschijnlijk een gevolg van het feit dat het niet mogelijk is om selectief een metaal laag af te zetten op het spiegel facet zonder tevens een zekere afzetting te krijgen op de tegenover liggende wand.

In het geval een TIR spiegel wordt gebruikt, is de 90° bundel deflectie gebaseerd op de TIR die optreedt aan de polymeer-lucht overgang. Het spiegel koppel verlies wordt geschat op ≤ 1 dB en zou eventueel nog kunnen worden verbeterd door gebruik te maken van een gladmakingstap met behulp van CO₂ laser. Omwille van het open karakter van deze spiegel configuratie, is hij gevoelig aan externe invloed. Hij kan tevens niet worden gebruikt in een meerlaagse structuur omdat dit de TIR conditie teniet zou doen. Deze problemen kunnen worden opgelost door het aanbrengen van een Au-coating op het spiegel facet. Het koppelverlies na de metalisatie stap is echter veel hoger dan ervoor. Het blijkt onmogelijk om een homogene Au-coating op het spiegelfacet te bekomen. SEM inspectie leert ons dat er gedurende de ablatie in True-mode een periodieke micro-structuur ontstaat, die mogelijks een verlaring vormt voor het hogere koppelverlies na de metalisatie stap. Een gladmakingstap met CO₂ laser zou ook hier mogelijk een oplossing vormen.

Omwille van deze redenen werd het gebruik van discrete koppel elementen, die in de optische laag gestoken kunnen worden, beschouwd. De discrete koppel elementen bevatten een 45° spiegel die gebruikt wordt om de lichtbundel over 90° te keren en zijn beschikbaar via nauwe samenwerking met Vrije Universiteit Brussel (VUB). Opnieuw zijn twee verschillende configuraties beschouwd: een verwijderbare aanpak en een waarbij de spiegel in de optische laag wordt ingebed. De verwijderbare discrete spie-

gel kan in een micro-caviteit in de optische laag worden gestoken en er weer worden uitgehaald. De ingebedde spiegel is geïntegreerd in de optische laag en levert op deze manier een vlak top oppervlak, wat het plaatsen van opto-electronische elementen of het lamineren van additionele lagen toelaat. De discrete koppelaar wordt in een caviteit in de optische laag bevestigd en bedekt met cladding materiaal. Hij is op deze manier beschermd van externe invloed en kan tevens gebruikt worden in een meerlaagse optische structuur. De ingebedde spiegel veroorzaakt een gemiddeld koppelverlies van 0.3dB, wat beter is dan de performantie van de verwijderbare koppelaar en concurrerend is met resultaten die door andere onderzoeksgroepen zijn bekomen. De hoge koppel-efficiëntie maakt het een ideale kandidaat voor praktische toepassingen.

De golfgeleiders en koppelstructuren die in het voorgaande zijn besproken, zijn in een volgende stap gebruikt in een actieve demonstrator, die werd gebouwd binnen het kader van het network of excellence on micro-optics (NEMO) in samenwerking met partners VUB en VTT Research Centre(Finland). Het gaat over de realisatie van een complete optische link voor een hoge snelheid parallelle optische interconnectie demonstrator, waarvan het ontwerp gebaseerd is op een demonstrator die door VTT werd gebouwd. Belangrijkste doel is de performantie van de originele demonstrator te verbeteren en tevens het aantal gebruikte componenten te reduceren door bijvoorbeeld het weglaten van de micro-lenzen die in de originele demonstrator gebruikt werden om de alignatie vereisten te verlichten. De beste resultaten werden bekomen op een demonstrator bord dat UV-gedefinieerde golfgeleiders in Truemode droge film formulatie bevat en een ingebedde discrete spiegel. Het bord bevat een rij van vier golfgeleiders met een cross-section van $50 \mu\text{m} \times 50 \mu\text{m}$ op een pitch van $250 \mu\text{m}$ en een lengte van 4 cm. Het bord werd opgemeten door VTT in een zender configuratie, met een gelensde VCSEL aan de ingang. Een gemiddelde link efficiëntie van -4.5dB werd opgemeten. De efficiëntie zou nog kunnen verbeteren door de afstand tussen de VCSEL en de optische laag te optimaliseren. Deze link efficiëntie is veel hoger dan degene die werd gemeten op het originele demonstrator bord, en dit zonder gebruik te maken van micro-lenzen om de alignatie vereisten te verlichten. De gemaakte demonstrator maakt een belangrijke bijdrage naar de demonstratie en implementatie van optische interconnecties naar het bord-niveau. Het uitgevoerde werk toont duidelijk aan dat de technologie die binnen dit doctoraatsonderzoek werd ontwikkeld een waardevolle bijdrage levert, vooral op het gebied van koppelstructuren en golfgeleiders.

Naast het koppelen van licht uit het vlak van de optische laag, is het in sommige gevallen ook gewenst om licht horizontaal in te koppelen, in het vlak van de golfgeleiders. Binnen NEMO werd hiertoe een connector ontworpen die gebruikt kan worden om licht van een optische vezel naar een golfgeleider te koppelen en gebruik maakt van passieve alignatie mechanismen. De verschillende onderdelen van de connector worden momenteel samengevoegd en de performantie van de connector zal in de nabije toekomst worden geëvalueerd.

Summary

In present and future broadband networks, multi-gigabit transmission over longer distances is only feasible via optical interconnections that form the very heart of the network. Worldwide ongoing research aims at the extension of optical interconnects to the board-level and to the switching-level. Optical interconnections are an attractive solution to solve the bandwidth limitations of electrical transmission lines for board-level interconnections, typically covering distances of a couple of centimeters up to one meter. However, the integration of optical interconnects in a commercial printed circuit board (PCB) imposes severe restrictions on the used materials and processes. The main requirements on the light guiding medium are a low propagation loss, high thermal stability, cost-effective fabrication process and compatibility with the existing PCB manufacturing and soldering processes.

The integration of optical interconnections to the board-level can be done with the use of a polymer optical layer which contains multimode waveguides for the in-plane light propagation. Polymer materials offer a number of advantages over other alternative waveguide media such as glass sheets and optical fibers such as potentially low cost (for a large enough market), the large variety of potential technologies that can be used to pattern the polymer layers and the ability to tailor the properties such as the refractive index and the mechanical and thermal stability. Optical polymers have been developed by laboratories worldwide and some of them have excellent optical and thermal properties.

Main objectives within this PhD thesis is the development of a board-level optical link and the expansion from a single layer optical structure toward a multilayer optical structure. The expansion to multilayer optical structures is interesting because of the increased interconnection density and the possibility to make use of a more relaxed routing scheme. Multilayer structures can in addition fully use the characteristics of 2D opto-electronic elements such as VCSEL and photodiode arrays.

Laser ablation is being studied as an alternative micro-structuring technology that can be used for the patterning of the main building blocks of an optical interconnection into the polymer optical layer. Laser ablation is a flexible, mask-less technology that can be used for the structuring of a large variety of materials, depending on the used laser source. It can be used for fast prototyping, as opposed to mask-based technologies where a mask first has to be designed and fabricated. Changes/corrections can be made to the top surface of the sample in a very late phase of processing. Laser ablation is fully compatible with standard PCB manufacturing and is already used for the laser drilling of micro-vias in high density electrical boards.

The main focus within this research is placed on the use of Truemode Backplane™

Polymer (Truemode) for the optical layer. The material has a low propagation loss of 0.04dB/cm at the targeted wavelength of 850 nm, excellent thermal properties, is fully compatible with standard PCB manufacturing processes and is UV-sensitive, meaning that it can be directly patterned with use of UV-lithography. The material shows an excellent response to KrF excimer laser ablation, allowing the patterning of optical structures with a low surface roughness. The use of three alternative materials (Ormocer®, Epocore/clad, SU-8) is also mentioned. All three materials are UV-patternable and have excellent thermal properties. The optical loss at 850 nm however is higher than for the Truemode material (0.06dB for Ormocer, 0.2dB/cm for Epocore/clad, 0.55dB/cm for SU-8).

Truemode exists in two different formulations: a wet film, which was available from the start of this research, and a dry film, which became available in a later phase. The wet film formulation has to be UV-exposed in proximity mode in a nitrogen environment, which excluded the use of the available mask aligner. As was already mentioned, the Truemode material shows an excellent response to KrF excimer laser ablation. Waveguides with a cross-section of $50\ \mu\text{m} \times 50\ \mu\text{m}$ on a pitch of $125\ \mu\text{m}$ have been ablated into the optical layer and the performance has been evaluated. The waveguide cores have a low surface roughness (average RMS surface roughness of 35 nm on a scan area of $46\ \mu\text{m} \times 60\ \mu\text{m}$) and a propagation loss of 0.13dB/cm at 850 nm, which is acceptable for short-distance links. A two layer optical structure containing arrays of ablated waveguides has been presented. The achievable alignment accuracy is $\leq 5\ \mu\text{m}$, which is within the 0.2dB excess loss range resulting from a numerical study.

The compatibility requirement with standard PCB manufacturing implies that the material has to withstand the high temperature and pressure that occur during a lamination cycle. Measurements show that the performance of the ablated waveguides is not affected by the elevated temperature and pressure that occur during a lamination step, during which the optical layer is embedded between two PCBs. The waveguides also resist to two different accelerated aging tests: an accelerated humidity-aging test and a thermal cycling test. These tests are based on Telcordia 1209-CORE, which are well-accepted standards for passive optical components, and are used to test the performance of the waveguides over their expected lifetime. Thermographic analysis (TGA) measurements indicate that the Truemode material is thermally stable up to temperatures above 300°C. From the above mentioned results, we can conclude that Truemode is a suitable material to use as optical layer.

The dry film formulation can be UV-exposed in contact mode in standard environment, which allows the use of the available mask aligner. The throughput can in this way be considerably increased, in this way decreasing the processing time, because of the parallel character of the process, which means that multiple waveguides or arrays of waveguides can be patterned in the same processing step, in correspondence with the design that is present on the mask. This in contrast to the use of laser ablation, which is a serial process, meaning that the waveguides are patterned one by one. In addition, the propagation loss at 850 nm is lower than the one of the ablated waveguides (0.05dB/cm versus 0.12dB). For these reasons, for practical applications the use of the dry film formulation is preferred.

Besides the problems related to the integration of the optical layer into or on top of the FR4-stack, the major issue is the problem of getting light in and out of the optical layers. Vertical Cavity Surface Emitting Lasers (VSELs) have become the premier choice

for board-level optical interconnections due to their performance, cost and manufacturing advantages. It is clear that in order to be able to make use of these VCSELs efficient coupling structures are needed to deflect the light beam over 90° , out of the plane of the optical layer. 45° micro-mirrors are the most obvious choice for this purpose because of the fact that they are wavelength-independent, highly reproducible, and can be fabricated with a large variety of technologies. The KrF excimer laser beam can be tilted, which eases the patterning of the 45° mirror facet. The mirrors are directly integrated with the optical waveguides, which allows high achievable alignment accuracies.

Two different mirror configurations have been evaluated: a metalized micro-mirror and a total internal reflection (TIR) mirror. The metalized micro-mirrors are embedded into the optical layer, and in this way protected from external influence such as moist and dust. In addition, they can be used for out-of-plane and inter-plane coupling in a multilayer structure. The coupling loss induced by the metalized micro-mirrors however turns out to be unacceptably high. This is most probably a consequence of the fact that it is not possible to selectively deposit a metal coating on the mirror facet without deposition onto the opposite interface.

In the case of the TIR mirror, the 90° beam deflection is based on the TIR that occurs at the polymer-air interface. The mirror coupling loss is estimated to be $\leq 1\text{dB}$ and might be improved by submitting the ablated mirror to an additional smoothing step with use of CO_2 laser. Because of the uncovered nature of the mirror facet, this mirror is susceptible to external influence such as moist and dust. In addition, it can not be used in a multilayer structure. These problems can be solved by applying a Au-coating on the mirror facet and the filling of the ablated trench with cladding material. The performance of the mirror after the metalization of the mirror facet is much higher than before. The metalization of the TIR mirror facet is again the limiting step. It turns out to be impossible to get a homogeneous coating on the mirror facet. SEM inspection of the mirror facet shows that a periodical micro-structure is formed on the mirror facet during the ablation step, and might explain the enormous loss increase after the Au-coating step. A smoothing step with use of CO_2 laser might again solve this problem.

For this reason, the use of discrete coupling elements, which are plugged into the optical layer in a separate step, is considered. The discrete couplers contain a 45° micro-mirror and are available through close collaborations with Vrije Universiteit Brussel (VUB). Again, two different configurations can be considered: a pluggable coupler and an embedded mirror. The pluggable coupler is intended to be plugged in and out of a micro-cavity in the optical layer. The embedded mirror is embedded into the optical layer, in this way delivering a planarized top surface which allows the mounting of optoelectronic elements and/or the lamination of additional layers. The mirror insert is placed in an ablated cavity in the optical layer and covered with cladding material. It is in this way protected from external influence and can be used in a multilayer optical structure. The embedded mirror causes an average coupling loss of 0.3dB , which is much better than performance of the pluggable coupler and is competitive with the results that are currently obtained by other research groups. The high coupling efficiency makes it an interesting candidate for out-of-plane coupling in practical applications.

The waveguides and coupling structures that have been discussed above are in a next step used in an active demonstrator board, which has been built within the framework of the network of excellence on micro-optics (NEMO) in collaboration with partners Vrije Universiteit Brussel (VUB) and VTT Research Centre Finland. It deals with the

realization of a complete optical link for a high-speed parallel optical interconnection demonstrator, based on a demonstrator that has been fabricated at VTT. Main aim is to improve the performance of the original board while at the same time not making use of the micro-lenses which were in the original board used to relax the alignment requirements. The best results are obtained on a demonstrator board that contains an array of four waveguides with a cross-section of $50\ \mu\text{m} \times 50\ \mu\text{m}$ on a pitch of $250\ \mu\text{m}$ and 4 cm length and an embedded micro-mirror for out-of-plane coupling. The board has been evaluated by VTT in a transmitter configuration, with a lensed VCSEL at the input. The link has an average efficiency of 4.5 dB, which can most probably be improved by optimizing the distance between the lensed VCSEL and the optical layer. The link efficiency is much higher than the one measured on the original board, and this without making use of micro-optics to relax the alignment requirements. The fabricated demonstrator makes a significant contribution toward the demonstration and implementation of optical interconnections to the board-level. The work done clearly demonstrates the benefit of the technology developed in this thesis, and more specifically regarding the coupling structures and the waveguide fabrication.

Besides coupling out of the plane of the optical layer, it is in some cases also desirable to couple light in horizontally, in the plane of the waveguides. Within NEMO, a fiber-to-waveguide in-plane connector has been designed for this purpose, which uses passive alignment to arrange the alignment between the waveguide end facet and the fibers. The different parts of the in-plane connector are currently being put together and the performance will be evaluated in the near future.

Thanks

Ik zou graag mijn promotor Peter Van Daele bedanken voor de ondersteuning gedurende de duur van mijn doctoraat en de steeds optimistische blik op de zaak (zoals het mislukken van experimenten nooit gedacht dat spiegels metalizeren zo veel problemen ging geven) en om altijd klaar te staan om artikels kritisch na te lezen en suggesties te geven. Andre Van Calster, bedankt om de TOPIC groep op te nemen binnen CMST en om altijd geïnteresseerd naar onze vorderingen te luisteren.

Erwin, Geert, Jona, Nadine, Peter, Steven, Wim bedankt om het 4 jaar met me uit te houden. Ik heb echt een ongelofelijk leuke tijd gehad bij jullie! Zorg goed voor de sanseveria (hij heeft een woelige geschiedenis) en de reusachtige vetplant (waarvan we wel meer dan een keer hebben gedacht dat hij zelfmoord gepleegd had). Wim, nog eens extra bedankt voor het begrijpend gevoel tijdens het schrijven. Geert, bedankt om alles na te lezen!! Bram, ik hoop dat je er in slaagt mijn oude bureau iets minder chaotisch te houden dan bij mij het geval was een gouden raad, gooi tussen door eens samples weg, of schenk ze weg aan een ongelukkige voorbijganger.

Mensen van VUB (Christof, Heidi, Hugo en Michael en alle andere mensen die ik regelmatig zag in Jette): bedankt voor de fijne samenwerking. Jürgen, special thanks to you! Ik vond de samenwerking erg efficiënt en ben er nog steeds van overtuigd dat we een aantal heel toffe demonstratoren hebben gemaakt (en een hele hoop artikels samen geschreven). People at VTT (Pentti, Mikko, Teemu and all the others), I really enjoyed the collaborations and would like to thank you again for hosting two marvelous meetings in Oulu.

Ook zou ik graag de leden van de jury bedanken voor hun bereidwilligheid om in de jury te zetelen. Pentti, special thanks to you, for coming all the way from Oulu for my private defense!

Last but not least ... uiteraard zou ik ook graag mijn ouders bedanken, mijn broer en zus en hun aanhangsels en ook kleine Juliette. Bedankt om me op zijn minst de indruk te geven dat jullie mijn doctoraat echt interessant vinden (en ook zeker dit boek gaan lezen en daarna een ereplaats in de kast gaan geven). Bedankt aan iedereen die hier vandaag aanwezig is voor jullie interesse. Xavier, bedankt voor je enorme geduld en voor je steun ...

Contents

1	Introduction	1
1.1	Rationale to using optical interconnections	1
1.2	Optical board	6
1.2.1	Integration to the board-level	6
1.2.2	In-plane light propagation	9
1.2.3	Optical coupling concepts	11
1.2.4	Connectorization	12
1.3	Expansion to multilayer optical structures	13
1.4	State-of-the-art	13
1.4.1	Terabus (IBM): high-speed parallel optical link demonstrator .	13
1.4.2	Multilayer optical interconnection demonstration	14
1.4.3	Coupling structures	16
1.5	Objectives	19
	Bibliography	21
2	Optical polymers	27
2.1	Introduction	27
2.2	Polymers	28
2.2.1	Polymer classification	28
2.2.2	Polymerizability	30
2.2.3	Radical addition polymerization	31
2.2.4	Physical properties	32
2.2.5	Optical loss	35
2.3	Optical polymers	36
2.3.1	Truemode Backplane™ Polymer	38
2.3.2	Alternative polymer materials	48
2.3.3	Epocore/clad	52
2.4	Conclusion	53
	Bibliography	55
3	Multimode optical waveguides	57
3.1	Introduction	57
3.2	Requirements	57
3.3	Multimode optical waveguides	58
3.3.1	Waveguide structure	58
3.3.2	Waveguide processing	60

3.4	Laser ablated waveguides	61
3.4.1	Truemode Backplane™ Polymer	61
3.4.2	Laser ablation	63
3.4.3	Experimental results	67
3.5	Photolithographic waveguides	73
3.5.1	Dry Truemode formulation	75
3.5.2	Ormocer	77
3.5.3	SU-8	77
3.5.4	Epocore/Epoclad	78
3.6	Increased integration density	78
3.6.1	Experimental results	80
3.7	Small core waveguides	80
3.8	Multilayer optical structures	83
3.8.1	Numerical study alignment tolerance	85
3.8.2	Experimental results	88
3.9	Conclusions	92
	Bibliography	96
4	Integrated coupling structures	99
4.1	Introduction	99
4.2	Metalized 45° micro-mirror	101
4.2.1	Numerical simulations	101
4.2.2	Experimental results	113
4.2.3	Characterization	136
4.3	Total internal reflection mirror	136
4.3.1	Numerical simulations	137
4.3.2	Experimental results	140
4.3.3	Characterization	141
4.4	Conclusion	148
	Bibliography	148
5	Discrete coupling structures	151
5.1	Introduction	151
5.2	Pluggable couplers	152
5.2.1	Out-of-plane coupler	152
5.2.2	Inter-plane coupler	161
5.3	Embedded micro-mirror	165
5.3.1	Experimental results	166
5.4	Characterization	171
5.5	Conclusion	173
	Bibliography	174
6	Reliability and stability	177
6.1	Introduction	177
6.2	Reproducibility	179
6.3	Accelerated aging tests	182
6.3.1	85/85 test (85°C/85% relative humidity)	182
6.3.2	Thermal cycling	184

6.4	Thermal stability	186
6.5	PCB manufacturing	186
6.5.1	Lamination	186
6.6	Solder reflow	189
6.7	Conclusion	192
	Bibliography	192
7	Demonstration of on-board optical interconnects	195
7.1	Introduction	195
7.2	Active demonstrator	195
7.2.1	First generation active demonstrator	199
7.2.2	Second generation demonstrator board	205
7.2.3	Conclusion	208
7.3	In-plane connector	209
7.3.1	Connector design	210
7.3.2	Processing of the PCB substrate	215
7.3.3	Application of the optical layer	218
7.3.4	Ablation of the openings in the laminated stack	218
7.3.5	Insertion of the micro-spheres	222
7.3.6	Mounting of the base plate and the fiber alignment plate	222
7.3.7	Conclusion	224
7.4	Conclusion	224
	Bibliography	225
8	Conclusion	227
8.1	Placing the work into context	227
8.2	Future work	230
	Publication list of the PhD candidate	231
	List of figures	251
	List of tables	254

Chapter 1

Introduction

1.1 Rationale to using optical interconnections

In present and future broadband networks, multi-gigabit transmission over longer distances is only feasible via optical interconnections that form the very heart of the network. Worldwide ongoing research aims at the extension of optical interconnects to the board- and switching-level. In spite of repeated predictions that the all-optical interconnect is soon going to replace the electrical interconnect on the board-level, this turned out not to be yet the case. Several reasons can be given for this, but the two most important ones are that it turned out to be more difficult than expected to integrate optical interconnects in an easy and cost-effective way into or onto a board. The second reason is that, as can typically be expected from a technology with a large investment base, the possibilities in terms of maximum bitrates of electrical board interconnect are continuously being upgraded, postponing the need for replacement by optical interconnect [1], [2].

Many systems are rack-based backpanel configurations with interconnection lengths ranging from a few centimeters to a few meters. It is crucial that, in order to be low-cost and accepted by system engineers and designers, the introduction of optical interconnections on this level should be compatible with existing printed circuit board (PCB) manufacturing technology. Therefore, optical interconnections should be integrated in or on FR4-based printed circuit boards. The same can be said of the interconnections at even shorter distances (on MCM-level) where compatibility should be sought with existing MCM-technology, chip-packaging and Chip-on-Board technologies.

The required compatibility with the existing technology implies, in most cases, alignment tolerances of traditional electrical packaging and mounting technologies, which are not in line with required optical performances. Reasons for configuring optical interconnects for compatibility with surface mount assembly are low cost and compatibility with high-volume production rates. The assembly cost for optical interconnects is driven by optical alignment tolerance requirements. The alignment requirements can be relaxed by expanding the light beam at the assembly interface with use of micro-optics. The beam can in this way be expanded and collimated across the assembly interface and focused at the edges [3]. For this reason, micro-optics will play a crucial role in achieving good optical performances, together with existing tolerances within

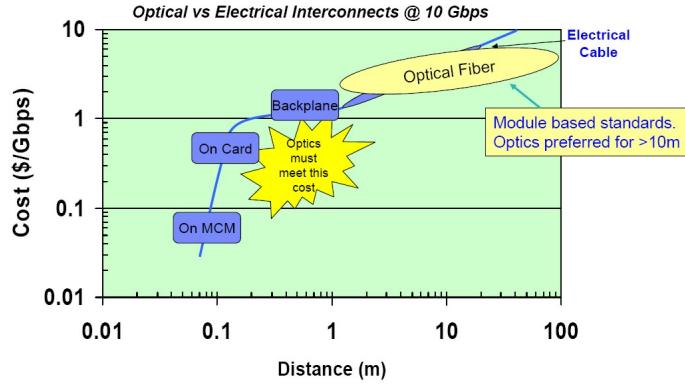


Figure 1.1: Relation between cost and distance for an electrical versus optical link at 10Gb/s (Courtesy of IBM).

the board manufacturing technology.

When discussing optical interconnections over short(er) distances, one should keep in mind the application one is looking for:

- the situation where optical signals are arriving into the cabinet from optical fibers coming from long haul interconnections, and into which signals have to be switched, repeated or decoded. In this case the arriving signal will be on a wavelength of 1.3 or 1.55 μm and the fibers will be single mode (SM), requiring similar wavelengths and modal structures on the boards
- the situation where processors on the same or different boards within the same system have to communicate at high bitrates, but over short distances, which will imply a multimode (MM) structure and most probably also a less stringent requirement on wavelength dependent losses.

Fiber-optic communication links dominate over copper wire electrical signaling in high-speed communication networks for distances over several hundred meters in length due to the superior bandwidth-distance performance of the optical channel. However, as distances become shorter, copper-based interconnects become the dominant solution because they are simpler, cheaper, and more reliable. A graphical representation of the relation between cost and link length for an electrical link versus an optical link at 10Gb/s is given in Fig. 1.1. From this graph, it is clear that the cost of electrical links increases considerably as the length increases. From a certain interconnection length on, the use of optical interconnections becomes more cost-effective than the use of electrical interconnects. This transition length decreases with increasing bandwidth. The biggest challenges for the introduction of optics to shorter lengths is the development of suitable coupling structures and the compatibility of the proposed solution with the existing PCB manufacturing and soldering technology.

Without any doubt, as the performance of microprocessors continues to increase, the data flow to and from the processors becomes a more and more dominant bottleneck for the overall system performance. The challenges in getting optical interconnections

into the product roadmap are numerous [4]. Due to the stringent reliability requirements of high-end servers, only mature technologies have a chance of being included on product roadmaps. Such machines are complex systems that have evolved over years. Changing one piece usually influences many other parts too. Product developers therefore consistently show a clear preference to change things only incrementally. We have to face the reality that a printed circuit board with integrated waveguides, in spite of being an attractive option, is a very disruptive step to start with. High-end servers continue to be prime candidates for employing PCBs with integrated optical layers, but realistically they cannot be a first application. The first question almost immediately leads to the question of cost and performance. If we could deliver an optical solution with the same performance as an existing electrical solution (incl. reliability, etc) at a lower overall cost, it would most certainly be used. Reducing cost of all elements and processes of the technology is therefore the central guideline for the further technology development. A very important task in this context will be standardization, because it enables economies of scale and facilitates acceptance. Clearly, the wish for standardization comes along with the wish to narrow down the large number of technical concepts that are being considered in this area. Betting on large volumes alone to reduce cost, however, will not be enough, because board-level optical interconnects are unlikely to be used in large volumes anytime soon if the cost does not come down in the first place. Additional innovation will be required to break out of this predicament. Several drivers exist for using optical interconnections:

- higher speed, higher bandwidth
- higher density (Gb/s/mm² and Gb/s/cm²)
- lower electro-magnetic interference
- lower weight
- lower power consumption (Gb/s/W)
- cooling/heat dissipation.

Optical interconnections without any doubt offer a considerable bandwidth advantage over electrical interconnects. Beyond 10 GHz, copper interconnects on printed circuit boards (PCBs) made of FR4 material, become bandwidth-limited due to frequency-dependent losses such as the skin effect in conductors and the dielectric loss from the substrate material. Above 1 GHz, dielectric losses rapidly become larger than the skin effect losses, leading to a predicted insertion loss of approximately 50 dB for a 50 centimeter long link in a standard FR4 material at 10 GHz [5]. The evolution of the FR4 losses as a function of frequency is given in Fig. 1.2. It has been reported that replacing the FR4 material with newer laminates such as Rogers 4000, the bandwidth of electrical interconnects can be extended by a factor of two, but also increases the cost by a factor of five [6]. This effect can be seen in the graph in Fig. 1.3, which shows that the use of Rogers instead of standard FR4 material allows an increase in the maximum achievable data rate for a given link length.

It should however be emphasized that bandwidth is not the only driver. A first motivation to make use of optical interconnects is the increased interconnection density, which implies that they can solve the space-bottleneck on backplanes. The bandwidth

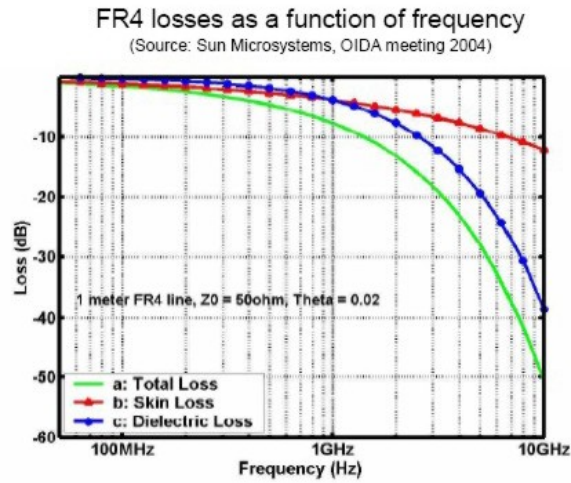


Figure 1.2: Evolution of the FR4 losses as a function of frequency.

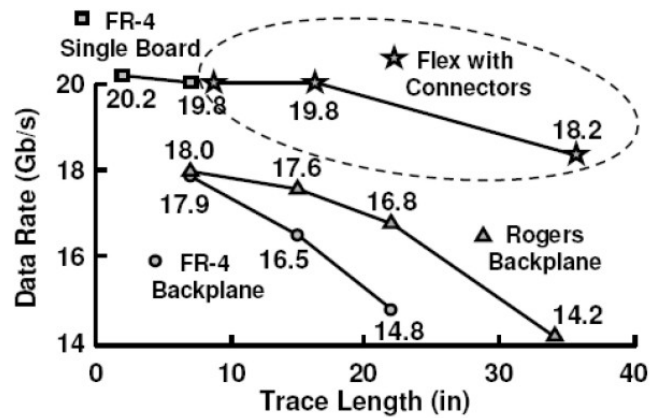


Figure 1.3: The graph shows that the use of low loss tangent dielectric material such as Rogers instead of FR4 has a positive effect on the maximum data rate that can be achieved for a given link length [7].

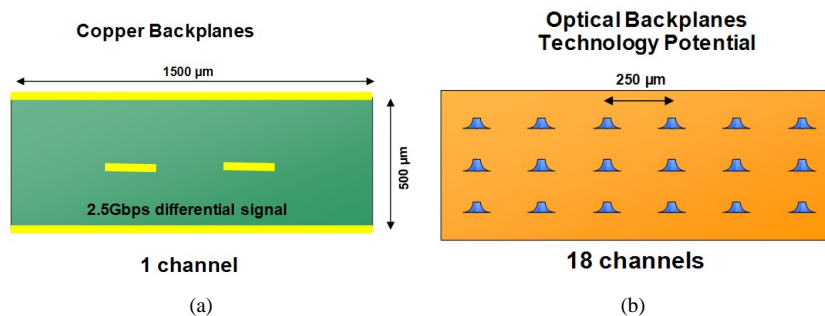


Figure 1.4: (a) Typical dimension of a copper channel; (b) number of optical channels that fit the same cross-section as the copper channel (Courtesy of FCI).

of electrical links is proportional to the cross-sectional diameter and inversely proportional to the link length. This means that narrow line widths and spacings are required to obtain a high density. This consequently also increases the cross-talk and parasitic capacitance, with a higher power consumption as a result. In Fig. 1.4, the dimension of a copper channel is compared to the number of optical channels that fit the same cross-section, and clearly demonstrates the density advantage.

The practical difficulties of dealing with the weight and bulk of electrical cables is a major incentive to utilization of optics. The weight reduction is not only positive for the connector reliability, the use of optical channels also makes the systems less bulky and better organized. In addition, it offers a possible way to solve the cooling bottleneck in computing systems. Densely packed copper cables obstruct the air flow, in this way negatively influencing the cooling.

Weight is currently a major driver for shifting from the electrical to the optical domain in practical applications. This is mainly because the weight reduction can cause a considerable cost reduction. Optical interconnections are nowadays already present in high-end cars, where they introduce a substantial weight reduction, and consequently lower fuel consumption. A standard car has approximately 3 km of Cu-wires in it, with an associated weight of about 50 kg. Replacing these Cu-wires with (plastic) optical fibers can reduce the weight considerably. Modern cars have between 300 and 3000 information-nodes and contain a network for multimedia applications and a network of sensors for extra security and safety. The same holds for airplanes and satellites, where the use of optical interconnections can introduce a considerable decrease in fuel consumption and associated cost reduction because of the lower weight.

The signal integrity at higher speed in electrical links has over the last few years been improved considerably through the use of low-loss tangent materials, with the associated increase in cost, and techniques such as pre-emphasis and equalization, which improve the signal quality but also increase the power consumption [8]. Optical links offer a possible power advantage because of the fact that they can be more closely integrated with the transmitter and receiver units.

1.2 Optical board

Within and between systems, different levels of interconnection can be recognized:

- multi-chip module (MCM) level interconnections which can be either intra- or inter-chip, with distances typically on the order of a few microns to tens of microns (intra-chip) to 100mm (inter-chip)
- board-level or inter-MCM interconnections with typical link distances up to 50cm
- board-to-board or backplane level interconnections with typical link distances below 5m
- interconnection between systems or inter-cabinet or frame-to-frame interconnections with typical distances up to 500m.

Main focus within this PhD thesis is at the backplane level. The approach that can be followed to integrate optical interconnections to the backplane-level will be discussed in the next section. We will first have a look at the different guiding media that can be used and then focus on the main building blocks: optical waveguides, coupling structures and connectorization.

1.2.1 Integration to the board-level

The integration of optical interconnects in or on a commercial PCB imposes severe restrictions on the used materials and processes. The main requirements on the light guiding medium are a low propagation loss at the targeted operating wavelength, high thermal stability, cost-effective fabrication process and compatibility with the existing PCB manufacturing and soldering processes.

The integration of the optical interconnections to the board-level can be done in a variety of ways. The use of glass fibers, which have already proved their potential for long-haul links, seemed the logical first choice. Glass optical fibers have an extremely low propagation loss, and excellent thermal and mechanical properties. However, the routing of optical fibers on top of the mounted electronic components and on top of the FR4 board, requires extra fiber length to overcome the problems related to the minimum radius of curvature of the optical fiber to minimize optical losses and to allow re-cleave and re-connectorization of the fibers [9] [10]. In addition, it is rather complicated to create passive splitters or couplers. To provide these functions, a splitter or combiner has to be spliced to the necessary fibers. This makes it a rather expensible and expensive solution. Optical backplanes based on this solution are commercially available, but in most cases it consists of passive backplanes where the optical layer is used for purely passive interconnection [11]- [13]. The approach of using optical fibers is currently still being studied, in an attempt to exploit the advantages offered by optical fibers and overcome the limitation, for instance with the use of a special high index optical fiber with reduced cross-sectional dimension, shown in Fig. 1.5, and enhanced coupling method [14].

Instead of using optical fibers as the guiding medium, one can also turn to waveguiding solutions, where optical waveguides are defined in a layer, which is integrated inside

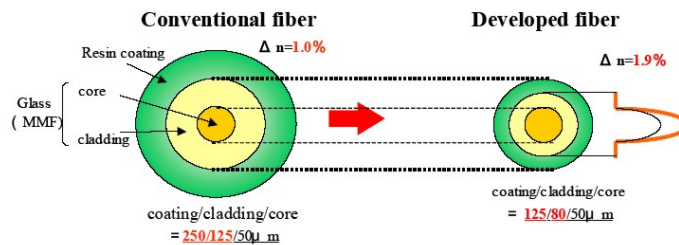


Figure 1.5: Schematic of the developed fiber with small diameter and high refractive index contrast [14].



Figure 1.6: Double-sided optically functionalized thin glass with waveguide dimensions of approx. $53 \mu\text{m} \times 110 \mu\text{m}$, fabricated by silver-ion exchange using a salt melt [15].

or on top of the PCB-stack. This optical layer can be based on several materials such as for instance glass sheets and polymers. The use of glass sheets offers some advantages over polymer materials: glass has a very high transparency at 850 nm; its coefficient of thermal expansion (CTE) is around 7 ppm/K, matching the CTE of the FR4 material, typically 14-16 ppm/K, which improves the thermal stability of the PCB stack; excellent thermal and mechanical behaviour (glass typically has a glass transition temperature over 550°C); and compatibility with the existing PCB manufacturing processes. The waveguides can be patterned into the glass sheets using technologies such as ion-exchange [15], and chemical etching, even though the use of the latter requires the filling of the patterned layer with for instance a polymeric material [16]. The use of ion-exchange for the patterning of low loss waveguides into the glass sheet is promising, main drawback are the high required process temperature (350°C) and clean environment, which makes the technology less compatible with current PCB manufacturing processes.

Currently, the use of a polymer optical layer is being studied by groups worldwide [17]-



Figure 1.7: Cross-section of a polymer waveguides with a cross-section of $50 \mu\text{m} \times 50 \mu\text{m}$ (left) and $35 \mu\text{m} \times 35 \mu\text{m}$ (right) [18].

[26]. An example of a patterned polymer waveguide is shown in Fig. 1.7. It is also the approach that is followed in this PhD-thesis to integrate the optical interconnection to the board-level. Optical polymers with excellent optical and thermal properties have been engineered in laboratories worldwide over the last few years [27]. Polymeric materials are particularly attractive in integrated optics because of their ability to be processed rapidly, cost-effectively, and with high yields. An important feature of polymers is the possibility to tune the refractive index contrast, which can have values up to 35%, enabling high-density compact waveguiding structures with small radii of curvature.

The main requirements on the polymer optical layer, which can be integrated into or on top of the PCB, are the following:

- possibility to pattern polymer waveguides into the optical layer, which have a low propagation loss at the targeted operating wavelength of 850 nm. The used patterning process be simple, cost-effective and preferably compatible with PCB manufacturing techniques.
- the polymer material must have a high temperature resistance to withstand temperatures incurred during standard PCB lamination and component solder reflow processes. This means that the technology must achieve reliable operation at temperatures up to 180°C over a period of one hour, in a high pressure environment, similar to the temperature and pressure conditions that the board would endure in the course of a lamination step. The board must also be able to experience temperatures of up to 240°C for a period of 10 seconds, as this can be expected during a solder reflow process,
- the optical backplane must be sufficiently robust to environmental factors such as humidity, fluctuations in temperature, mechanical stress and corrosive environment. This is especially an issue for the case where the optical layer is integrated on top of the PCB. The performance of the optical backplane has to be reliable, not only on the short-term but also on the longer-term.
- the coupling technology used to interconnect active opto-electronic devices to the passive waveguides must be simple, cost-effective and where possible use conventional pick-and-place assembly equipment.

Currently, a couple of optical polymers exist that have excellent optical and thermal properties, however they only have a limited availability and a high price. Polymers with acceptable optical loss and good thermal and mechanical properties that are commercially available at lower cost, also exist but can only be used for shorter interconnection lengths.

Looking at the use of conventional pick-and-place assembly equipment, it should be mentioned that the alignment of active devices to passive waveguides is a huge challenge. For example, for a single mode structure with a 5 μm diameter core the necessary alignment tolerance is $\pm 0.5 \mu\text{m}$. For multimode structures, where the core diameter is typically between 30 and 100 μm , an alignment accuracy of $\pm 10 \mu\text{m}$ is required. For this reason, multimode technologies are being focused upon. One of the major disadvantages with multimodal transmission is the high level of dispersion that exists within such waveguides. However, for the optical backplane, with targeted distances

ranging from a couple of centimeters up to one meter, it is expected that this problem will not play a significant role and are ruled out by the advantage of the more relaxed alignment tolerance. For this reason, multimode waveguides are used to guide the light in the plane of the polymer optical layer.

Multimode optical technologies have the advantage of being potentially low-cost in comparison with single-mode solutions because of the more relaxed alignment requirements. The major drawback stems from the limited bandwidth-length product due to modal dispersion, which is however acceptable for the targeted propagation distances of a couple of centimeters up to one meter. Several factors contribute to the low-cost prospect of multimode technologies:

- the large core of the multimode fiber/waveguide, typically $30\ \mu\text{m}$ to $100\ \mu\text{m}$, allows relaxed alignment tolerances for coupling to an optical receiver or to other fiber segments. Expensive alignment tools and procedures, needed in the case of single mode technology, can be avoided. The aim is to obtain compatibility with standard SMD assembly for the mounting of the opto-electronic elements onto the board, in order to reduce the assembly cost.
- in general, the multimode integrated optical components require a lower fabrication precision than single mode components.
- cheap and reliable light sources such as VCSEL arrays are widely available in the range of 600-900nm. These light sources can be coupled to multimode fibers or planar waveguides with the use of suitable coupling structures.

It is clear that with the use of vertical emitting light sources such as VCSELs, coupling structures are required to couple the light signals in and out of the optical waveguides. Another important issue is the connectorization between an optical fiber and a board-level integrated waveguide. In the following sections, we will first discuss the use of multimode waveguides for the in-plane light propagation and then focus a bit more on coupling structures and connectorization .

1.2.2 In-plane light propagation

Multimode waveguides can be patterned into the polymer optical layer with a large variety of technologies among which UV-lithography, embossing and laser direct writing are the most widely studied. We will briefly discuss these technologies in the following paragraphs.

UV-lithography

Some of the developed optical polymers are UV-sensitive, meaning that they can be directly patterned using standard UV-lithography. Photolithographic waveguides have been structured into the polymer optical layer by a number of research groups for different polymer materials. Multimode waveguides with propagation losses $\leq 0.05\text{dB/cm}$ have been presented, for instance in [28]. The processing steps that are required for the patterning of the waveguides into the optical layer are the following:

- application and curing of the lower cladding layer.

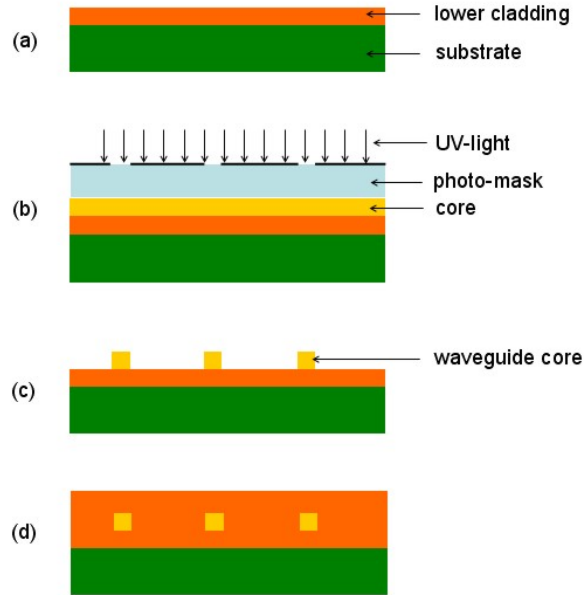


Figure 1.8: (a) Application and curing of the lower cladding layer; (b) application of the core layer, followed by the patterning of the core layer using UV-exposure through a suitable mask and the development of the UV-exposed layer; (c) after the development step, for the case of a negative resist type polymer, the waveguide cores remain on the sample while the remaining part of the layer is washed off; (d) the waveguide cores are coated with the top cladding layer, and are after this step surrounded by cladding material.

- application of the core layer.
- patterning of the core layer by UV-exposure through a lithographic mask with the desired waveguide pattern. The mask can be placed either in contact mode, in which case the mask and the sample are in physical contact, or in proximity mode, in which case a small air gap is present between the sample and the mask.
- development of the patterned core layer using a suitable developer, leaving the desired waveguide pattern.

The processing steps for a negative resist type of polymer, meaning that the UV-exposed areas are cross-linked and will remain on the sample after the development step, are schematically depicted in Fig. 1.8.

UV-lithography is compatible with standard PCB manufacturing and is a parallel process, meaning that multiple waveguides can be patterned at the same time according to the mask design, which allows a high throughput and low processing time. The quality of the patterned waveguides depends on the quality of the photomask and the homogeneity of the light intensity of the used UV-source. The surface roughness of the waveguide sidewalls can be extremely low, in this way minimizing the scattering loss. Main drawback is the limited size of the mask, which requires the use of a stepper for

the patterning of meter-long waveguides.

Embossing

The main investment for embossed structures is the cost of a good shim or mold [29], which can be either rigid or flexible [30]. Both hot embossing [31], [32], [33], in which case an increased temperature is used to transfer the pattern from the mold to the polymer layer, and UV-embossing [34], [35], in which case UV-exposure is used to transfer the pattern, can be used. The advantage of UV-embossing is the fact that shrinking of the polymer can be avoided because there is no cooling step involved. The quality of the mold will to a large extent determine the quality (i.e. surface roughness) of the waveguide sidewalls.

The embossing process can be easily integrated into the existing PCB manufacturing processes, and is a relatively easy process. Main drawback of the embossing technique is the fact that it is difficult to pattern waveguides on large panels because of the difficulty of producing a large high-quality mold.

Laser direct writing

Another approach to forming waveguides in photosensitive optical polymers is the use of laser direct writing. The technique of laser direct writing has the advantage of being maskless, allowing rapid and inexpensive prototyping in contrast to conventional mask-based photolithographic approaches in which case a mask first has to be designed and fabricated before waveguides can be produced. The waveguide cores can be written into the core layer by scanning the laser beam over the surface according to the desired pattern [36], [37], [38]. The technique is capable of patterning features with long and linear dimensions over comparatively large planar areas. Features can be written in restricted regions on the sample, without affecting the surrounding area. Laser direct writing can play a role in the fabrication of large dimension parts where masks can not be produced. High scanning speeds can be obtained (up to 5 cm/s) which makes it a fast patterning technique, despite the serial character.

1.2.3 Optical coupling concepts

Besides the problems related to the integration of the optical layer into the FR4-stack, the major issue is the problem of getting light in and out of the optical layers. The coupling problem might ultimately decide on which technology will be used. As in most cases, both in micro-electronics and opto-electronics, the mounting and packaging of the components is by far the most expensive part of the whole fabrication process, and in this case, this is not different. The choice of a good, flexible, cheap, stable and preferably quite standard coupling process might be detrimental for introducing the optical layers into mass production PCBs.

Vertical Cavity Surface Emitting Lasers (VSELs) have become the premier choice for optical interconnections due to their performance (high-modulation bandwidth, low power consumption, high efficiency) and manufacturing advantages (amenable to high-volume production, wafer-level testing, and ease of integration). 90° beam deflection is required to couple light from the VCSEL to the optical waveguide. This can for

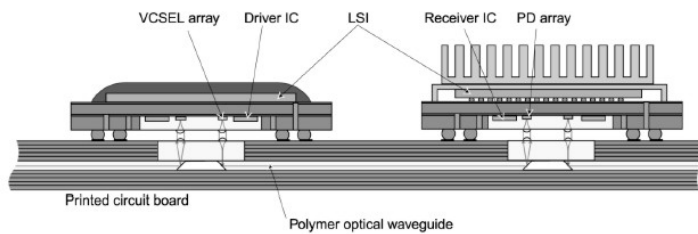


Figure 1.9: Flip-chip optical interconnection based on the Optobump concept [50].

instance be done with the use of a 45° micro-mirror. 45° micro-mirrors have the advantage of being wavelength independent, highly reproducible and can be fabricated with a large variety of technologies such as micro-dicing [39], V-shaped diamond blade [40], [41], embossing [30], [34], reactive ion etching [42] [43] and X-ray lithography. This makes them advantageous over other coupling approaches such as for instance the use of grating couplers [44], which are highly wavelength dependent and require more complicated fabrication processes, not always compatible with the PCB manufacturing and soldering processes.

Alternative coupling approaches are the use of a discrete coupling element [45], [46], a 45° -ended connection rod, 45° -ended waveguide with active interposer or the use of an optical pillar to increase the coupling efficiency [47], [48].

1.2.4 Connectorization

Another challenge on the way to the envisioned integration of optical links with PCBs is the gap in typical alignment tolerances between the world of PCBs and the world of optics. In PCB manufacturing, the precision of single process steps is in the order of $20\ \mu\text{m}$, which typically sums up to $100\text{-}200\ \mu\text{m}$ for a finished PCB, depending on its size. In optics however, a typical channel pitch is $250\ \mu\text{m}$, and the mutual alignment tolerances in the order of $5\text{-}10\ \mu\text{m}$ are required to avoid excess losses and crosstalk. The aim is to bridge this gap in a cost-effective way, using passive alignment concepts. The proposed solution should in addition be compatible with standard PCB manufacturing and soldering processes. An example of such a large-tolerance integration concept that is fully compatible with standard surface-mount technology is briefly discussed in the following paragraph. This example clearly shows that it is possible to make use of surface mounting technology in case micro-optics is used to increase the alignment tolerance range.

Optobump

In the last few decades, the cost of PCB assembly has decreased by the introduction of surface-mount technology (SMT). In addition to making both-sides assembly possible, the SMT has great advantages in low-cost mass-production supported by high-speed pick-and-place machines. As a further step toward low-cost packaging and assembly, an optical I/O packaging concept called Optobump, which is fully compatible with SMT is presented in [49] [50] [51]. The Optobump principle is shown in Fig. 1.9.

Multi Gb/s signals are E/O converted in the package and transmitted to the PCB across a narrow air gap. The package is surface-mounted on a PCB containing a polymer optical waveguide as an inner layer. An array of solder bumps and an array of polymer microlenses are situated on the bottom of the package. Another array of polymer micro-lenses is formed on top of the PCB to optically couple the package and the PCB by means of collimated beams which are wide enough to provide a large tolerance to unavoidable misalignments during SMT processes. To achieve a high density in the interface, solder bumps serve to increase the mounting accuracy through a self-alignment technology. An optical interface like this employing microlenses is called an OptoBumps interface, in accordance with the electrical interface using solder bumps. Total internal reflection (TIR) mirrors are formed at both end facets of the waveguides in the PCB to deflect the light beam over 90° . The 45° mirrors are fabricated by using a dicing saw with a 90° V-shaped diamond blade. Experiments on the alignment tolerance between a VCSEL and a waveguide revealed that the OptoBump interface provides a tolerance of $\pm 50 \mu\text{m}$, which is large enough for use with the SMT process.

1.3 Expansion to multilayer optical structures

The use of multiple optical layers, stacked on top of each other, is a possible way to increase the interconnection density. The light signals can be guided from one layer to another with the use of 45° micro-mirrors, which are embedded into the optical layer. For high-density interconnects, this option can be more interesting than the use of one single layer, because a much lower number of cross-overs are required to route the signals from source to destination. It is clear however that the coupling between the layers has to be sufficiently efficient in order to get an advantage over the use of a single layer. Next to allowing a more relaxed routing scheme, the characteristics of two dimensional opto-electronic elements such as VCSEL and photodetector arrays can be fully exploited.

The alignment between the optical elements such as waveguides and mirrors has to be sufficiently accurate in order to allow high achievable coupling efficiencies between the different layers. It is believed that a two layer optical structure is sufficient to fulfill the current density needs. Each additional layers requires a longer processing time and also increases the propagation distance that the light signals have to cover when they are coupled from one layer to another or coupled out of the plane of the waveguides.

1.4 State-of-the-art

1.4.1 Terabus (IBM): high-speed parallel optical link demonstrator

In the Terabus program, parallel optical interconnects are being developed for terabit/s-class chip-to-chip and module-to-module communications through printed circuit boards with integrated optical waveguides. The data links are enabled by parallel transceiver modules, or Optomodules, that incorporate key technologies including: high-speed, low-power CMOS analog amplifier circuits; efficient, high-speed 985 nm substrate illuminated/emitting photodiode (PD) and VCSEL arrays with integrated collimating

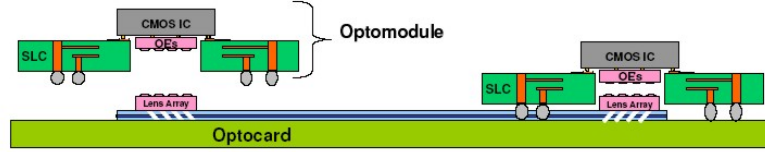


Figure 1.10: Schematic of the Terabus board-level optical link. Two optomodules are connected through an array of polymer waveguides in the optocard [52].

lenses; and the extensive use of flip-chip packaging to minimize the module dimensions and associated packaging parasitics. The core of the module is an Optochip: a $5.25\text{mm} \times 3.25\text{mm}$ single-chip CMOS optical transceiver IC with flip-chip attached 4×4 VCSEL and PD arrays. The Optochip is then flip-chip attached to a high-density organic package to form the Optomodule. A conventional ball grid array (BGA) solder process is then used to mount this low-cost, low-profile package on a printed circuit board with integrated optical waveguides (Optocard). Polymer waveguides with a cross-section of $35\mu\text{m} \times 35\mu\text{m}$ on a $62.5\mu\text{m}$ pitch are incorporated in the FR4-based Optocard. Optical and electrical connections are simultaneously established during the Optomodule-to-Optocard attachment. A schematic of the Terabus board-level optical link is shown in Fig. 1.10. More details on the built-up and fabrication of the modules and an evaluation of the performance can be found in [52].

The transceiver is designed to be used with 985 nm substrate-emitting opto-electronic arrays. The VCSEL and photodiode arrays incorporate lenses into the back surface, which are designed to collimate the VCSEL output or to focus the light onto the photodiode. The optomodule incorporates a cutout in the center of the module, fabricated at the position of the opto-electronic array. The cutout enables the optical coupling from the opto-electronic array to the waveguides on the optocard. A photolithographic process is used to fabricate the waveguide cores using a photo-sensitive acrylate polymer material. Total internal reflection (TIR) mirror arrays were also fabricated in the waveguides using a laser ablation process to provide the 90° -turning from the waveguides. A collimating lens array is aligned and attached to the mirror array to facilitate optical coupling from the optocard to the optomodule.

The alignment tolerance realized in the prototype optical system allows offsets up to $\pm 35\mu\text{m}$ for the transmitter and up to $\pm 70\mu\text{m}$ for the receiver. The relaxed tolerances provide greater compatibility with typical board-level package assembly tools. The optocard full link assembly demonstrates a complete chip-to-chip optical interconnect on a printed circuit board. The optocard link demonstrates a highly integrated board-level optical data bus providing 160Gb/s bidirectional transfer rate.

1.4.2 Multilayer optical interconnection demonstration

Only a limited number of groups have demonstrated the fabrication of a multilayer optical structure. Both the stacking of individual waveguide layers and UV-lithography can be used to fabricate a multilayer waveguide structure. We will highlight two results that have been presented using these two technologies. This problem limits the number of stacked layers and leads to the large variation of optical losses. It should be noticed

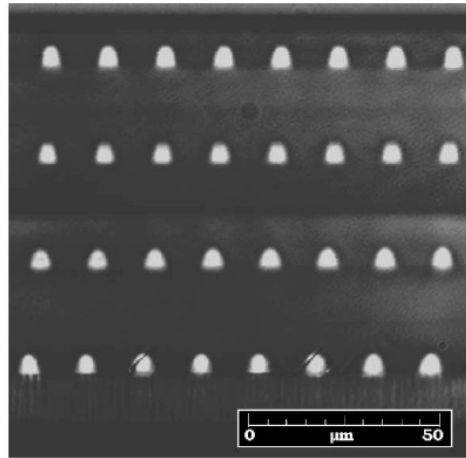


Figure 1.11: Cross-section of a four layer waveguide structure in Ormocer, patterned using UV-lithography [53].

that the stack of waveguides causes coupling losses because the coupling efficiencies between VCSELs and mirrors, and between mirrors and photodetectors, are dependent on the vertical distance between them. Because of this reason, two-dimensional interconnects using optical waveguides with mirrors have to our knowledge only been reported once, even though the stacking optical waveguides without mirrors were reported.

UV-lithography

In [53], a four layer waveguide structure is presented in Ormocer material. After optimization of the process parameters, the use of a mask aligner and a high-quality mask allows a high achievable alignment accuracy between the waveguides in the different layers. The main requirement to achieve a perfect homogeneity of the structure cross-sections and the refractive index distributions over the whole stack, is to assure the same exposure conditions for all layers. The simple repetition of planar processes is not able to meet this demand, because of scattering effects during UV exposure and a resulting inhomogeneous effective exposure intensity, which depends on the particular stack height and the already manufactured structures in deeper layers. Fig. 1.11 shows a cross-section of a four layer waveguide structure, without mirrors. The waveguides have a cross-section of $5\mu\text{m} \times 5\mu\text{m}$, the vertical height of the four layer structure is $90\mu\text{m}$. No achievable alignment accuracies have however been reported.

Stacking of individual waveguide layers

In [54], individual waveguide layers are stacked on top of each other, in this forming a multilayer structure. For this purpose, one-dimensional planar waveguide arrays are fabricated first, and the diced one-dimensional arrays are stacked to form two-dimensional waveguide arrays, as illustrated in Fig. 1.12. The waveguides are patterned in SU8 using UV-lithography. The fabricated waveguide arrays are diced on the same

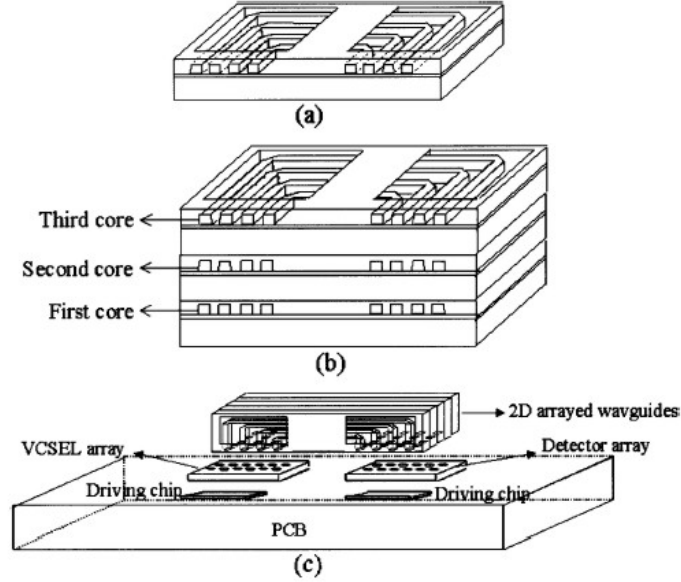


Figure 1.12: Illustration showing the processing steps used to fabricate the two-dimensional waveguide structure: (a) fabrication of one-dimensional waveguide arrays; (b) stacking of the diced waveguide layers; (c) two-dimensional waveguide structure with integrated mirrors used to couple light to/from the photodetector/VCSEL array [53].

size using a diamond saw and stacked using a fixture that has the same dimension as the waveguide arrays. A UV-curable adhesive was coated and cured on the three sides of the stacked waveguide arrays to fix them. The vertical and lateral positional error of the stacked waveguide arrays are about $\pm 5\mu\text{m}$ and $\pm 20\mu\text{m}$, respectively, due to passive alignment using the fixture.

1.4.3 Coupling structures

In optical boards, 45° reflecting micro-mirrors enable out-of-plane light coupling. The micro-mirror performance significantly affects the total insertion loss of the optical interconnect system, which has a crucial role on the system bit error rate (BER) characteristics. Fabrication of a stand-alone mirror can be performed by many techniques such as moulding and micro-dicing. However, integration of micro-mirrors into a back-plane with waveguides and optical connectors poses a number of strict requirements on the mirror characteristics. For example, air terminated total internal reflection (TIR) mirrors cannot be used in real boards operating outside of clean conditions, because any contamination or moisture adsorption can severely impair the mirror reflectance. A short list of requirements, which the micro-mirrors have to comply with, includes high reflectivity, precise mirror plane positioning control, ability to direct light up and down out of the propagation plane, full integration with planar waveguides, and robust

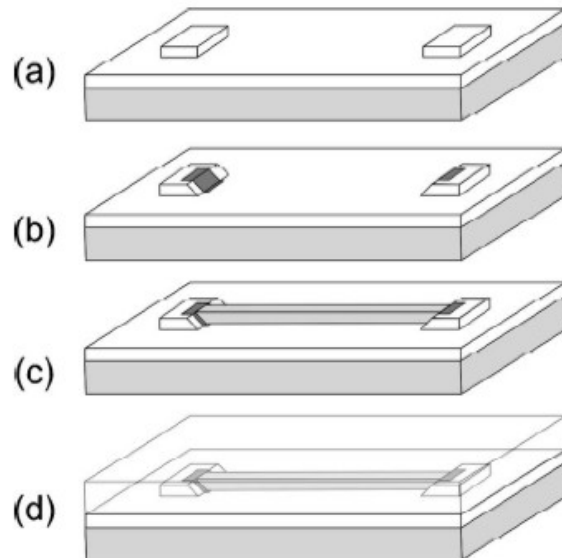


Figure 1.13: (a) The lower cladding and wedge layers are deposited and the wedge base is patterned; (b) one side of the wedge base is tapered to 45° by micro-dicing and a thin Au film is deposited on the tapered wedge side; (c) the waveguide core layer is deposited and the channel waveguide is patterned with photolithography; (d) the top cladding layer is coated on top of the formed waveguide and mirror structure [55].

and cost-effective manufacturing process.

As was already mentioned, two different approaches can be followed: the use of an embedded micro-mirror or the use of a discrete coupling element. We will briefly discuss experimental results that have been reported and that can potentially be used for practical applications.

Embedded mirror: Fujitsu

Fujitsu has developed a micro-wedge dicing technology for the patterning of embedded 45° micro-mirrors. The fabrication flow is shown in 1.13: (a) the lower cladding and wedge layers are deposited and the wedge base is patterned; (b) one side of the wedge base is tapered to 45° by micro-dicing and a thin Au film is deposited on the tapered wedge side; (c) the waveguide core layer is deposited and the channel waveguide is patterned with photolithography; (d) the top cladding layer is coated on top of the formed waveguide and mirror structure.

The 45° tapering of the wedge is accomplished using a mechanical saw dicing of the polymer with a 90° V-shaped diamond blade. The dicing technology was used previously to form 45° sloped optical polymer surfaces. Commercial dicing saws available in most semiconductor assembly facilities can control the positioning of the cut within several microns in the vertical and lateral directions. Loss measurements at 850 nm

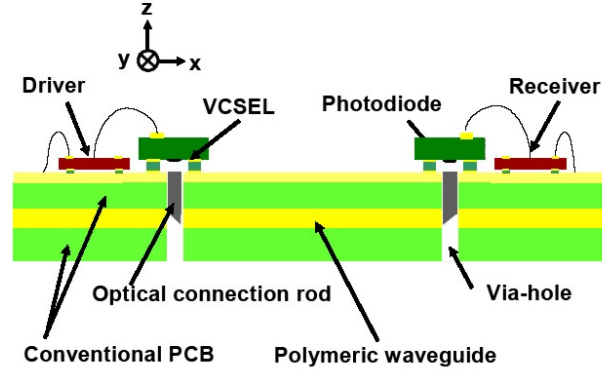


Figure 1.14: Schematic representation of the use of a 45° ended optical fiber that is used to couple the light from transmitter to the waveguides and from the waveguides to the receiver [56].

with a detector fiber with core diameter $200\mu\text{m}$ indicate that the mirrors induce a coupling loss of 0.3-0.5dB [55].

Discrete coupling element

In [56], the use of a discrete fiber connection rod is presented to couple the light in and out of the optical layer. The connection rod consists of a 45° ended optical fiber which can be inserted into micro-cavities in the optical board, as is schematically shown in Fig. 1.14. Under the VCSEL and photodetector windows, via-holes are formed through the electrical and the optical layers, and the optical connection rods (or blocks) are inserted in these via-holes. Each rod has a 45° mirror plane at the end on the optical layer side and a flat surface on the VCSEL or PD side. The main benefit of this optical interconnection architecture is the chuck-off from the handling of a 45° ended waveguide into the PCB layer, and this architecture is applicable to the 2-dimensional optical interconnection and multiple waveguide layers by simply controlling the length of the optical connection rods or blocks. Mirror coupling losses of 0.5dB have been reported [56], without details on the used measurement set-up.

1.5 Objectives

This PhD work entitled: "Multilayer optical interconnections integrated on a printed circuit board" aims at the realization of an on-board optical interconnection demonstrator. The integration to the board-level can be done with the use of a polymer optical layer. It is clear that the realization of a working demonstrator is very challenging, and that not all these challenges can be handled within the scope of this thesis. The main focus within this thesis is placed on the following parts:

- the development and realization of an efficient coupling approach, which can be used to couple the light in and out of the optical layer,
- the expansion of this single layer optical system to a multilayer optical system. The use of multiple optical layers, stacked on top of each other, allows to increase the integration density and for high-density interconnections the use of a more relaxed routing scheme. In addition, the characteristics of 2-dimensional opto-electronic elements such as VCSEL and photodetector arrays can be fully exploited.

The objective is to come to a working demonstrator board that shows the potential of optical interconnections, keeping in mind the required compatibility with existing PCB manufacturing processes. Laser ablation is studied as an alternative micro-structuring technology, that can be used for the patterning of the main building blocks of the optical interconnection. The technology is compatible with standard PCB manufacturing processes and is already used for the drilling of micro-vias in high-density electrical boards.

The discussion of the work that has been carried out within this thesis has been split up into 7 chapters, which deal with the main aspects of the research: polymers, multimode waveguides, coupling structures, reliability and stability, fabrication of an active optical interconnect demonstrator and conclusions.

Chapter 2: Optical polymers

Polymer materials are viable candidates for the integration of optical interconnections to the board-level. Optical polymers with excellent optical and thermal properties have been presented, however with a limited commercial availability and associated high price. Optical polymers with slightly inferior optical and thermal properties are commercially available at reasonable price. The application and the interconnection distance will however determine the propagation loss that can be accepted, which in some cases means that only the expensive polymers are suitable.

Some of the main characteristics that determine the properties that are of interest for the integration to the board-level are discussed. Four different optical polymers (Truemode Backplane™ Polymer, Ormocer®, SU-8, Epocore/clad) are discussed, with the main focus on Truemode Backplane™ Polymer because of its excellent response to KrF excimer laser ablation. The main properties of the studied optical polymers are given and the processing cycle is discussed in detail. A lot of work has been dedicated to the optimization of the process parameters that are used for the application and patterning of the polymer layers. The process parameters that result from this study allow us to pattern the optical layer in a reproducible way.

Chapter 3: Multimode waveguides

Multimode optical waveguides are used to guide the light in the plane of the optical layer. Different technologies such as UV-lithography, embossing and direct laser writing can be used for the patterning of the waveguides. In this chapter, we study the use of laser ablation and UV-lithography for the patterning of the waveguide cores into the studied optical polymers.

The use of KrF excimer laser ablation for the patterning of waveguides into the Truemode material has been discussed in [57]. The work carried out within that PhD thesis is used as a basis for further optimization of the process. The ablated waveguides have a higher propagation loss than the UV-defined waveguides but also show a number of advantages:

- laser ablation is a maskless technology, which allows fast prototyping,
- the ablation process is carried out in standard environment. This opposed to UV-exposure of Truemode wet film formulation, which has to be carried out in a nitrogen environment.

Special attention goes out to the realization of a two layer waveguide structure, which means that two optical layers that contain waveguides are stacked on top of each other. The approach that is followed to obtain a good alignment between the waveguides in both layers is explained in detail. The alignment tolerance range for a two layer waveguide structure in Truemode material is first studied numerically and in a next step compared to the experimental results obtained using laser ablation.

Chapter 4: Integrated coupling structures

Within this chapter, the design and fabrication of two different integrated mirror configurations is discussed: a total internal reflection (TIR) mirror and a metalized micro-mirror, which can both be used to deflect the light beam over 90° , out of the plane of the optical layer. Both mirror configurations are patterned with use of KrF excimer laser ablation and are directly integrated into the optical waveguide, which allows a high achievable alignment accuracy. The excimer laser beam can be tilted, which eases the patterning of angled features such as mirrors considerably. Numerical simulations have been carried out to determine the tolerance range on the mirror angle for both mirror configurations. Besides out-of-plane coupling, the metalized micro-mirror can also be used for inter-plane coupling in a multilayer structure.

The alignment tolerance range on the use of the metalized mirror for out-of-plane and inter-plane coupling in a two layer optical structure is first studied numerically and in a next step compared to the experimental results. The metalization of the mirror facet is a critical step and is for that reason discussed in detail. The performance of both mirror configurations is evaluated with loss measurements and the results discussed in a critical way.

Chapter 5: Discrete coupling structures

An alternative approach to the use of an integrated micro-mirror is the use of discrete coupling elements, which are plugged into the optical layer in a separate step. The

discrete couplers contain a 45° micro-mirror that is used for the 90° beam deflection. Two different configurations have been studied: a pluggable coupler, which can be plugged into and out of a micro-cavity in the optical layer, and an embedded mirror, which is plugged into a micro-cavity in the optical layer and in a next step embedded. The performance of both mirror configurations is evaluated with loss measurements and compared.

The main contribution in this chapter is the fabrication of demonstrator boards that are used to evaluate the performance of the discrete coupling elements. The coupling elements are fabricated at VUB with use of deep proton writing and are obtained through close collaborations. They are currently made of PMMA, which has a low thermal stability but can be replicated in a high quality plastic.

Chapter 6: Reliability and stability

A very relevant and sometimes forgotten item is the reliability and stability of the optical elements. In this chapter, the performance of ablated Truemode waveguides is evaluated after submitting them to two different accelerated aging tests and two different PCB manufacturing related processing steps. The results from this study determines whether or not it is feasible to make use of these elements in practical applications.

Chapter 7: Demonstration of on-board optical interconnects

A lot of the work that is presented in this thesis is used within the network of excellence on micro-optics (NEMO) supported by the European Commission through the sixth framework program. The main achievements that are obtained within the network are explained in this chapter. The first achievement is the fabrication of a first and second generation active demonstrator board. The boards demonstrate an on-board optical interconnection, making use of waveguides and coupling structures that are discussed in the previous chapters of this thesis. The fabrication of the boards and the evaluation of their performance is discussed.

The second achievement is the design and fabrication of an fiber-to-waveguide in-plane connector. The design and fabrication of the connector are discussed in detail. The evaluation of this in-plane connector is foreseen in the near future.

Chapter 8: Conclusions

In the final chapter, an overview is given of the work explained in this thesis. An outlook toward the future is also given.

Bibliography

- [1] A. F. Benner *et al*, "Exploitation of optical interconnects in future server architectures," *IBM J. Res. & Dev.*, Vol. 49, No. 4/5, pp. 755-775, 2005
- [2] J. Weiss, C. Berger, M. Witzig, T. Morf, R. Dangel, F. Horst, M. Schmatz, "Low-cost electro-optical package for use with PCB-embedded waveguides," *Proc. SPIE*, Vol. 6775, 677507-1, 2007

- [3] E. Palen, "Surface Mount Optical Interconnects," *Proc. SPIE*, Vol. 6899, 61240B, 2008
- [4] C. Berger, B. J. Offrein, M. Schmatz, "Challenges for the introduction of board-level optical interconnect technology into product development roadmaps," *Proc. SPIE*, Vol. 6124, 61240J, 2006
- [5] E. Mohammed *et al.*, "Optical interconnect system integration for ultra-short-reach applications," *Intel Technology Journal*, Vol. 8, No. 2, pp. 115-128, 2004
- [6] D. Huang *et al.*, "Optical interconnect: out of the box forever?," *IEEE J. Sel. Top. in Quantum Elec.*, Vol. 9, No. 2, pp. 614-623, 2003
- [7] D. Alsuino *et al.*, "Integration Challenges for Optical Interconnects," *Proc. of SPIE*, Vol. 6899, 689910-1, 2008
- [8] D.A.B. Miller, "Rationale and challenges for optical interconnects to electronic chips," *Proc. SPIE*, vol. 88, no. 6, pp. 728-749, 2000
- [9] J. Hossfeld *et al.*, "Micro-optical components for parallel optical networks," *Proc. IEEE/LEOS Summer Topical Meeting*, IEEE catalog no. 98TH8396 (ISBN 0-7803-4953-9), pp. 39-40, 1998
- [10] K. Vandeputte *et al.*, "Low cost multi-fiber add/drop multiplexer demonstrator system," *Proc. ECOC '99*, pp. I112-I113, 1999
- [11] <http://www.rci-france.com>
- [12] <http://www.hitachi.com>
- [13] <http://www.coretec-inc.com>
- [14] T. Mikawa, "Low-cost, high-density optical parallel link modules and optical backplane for the last 1 meter regime applications," *Proc. SPIE*, Vol. 6899, 689902, 2008
- [15] A. Beier *et al.*, "Electro-optical circuit boards using thin-glass sheets with integrated optical waveguides," *Proc. SPIE*, Vol. 6899, 68990X, 2008
- [16] PPC Electronic Optoboard: <http://www.ppc-electronic.com/english/products/optoboard.html>
- [17] S. Musa *et al.*, "Fabrication of polymeric multimode waveguides for applications in the local area network and optical interconnects," *Proc. IEEE/LEOS Benelux Chapter*, pp. 95-98, 2000
- [18] G. L. Bona *et al.*, "Characterization of parallel optical-interconnect waveguides integrated on a printed circuit board," *Proc. SPIE*, Vol. 5453, 2004
- [19] J.-S. Kim, J.-J. Kim, "Fabrication of multimode polymeric waveguides and micro-mirrors using deep X-ray lithography," *IEEE Photon. Techn. Lett.*, Vol. 16, No. 3, pp. 798-800, 2004

- [20] H. S. Cho *et al.*, "Demonstration of 2.5Gb/s optical interconnection using 45^{circ}-ended connection blocks in fiber- and waveguide-embedded PCBs," *Proc. ECTC*, pp. 1547-1551, 2004
- [21] A. L. Glebov, J. Roman, M. G. Lee, K. Yokouchi, "Optical interconnect modules with fully integrated reflector mirrors," *IEEE Photon. Techn. Lett.*, Vol. 17, No. 7, pp. 1540-1542, 2005
- [22] D. A. Zauner *et al.*, "High-density multimode integrated polymer optics," *J. of Optics A: Pure and Applied Optics*, Vol. 7, pp. 445-449, 2005
- [23] Y. Yadin, M. Orenstein, "Parallel Optical Interconnects Over Multimode Waveguides," *IEEE Journal of Lightwave Technology*, Vol. 24, No. 1, pp. 380-386
- [24] W.C. Chuang *et al.*, "Fabrication of polymer waveguides using a molding process," *Optical Engineering*, Vol. 45, No. 10, 2006
- [25] S.-H. Ahn, I.-K. Cho, S.-P. Han, "Demonstration of high-speed transmission through waveguide-embedded optical backplane," *Optical Engineering*, Vol. 45, No. 8, 2006
- [26] C. Berger, B. J. Offrein, M. Schmatz, "Challenges for the introduction of board-level optical interconnect technology into product development roadmaps," *Proc. SPIE*, Vol. 6124, 2006
- [27] L. Eldada, "Polymer integrated optics: promise vs. practicality," *Proc. SPIE*, Vol. 6185 618501, 2006
- [28] A. L. Glebov, M. G. Lee, K. Yokouchi, "10+ Gb/s Board-Level Optical Interconnects: Fabrication, Assembly, and Testing," *Proc. SPIE*, Vol. 6185, 618501, 2006
- [29] E. Griese, "A high-performance hybrid electrical-optical interconnection technology for high-speed electronic systems," *Transactions on Advanced Packaging*, Vol. 24, No. 3, 2001
- [30] X. Wang, R. T. Chen, "Fully embedded board level optical interconnects - from point-to-point interconnection to optical bus architecture," *Proc. SPIE*, Vol. 6899, 689903, 2008
- [31] D. Krabe *et al.*, "New technology for electrical/optical systems on module and board-level: the EOCB approach," *Proc. ECTC*, pp. 970-974, 2000
- [32] K. B. Yoon, I.-K. Cho, S.-H. Ahn, "10-Gb/s data transmission experiments over polymeric waveguides with 850-nm wavelength multimode VCSEL array," *IEEE Photon. Techn. Lett.*, Vol. 16, No. 9, pp. 2147-2149, 2004
- [33] S. Lehmacher, A. Neyer, "Integration of polymer optical waveguides into printed circuit boards," *Electr. Lett.*, Vol. 36, No. 12, pp. 1052-1053, 2000
- [34] A. Fujii *et al.*, "A novel fabrication technology of a polymer optical waveguide and its application," *Proc. SPIE*, Vol. 6775, 677506-1, 2007

- [35] W.-S. Kim *et al.*, "Fabrication of ridge waveguides by UV-embossing and stamping of sol-gel hybrid materials," *IEEE Phot. Techn. Lett.*, Vol. 16, No. 8, 2004
- [36] R. R. Krchnavek, G. L. Lalk, D. H. Hartman, "Laser direct writing of channel waveguides using spin-on polymers," *J. Appl. Phys.*, Vol. 66, No. 11, 1989
- [37] Schroder paper Waveguide and packaging technology for optical backplanes and hybrid electrical-optical circuit boards
- [38] B. Offrein, C. Berger, R. Beyeler, R. Dangel, L. Dellmann, F. Horst, T. Lamprecht, N. Meier, R. Budd, F. Libsch, and J. Kash, "Parallel optical interconnects in printed circuit boards," *Proc. SPIE*, Vol. 5990, pp. 117-125, 2005
- [39] A. Glebov *et al.*, "Optical Interconnect Modules With Fully Integrated reflector mirrors," *Photonics Technology Letters*, Vol. 17, No. 7, 2005
- [40] Y. Ishii, S. Koike, Y. Arai, Y. Ando, "SMT-compatible optical I/O chip packaging for chip-level optical interconnects," *Proc. ECTC*, 2001
- [41] M. Hikita *et al.*, "Polymeric optical waveguide films for short-distance optical interconnects," *Journal of Selected Topics in Quantum electronics*, Vol. 5, No. 5
- [42] M. Kagami, A. Kawasaki, H. Ito, "A Polymer Optical Waveguide With Out-of-Plane Branching Mirrors for Surface-Normal Optical Interconnections," *IEEE Journal of Lightwave Technology*, Vol. 19, No. 12, pp. 1949-1955, 2001
- [43] J.-H. Kim, R. T. Chen, "A Collimation Mirror in Polymeric Planar Waveguide Formed by Reactive Ion Etching," *IEEE Phot. Techn. Letters*, Vol. 15, No. 3, pp. 422-424, 2003
- [44] N. Destouches, D. Blanc, J. Franc, S. Tonchev, N. Hendrickx, P. Van Daele, and O. Parriaux, "Efficient and tolerant resonant grating coupler for multimode optical interconnections," *Optics Express*, Vol. 15, No. 25, pp. 16870-16879
- [45] M. H. Cho, S. H. Hwang, H. S. Cho, H.-H. Park, "High-Coupling-Efficiency Optical Interconnection Using a 90° Bent Fiber Array Connector in Optical Printed Circuit Boards," *Phot. Techn. Lett.*, Vol. 17, No. 3, pp. 690-692, 2005
- [46] S. Hiramatsu, M. Kinoshita, "Three-dimensional waveguide arrays for coupling between fiber-optic connectors and surface-mounted optoelectronic devices," *Journal of Lightwave Technology*, Vol. 23, No. 9, 2005
- [47] S. Hiramatsu, T. Mikawa, "Optical design of active interposer for high-speed chip-level optical interconnects", *Journal of Lightwave Technology*, Vol. 24, pp. 927-934, 2006
- [48] A. L. Glebov *et al.*, "Flexible pillars for displacement compensation in optical chip assembly", *Photonics Technology Letters*, Vol. 18, pp. 974-976, 2006
- [49] Y. Ishii *et al.*, "Fully SMT-compatible optical I/O package with microlens array interface," *Journal of Lightwave Technology*, Vol. 21, No. 1, 2003

- [50] Y. Ishii *et al.*, "SMT-compatible large-tolerance Optobump interface for interchip optical interconnections," *Transactions on Advanced Packaging*, Vol. 26, No. 2, 2003
- [51] H. Takahara, "Optoelectronic multichip module packaging technologies and optical input/output interface chip-level packages for the next generation of hardware systems," *Journal of Selected Topics in Quantum Electronics*, Vol. 9, No. 2, 2003
- [52] F. Doany *et al.*, "Waveguide-coupled parallel optical transceiver technology for Tb/s-class chip-to-chip data transmission," *Proc. SPIE*, Vol. 6899, 68990V, 2008
- [53] U. Streppel *et al.*, "New wafer-scale fabrication method for stacked optical waveguide interconnects and 3D micro-optic structures using photoresponsive (inorganicorganic hybrid) polymers," *Optical materials*, Vol. 21, pp. 475-483, 2002
- [54] J.-S. Kim, J.-J Kim, "Stacked Polymeric Multimode Waveguide Arrays for Two-Dimensional Optical Interconnects," *J. of Lightwave Techn.*, Vol. 22, No. 3, pp. 840-844, 2004
- [55] A. L. Glebov, M. G. Lee, K. Yokouchi, "Integration technologies for pluggable backplane optical interconnect systems," *Optical Engineering*, Vol. 46, No. 1, 2007
- [56] B. S. Rho, S. Kang, H. S. Cho, H.-H. Park, S.-W. Ha, B.-H. Rhee, "PCB-compatible optical interconnection using 45°-ended connection rods and via-holed waveguides," *Journal of Lightwave Technology*, Vol. 22, No. 9, 2004
- [57] G. Van Steenberge, "Parallel Optical Interconnections Integrated on a Printed Circuit Board," *PhD Thesis*, Ghent University, 2006

Chapter 2

Optical polymers

2.1 Introduction

As was mentioned in the previous chapter, the integration of optical interconnections to the board-level can be done using a polymer optical layer which can be integrated in or on top of the PCB. The polymer optical layer contains multimode waveguides for the in-plane light propagation. Coupling structures are used to direct the light in and out of the optical layer. Polymer materials offer a number of advantages over other alternative waveguide media such as glass sheets and optical fibers such as potentially low cost (for a large enough market), the large variety of potential technologies that can be used to pattern the polymer layers and the ability to tailor the properties such as the refractive index and the mechanical properties [1] [2]. Main disadvantages are the long-term stability and reliability, which have not up to now not been proven, mainly because of the lack of standardization [3]. Since cost is one of the main factors affecting the practical use of optical interconnections, compatibility with the existing PCB manufacturing and soldering processes is an important requirement.

The requirements that the optical material has to fulfill are the following:

- low optical loss at the targeted wavelength of 850 nm,
- waveguides should be patternable with a technology that is compatible with current PCB manufacturing, while at the same time delivering structures with low surface roughness,
- excellent adhesion to the PCB substrate,
- cost is a major issue for the practical use of optical interconnections. Reason for this is the required compatibility with standard PCB manufacturing and soldering processes. This means the polymer material has to withstand the high temperature and pressure that occur during a lamination step (typically 180°C) and solder reflow step (typically 240°C, but this can be even higher in case lead-free solder is used),
- excellent planarization properties. The PCB substrate has a relatively high surface roughness that should be compensated in order to minimize the scattering

loss in the patterned waveguides. In addition, a planarized top surface allows the mounting of opto-electronic components on top of the optical layer or the lamination of additional layers,

- good electrical properties: dielectric strength and isolation resistance,
- climatic requirements: the material has to withstand fast temperature changes, humidity, and corrosion to name only a few. The stability of the optical and mechanical properties of the polymer have to be guaranteed, not only on the short term but also on the long term.

In this chapter, we will first discuss some of the main properties of polymer materials, which have a decisive influence on the properties that are of importance for the the integration of the material to the board-level. In the next section, we will look at optical polymers more specifically and on their main properties. Four commercially available optical polymer are evaluated.

2.2 Polymers

A polymer is a substance, the molecules of which consist of a large number of low molecular monomer residues, which are connected by primary bonds. If A is a monomer molecule, then a polymer molecule is represented by:



where n is an integer, called the degree of polymerization of this polymer molecule, and $-A-$ is also called the repeating unit. A monomer is a low molecular weight compound which can react with each other and with another monomer molecule, i. e. they polymerize to a polymer molecule. In this section, we will first give some of the main basic characteristics of polymers concerning their build-up, the polymerization mechanism and the main physical properties. Focus in put on those properties that are of interest for the integration of a polymer optical layer into or on a PCB.

2.2.1 Polymer classification

Classification by chain structure

Polymers can be classified by chain structure. We can distinguish four different groups, which are schematically shown in Fig. 2.1:

- linear polymers: the structural unit is chainwise bonded
- branched polymers: the polymer is built-up of branched macromolecules
- polymer networks: the polymer chains are bonded to each other, forming a 3D network
- ladder polymers: there is a repetition of crosslinks between two chains.

Classification by polymerization mechanism

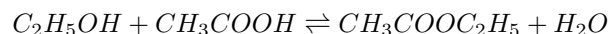
Polymers can also be classified by polymerization mechanism. The original classification involves condensation, during which a low molecular weight molecule (e.g. H_2O) is split off, and addition polymerization, in which case this is not the case. A good way to distinguish between the two mechanisms is to consider the polymerization mechanism as such. This leads to step-growth polymerization and chain-growth polymerization. At the beginning of a condensation polymerization the whole system gradually transforms into a mixture of short chains (monomer, dimer, trimer, etc.); whereas at the beginning of the addition polymerization only a few, but very long, chains are formed. Besides these long chains only unreacted monomer is present. In later stages of the reaction, newly formed chains cannot attain the same length, so that the overall average degree of polymerization of the formed polymer gradually decreases during the addition polymerization.

2.2.2 Polymerizability

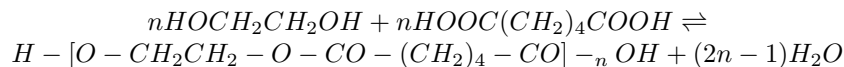
The basic requirements to transform a monomer or a mixture of monomers into a polymer are:

- the monomer or mixture of monomers must be at least bifunctional, meaning that the monomer can form at least two chemical bonds with other molecules,
- the monomer must be sufficiently reactive,
- the monomer must be very pure.

The functionality of a monomer molecule is the number of chemical bonds it can form with other molecules under the prevailing reaction conditions. Ethylalcohol (C_2H_5OH) and acetic acid (CH_3COOH) are both monofunctional because they can react only once with each other in a condensation reaction:



The esterification product ethyl acetate ($CH_3COOC_2H_5$) can be considered as a dimer. It is obvious that for polymerization, at least formation of linear chains must be possible and this requires a minimum functionality of 2 of the monomers. So, polyesterification is possible by taking a diol, a molecule that contains two -OH groups, and a diacid, a molecule that contains two -COOH groups:



Bifunctional monomers can form linear; monomers that have a functionality ≥ 3 can form branched and possibly also cross-linked structures, meaning that the branches are also interconnected. When part of the monomer is more than bifunctional, there is usually first the formation of a branched polymer that can be transformed into a 3D network, often after a temperature increase. It is clear that a slowly reacting monomer would be unattractive because high degrees of polymerization would require unacceptable long reaction times, with a greater risk for undesired side reactions, for instance

with contaminants that are present in the mixture or oxidation. This explains the requirement for a sufficiently reactive monomer. The purity of the monomer is important because of the fact that monofunctional impurities may cause premature stopping of the chain growth.

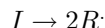
2.2.3 Radical addition polymerization

If we focus on the commercially available photo-sensitive optical polymers, it can be noticed that the main polymerization mechanism is radical addition polymerization which is the most common used form of addition polymerization. The general reaction can be subdivided into 3 stages:

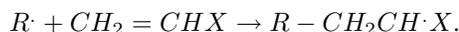
- start of the chain growth or *initiation*
- continuation of the chain growth or *propagation*
- stop of the chain growth or *termination*.

Initiation

During the initiation, the decomposition of the initiator occurs, meaning that free radicals are formed starting from the initiator:



with I the initiator and $R\cdot$ the free radical. The radical $R\cdot$ contains an unpaired electron; a free radical is very reactive and can be used to initiate the polymerization. The next step is the initiation of the monomer. The initiator radical is added to a monomer, by which the monomer adopts the reactive character by creating an active center, because of the presence of an unpaired electron:



In this way, the initiator becomes part of the polymer chain, as is also schematically depicted in Fig. 2.2.

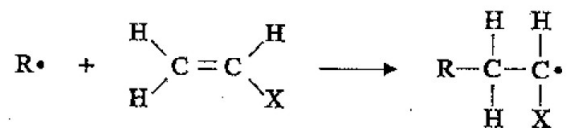
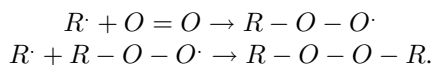


Figure 2.2: Schematic representation of the initiation of the monomer [4].

Initiator radicals can react with bonds that are accidentally or on purpose present in the reaction mixture and that will function as an inhibitor. The inhibitor will react with the radical and in this way prohibit the polymerization. Inhibitors are sometimes added in order to increase the preservation time of the polymer material but are in most other cases undesirable. Oxygen is an important inhibitor which can react with radicals and form peroxides by the following reaction:



For this reason, it is better to perform the polymerization in an inert medium such as vacuum or nitrogen environment.

Propagation

The second phase is the propagation during which the polymer chain grows by consequent addition of monomer to the radical active center. The propagation speed is very high: hundreds of monomer molecules are transformed into a polymer chain within a couple of seconds. The reactions that take place during the propagation phase are schematically represented in Fig. 2.3.

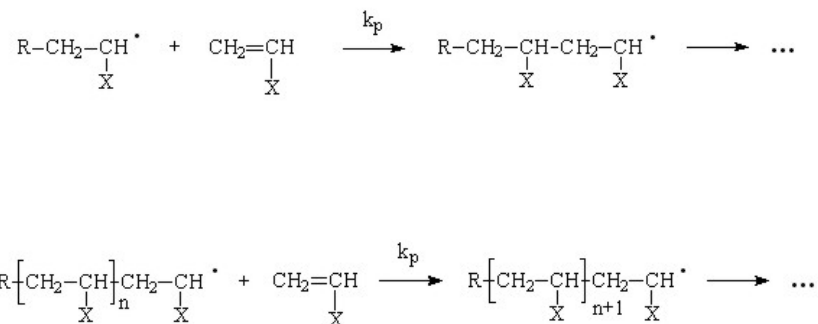


Figure 2.3: Schematic representation of the reactions that take place during the propagation phase [4].

Termination

The final phase consists of the termination of the polymer chain. The polymer chain will continue to grow until the radical end group disappears with some reaction. Usually, this is done by combining two growing centers to one polymer molecule, as is schematically shown in Fig. 2.4: The initiator can for instance be a photoinitiator, in which case the radicals are formed under influence of UV-light. This is typically the case for thin-film applications.

2.2.4 Physical properties

Polymer materials exist in various forms: some of them are hard and brittle while others are flexible and soft. These differences in appearance and characteristics can be linked to the internal structure of the polymer materials. As a consequence, the properties can be tailored by changing the internal built-up, which is one of the big advantages of polymers. When a polymer material is heated from a low temperature, in general it goes through different phases: from a hard, glasslike plastic to a tough intermediate rubberlike mass that will finally change into a high-viscosity fluid. The differences in properties between polymers can often be explained by differences in the transition

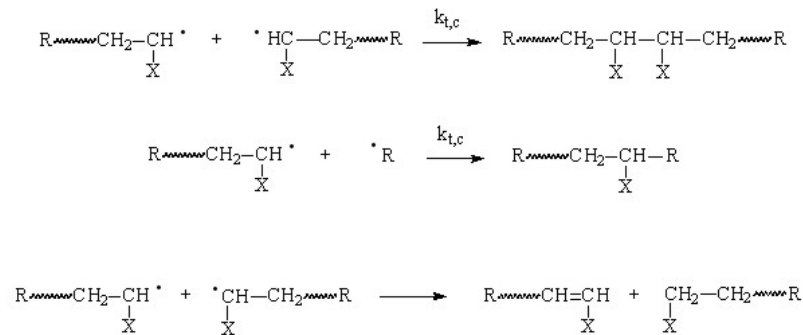


Figure 2.4: Schematic representation of the termination phase [4]. In this case the termination is done by combining radicals.

temperatures between these different phases. If we order the different phases for the case of an amorphous polymer in function of increasing temperature, we get: glasslike state - rubberlike state - fluid state. For the case of a partially crystalline polymer the phase transition solid-fluid has to be added to the previous sequence.

A good way to study the transition between the different phases is to look at the stiffness of the material. The stiffness is the force F that is required to incite a certain deformation ΔL , and is expressed as the modulus of elasticity E (also known as Young's modulus):

$$E = F/S \frac{\Delta L}{L},$$

in which L is the original length of the sample and S the cross-sectional surface of the sample. The elasticity modulus E is a measure for the resistance that a material shows against deformation. The change in E with temperature gives a good insight into the properties and applicability of a polymer in different temperature ranges.

Influence of temperature on the elasticity modulus

An example of a typical graph for an amorphous non-crosslinked polymer are given in Fig. 2.5. Two important transition temperatures can be defined: the glass transition temperature T_g and the flowing temperature T_{fl} . It is clear from this graph that amorphous polymers in the glassy solid state below T_g have high E values and do not directly transform into a viscous liquid above T_g because this would require that E approaches zero, as is found for low molar mass substances. The polymer chains are strongly entangled and these physical crosslinks give rise to a leathery region just above T_g and a long rubbery region up to the flow temperature T_{fl} .

For $T \leq T_g$, the polymer material is in a glasslike phase, meaning that the chain segments have a limited freedom of movement. The atoms are fixed around a certain position. The material is stiff and little flexible. Around the glass transition temperature, the different chain segments gain flexibility. The end of the glass-like phase is reached when the chain segments can rotate around the bonds. The glass transition temperature is determined by the chain flexibility, the chain distance and the interaction forces between the chains. Cross-linked polymers typically have a higher T_g and

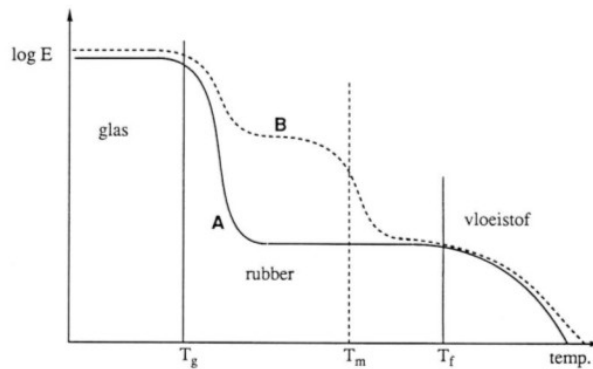


Figure 2.5: Young's modulus in function of temperature for an amorphous polymer material.

a higher E modulus than linear or branched polymers. This allows the tailoring of the T_g by changing the internal structure of the polymer. In the rubbery region, E is rather low and a small stress can give a long elongation. Moreover, if stress is applied for a very short time and then removed, the sample can regain (to a certain extent) its original length. After a long duration of stress, however, much less retraction takes place and a great part of the deformation has become permanent.

If a non-crosslinked polymer is partially crystalline, with T_m the melting temperature of the crystalline part, only the amorphous fraction will show the glass-rubbery transition near T_g . Consequently, the lowering of the modulus will be proportional to the amorphous content and is much less than that of a completely amorphous polymer. Amorphous non-crosslinked polymers can be applied in the temperature range of the glassy state, where their stiffness is high enough. The advantage of crystallinity is clearly shown in Fig. The range of applicability is extended from T_g to T_m , although for a partially crystalline polymer above T_g E is considerably lower than in the glassy state. However, the rubbery behaviour of the amorphous fraction makes the polymer far less brittle. The fall in E at T_g will be much lower for highly cross-linked polymers than for non-cross-linked and T_g will also shift to a higher temperature with the degree of cross-linking. It is clear that the temperature behaviour of a polymer can be tailored by changing the internal structure.

Measurement techniques

The glass transition temperature can be measured experimentally using differential scanning calorimetry (DSC). In this method, two small containers, one containing the sample and the other a reference material, are heated by individual heaters. The temperature of each container is monitored by a heat sensor. If the sample suddenly absorbs heat during a transition, this change will be detected by the heat sensor, which will initiate a greater current flow through the heater to compensate for the loss. Thus, absorption of heat by the sample results in a greater current flow. Since the change in electric current can be monitored accurately, this method provides a sensitive measure of transition temperatures.

Thermogravimetric Analysis (TGA) measures weight changes in a material as a function of temperature (or time) under a controlled atmosphere. It is mainly used to measure the thermal stability and composition of a material. Typically, the temperature at which a 5% weight loss occurs is listed as the maximum applicable temperature for reliable use. This is a very interesting method to determine the temperature range in which a polymer can be used with preservation of its original properties.

2.2.5 Optical loss

For polymer materials, both electronic and vibrational absorptions are likely to contribute to the optical loss [5]. The absorption of an optical polymer at datacom wavelength (850 nm) and in some cases also at the major telecom wavelengths (1310 nm and 1550 nm) should be sufficiently low if the polymer is to be used as optical layer in a board-level integrated optical interconnection. Reason for this is the power budget that applies to the link. Lower link losses allow a lower power consumption at the transmitter and receiver side. Polymeric media generally have large absorptions in the UV owing to fundamental excitations of their electrons. These absorptions tend to be in the deep UV (less than 200 nm) for polymers with predominantly aliphatic hydrogen atoms, and in the near UV (200-400 nm) for polymers with a significant number of aromatic hydrogens. Partially or fully fluorinated polymers tend to have their UV absorption at higher energies. For energies well below electronic energy levels of the polymer, where the polymer is basically transparent, weak absorption can result from a number of sources including singlet-triplet absorption and vibration mediated absorption inharmonic interactions. In general, electronic absorptions in polymers, with the viable exception of highly colored electro-optics polymers, are very unlikely to contribute significantly to optical losses in the major telecom window [2].

In the 1300-1600 nm range, absorptions coming from the overtones of fundamental molecular vibrations are dominant. Since the strength of the absorption tends to decrease by approximately an order of magnitude between each harmonic order, higher harmonics are generally weak enough to not be of concern for waveguide applications. Clearly, the highest energy vibrations will be those that have a high spring constant (stiff bonds, such as double bonds) and/or small reduced masses. The smallest reduced mass occurs when one of the atoms is hydrogen, and the C-H aliphatic bond is typically used as the benchmark for infrared absorptions. Its absorption is located at 3390 nm. In Table 2.1, a comparison is given of the position and intensity of various vibrational overtone absorptions of interest when considering optical polymers.

Both C-H and O-H overtones are seen to be highly absorptive in the telecom window, whereas C-F overtones for example show extremely low absorption throughout the range of interest, owing to their higher harmonic order. As hydrogens are removed through partial fluorination, the absorption of optical polymers reduces significantly. In general, it is difficult to directly determine the absorption of an optical material, since scattering contributions to the overall attenuation are often indistinguishable from those coming from absorption. The one signature that distinguishes absorption from scattering is the inevitable generation of heat in the absorption process. Optical polymers can be highly transparent, with absorption loss values below 0.1dB/cm at all key communication wavelengths. The absorption of the optical polymers can be significantly reduced by partial or full fluorination.

Bond	Overtone order	Wavelength (nm)	Intensity (relative)
C-H	1	3390	1
C-H	2	1729	7.2×10^{-2}
C-H	3	1176	6.8×10^{-3}
C-D	3	1541	1.6×10^{-3}
C-D	4	1176	1.3×10^{-4}
C-F	5	1626	6.4×10^{-6}
C-F	6	1361	1.9×10^{-7}
C-F	7	1171	6.4×10^{-9}
C=O	3	1836	1.2×10^{-2}
C=O	4	1382	4.3×10^{-4}
C=O	5	1113	1.8×10^{-5}
O-H	2	1438	7.2×10^{-2}

Table 2.1: Wavelengths and intensities of some important vibrational overtones [5].

Physical failures such as micro-cracks and delamination can significantly increase the optical loss. This is not always noticed initially but often only after a while because of the aging of the polymer. The minimum acceptable optical loss is determined by the overall system power budget, which will be a function of the transmitter power, the efficiency of coupling structures, the optical amplifier gain and receiver sensitivity to name only a few. Complete cross-linking is required in order to get the desired chemical, mechanical and electrical properties of the polymer material. The T_g can for instance increase by more than 100°C as the resin approaches full cure. Different cure conditions can result in different values for optical loss in a polymer waveguide.

2.3 Optical polymers

As explained in the previous chapter, the integration of optical interconnections to the board-level can be done with the use of a polymer optical layer. Polymer materials are interesting candidates for this because of the potentially low cost for large area and large range of processing technologies that can be used for the patterning of the layers. The optical layer can be applied onto the PCB with different technologies such as spincoating, spraycoating and inkjet-printing. Spincoating is a standard process in PCB manufacturing; drawback is the amount of material that is lost in the application process, especially in case an expensive optical polymer is used. Spray-coating, where the polymer material is sprayed onto the surface of the substrate, is interesting because of its compatibility with the coating of large area boards and efficient use of the material. Inkjet-printing allows an efficient material use, because of the fact that the material deposition can be limited to the designated areas. The nozzle that is used to deposit the material determines the type of material that can be used, mainly based on the viscosity. A suitable material choice is crucial for the performance of the optical interconnections. Important properties that have to be considered when making material choice are: low optical loss, low birefringence, low dispersion, mechanical and thermal stability and good adhesion to the substrate. In addition, the polymer material should be compatible

with the high temperature and pressure that occur during the PCB manufacturing and soldering processes. It is clear that a combination of all these properties is not easy to find. Optical polymers were engineered in many laboratories worldwide and some are available commercially [1]. Some of these polymers are not photosensitive, and are typically processed using photoresist patterning and reactive ion etching (RIE). Other polymers are photosensitive and as such are directly photopatternable, resulting in a considerably higher throughput. Furthermore, this technology uses potentially low-cost materials, for large enough market, and low-cost processing equipment that is already used in the current PCB manufacturing.

Generally speaking, for board-level optical interconnect applications, the material should have low optical loss at 850 nm and/or 1310 nm and it should be possible to pattern multi-mode waveguides in lengths up to one meter in an easy way. Material process compatibility with existing board manufacturing schemes and waste streams is essential for minimizing capital investments and processing costs. The material should be able to withstand board process temperatures up to 240°C for short periods of time, in accordance with the temperature that occurs during a solder reflow cycle, and the high temperature and pressure that occur during a lamination step. The material should also survive reliability testing, such as thermal cycling and accelerated aging tests. The CTE of the polymer material is preferably matched to the CTE of the substrate, in order to avoid the build-up of stress during the processing, which can lead to cracks and in some cases complete delamination. High T_g and low CTE polymers provide thermal-mechanical and environmental robustness and performance stability.

The environmental stability of optical polymers, the stability of their optical and mechanical characteristics with temperature and humidity, is an important issue that to a large extent determines the commercial feasibility of polymer integrated optics. The thermal stability of the optical properties is very important since organic materials may be subject to yellowing upon thermal aging due to oxidation. The presence of hydrogen in a polymer allows the formation of H-Halogen elimination products, which results in double carbon bonds, which are subject to oxidation. Fortunately, the absorbing species from the thermal decomposition are centered near the blue region of the spectrum. The thermal stability can be high at the datacom wavelength of 840/850 nm and even greater at the telecom wavelengths of 1310 nm and 1550 nm. The resistance of polymers to water incursion is critical since optical absorption results from overtone bands of the OH-stretch of water.

The optical layer consists of a stack of cladding-core-cladding material and contains multimode waveguides and other passive optical structures such as splitters and crossovers, used to guide the light signal in-plane. The FR4 substrate has a relatively high surface roughness and suffers from twist and bow, which means that the surface is not planarized but shows a certain deformation, as can be seen in Fig. 2.6. FR4 substrates have a $\pm 10 \mu\text{m}$ waviness with a period ranging from 400 to 800 μm and a local roughness of $\pm 0.5 \mu\text{m}$. The waviness arises from the woven glass fibers buried inside for reinforcement. Optical waveguides must be made with smooth surfaces and walls, to reduce the scattering loss. To minimize the effect of the surface roughness of the FR4 substrate on the waveguide performance, the optical layer has to planarize the substrate sufficiently. A buffer layer should be applied in case the planarization properties of the used optical polymer are not sufficient. A planarized top surface in addition allows the mounting of opto-electronic elements or the lamination of additional layers. The abil-

ity to progressively laminate and bond successive layers onto the optical layer provides a significant and essential attribute for performance, applicability and manufacturability [6].

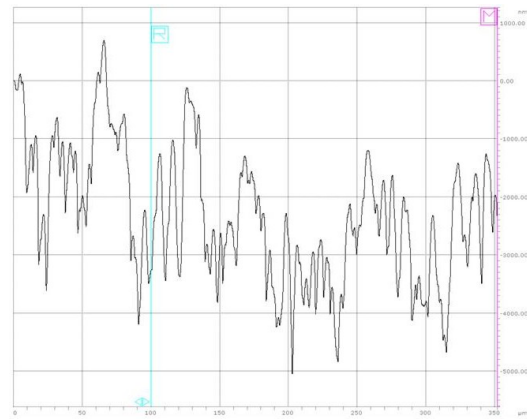
Four different optical polymer materials, Truemode Backplane™ Polymer, Ormocer®, SU8 and Epocore/clad, will be evaluated in the next paragraphs. All four materials are photo-sensitive, which means that they can be directly patterned with use of UV-lithography, and behave like a negative photoresist. The difference between the patterning of a positive and negative photoresist is shown in Fig. 2.7. The optical layer is applied onto the FR4 substrate with use of spincoating, which is a standard process in PCB manufacturing. Main focus within this work is on the use of Truemode Backplane™ Polymer. The three other optical polymers have been studied in a less intense way, and are mainly intended as a backup solution in case problems arise with the Truemode material.

2.3.1 Truemode Backplane™ Polymer

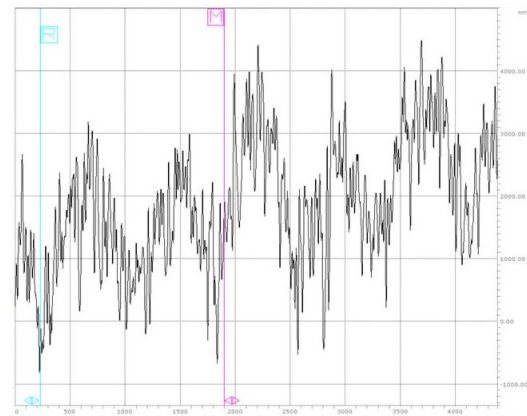
The first studied polymer, Truemode Backplane™ Polymer (Truemode), is a highly cross-linked multifunctional (meth)acrylate-based polymer material that has been developed for optical backplane applications by Exxelis Ltd. (UK) [7]. It has a low optical loss at 850nm, as shown in Fig. 2.8, a high thermal stability (with T_g higher than 150°C and decomposition temperature higher than 350°C) and an excellent adhesion to the FR4 substrate. The high T_g is a consequence of the highly cross-linked nature of the material. The exact composition of the Truemode material is patented and therefore not available to the public. However, from the datasheet we do know that it is an (meth)acrylate-based polymer and the main optical and thermal properties, which are listed in Table 2.2.

The basic structure of a methacrylate is shown in Fig. 2.9(a), where R can differ such as for instance CH_3 , in which case methylmethacrylate is formed. It is a photo-sensitive material that is polymerized using a radical addition polymerization reaction, which means that an initiator is used to start the polymerization reaction. The initiation is done with a UV-initiator, which means that the initiation is started under the influence of UV-light, (Irgacure 651) according to the reaction described in 2.2.3. The basic structure of the photo-initiator is shown in Fig. 2.9(b). The photo-initiator can be split into two radicals by the UV-induced cleavage of the bond that is marked with the arrow in the schematic. The UV-exposure has to be done in an inert environment in order to prevent inhibition by oxygen molecules present in standard environment.

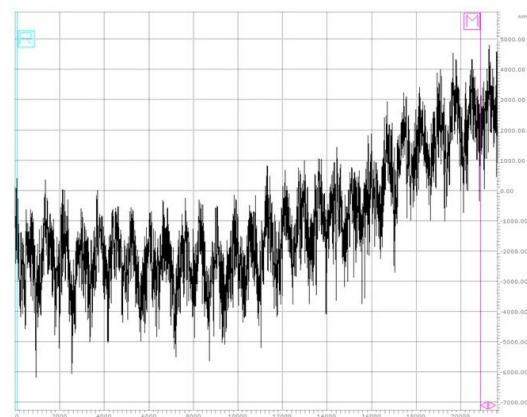
The optical layer is applied onto the FR4 substrate with use of a spincoating step. The spincurve, which graphically represents the relation between the spin speed and the layer thickness, is given in Fig. 2.10. For the remaining part of this work, the thickness of the core and cladding layers is chosen to be 50 μm , in this way forming a 150 μm thick optical layer, unless specified in a different way. The material has a low viscosity, which necessitates the use of a low spin speed for the application of the core and cladding layers, as can be read from the spin curve. We can see that a layer thickness of 50 μm corresponds to a spin speed of 250rpm respectively 200rpm for the core respectively cladding material. Ideally, in order to obtain a homogeneous layer thickness across the sample, the spincoating step has to be done at a spinspeed $\geq 1500\text{rpm}$. At lower spinspeed, edge bead, which means that the material accumulates



(a) Scan length 350 μm



(b) Scan length 4mm



(c) Scan length 21mm

Figure 2.6: Surface roughness of the FR4 substrate, measured with a stylus profiler on 3 different scan lengths. In (a) and (b) the high surface roughness of the FR4 substrate can be clearly observed. In (c) the tilting of the FR4 substrate can be observed.

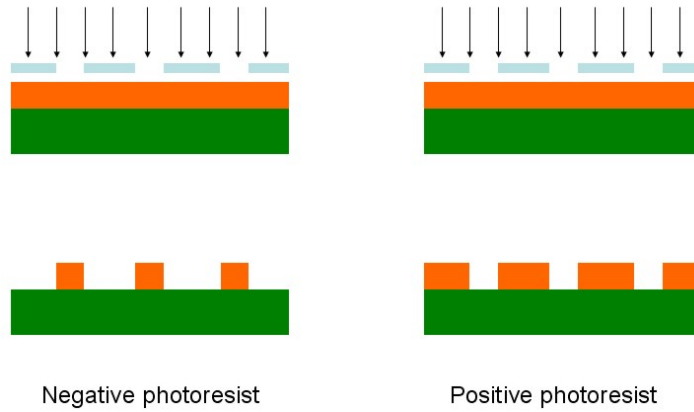


Figure 2.7: Patterning of negative versus positive type photoresist. The studied polymer materials behave like a negative photo-resist, which means that the UV-exposed zones will remain after the development step.

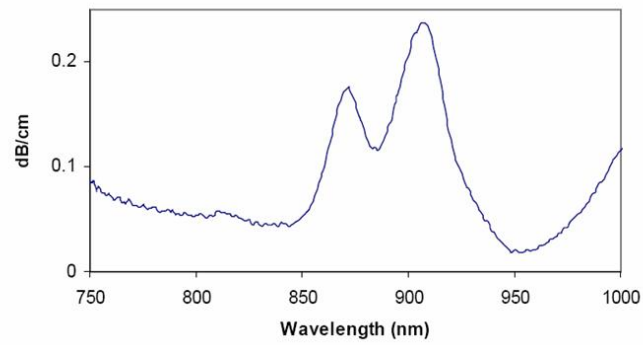


Figure 2.8: Absorption spectrum of the Truemode material [7]. From this graph, we can see that the absorption reaches a minimum around 850 nm, which is the targeted wavelength.

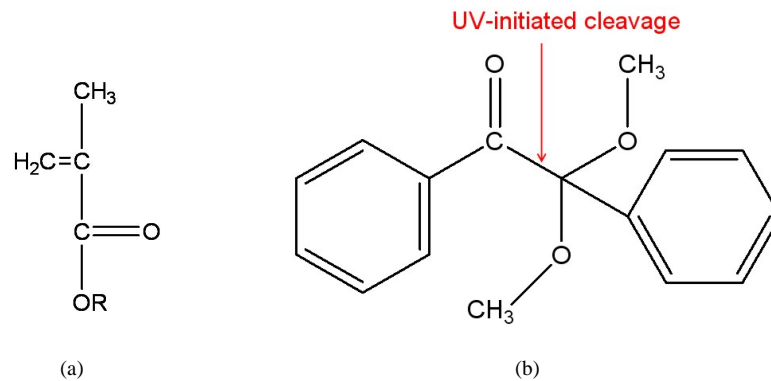
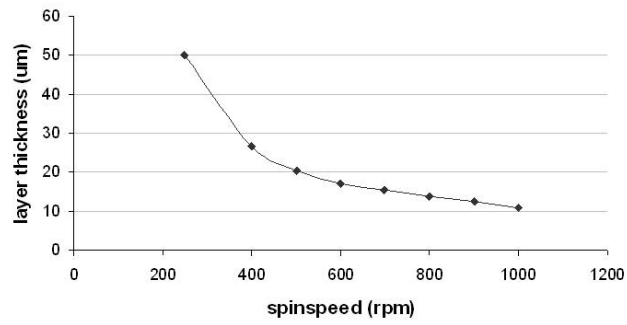


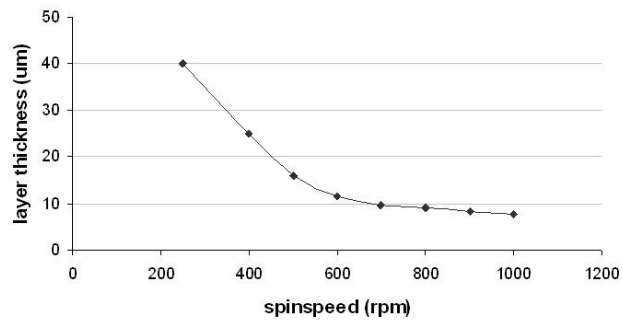
Figure 2.9: (a) Basic structure of a metacrylate ;(b) basic structure of the photo-initiator Irgacure 651 that is used for the radical polymerization of Truemode. The photo-initiator can be split into two radicals by the UV-induced cleavage of the bond that is marked with the arrow.

Optical properties	
Propagation loss at 850nm	≤ 0.04 dB/cm
Refractive index core	1.5266
Refractive index cladding	1.5642
Thermal properties	
Degradation temperature	≥ 350 °C
Coefficient of Thermal Expansion (CTE)	60 ppm/K
Glass transition temperature (T_g)	180 °C

Table 2.2: Main properties of Truemode Backplane™ Polymer, as they are given in the datasheet [7].



(a)



(b)

Figure 2.10: (a) The spincurve for the Truemode core material; (b) the spincurve of the Truemode cladding material.

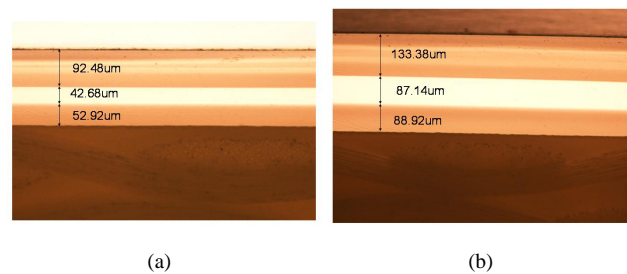


Figure 2.11: (a) Cross-section of the optical layer in the center of the sample; (b) cross-section of the same sample taken at the edge of the sample, where the edge bead can be very clearly observed. Two approximately $50 \mu\text{m}$ thick cladding layers are in this case applied onto the core layer in this sample.

near the edges of the sample during the spincoating step, can become a considerable problem, making the edges of the samples unusable. This is especially the case if the layer is to be UV-exposed in contact mode in a subsequent step because of the fact that the edge bead will prevent placing the mask in contact with the part of the optical layer that is located in the center of the sample, where the layers are thinner. The edge bead problems can be clearly observed at the edges of the sample; the layer thickness in that area is locally thicker than the targeted value as shown in Fig. 2.11.

When the mask is placed in contact or proximity mode, the vertical distance between the mask and the layer will be limited by the edge bead. The air gap between the mask and the layer is increased, which consequently means that the imaged pattern will be larger than targeted width in the mask design. A possible solution to this problem is the removal of the edge bead with a clean room wipe prior to the UV-exposure, but this still makes the edges of the sample unusable. An other solution is the application of two or more thinner layers which can be spin-coated at higher spin speed and will thus suffer less from the edge bead. However, this solution is only suitable for layers that are blanket cured, meaning that the sample is UV-cured without the use of a mask. In case we want to pattern a layer that is spun on in multiple steps, the alignment of the mask with respect to the layer becomes critical and requires the use of a mask aligner. Especially for the patterning of optical structures, the formation of rough edges or discontinuities between the different layers is highly undesirable because of the additional scattering loss.

Truemode, however, has to be UV-exposed in proximity mode in an inert medium such as nitrogen or vacuum, because of the fact that oxygen can inhibit the polymerization by reacting with radicals that initiate the polymerization. These requirements exclude the use of the mask aligner that is available at our lab because it can only be used in contact mode in standard environment. The alignment of the mask is therefore arranged manually. During the UV-exposure, the sample is placed in a closed box into which a continuous nitrogen flow is launched.

The processing of the cladding and core layer for the formation of the optical layer consists of the following steps, as is schematically depicted in Fig. 2.12:

- Spincoating of the core/cladding layer onto the FR4 substrate at the spinspeed that delivers the desired layer thickness according to the experimentally mea-

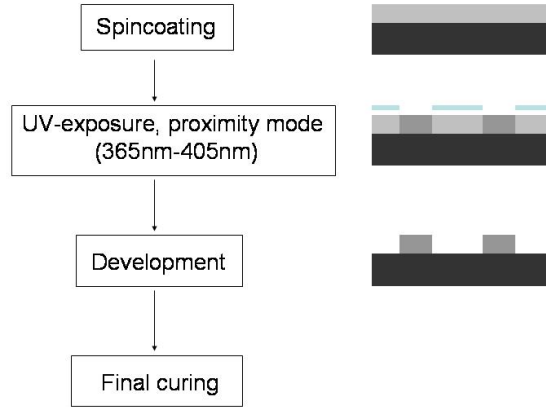


Figure 2.12: Processing steps used for the patterning of the Truemode layers.

sured spincurve. For a $50\ \mu\text{m}$ thick core respectively cladding layer, this corresponds to a spin speed of 250rpm respectively 200rpm.

- UV-exposure in proximity mode in a nitrogen environment. UV-exposure can be either through a suitable mask if the layer is to be patterned, as is the case for the core layer, or using flood exposure if the layer is not to be patterned, as is the case for the cladding layers. For a $50\ \mu\text{m}$ thick film, the exposure time is 60s for both the cladding and the core layers with a broadband UV-lamp, which has an intensity of $4\text{mW}/\text{cm}^2$. During the UV-exposure, radicals are created that will initiate the polymerization.
- In the case that the UV-exposure is done through a mask, the patterned layer has to be developed in MIBK (methyl isobutyl ketone). The non-exposed areas are washed away during this step, transferring the mask pattern to the layer.
- Final curing step in convection oven: 1 hour at 120°C . In this final curing step, a highly cross-linked material is formed that has excellent optical and thermal properties.

The above described procedure is used for the patterning of the original Truemode material, which we will refer to as the wet film formulation. Recently, the core material became available in a dry film formulation, which can be UV-exposed in contact mode in standard environment, allowing the use of the available mask-aligner (Süss Electro Technique). The viscosity of the dry film core material is higher than the wet film core material, $50\ \mu\text{m}$ thick films can be spun at 1500rpm, limiting the edge bead problems encountered with the wet film material. This allows the use of standard UV-lithography for the patterning of the layer using the available mask aligner, which can lead to considerably higher throughput and better reproducibility. The processing of the dry film material corresponds to the processing steps used for the patterning of the wet film material. Main difference is the fact that the UV-exposure can be done in contact mode in standard environment.

The thermal stability and behaviour of the Truemode material has been tested with TGA and DSC measurement, which were carried out by the research group PBM (Polymerchemie en Biomaterialen) of Ghent University. The TGA measurements were carried out with Hi-Rs TGA 2950 Thermogravimetric Analyser (TA instruments). The sample was first equilibrated at a temperature of 30°C and then heated to 500°C at a ramp of 10°C/min. The results are given in Table 2.3. The temperature at which a 5% weight loss occurs is typically considered as the limit of the range within which the polymer is considered to be stable. This temperature indicates the applicability range of the polymer. The measured TGA curves for the Truemode cladding and core material are shown in Fig. 2.13. From these measurement results, we can conclude that the Truemode cladding material is thermally stable up to a temperature of 346°C and the core material up to a temperature of 305°C. This difference in thermal stability can to a certain extent be explained by the difference in composition between the core and cladding material, and assumes that the cladding material has a higher degree of cross-linking than the core material.

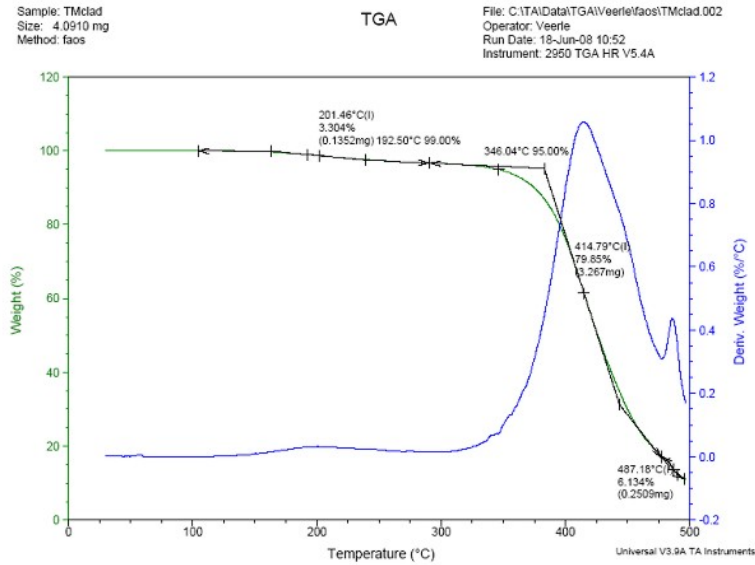
	5% weight loss
Truemode cladding	346°C
Truemode core	305°C

Table 2.3: Results of the TGA measurement on Truemode Backplane™ Polymer cladding and core material.

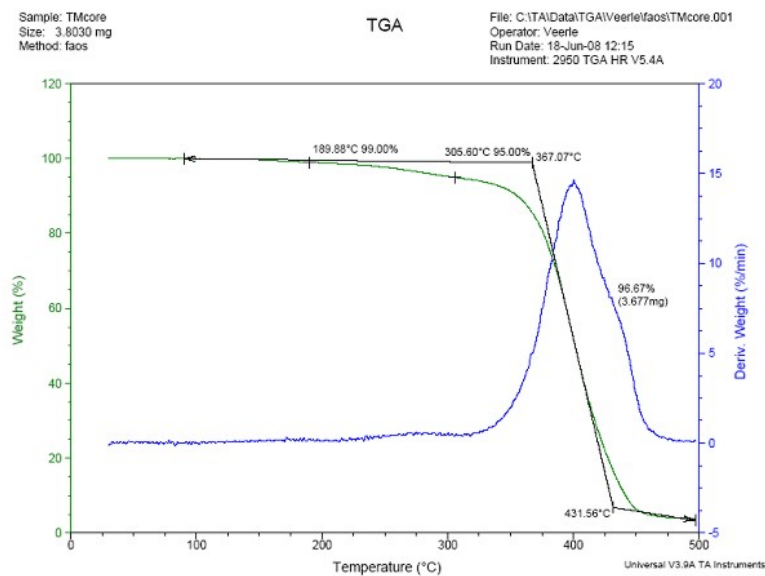
DSC measurements were carried out with DSC 2920 Modulated DSC (TA instruments). The measurement method is as follows:

- equilibrate at 30°C
- isothermal for 3 minutes
- ramp 10°C/min to 150°C
- isothermal for 3 minutes
- ramp 10°C/min to -40°C/-60°C
- isothermal for 5 minutes
- ramp 10°C/min to 150°C
- isothermal for 3 minutes
- ramp 10°C to -40°C/-60°C
- isothermal for 5 minutes
- ramp 10°C/min to 200°C

The measured DSC curves are shown in Fig. 2.14. From these curves, we can conclude that the glass transition temperature of the both the cladding and core material is around 65°C, which is much lower than the value given in the datasheet. Multiple measurements have been carried out, each time giving the same result. We do not have an explanation for this discrepancy.

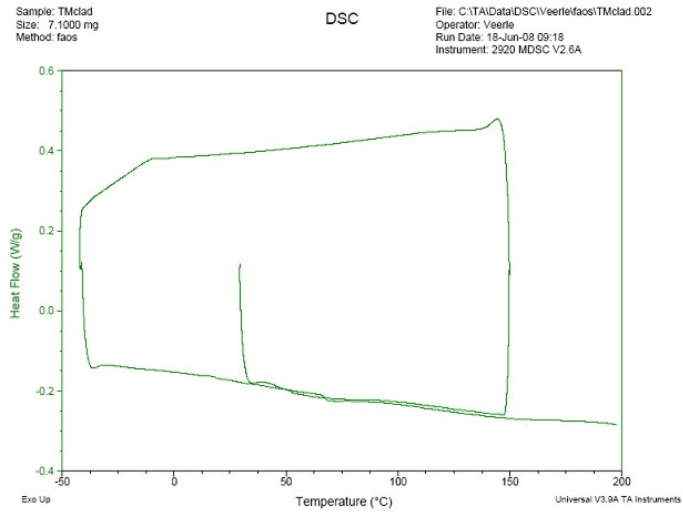


(a)

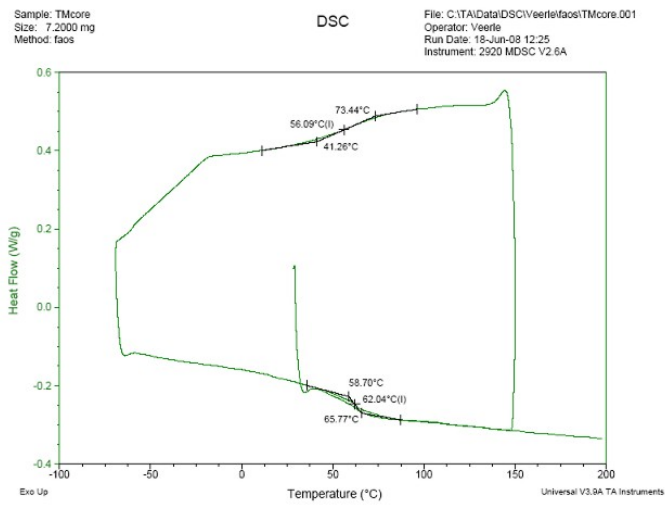


(b)

Figure 2.13: (a) TGA curve measured on the Truemode cladding material. From this curve, we can conclude that the Truemode cladding material is thermally stable up to a temperature of 346°C; (b) TGA curve measured on the Truemode core material. From this curve, we can conclude that the Truemode core material is thermally stable up to a temperature of 305°C



(a)



(b)

Figure 2.14: (a) DSC curve measured on the Truemode cladding material; (b) DSC curve measured on the Truemode core material.

2.3.2 Alternative polymer materials

At this moment, the Truemode material has a limited commercial availability, mainly because it is being studied by a couple of research groups and not yet used for a commercial application. Other optical polymers have been developed at laboratories worldwide. Three alternative optical polymers have been chosen that can also be used for the optical layer. Main criteria for choosing these materials is a low propagation loss at 850 nm, a high thermal stability and compatibility with standard PCB manufacturing. Preference is given to polymer materials that are already used by other laboratories in order to be able to exchange experience and work toward one common solution. In addition, it is always a good idea to have a back-up solution in case something goes wrong. Three polymer material will be discussed in the following paragraphs: Ormocer®, Epocore/clad and SU8.

Ormocer®

Ormocer®s are hybrid organic-inorganic polymer materials synthesized by sol-gel process. This process starts by building up an inorganic network through controlled hydrolysis, which means that one or more water molecules are split into hydrogen (H^+) and hydroxide (OH^-) ions which may go on to participate in further reactions, and condensation, which means that a molecule of water is split of during the reaction, of organically modified Si alkoxides. Co-condensation with other metal alkoxides (Ti, Zr, Al alkoxides) is also possible and allows the tailoring of the mechanical and optical properties of the material. In a subsequent step the polymerizable groups, which are fixed to the inorganic network, react with each other in a thermal or UV-initiated process. In this two-stage process an inorganic-organic copolymer is synthesized. In addition, it is possible to use organically modified Si alkoxides, which do not enter into any organic polymerization reaction and thereby contribute to an organic functionalization of the inorganic network. The idea of forming a hybrid structure is to shift the stability properties and optical quality of inorganic materials, the high thermal stability and mechanical strength, towards polymers but still offering simultaneously the processing possibilities of conventional polymers [8]- [11].

Inorganic polymers often show improved properties like better heat resistance, chemical stability and improved electrical properties. The properties of the Ormocers can be tailored according to wish; the material is for this reason used for a variety of applications such as anti-reflective coating, passivation layer, optics and even as dental filling material [12]. The relative proportions of the structural elements determine the material properties. The properties are controlled by the choice of base materials, by how the inorganic polycondensation reaction is conducted, and by controlling the linking reactions which lead to the construction of the organic network. The refractive index of the material can be precisely adjusted by the mixing of different Ormocer®resins. The absorption spectrum is given in fig. 2.15. The properties of the used Ormocer material that are of importance for the use as an optical layer are given in Table. 2.4.

The processing of the layers consists of the following steps:

- Spincoating of the core/cladding layer onto the FR4 substrate at spinspeed that corresponds to the desired layer thickness according to the experimentally measured spincurve.

Optical properties	
Propagation loss core material at 633nm	0.06 dB/cm
Refractive index core	1.538
Refractive index cladding	1.5214
Thermal properties	
Coefficient of thermal expansion	100-130 ppm/K
Thermal stability	up to 270°C

Table 2.4: Main properties of used Ormocer material.

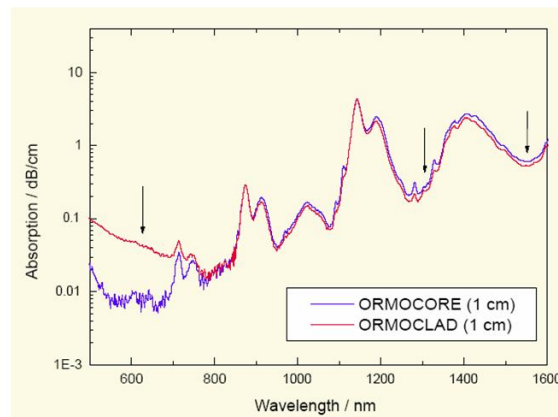


Figure 2.15: Absorption spectrum of Ormocer® [12].

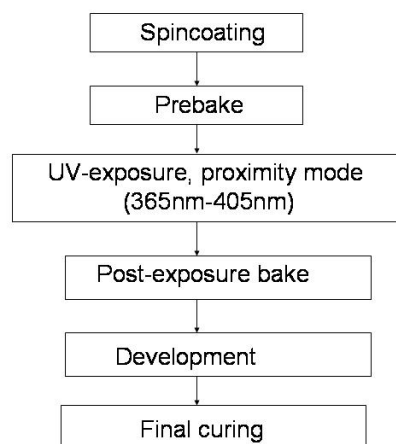
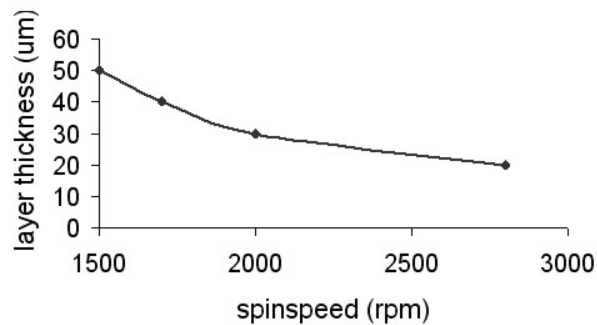
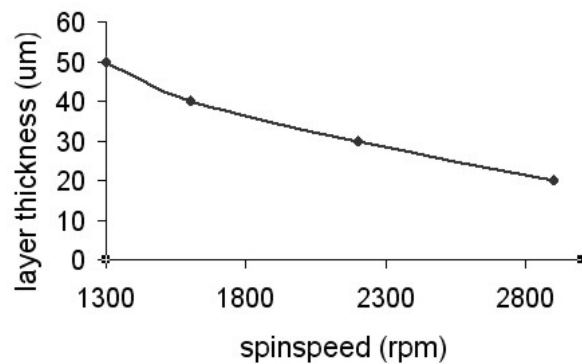


Figure 2.16: Application process for the Ormocer layers.



(a)



(b)

Figure 2.17: (a) Spincurve of the Ormoclad material; (b) spincurve of the Ormocore material.

- Prebake step: 2 minutes at 80°C on a hotplate.
- UV-exposure through a suitable mask in proximity mode in case the layer is to be patterned, as is the case for the core layer, or flood exposure in case the layer is not to be patterned, as is the case for the cladding layers. The use of the mask in proximity mode is required because of the sticky character of the material.
- Post-exposure bake: 5 minutes at 80°C-120°C on a hotplate.
- Development step: at least 60s in ORMODEV, which is the dedicated developer. The non-exposed areas are washed away, transferring the desired pattern to the layer.
- Hard-bake step: one hour at 150°C on hotplate.

The spincurve, which gives the layer thickness in function of the spin speed, is given in Fig. 2.17. The required spinspaceed for a layer thickness of 50μm is 1300 rpm for the Ormocore and 1500 rpm for the ormoclad material. The spinspaceed is much higher than for the case of the Truemode material, which minimizes the appearance of edge

bead. In addition, the reproducibility of the layer thickness is much better than for the Truemode material, mainly because of the higher spinspeed. Drawback is the fact that the UV-exposure has to be done in proximity mode, which means that the air gap between the mask and the layer will determine the width of the patterned structures. It is for this reason important to control the thickness of the air gap between the mask and the sample.

The Ormocer material can be UV-exposed in a standard environment, which means that the available mask aligner can be used for the patterning of the layers. The distance between the mask and the sample can be arranged with the use of a micro-screw. Contact between the mask and the optical layer should be avoided because of the sticky character of the optical layer. The contact between the mask and the polymer layer will induce surface roughness or defects to the layer after the UV-exposure.

SU-8

SU-8 is a high contrast, epoxy-based negative photoresist designed for micromachining and other microelectronic applications, where a thick chemically and thermally stable image is desired. The exposed and subsequently cross-linked portions of the film are rendered insoluble to liquid developers. SU-8 is best suited for permanent applications where it is imaged, cured and left in place. SU-8 is most commonly processed with conventional near UV (350-400nm) radiation, although it may be imaged with e-beam or x-ray. However, i-line (365nm) is recommended when vertical side walls are desired. Upon exposure, cross-linking proceeds in two steps: formation of a Lewis acid during the exposure process, followed by acid-initiated, thermally driven epoxy cross-linking during the post exposure bake (PEB) step. A normal process is: spin coating, soft bake step on a hotplate, UV-exposure in contact mode, post expose bake (PEB) on hotplate and development. A controlled hard bake is recommended to further crosslink the imaged SU-8 structures, making the patterned layer even more stable and protected from outside influences such as moist.

The application of the SU-8 material consists of the following steps:

- spincoating of the material onto the substrate at a spinspeed that corresponds to the desired film thickness.
- soft-bake step: 6 minutes at 65°C and subsequently 20 minutes at 95°C on hotplate. This step is carried out to evaporate the solvent and densify the film.
- UV-exposure in contact mode: a strong acid is formed in the exposed area. The resist film is sufficiently dense to expose it in contact mode, which allows a good transfer of the mask pattern to the film.
- post-exposure bake: 1 minute at 65°C and subsequently 5 minutes at 95° on a hotplate. During this step, there is a selectively acid-initiated cross-linking the exposed material.
- development: SU8 developer and subsequently wash the sample in isopropylalcohol.

The experimental spincurve of the available SU-8 material is given in Fig. 2.18. The curve indicates that a spinspeed of 2000rpm is required for a thickness of 50 μ m.

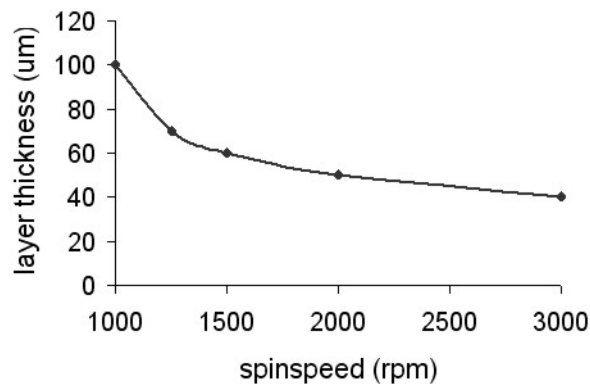


Figure 2.18: Spincurve of the SU-8 material.

SU8 is negative-type resist that can be patterned by UV-exposure at 365nm in contact mode. This allows a good imaging of the mask pattern onto the underlying SU-8 layer. The UV-exposure at 365nm is necessary in order to obtain structures with straight sidewalls. In case a broadband UV-source is used, the resulting imaged structures will show a negative wall or T-topping. In order to minimize stress built up, the post-exposure bake is done in three temperature steps. SU-8 has good mechanical properties, therefore hard bakes are normally not required. For applications where the imaged resist is to be left as part of the final device, the resist may be hard baked between 150-200°C on a hot plate or in a convection oven to further cross link the material. Bake times vary based on the type of bake process and film thickness.

The optical loss of the material at 850nm is rather high ($\leq 0.5\text{dB/cm}$ [13]) but might be acceptable for short-distance applications. The material has very good planarization properties and shows an excellent adhesion to the FR4 substrate, which makes it interesting as planarization layer for the rough FR4 substrate. Its high mechanical and thermal stability make it an interesting candidate for optical interconnections and in addition it is commonly used in PCB manufacturing. The material has a refractive index of 1.58 at 850 nm, which is relatively high and makes it not so straightforward to find a suitable cladding material.

2.3.3 Epocore/clad

The Epocore/Epoclad material has been developed as a new material for PCB optical waveguides (Microresist). The material can be patterned with standard photolithography and is compatible with the elevated temperature and pressure that occur during standard PCB manufacturing [14]. The material can be UV-exposed in contact mode, meaning that the mask pattern can be imaged onto the optical layer in a very reliable way. The optical loss at 850 nm wavelength is higher than the other polymers that have been studied, around 0.2dB/cm, but is acceptable for links with a limited length. Epoxy resins only reach their final properties as reactive resins after they have successfully undergone final curing. As the degree of crosslinking increases, the glass temperature of a polymer rises, and, therefore too, the temperature necessary for curing. This is

Optical properties	
Propagation loss at 850 nm	0.2 dB/cm
Refractive index core	1.58
Refractive index cladding	1.57
Thermal properties	
Glass transition temperature	$\geq 180^{\circ}\text{C}$
Thermal stability	$\geq 230^{\circ}\text{C}$

Table 2.5: Main properties of used Epocore/Epoclad material.

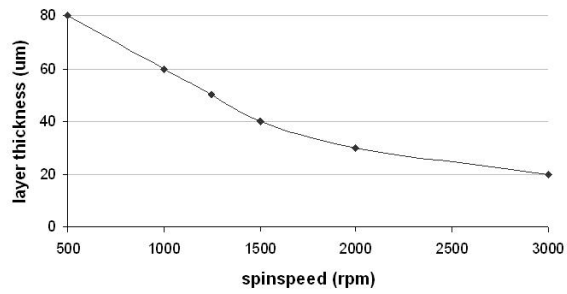
also true of the modified resist materials EpoCore and EpoClad. The processing of the layers consists of the following steps:

- Spincoating of the material onto the FR4 substrate at the spinspeed that corresponds to the desired film thickness.
- Prebake at 120°C on hotplate.
- UV-exposure in contact mode.
- Post-exposure bake at 140°C on hotplate.
- Hard bake

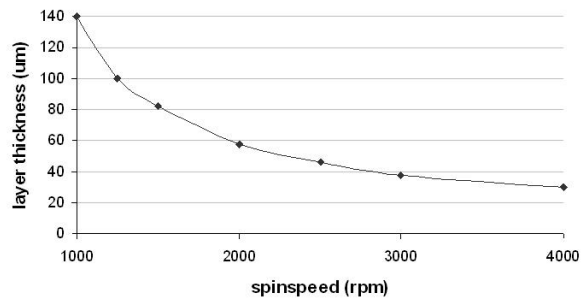
The experimentally measured spincurve for the core and cladding material is given in Fig. 2.19. The material has excellent thermal and mechanical properties and is compatible with the high temperatures and pressures that occur during PCB manufacturing and soldering.

2.4 Conclusion

Polymer materials offer a number of advantages over other alternative waveguide media such as glass sheets and optical fibers such as potentially low cost (for a large enough market), the large variety of potential technologies that can be used to pattern the polymer layers and the ability to tailor the properties such as the refractive index and the mechanical properties. The main requirement on the polymer material are a low optical loss, a high thermal and mechanical stability and compatibility with the existing PCB manufacturing processes. Four different commercially available polymers have been discussed in this chapter: Truemode BackplaneTMPolymer, Ormocer, SU8 and Epocore/clad. All four materials are UV-patternable and have excellent optical and thermal properties. Main focus within this PhD is placed on Truemode, because of its low propagation loss (0.04dB/cm at 850 nm), excellent thermal properties (T_g theoretically above 150°C and degradation temperature around 350°C) and compatibility with the main PCB manufacturing processes. The other three polymers are studied as alternative materials for use as optical layer.



(a)



(b)

Figure 2.19: (a) Spincurve of the Epocore material; (b) spincurve of the Epoclad material.

Bibliography

- [1] L. Eldada, "Advances in polymer integrated optics," *Journal of selected topics in quantum electronics*, Vol. 6, No. 1, 2000
- [2] L. Eldada, "Polymer integrated optics: promise vs. practicality," *Proc. SPIE*, Vol. 6185 618501, 2006
- [3] L. Eldada, "Telcordia qualification and beyond: reliability of today's polymer photonic components," *Proc. SPIE*, Vol. 5724, pp. 96-106, 2005
- [4] G. Challa, "Polymer chemistry: an introduction," *Ellis Horwood series in polymer science*, Ellis Horwood Limited, ISBN 0-13-489691
- [5] H. Ma, A. K.-Y. Jen, L. R. Dalton, "Polymer-based optical waveguides: materials, processing and devices," *Advanced materials*, Vol. 14, No. 19, 2002
- [6] M. Moynihan, B. Sicard, T. Ho, L. Little, N. Pugliano, J. Shelnut, H. B. Zheng, P. Knudsen, D. Lundy, N. Chiarotto, C. Lustig, and C. Allen, "Progress Towards Board-level Optical Interconnect Technology," *Proc. SPIE*, Vol. 6185, 2006
- [7] www.exxelis.com
- [8] S. Uhlig *et al.*, "Polymer Optical Interconnects - A Scalable Large-Area Panel Processing Approach," *IEEE Transactions on advanced packaging*, Vol. 29, no. 1, pp. 158-170, 2006
- [9] U. Streppel *et al.*, "New wafer-scale fabrication method for stacked optical waveguide interconnects and 3D micro-optic structures using photoresponsive (inorganic-organic hybrid) polymers," *Optical materials*, Vol. 21, pp. 475-483, 2002
- [10] R. Houbertz *et al.*, "Inorganic-organic hybrid materials for application in optical devices", *Thin Solid Films*, Vol. 442, pp. 194-200, 2003
- [11] S. Uhlig, M. Robertsson, "Limitations to and Solutions for Optical Loss in Optical Backplanes," *Journal of Lightwave Technology*, Vol. 24, no. 4, pp. 1710-1724, 2006
- [12] www.microresist.de
- [13] M. Karppinen *et al.*, "Embedded optical interconnect between ceramic BGA packages on FR4 board using embedded waveguides and passive optical alignments," *Proc. 56th Electronic Components and Technology Conference*, pp. 799-805, 2006
- [14] H. Schröder, J. Bauer, F. Ebling, M. Franke, A. Beier, P. Demmer, W. Stilla, J. Kostelnik, R. Mödinger, K. Pfeiffer, U. Ostrzinski, E. Griese "Waveguide and packaging technology for optical backplanes and hybrid electrical-optical circuit boards", *Proceedings SPIE*, Vol. 6124, 612407-1, 2006

Chapter 3

Multimode optical waveguides

3.1 Introduction

One of the basic building blocks of an optical interconnection are polymer optical waveguides, used to guide the light in the plane of the optical layer. A key advantage of optical polymer-based processes is the possibility of using large-area, low-cost fabrication of optical waveguides through simple deposition techniques such as spincoating or spraycoating and low-temperature processing. However, for a successful adoption in the field of optical interconnects such polymer waveguides have to fulfill stringent requirements such as low propagation loss ($\leq 0.05\text{dB/cm}$ (depending on the interconnection length) at 850 nm) as well as process compatibility with PCB manufacturing. A number of photopatternable optical polymers with rather low optical absorption at the light wavelength of 650-980 nm are available on the market [1]. However, most of the polymers with optical losses of about 0.05 dB/cm have only limited commercial availability, which in part is due to the high polymer cost. Fully commercially available photopatternable polymers typically have higher losses of about 0.2 dB/cm. The waveguide propagation losses have a significant effect on the performance of optical boards with large dimensions. Therefore, the use of low loss waveguides for large boards is of keen importance.

3.2 Requirements

The optical waveguides need to have low optical loss at the datacom wavelength 850 nm and in some cases also at the major telecom wavelengths 1310 and 1550 nm. There are several sources of optical loss including absorption loss, scattering loss, reflections, radiation loss and fiber coupling losses [2]. Extrinsic scattering loss is mainly caused by large inclusions such as particles, voids, cracks and bubbles. Generally, an inclusion is called large if it is greater than $1\mu\text{m}$ in diameter, in which case the scattering intensity becomes largely wavelength independent. It can be minimized by rigorously following the guide lines given in the datasheet of the material and by performing the processing in clean room environment. Intrinsic scattering results from density fluctuations and compositional inhomogeneities, both of which occur on very short length scales

(0.1 μm or less). Polymer waveguides are typically formed by spincoating processes in which polymers are deposited from solution, patterned and subsequently dried by heating on a hotplate or in an oven. The resulting films are generally uniform, but can have a surface roughness that will contribute to the scattering losses. The surface roughness of the sidewalls of the waveguides should be as low as possible in order to reduce the induced scattering loss.

When thin films are deposited on a substrate, an important aspect of the process is managing the stress that can develop. Polymer waveguides are deposited at room temperature in most cases, but solvent bakes and annealing often occur at moderately high temperatures (120°C for Truemode material). These temperature excursions, when coupled with the coefficient of thermal expansion (CTE) mismatch between the film and the substrate, result in stress induced scattering.

As scattering often comes from a number of sources, experimental scattering data is often fit with an empirical law of the form:

$$\alpha_{scatter} = A + \frac{B}{\lambda^2} + \frac{D}{\lambda^4}$$

where A is the contribution from large particle scattering ($\gg \lambda$), B the contribution from inhomogeneities on the order of λ in size (Mie scattering) and D the contribution from small inhomogeneities ($\ll \lambda$, Rayleigh scattering). The scattering loss can be minimized in polymer waveguides by using direct photopatterning as opposed to surface roughness inducing reactive ion etching. It can also be reduced by ensuring the homogeneity of the medium and by minimizing intrinsic stresses.

Insertion loss is defined as:

$$-10 \log_{10}(P_{out}/P_{in})$$

with P_{in} the input and P_{out} the output power. Acceptable insertion loss is determined by the overall system loss budget, which will be a function of transmitter power, optical amplifier gain, and receiver sensitivity among other factors. The total insertion loss achieved in planar polymer components can approach the value of the material absorption loss when fabrication techniques are optimized.

3.3 Multimode optical waveguides

3.3.1 Waveguide structure

Optical fibers and waveguides consist of a core, in which light is confined, and a cladding, a material surrounding the core, as shown in Fig. 3.1. The refractive index of the core n_1 is higher than that of the cladding n_0 . Therefore the light beam that is coupled to the end face of the waveguide is confined in the core by total internal reflection. The condition for TIR at the core-cladding interface is given by:

$$n_1 \sin(\pi/2 - \phi) \geq n_0$$

The angle ϕ is related with the incidence angle θ by Snell's law of refraction:

$$\sin \theta = n_1 \sin \phi \leq \sqrt{n_1^2 - n_0^2}$$

We obtain the critical condition for TIR as:

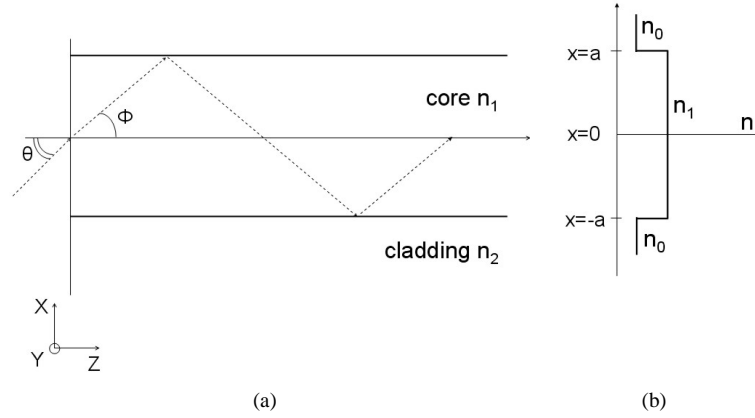


Figure 3.1: (a) Waveguide cross-section; (b) cross-sectional refractive index profile.

	NA	θ_{max}	ϕ_{max}
Truemode	0.3	17.6°	11.3°
Ormocer	0.23	13°	8.46°
Epocore/clad	0.18	17.6°	6.47°

Table 3.1: Value of the NA, θ_{max} and ϕ_{max} for Truemode, Ormocer, Epocore/clad.

$$\theta \leq \arcsin \sqrt{n_1^2 - n_0^2} \equiv \theta_{max}$$

The refractive index difference between core and cladding material is typically 1 to 3%, meaning that $\sin \theta \approx \theta$. This means that θ_{max} can be approximated by:

$$\theta_{max} \cong \sqrt{n_1^2 - n_0^2}$$

In this formula θ_{max} denotes the acceptance angle of the waveguide and is related to the numerical aperture (NA) by $NA = \sin \theta_{max}$ which approximates θ_{max} for $\sqrt{n_1^2 - n_0^2}$ much smaller than 1. The relative index difference Δ between n_0 and n_1 is defined as:

$$\Delta = \frac{n_1^2 - n_0^2}{2n_1^2} \cong \frac{n_1 - n_0}{n_1}$$

and is commonly expressed as a percentage. The numerical aperture NA is related to the relative refractive index difference Δ by:

$$NA = \theta_{max} \cong n_1 \sqrt{2\Delta}$$

The maximum angle for the propagating light within the core is given by $\phi_{max} \cong \theta_{max}/n_1 \cong \sqrt{2\Delta}$. The value of the NA, θ_{max} and ϕ_{max} for the different optical polymers mentioned in the previous chapter, are given in Table 3.1. The value for SU-8 is not given, because of the fact that no suitable cladding material was available at the time of the experiments. From this Table, we can see that for each application, an optical polymer can be found that has suitable properties.

A waveguide with a large NA consequently has a large acceptance angle, given by θ_{max} , which facilitates the coupling of light into the waveguide. On the other hand,

a large NA also means that the waveguide has a large divergence angle, which means that the light spot will diffract considerably after the being coupled out at the waveguide output facet, in this way complicating the detection of the outcoupled light beam. This is especially the case when an optical fiber is used to detect the outcoupled spot, because the acceptance angle is determined by the NA of the detector fiber. Optimal coupling efficiencies are obtained when the NA of the waveguide and the detector fiber are matching. A second important factor that influences the maximum achievable coupling efficiency, is the air gap that exists between the output facet of the waveguide and the detector fiber, because of the fact that the spreading of the outcoupled light spot will increase with the propagation distance. The coupling efficiency can however be increased with the use of micro-lenses to collimate or focus the light beam or by applying index matching gel between the output of the waveguides and the input of the detector, in this way limiting the spreading of the light spot. Waveguides with a large NA, and thus large refractive index contrast, can be bent in a very compact way which is advantageous for the fabrication of compact planar waveguide structures. The choice for NA will in most cases rest on a compromise between on one hand a compact optical system and on the other hand an efficient detection.

We have accounted for the mechanism of mode confinement and have indicated that the angle ϕ must not exceed the critical angle. Even though the angle ϕ is smaller than the critical angle, light rays with arbitrary angles are not able to propagate in the waveguide. Each mode is associated with light rays at a discrete angle of propagation, as given by the electromagnetic wave analysis. The number of modes M that propagates in a waveguide with diameter d and NA can for a large number of modes be approximated by $M \approx 2(d/\lambda)^2 NA^2$. An excellent analysis is given in [3].

3.3.2 Waveguide processing

The techniques and relevant issues for processing polymer optical waveguides are quite similar to those for polymers in micro-electronic packaging. Common techniques for casting polymer films include spincoating, doctor blading and spray coating. The major concerns when fabricating a film are a uniform film-thickness, absence of air bubbles and striations, good adhesion to the substrate, and reliable film thickness. Each technique has associated advantages and disadvantages. For example, spincoating allows suitable control of film thickness and uniformity; however, eliminating striations in films can be difficult and for low spinspeeds edge bead, which is the accumulation of material near the edges of the sample, can become a considerable problem.

Techniques that have been used for patterning optical waveguides in polymer films include photo-resist based patterning, direct lithographic patterning [4] [5], laser direct writing [6] and soft lithography [7] [8]. We also mention patterning of the optical waveguides with laser ablation, even though this is not a mass fabrication technology but an interesting prototyping technique. Photo-resist based patterning requires a reactive ion etching step, which gives rough structures and thus necessitates the use of an extra smoothing step in order to obtain structures with a low surface roughness. In direct lithographic patterning, the desired waveguide pattern is transferred to the optical layer by UV-exposure through a suitable mask, either in contact mode or proximity mode. This process allows a high throughput and is compatible with standard PCB manufacturing. Main drawback is the fact that a new mask has to be designed and fabricated every

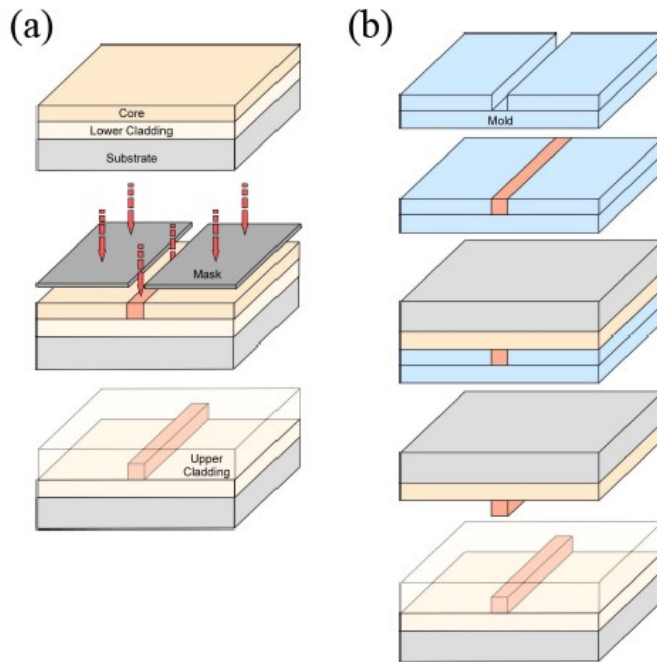


Figure 3.2: (a) Processing steps that are required for the patterning of the waveguides in the optical layer using direct lithography; (b) processing steps that are required for the patterning of the waveguides in the optical layer using embossing [9].

time a change is made to the design, with the associated cost. The patterning of the optical layer can also be done using laser direct writing, in which case the laser beam is scanned over the optical layer according to a predefined pattern. The wavelength and fluence of the laser source determine the materials that can be patterned. Laser direct writing can play a role in the fabrication of large dimension parts where masks cannot be produced; for instance, several meter-long polymer waveguides can be laser-written on large substrates such as rolls or flexible plastics. The term soft lithography is used for patterning technologies such as embossing [9] in which case a mold is formed first and then the core layer is formed in the mold by polymer casting. The surface roughness of the replicated structures depends largely on the quality of the master component, which also determines the price of the master component. The processing steps that are required for the patterning of the waveguides in the optical layer for both the direct lithographic and embossing technique are shown in Fig. 3.2.

3.4 Laser ablated waveguides

3.4.1 Truemode Backplane™ Polymer

Truemode material is photo-sensitive meaning that it can be directly patterned with UV-lithography, which is a standard technology used that is currently used in PCB

manufacturing. As was mentioned in the previous chapter, there exist two different material formulations: wet and dry film.

Wet film formulation

The UV-exposure of the wet film formulation has to be done in an inert medium such as nitrogen which excludes the use of the available mask aligner. In addition, the mask has to be placed in proximity mode because of the sticky character of the material in which case an air gap exists between the mask and the sample, as opposed to contact mode in which case the mask is placed in physical contact with the sample. This can affect the reproducibility of the waveguide width because the waveguide width is determined by the air gap that exists between the mask and the polymer film. In the current set-up, the sample is placed in a closed box into which a continuous flow of nitrogen is launched. The mask is placed on an FR4 spacer, which has a thickness of 1mm up to 1.6mm, in correspondence with the thickness of the FR4 substrates onto which the optical layer is applied. The square spacer with side 10 cm has an opening of 5 cm×5 cm in the centre for the insertion of the sample. Tape is glued on the edges of the FR4 spacer in order to have an air gap between the mask, that is placed on the tape, and the top surface of the polymer layer. The thickness of the air gap between the mask and the optical layer, is determined by the thickness of the optical layer. As was explained in the previous chapter, there is an uncertainty of $\pm 5\text{-}10\ \mu\text{m}$ on the layer thickness because of the low spinspeed that is used for the application of the layers. This makes it very difficult to reproduce the waveguide dimensions in an accurate way. The alignment between the mask and the sample is done manually, which makes it impossible to align the waveguides in a multilayer optical structure with respect to each other up to an accuracy of 5-10 μm .

The cured wet film layers show an excellent response to KrF excimer laser ablation. During the ablation there is a low deposition of debris, resulting in ablated structures that have a low surface roughness. The ablation of the waveguide cores into the optical layer is a serial process, in contrast to photolithography where multiple arrays of waveguides can be patterned simultaneously according to the mask design. However, it is a very flexible technology and does not necessitate the use of a mask, which allows fast adaptation to design changes, making it an interesting prototyping technology that can be used for the fabrication of proof-of-concept demonstrators. The demonstrator design can be optimized using laser ablation, and in a later phase, when the final design is ready, the demonstrator boards can be fabricated using technologies that have a lower cost and higher throughput technologies such as for instance photolithography.

Dry film formulation

As a solution to the processing problems experienced with the wet film material, the dry film formulation has been developed. Dry Truemode can be patterned in standard environment in contact mode, which allows the use of a standard mask aligner possible. This makes the process compatible with the photolithographic processes used nowadays in PCB manufacturing and makes a high throughput possible. This makes this approach preferable for practical applications.

3.4.2 Laser ablation

Laser ablation is a versatile micro-structuring technology that can be used to pattern a wide variety of materials, ranging from metals and ceramics to polymer materials. It is a flexible non-contact technology that is fully compatible with existing PCB manufacturing processes where it is already used for the drilling of micro-vias in high-density electrical boards. It is also used for the deposition of thin coatings of a wide range of target materials on a broad range of substrates at room temperature and for resistor trimming. It is a mask-less technology meaning that design changes can be implemented in a very fast and flexible way. This in contrast to photolithography where the mask design would have to be changed and a new mask would have to be made with the associated extra cost.

The ablation process relies on the controlled removal of material using the photon energy of the laser beam. The principle is schematically shown in Fig 3.3. The photon energy of the laser beam is deposited in the irradiated surface and the near-surface region down to a penetration depth that is characteristic of the laser wavelength and the material. The energy may be deposited either by exciting electronic or vibrational transitions in atoms, ions, molecules, or optically active defects. As soon as the photon density inside the material exceeds a certain threshold, the ablation threshold, the photon energy can be used for material decomposition. This leads to photochemical decomposition processes, in which the chemical bonds in the molecule are broken, and photothermal decomposition processes, in which the material decomposition is based on thermal reactions with associated local heating of the sample. An ablation plume is formed that expulses the decomposed material away from the surface and leaves an ablated crater. The ablation plume contains evaporated particles and also non-evaporated particles that can drop back to the surface of the sample near the ablated area. The deposition of these non-evaporated particles is called debris. The debris deposition increases the surface roughness of the ablated structures and is highly undesirable for optical structures. The use of a fume exhaust system reduces the debris deposition as does carrying out the ablation in an inert medium, which allows the ablation plume to expand more rapidly.

The material that can be patterned with a certain laser source depends on the wavelength and the fluence, which corresponds to the pulse energy measured on the translation stage divided by the surface of the mask after the projection onto the sample. An efficient ablation, with low debris deposition, is possible if the target material shows a high absorption for the wavelength that is emitted by the laser beam. Polymer materials show a high absorption in the UV-range, which makes them ideal candidates for ablation with UV-lasers such as excimer laser sources. The tight bonding of electrons to molecular groups in most organic systems results in electronic spectra that can be classified according to the molecular bonds present in the system. Strong absorption in organic systems is due to electronic transitions between molecular states. The energy required for such transitions corresponds approximately to bond energies (several electronvolts) with the result that most electronic transitions of organic molecules occur at UV-wavelengths [10]. Due to their high photon energy between 3.5 eV (351 nm) and 7.9 eV (157 nm) excimer laser radiation is strongly absorbed by molecules via electronic transitions into an excited state. Examples are the carbon double bonds (C=C) or the carboxyl group (C=O). The absorption is correlated to transitions between certain electronic states [11].

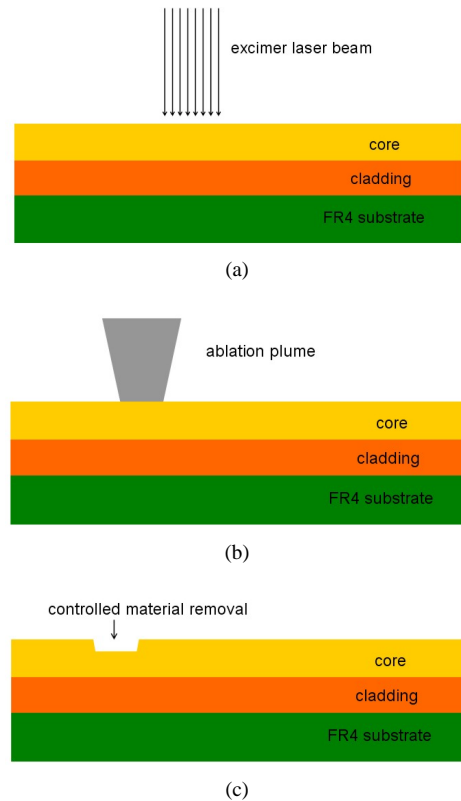


Figure 3.3: (a) The photon energy of the laser beam is deposited in the irradiated surface and the near-surface region down to a penetration depth that is characteristic of the laser wavelength and the material; (b) as soon as the photon density inside the material exceeds a certain threshold, the ablation threshold, the photon energy can be used for material decomposition. An ablation plume is formed that expulses the decomposed material away from the surface and leaves an ablated crater; (c) controlled material removal.

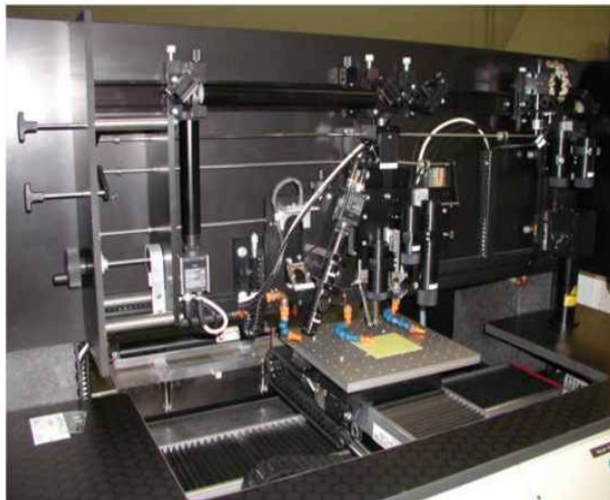


Figure 3.4: Picture of the ablation set-up.

The ablation set-up (Fig. 3.4) contains three different laser sources: a KrF excimer laser (248 nm), a frequency tripled Nd-YAG laser (355 nm) and a CO₂ laser (10.6 μ m). The excimer laser beam can be tilted, which eases the patterning of angled features. During the ablation, the sample is placed on a computer-controlled translation stage which has an accuracy of 1 μ m. The Nd-YAG laser can be used for the ablation of metals and ceramics which can be useful in case alignment features have to be ablated in a metal film. The CO₂ laser can be used for the ablation of the FR4 substrate, which can be used to ablated positioning holes into the substrate for instance for the insertion of MT-pins.

We study the ablation of Truemode Backplane™ Polymer with KrF excimer laser (248 nm), which is available at our research lab. The excimer laser beam, which has a rectangular cross-section, is sent through a mask with the desired cross-sectional dimension and pattern, and is projected onto the sample with an optical projection system with demagnification. The optical path of the laser beam is shown in Fig. 3.5. The pulse energy of the laser beam is monitored with an energy meter to ensure a good reproducibility of the ablation parameters. An attenuator is included in the optical path in order to be able to tune the pulse energy, especially in case low pulse energies are needed. Reason for this is that it is not possible to set the pulse energy lower than 2-3 mJ, this being the set value on the set-up which is higher the actual pulse energy that reaches the translation stage because of the losses that occur during the propagation in the optical path. The main properties of the available ATL-300 KrF excimer laser are given in Table 3.2.

The camera of the excimer laser is under a tilted position with respect to the translation stage. When the camera is focused on the top surface of the sample, the excimer laser beam will also be in focus. When the camera is put into focus on the sample, there is a lateral shift across the sample along the direction into which the camera is tilted. This shift can give cause alignment problems if it is not taken into account in a proper way.

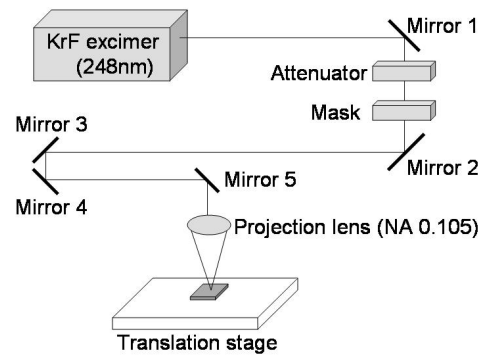


Figure 3.5: Optical path of the excimer laser beam.

Wavelength	248 nm
Maximum pulse energy	18 mJ
Maximum average power	5 W
Maximum repetition rate	300 Hz
Pulse duration	4-6 ns
Beam dimensions	4 mm × 6 mm
Beam divergence	2 mrad × 1 mrad
Energy stability	3%

Table 3.2: Main characteristics of KrF excimer laser

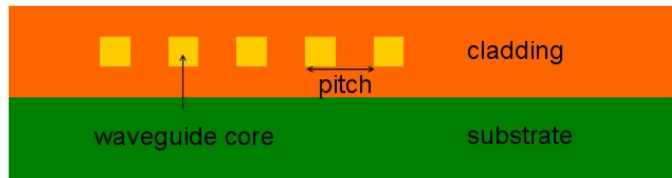


Figure 3.6: Array of five waveguides.

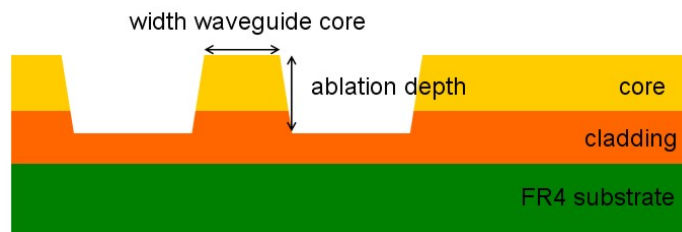


Figure 3.7: Ablation of the waveguide core features into the optical layer.

3.4.3 Experimental results

Multimode waveguides are ablated into the core layer by the controlled removal of material on both sides of the resulting waveguide core. The excimer laser beam is sent through a rectangular mask and projected onto the sample. In a first step, material is removed on one side of the waveguide core by scanning the laser beam over the sample at a certain velocity. The width of the mask determined the width of the ablated line; the laser fluence and the ablation speed determine the ablation depth. In a second step, the laser beam is shifted with respect to the sample over a certain distance and material is removed on the other side of the waveguide core by scanning the laser beam over the sample at the same ablation speed. This way a waveguide core is patterned into the optical layer as shown in Fig. 3.7. The shift of the laser beam determines the width of the waveguide core. Multiple waveguides are normally ablated next to each other, forming an array as is schematically shown in Fig. 3.6 for an array of five waveguides. The pitch between the waveguide cores in an array is determined by the shift of the laser beam and the width of the mask.

There is always a certain degree of tapering during the ablation, also called natural ablation. This means that the cross-section of the waveguides is not rectangular but slightly trapezoidal, as can be seen in fig. 3.7. The tapering angle depends on the laser pulse energy and the ablation depth. The tapering angle typically decreases from 15° to 12° when the pulse is increased from 6mJ to 12mJ and also decreases with increasing ablation depth.

The waveguide cores are ablated into the cured Truemode core layer in standard environment. Multimode waveguides with cross-section of approximately $50\mu\text{m} \times 50\mu\text{m}$, the width at the top of the waveguide core will be about $10\mu\text{m}$ smaller than at the bottom, on pitch $125\mu\text{m}$ can be patterned by sending the excimer laser beam through



Figure 3.8: Cross-section of an array of ablated waveguides in Truemode, the waveguides have a cross-section of approximately $50\mu\text{m} \times 50\mu\text{m}$ on pitch $125\mu\text{m}$ and are ablated with a pulse energy of 12mJ. The thermal ablation process is in this case dominant, giving a black appearance to the waveguide cores and the surrounding optical material.

a mask with dimensions $750\mu\text{m} \times 3000\mu\text{m}$. The masked laser beam is focused onto the translation stage with an optical projection system with demagnification 10. The cross-sectional dimensions and pitch of the waveguides in an array can be changed by using a mask with suitable dimensions.

The waveguides are ablated dynamically, meaning that the laser beam is scanned over the sample at a given velocity, firing a fixed number of pulses at each location. The ablation speed that is needed to deposit N pulses at each location is given by the following formula:

$$v = \frac{f \cdot l}{N}$$

with l the length of the mask, projected onto the sample, in the direction of movement and f the pulse repetition rate. From this formula, we can see that it is advantageous to choose the frequency sufficiently as high as possible. The length l of the mask is limited by the cross-sectional diameter of the laser beam. It is clear that the energy that is deposited onto the sample should be homogeneous over the entire surface of the mask projection in order to get a homogeneous ablation.

The surface roughness of the waveguide sidewalls should be lower than $\lambda/10$, with λ the operating wavelength, in order to minimize the scattering loss. The pulse energy of the excimer laser has been optimized in order to obtain waveguide cores with minimal surface roughness. This has been done by ablating the waveguide cores into the Truemode core layer at pulse energies between 3mJ and 12mJ and measuring the surface roughness of the ablated structures of the waveguide core sidewalls with a non-contact optical profiler (Wyko NT3300). The pulse repetition rate f has a very limited influence on the surface roughness of the ablated structures, and is for this reason set to 200Hz.

The average RMS surface roughness of the ablated waveguide core, measured on a scan area of $46\mu\text{m} \times 60\mu\text{m}$, is 35nm for a pulse energy of 3mJ, 48nm for a pulse energy of 6mJ and 49nm for a pulse energy of 12mJ. The thermal ablation process is dominant for the ablation with a pulse energy of 12mJ and 6mJ, giving a black appearance to the waveguide cores and the surrounding optical material. In Fig. 3.8 an array of waveguides is shown that are ablated with a pulse energy of 12mJ. The best results are obtained with the pulse energy of 3mJ, and for this reason this value will be used for the ablation of the waveguide cores into the optical layer. The ablated waveguide cores have a smooth sidewalls and show no change of colour, as can be seen in the cross-section shown in Fig. 3.9.

The patterning of the waveguide core features is done with the following parameters:



Figure 3.9: Cross-section of an array of ablated waveguides in Truemode, the waveguides have a cross-section of $\approx 50\mu\text{m} \times 50\mu\text{m}$ on pitch $125\mu\text{m}$. The waveguide core has a height of $50\mu\text{m}$ and a width of $45\mu\text{m}$ at the top of the core layer and $60\mu\text{m}$ at the bottom of the core layer.

- Pulse energy: 0.71 mJ/mm^2 , measured on the translation stage with an energy meter
- Pulse repetition rate: 200Hz
- Ablation speed: $360\mu\text{m/s}$
- Laser beam shift: $125\mu\text{m}$

The ablation speed is relatively low: the ablation of a 5 cm long waveguide takes approximately 5 minutes, at least for the first waveguide in an array because of the fact that material has to be removed on both sides of the waveguide core. The processing time is 2.5 minutes for the following waveguides in the array. Despite the serial character of the ablation process and the high processing time, the ablation process remains interesting because of its high flexibility, which allows us to adopt design changes in a very late stage of processing, making it an interesting patterning technology for practical applications where the design is typically optimized in multiple steps. However, it is clear that laser ablation is not suitable for the patterning of large-area boards because of the high cost and low throughput.

The top surface of the waveguide core has an average RMS surface roughness of 35nm on a scan area of $46\mu\text{m} \times 60\mu\text{m}$, measured with a non-contact optical profiler (Wyko NT3300), as is shown in Fig. 3.11. An SEM image of the patterned core layer is given in Fig. 3.10, and confirms the smooth character of the ablated waveguides. The waveguide core has a width of $45\mu\text{m}$ at the top of the core layer and $60\mu\text{m}$ at the bottom of the core layer.

The surface corrugation of the optical layer, after the application of a $50\mu\text{m}$ thick top cladding layer is $\leq 700\text{nm}$, as can be seen in Fig. 3.12. The core material is removed on both sides of the waveguide core. As can be seen in Fig. 3.12, the height difference between the top surface of the top cladding layer on the waveguide array and the top surface of the top cladding layer in the unpatterned area is approximately $2\mu\text{m}$. The filling of the ablated area with cladding material is good, giving a planarized top surface, which is a requirement in case opto-electronic elements are to be mounted onto the optical layer. For certain applications, a top cladding layer with a thickness $\leq 50\mu\text{m}$ is preferred, for instance because the light beam is to be coupled out of the plane of the optical waveguide. In this case, a minimal propagation distance between the out-of-plane coupling element and the detector will give an optimal coupling efficiency. The minimum acceptable top cladding layer thickness is determined by the planarity of the top cladding layer. Experiments indicate that a $30\text{-}50\mu\text{m}$ thick top cladding layer gives

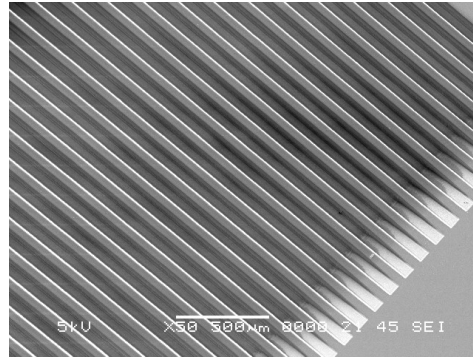


Figure 3.10: SEM image of the patterned core layer.

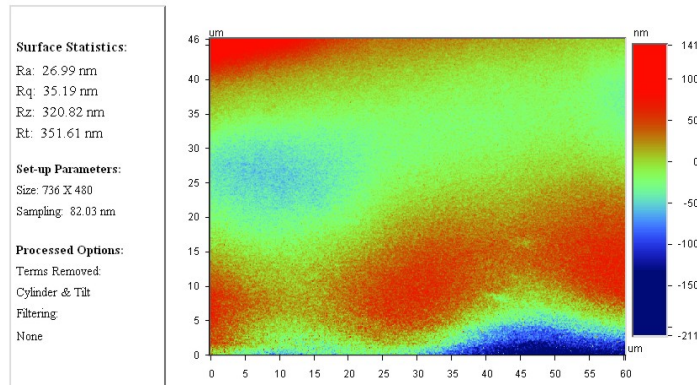


Figure 3.11: Surface roughness of the top of an ablated waveguide core, prior to the deposition of the top cladding layer, measured with a non-contact optical profiler (Wyko NT3300).

a good result. The surface corrugation of a $30\ \mu\text{m}$ thick top cladding layer is shown in Fig. 3.13. The surface corrugation is about six times higher than the one measured with the $50\ \mu\text{m}$ thick top cladding layer, but is still acceptable. For layer thicknesses $\leq 30\ \mu\text{m}$ the filling of the ablated areas is not sufficient to get a planarized top surface. Cut-back measurements indicate an average propagation loss of 0.13dB/cm [12]. For a more detailed description of these measurements, we refer to [13]. For the measurements, an $850\ \text{nm}$ light signal was coupled in horizontally into the waveguides with a graded index (GI) optical fiber with cross-section $50\ \mu\text{m}$ and NA 0.2. The light spot that is coupled out horizontally at the output facet of the waveguide is detected with a GI optical fiber with core diameter $100\ \mu\text{m}$ and NA 0.29. A picture of the sample, placed on the measurement set-up is shown in Fig. 3.14. The input and output facet of the waveguides are prepared manually by cutting the sample near the edges and polishing the edges in four steps, each time using a polishing plate with a lower roughness. The propagation loss of the ablated waveguides is higher than the 0.04dB/cm propagation loss that is given in the datasheet for the case of photolithographically defined waveguides, even though we have not been able to reproduce this value. However, the

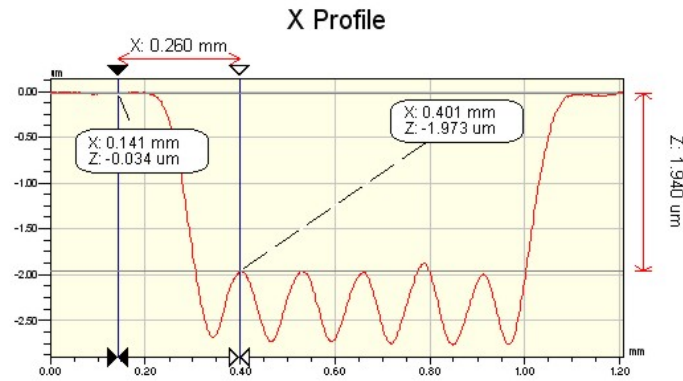


Figure 3.12: Surface corrugation of a $50\ \mu\text{m}$ top cladding layer, applied on top of an array of ablated waveguides.

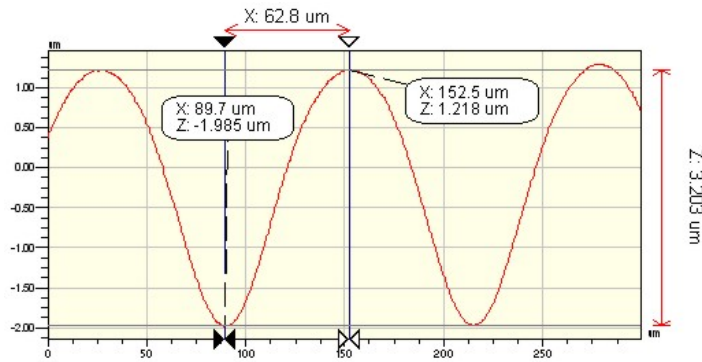


Figure 3.13: Surface corrugation of the top cladding layer, applied on top of an array of ablated waveguides, for a cladding layer thickness of $30\ \mu\text{m}$.

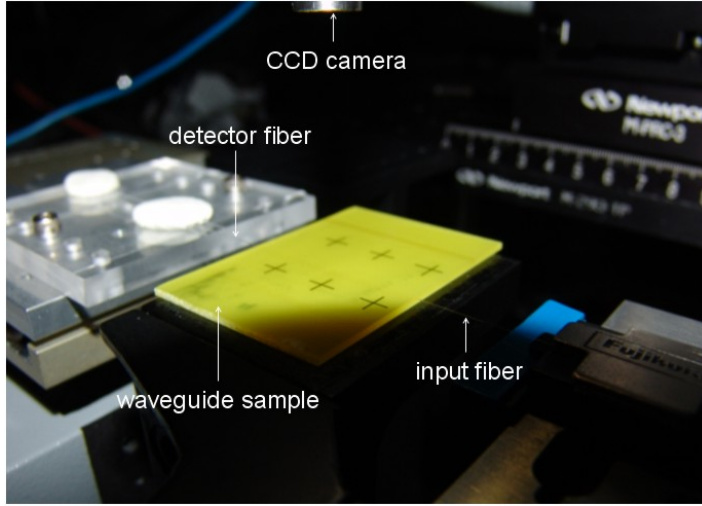


Figure 3.14: Picture of a sample placed on the measurement set-up in the configuration that is used to evaluate the performance of arrays of multimode waveguides.

propagation loss is acceptable for shorter interconnection lengths and the fabrication of basic proof-of-principle demonstrator boards. The lateral scan of the light spot that is coupled out at the output facet is given in Fig. 3.16. Crosstalk measurements have been carried out by sending an 850 nm light signal into an ablated waveguide and measuring the detected output power at the output facet of the adjacent waveguide. The average measured cross-talk is smaller than -30dB.

Multimode waveguides have been also been ablated into the alternative optical materials: Ormocer, SU8 and Epocore/Epoclad. The surface roughness of the ablated waveguide cores is much higher than for roughness measured for the Truemode material, even after optimization of the laser fluence. The average RMS surface roughness of the top of an ablated waveguide in Ormocer is 122nm measured on a scan area of $33 \mu\text{m} \times 84 \mu\text{m}$, which is more than three times higher than for the Truemode waveguide,

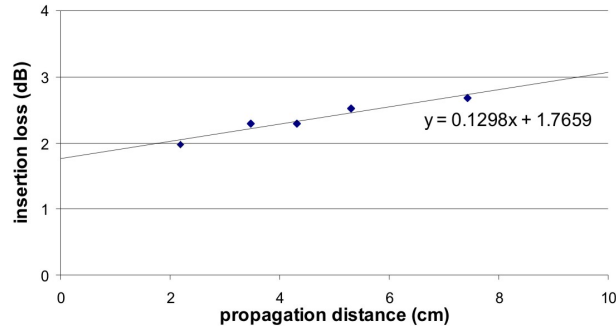


Figure 3.15: Propagation loss of a laser ablated waveguide, obtained with cut-back measurements. The waveguides have a propagation loss of 0.13dB/cm [13].

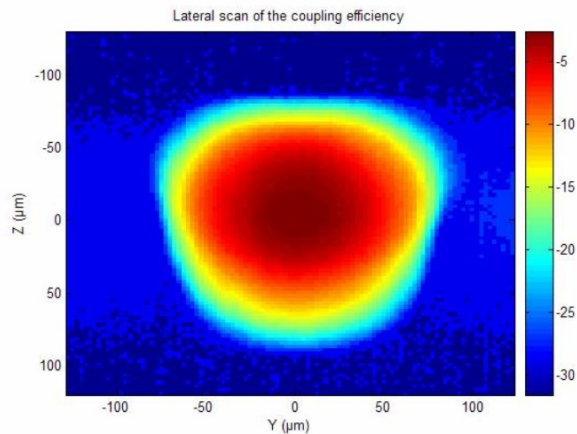


Figure 3.16: Lateral scan of the light spot that is detected by the detector fiber.

as is shown in Fig. 3.17, taking into account that the average is taken over a larger scan area. In case the ablation is done into an Epocore layer, an RMS surface roughness of 157.41 nm is measured on a scan area of $44 \mu\text{m} \times 41 \mu\text{m}$, as can be seen in Fig. 3.18. The ablated waveguide cores in SU8 have an RMS surface roughness of 157.41 nm is measured on a scan area of $44 \mu\text{m} \times 41 \mu\text{m}$, as can be seen in Fig. 3.18. This means that the average surface roughness of the waveguide cores ablated in Epocore and SU8 is more than four times higher than the value measured on the ablated Truemode waveguides.

The photothermal ablation process is dominant for all three optical materials, giving waveguide cores with a black appearance. The tuning of the pulse energy of the laser beam does not offer a solution, probably because of the fact that these materials do not absorb the wavelength emitted by the KrF excimer in an efficient way. Standard UV-lithography is preferable in this case, even though for the case of ormocer the UV-exposure can not be done in contact mode. In the next section, the patterning of multi-mode waveguides in Dry Truemode, Ormocer, SU8 and Epocore/clad are discussed.

3.5 Photolithographic waveguides

In the previous section, we have evaluated the use of laser ablation for the patterning of waveguides into the cured Truemode core layer. As was already mentioned in the previous chapter, the four different studied optical polymers are all UV-sensitive, which means that they can be directly patterned using UV-lithography. Truemode exist in two different formulations: a wet and dry film. For the wet film formulation, the main limitation is the fact that the UV-exposure has to be done in a nitrogen environment in proximity mode. The dry film formulation, which can be UV-exposed in contact mode in standard environment, however has become available in a later stage of this research. UV-lithography is a parallel process, which means that multiple waveguides or arrays of waveguides can be patterned in the same processing step, in accordance with the design on the photomask. This in contrast to laser ablation, which is a serial process. The

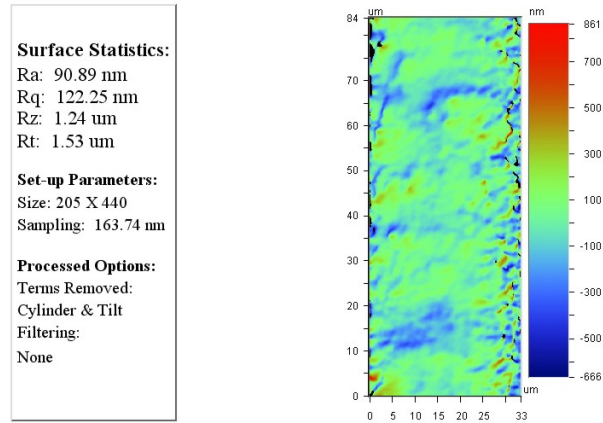


Figure 3.17: Surface roughness plot of the top of a waveguide core ablated in Ormocer.

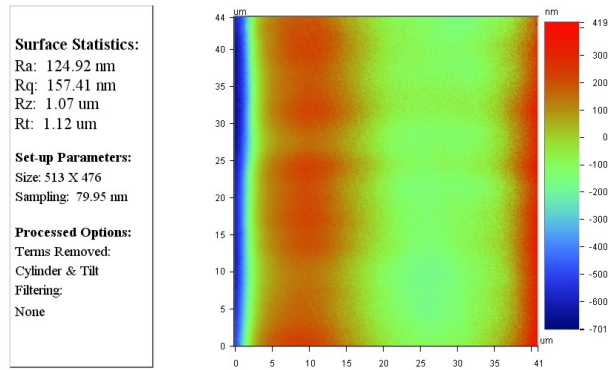


Figure 3.18: Surface roughness plot of the top of a waveguide core ablated in Epocore.

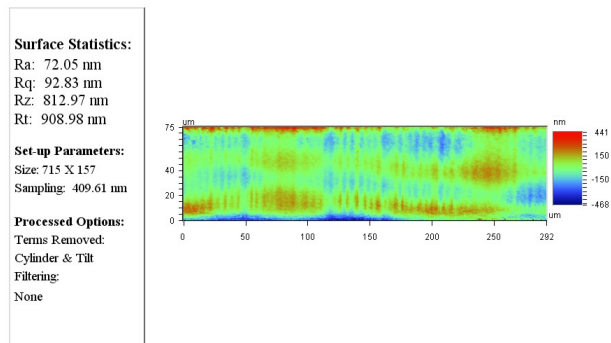


Figure 3.19: Surface roughness plot of the top of a waveguide core ablated in SU-8.

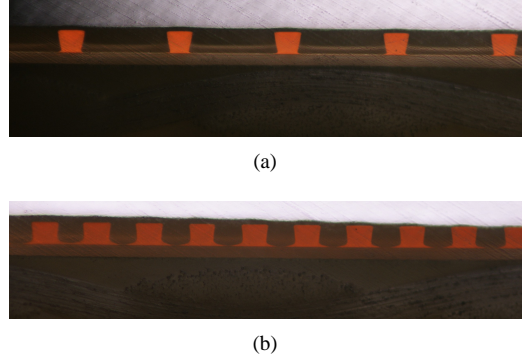


Figure 3.20: (a) Cross-section of an array of waveguides with cross-section $\approx 50 \mu\text{m} \times 50 \mu\text{m}$ on pitch $125 \mu\text{m}$; (b) cross-section of an array of waveguides with cross-section $\approx 50 \mu\text{m} \times 50 \mu\text{m}$ on pitch $250 \mu\text{m}$.

use of UV-lithography allows a higher throughput and lower processing time, which makes it an attractive technology for practical applications. In the following paragraphs, the use of UV-lithography for the patterning of the waveguide cores into the optical layer will be evaluated. We will briefly discuss the experimental results obtained with dry Truemode, Ormocer, Epocore/clad and SU8. It is not our intention to give an exhaustive study, but to give a short overview.

3.5.1 Dry Truemode formulation

The waveguides are patterned into the core layer with use of UV-lithography in standard environment, with the mask placed in contact mode. The material behaves like a negative resist, meaning that the mask contains openings with a width of $50 \mu\text{m}$ on pitch of either $125 \mu\text{m}$ or $250 \mu\text{m}$. The processing parameters used for the patterning and curing of the core layer and the curing of cladding layers were given in the previous chapter. Cross-sections of arrays of photolithographic waveguides with a cross-section of $50 \mu\text{m} \times 50 \mu\text{m}$ on pitch $250 \mu\text{m}$ are given in Fig. 3.20. The top of the waveguides has an average RMS surface roughness of 7.85 nm on a scan area of $45 \mu\text{m} \times 59 \mu\text{m}$, as is shown in Fig. 3.21. The surface corrugation of the top cladding layer, applied on top of an array of photolithographic waveguides, is $\leq 1 \mu\text{m}$ as is shown in Fig. 3.22.

Loss measurements have been carried out on samples with a length of 4.5 cm and 3.5 cm in order to test the performance of the UV-defined waveguides. No cut-back measurements have been carried out. When comparing the link efficiency to the link efficiency measured on samples with ablated Truemode waveguides, we can assume that the propagation loss of the waveguides to be 0.05 dB/cm at 850 nm , as it is given in the datasheet. This makes the UV-defined waveguides in dry Truemode material excellent candidates for in-plane light propagation in practical applications.

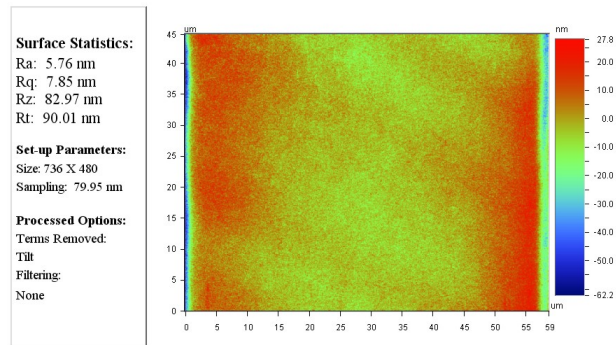


Figure 3.21: Surface roughness plot of the top of a photolithographic waveguide in dry True-mode.

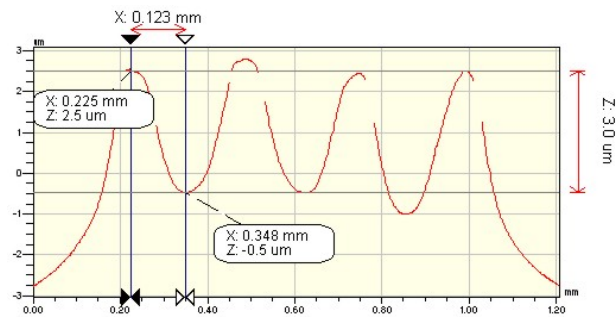


Figure 3.22: Surface corrugation of the top cladding layer applied on top of an array of photolithographic waveguides in dry Truemode.



Figure 3.23: Cross-section of an array of photolithographic waveguides with a cross-section of $100\ \mu\text{m} \times 50\ \mu\text{m}$ on pitch $125\ \mu\text{m}$ in Ormocor.

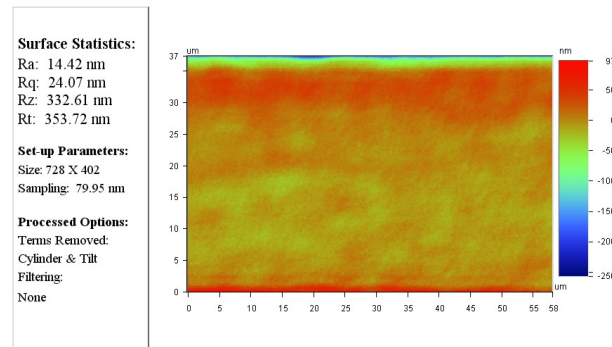


Figure 3.24: Surface roughness plot of the top of a photolithographic waveguide in Ormocor.

3.5.2 Ormocor

The waveguide core features can be patterned into the Ormocore layer with standard UV-lithography. Main drawback is the requirement to do the UV-exposure in proximity mode, which limits the reproducibility of the patterned structures because of the fact that the width of the imaged structures depends on the air gap between the mask and the optical layer. According to the datasheet, the Ormocor photolithographically defined waveguides have a propagation loss of 0.06 dB/cm at 850 nm [14]. A cross-section of an array of waveguides on pitch $125\ \mu\text{m}$ is given in Fig. 3.23. The patterned waveguide cores have an average RMS surface roughness of 24.09 nm on a scan area of $37\ \mu\text{m} \times 58\ \mu\text{m}$, as is shown in Fig. 3.24.

The air gap between the mask and the optical layer has to be arranged accurately in order to be able to pattern the waveguides in a reproducible way [15]. If the air gap is too large, the patterned features will broaden by diffraction and scattering. With the available mask aligner, it is very difficult to arrange the width of the air gap accurately. For this reason, only a limited number of experiments have been carried out.

3.5.3 SU-8

The patterning of the waveguide core features into the SU-8 layer requires UV-exposure at 365 nm with the mask placed in contact mode. T-topping of the waveguide core occurs with the use of a broadband light source, meaning that the width of the waveguide core at the top is larger than the width at the bottom, as can be seen in Fig. 3.25(a). This problem can be solved with the use of a UV-filter that selectively transmits the wavelengths except 365 nm, as can be seen in Fig. 3.25(b). Waveguides with straight sidewalls can in this case be obtained. Main drawback of the SU-8 waveguides is its

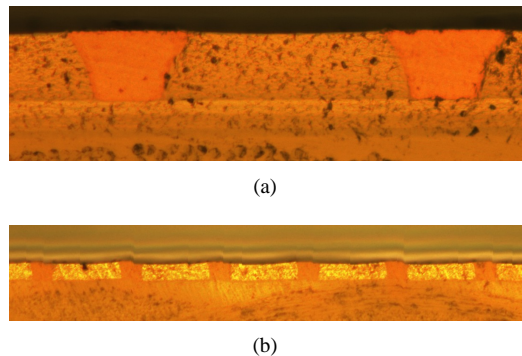


Figure 3.25: (a) Cross-section of an array of photolithographic waveguides in SU8, without the use of the UV-filter. The T-topping of the waveguide cores can be clearly observed; (b) cross-section of an array of photolithographic waveguides in SU8 in case the UV-filter is used.

high optical loss at 850 nm, which is ≤ 0.5 dB/cm [16]. At the moment of this study, there was in addition no compatible cladding material available. For this reason, the SU-8 material will only be used as buffer layer because of its excellent planarization properties.

3.5.4 Epocore/Epoclad

Epocore/clad is a modified epoxy-based material that has been developed for optical backplane purposes. We have done a limited number of tests on patterning waveguides with use of UV-lithography. We refer to [17] for an extensive study on the use of the material as optical layer for board-level interconnections. A cross-section of an array of waveguides on a pitch of 125 μm and 250 μm are given in Fig. 3.26. The top of the UV-defined waveguides has an RMS surface roughness of 6.7 nm on a scan area of 44 $\mu\text{m} \times 56 \mu\text{m}$, as is shown in Fig. 3.27. Propagation losses between 0.1 dB/cm and 0.15 dB/cm at 850 nm have been reported [17].

3.6 Increased integration density

A trend that has been observed over the last few years is the continuous search for an increased integration density, and consequently increased bandwidth density. The speed and complexity of integrated circuits are increasing rapidly as integrated circuit technology advances from very-large-scale integrated (VLSI) circuits to ultra-large-scale integrated (ULSI) circuits. The number of devices per chip, the number of chips per board, the modulation speed, and the degree of integration continue to increase. Advanced high performance chips and multi-chip modules are increasingly limited by their offchip or off-module bandwidth. Board-level optical data buses offer the potential alleviate this I/O bottleneck by providing dense, parallel high speed data links [18].

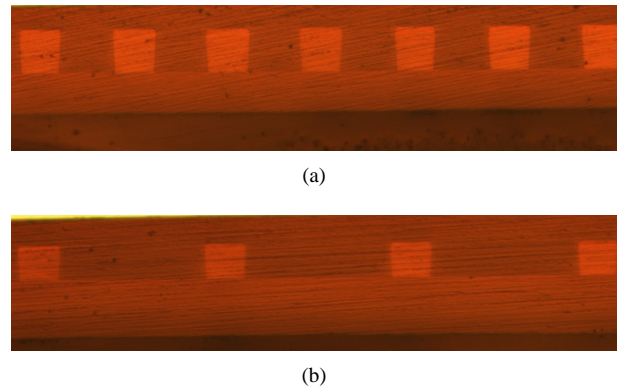


Figure 3.26: (a) Cross-section of an array of photolithographic waveguides with cross-section $50\ \mu\text{m} \times 50\ \mu\text{m}$ on pitch $125\ \mu\text{m}$ in Epocore/clad; (b) cross-section of an array of photolithographic waveguides with cross-section $50\ \mu\text{m} \times 50\ \mu\text{m}$ on pitch $250\ \mu\text{m}$ in Epocore/clad.

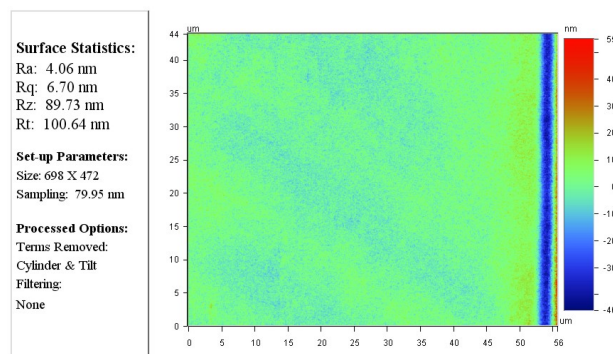


Figure 3.27: Surface roughness plot of the top of a photolithographic waveguide in Epocore.

The interconnection density can be increased by decreasing the pitch of the waveguides. This in contrast to electrical interconnections where a decrease in pitch size can cause electromagnetic interference and compatibility problems. The $125\mu\text{m}$ pitch of the ablated waveguides with cross-section $50\mu\text{m}\times 50\mu\text{m}$ in an array can be decreased to $62.5\mu\text{m}$. The cross-sectional dimension of the waveguide cores is in most cases scaled proportionally, in order to maintain sufficiently low cross-talk. As was explained in a previous section, the cross-sectional dimension of the waveguide core and the pitch of the waveguides in an array can be changed by using a mask with the appropriate dimensions and by shifting the laser beam over the desired pitch across the sample. This flexibility is one of the main advantages of the ablation process, and can be fully explored in this case.

3.6.1 Experimental results

The pitch of the array of waveguides can be decreased to $62.5\mu\text{m}$, in this way doubling the interconnection density in comparison to the $125\mu\text{m}$ pitch. This can be done by sending the laser beam through a suitable mask and by shifting the laser beam over $62.5\mu\text{m}$ after the ablation of each waveguide core. Because of its good ablation properties, the waveguides are patterned into Truemode wet film formulation. The laser beam is sent through a mask with dimensions $100\mu\text{m}\times 3000\mu\text{m}$ and is projected onto the translation stage with an optical projection system with demagnification 10. The waveguide arrays are ablated with the following parameters:

- Pulse energy: 0.71 J/cm^2 , measured on the translation stage with an energy meter
- Pulse repetition rate: 200Hz
- Ablation speed: $360\mu\text{m/s}$
- Laser beam shift: $62.5\mu\text{m}$, in this way creating an array of waveguides on pitch $62.5\mu\text{m}$

A cross-section of an array of ablated waveguides on pitch $62.5\mu\text{m}$ is shown in Fig. 3.28. The $50\mu\text{m}$ thickness of the core layer is maintained here, but can just as well be decreased by spinning the layer at a higher speed, that corresponds to the desired layer thickness on the spincurve. The waveguide cores have a width of $35\mu\text{m}$ at the top and of $42\mu\text{m}$ at the bottom. The surface corrugation of the $50\mu\text{m}$ thick top cladding layer is $\leq 0.100\mu\text{m}$, as can be seen in Fig. 3.29, measured locally on top of the waveguide array. As was the case for the $50\mu\text{m}\times 50\mu\text{m}$ waveguides on pitch $125\mu\text{m}$, the area into which the waveguides are patterned lies approximately $2.5\mu\text{m}$ lower than the area of the optical layer where no waveguides have been patterned.

3.7 Small core waveguides

Higher data rates require photodiodes with smaller cross-sections, which implies that waveguides with a smaller cross-section are required to interface these devices. As the speed of photodetectors increases, the diameter of the photosensitive area decreases. This means that for higher speed applications it is preferable to work with waveguides

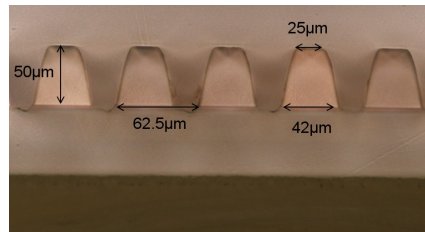


Figure 3.28: Cross-section of an array of ablated waveguides in Truemode with cross-sectional dimension $25\ \mu\text{m} \times 42\ \mu\text{m}$ on pitch $62.5\ \mu\text{m}$.

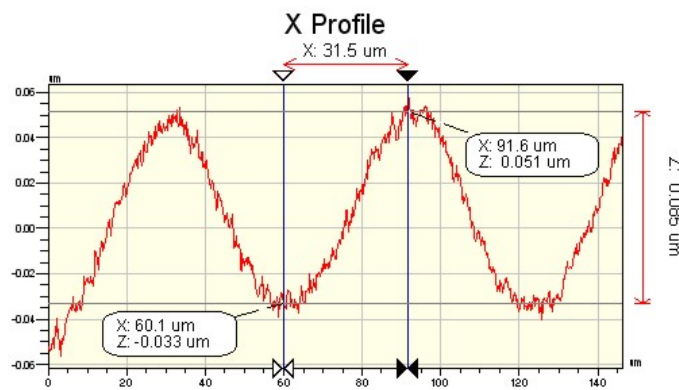


Figure 3.29: Surface corrugation of the $50\ \mu\text{m}$ thick top cladding layer, applied on top of an array of ablated waveguides with cross-section $25\ \mu\text{m} \times 42\ \mu\text{m}$ on pitch $62.5\ \mu\text{m}$.

that have a smaller core width and height. It is however not necessary to use single mode structures; the performance of multimodal structures is sufficient for the targeted distances of a couple of centimeters up to one meter. The required alignment accuracy is higher than for the larger core waveguides, but not as strict as for the single mode case. The small core waveguides can be very performant, but we should keep in mind that a misalignment of $5 \mu\text{m}$ will have a much larger influence on the efficiency of the system for the small core waveguides than for the case where $50 \mu\text{m} \times 50 \mu\text{m}$ waveguides are used. The advantages of a higher speed will have to be compared to the extra cost associated with the more stringent alignment requirements. In the end, for most applications cost will play a crucial role for the willingness to develop and adopt a certain technology.

It does however remain interesting to find out whether or not laser ablation is a suitable technology for the patterning of single mode structures. For this, we first have to calculate what the required cross-sectional dimensions are for operation in single mode regime. A second task is the determination of the minimum feature size that can be patterned using laser ablation. In a next step, the minimum feature size can be compared to the required cross-sectional dimension for single mode operation and in this way evaluate laser ablation as a potential technology for the ablation of single mode structures.

The condition for single mode operation is calculated with use of the normalized frequency v , which is given by the following formula:

$$v = kn_1a\sqrt{2\Delta}$$

in which $k = 2\pi/\lambda$ is the wave number, n_1 the refractive index of the core layer, Δ the relative index difference between the core and cladding material and a half the diameter of the waveguide core. The waveguide will operate in single mode operation for $v \leq v_c = \pi/2$. If we rewrite this equation in terms of wavelength, we obtain:

$$\lambda_c = \frac{2\pi}{v_c}an_1\sqrt{2\Delta}.$$

λ_c is called the cutoff wavelength. The waveguide operates in a single mode for wavelengths longer than λ_c . If we do the calculation for Truemode we get the following results:

- 1550 nm: core diameter $2.2 \mu\text{m}$
- 1310 nm: core diameter $1.9 \mu\text{m}$
- 850 nm: core diameter $1.24 \mu\text{m}$

The small core diameter that are required for single mode operation are mainly caused by the high index contrast between the Truemode core and cladding material. The required core diameter can be increased by using a lower index contrast between the core and cladding material, which on the other hand makes the system less compact because of the fact that bends with a higher radius of curvature will be needed for the same bend loss as the one encountered in the higher index contrast system. If we compare the required core diameter for single mode operation at 850 nm for the alternative optical materials, we get $1.9 \mu\text{m}$ for Ormocer and $2.4 \mu\text{m}$ for the Epocore/clad material. These dimensions are very demanding, even using photolithography, and require the use of

a thin mask with excellent optical quality. Especially the patterning of single mode waveguides in Ormocer can give problems because of the fact that the UV-exposure is done with the mask in proximity mode.

The minimum feature size that can be obtained with use of excimer laser ablation has been determined experimentally. The laser beam is sent through a rectangular mask with a cross-section of $250\mu\text{m}\times 3000\mu\text{m}$ which is projected onto the translation stage with demagnification 10. The laser beam is shifted after each ablation over a decreasing distance, as can be seen in Fig. 3.30(a) from right to left. At a certain shift, the top of the ablated waveguide core becomes more and more circular, and with a further decrease eventually mean that the top of the waveguide core is ablated. The minimum feature size that can be ablated in the Truemode core layer is $\approx 7\mu\text{m}$, in which case about 20 modes will propagate in the waveguide, which is larger than the required dimensions for single mode operation. It can be concluded that laser ablation is not suitable for the patterning of single mode waveguides in Truemode, at least not with the existing index contrast.

The ablation process can however be used for the patterning of small core waveguides, which typically have a cross-section ranging from $20\mu\text{m}\times 20\mu\text{m}$ to $10\mu\text{m}\times 10\mu\text{m}$. The integration density can be increased considerably in this way, especially for applications where the compatibility with the commercially available pitches of $250\mu\text{m}$, $125\mu\text{m}$ and $62.5\mu\text{m}$ is not required.

The rounding of the top of the waveguide core can be avoided by applying a 5 to $10\mu\text{m}$ thick cladding layer on top of the core layer prior to the ablation of the waveguide cores. In this way, the rounded part will be situated in the thin cladding layer. A cross-section of an array of waveguides with cross-section of $13\mu\text{m}\times 17\mu\text{m}$ ablated in a Truemode optical layer with a $16\mu\text{m}$ thick core layer and a $10\mu\text{m}$ thick cladding layer, and after the ablation covered with a $30\mu\text{m}$ thick cladding layer is shown in Fig. 3.30(b).

Loss measurements have been carried out at 850 nm on a sample with 4 arrays of ablated waveguides with cross-section $13\mu\text{m}\times 17\mu\text{m}$ on pitch $125\mu\text{m}$. The light is coupled in with single mode fiber SMF-28 (Newport) which has a core diameter of $8.3\mu\text{m}$ and NA 0.14. The light that is coupled out at the output facet of the waveguides is detected with a GI multimode optical fiber with core diameter $100\mu\text{m}$ and NA 0.29. The average overall efficiency of a 3cm long link is -0.86dB, measured on 10 waveguides in two different arrays on the board. This value looks promising, but cut-back measurement should be carried out to determine the waveguide propagation loss. The detector fiber will capture most the light that is coupled out at the output facet of the waveguides because of its large cross-sectional diameter, keeping in mind however the loss caused by the mismatch between the NA 0.3 of the Truemode waveguides and NA 0.29 of the detector fiber.

3.8 Multilayer optical structures

Multilayer structures have gained interest because they offer an increased interconnection density and the possibility to use more flexible routing schemes. In addition, the characteristics of 2D opto-electronic elements, which are widely available at reasonable cost at 850 nm, can be fully explored.

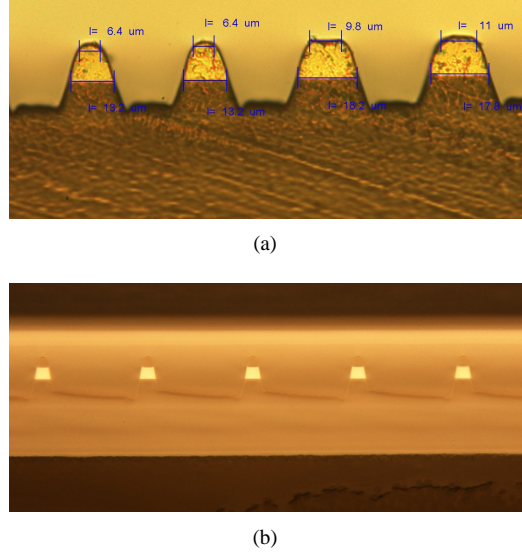


Figure 3.30: (a) Cross-section of an array of ablated small core waveguides in TM; (b) the waveguides have a cross-section of $\approx 15\mu\text{m} \times 15\mu\text{m}$ on pitch $125\mu\text{m}$.

Multimode optical waveguides are used to route the optical signals on-board from a transmitter to receiver location. In general the interconnection between the transmitter and the receiver can only be realized by means of waveguide crossings and in some cases also other passive elements such as splitters and tapers. This is schematically shown for a 4×4 interconnection in Fig. 3.31. Each waveguide crossing causes a certain loss, which is typically $\leq 0.05\text{dB}$ [19], depending on the crossing angle. For a low density interconnection, where a limited number of points are interconnected, the total loss caused by the waveguide crossings is acceptable, even for a fully interconnected system. However, as the interconnection density increases, the routing scheme becomes more complicated and the number of crossings will significantly increase. From a certain interconnection density on, the crossing loss will become unacceptably high and the use of multilayer structures comes into play.

A two layer optical structure should be sufficient to satisfy the current needs required by high density interconnections [19]. For lower density interconnections, the use of one single layer should be sufficient and is also preferred because of the lower manufacturing cost and time. The use of multiple optical layers can only be justified in case the loss caused by the use of passive optical elements for the routing in the optical layer cause a unacceptably high loss. The adoption of multilayer structures however relies very strongly on the availability of low loss coupling structures, which are used to couple the light signal between the different layers. Numerical simulations have been carried out to determine the alignment tolerance range for a two layer waveguide structure, in which two optical layers containing multimode waveguides are stacked on top of each other. In a next step, the experimentally achieved results can be compared to the results from the numerical study.

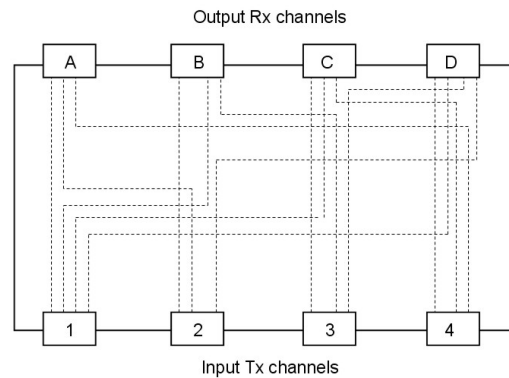


Figure 3.31: Interconnection scheme for a board with 4 input Tx channels and 4 output Rx channels.

3.8.1 Numerical study alignment tolerance

The Advanced System Analysis Program ASAP 2005 V2R2 (Breault Research) is used to carry out the numerical simulations. In view of the highly multimodal character of the considered structures, non-sequential ray tracing is used. Fresnel losses at the different interfaces are taken into account, whereas the scattering losses caused by the surface roughness of the ablated structures are not taken into account. The surface roughness of the optical waveguides is however low and homogeneously spread over the surface. As was mentioned in a previous section, the average surface roughness of the ablated waveguide core in Truemode is 35 nm, measured on a scan area of $46 \mu\text{m} \times 60 \mu\text{m}$.

A good alignment accuracy is required between a waveguide in the top optical layer and the corresponding waveguide in the bottom optical layer when a light signal is to be routed from the bottom layer to the top layer and vice versa. The coupling from one layer to the other can be done with the use of metallized 45° micro-mirrors, which are directly integrated with the optical waveguides. These metallized micro-mirrors are used to deflect the light beam over 90° , out of the plane of the optical waveguides. The considered two layer waveguide structure is given in Fig. 3.32. It consists of an FR4 substrate with two optical layers, which contain arrays of rectangular waveguides. The cross-section of the input facet of the waveguides is schematically shown in Fig. 3.32(a). Each optical layer contains an integrated metallized mirror that is used to deflect the light beam over 90° out of the plane of the optical layer, towards the detector, as is schematically shown in Fig. 3.32(b).

Because of the tapering that occurs during the ablation, the laser ablated waveguides have a trapezoidal cross-section. The influence of the trapezoidal cross-section on the coupling efficiency has been studied numerically by varying the top angle β , shown in Fig. 3.33(a). An 850 nm light signal is coupled in horizontally at the input facet of the waveguide with a GI optical fiber with core diameter $50 \mu\text{m}$ and NA 0.2. The light that is detected at the output facet of the Truemode waveguides is detected with a GI optical fiber with core diameter $100 \mu\text{m}$ and NA 0.29. The simulation results, shown in Fig. 3.33(b), indicate that the influence on the coupling efficiency is very limited

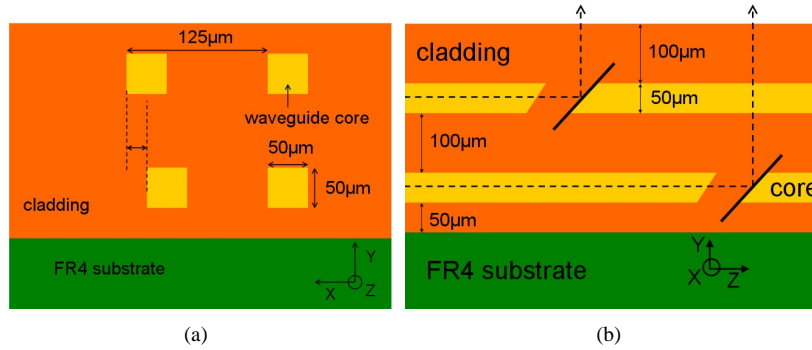


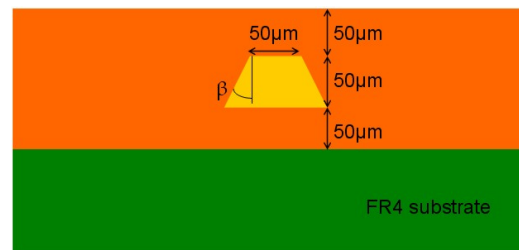
Figure 3.32: (a) Input facet of the waveguides; (b) cross-section of the two layer waveguide structure with integrated metallized micro-mirrors.

for $\beta \leq 25^\circ$. The decreasing coupling efficiency for larger top angles is mainly caused by the increasing cross-sectional dimension of the waveguide, meaning that part of the outcoupled light will not be detected. The top angle of the ablated waveguides is typically $\leq 15^\circ$, depending on the pulse energy of the laser and on the used material. The influence on the coupling efficiency is in this case very limited. For this reason, rectangular waveguides are used in the simulations.

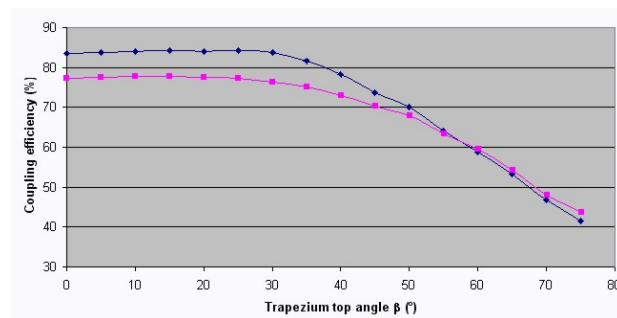
The simulations on the two layer structure are carried out with the technical parameters given in Table 3.3. Light with wavelength 850nm is coupled into the Truemode multimode waveguide with an optical fiber with core diameter 50 μm and NA 0.2. The waveguides have a cross-section of 50 μm × 50 μm on pitch 125 μm, NA 0.3 and have a length of 10 cm, in order to obtain a sufficient degree of mode scrambling. The light is deflected over 90° at the metallized mirror facet and detected with a multimode optical fiber with core diameter 100 μm and NA 0.29 or a flat isotropic, which means that no NA has been attributed, detector with cross-section 70 μm. The bottom respectively top waveguide is shifted in X-direction around its ideal position, where the center of the mirror facet and the center of the detector fiber are perfectly aligned; the detector fiber or flat detector are fixed at the ideal position. The alignment tolerance range for different excess loss values is given in Table 3.4. The alignment tolerance curve is given in Fig. 3.34.

In the case of the MMF detector, the detected power depends strongly on the misalignment of the waveguide because of the limited acceptance angle of the detector fiber, which is determined by its NA. For the flat detector, the detected power is mainly determined by its cross-sectional dimension because of the fact that no NA has been attributed to it. As the waveguide is shifted further away from the ideal position, the detected power will decrease. For the MMF detector this decrease is due to the decreasing number of light rays that are within the acceptance angle combined with the decreasing overlap between the detector fiber and the outcoupled spot. For the flat detector, this decrease is due to the decreasing overlap between the outcoupled light spot and the photo-sensitive area of the detector.

The light spot that is coupled out at the bottom mirror has to propagate through the top cladding layer of the bottom layer and the entire top layer before it reaches the detector



(a)

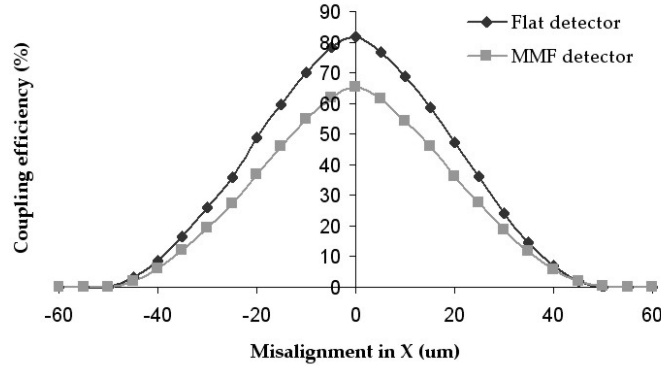


(b)

Figure 3.33: (a) Cross-section of a trapezoidal waveguide core, with top angle β ; (b) influence of the top angle β on the coupling efficiency.

Table 3.3: Technical parameters used for the simulations.

Input fiber	MMF diameter $50\mu\text{m}$, NA=0.2
Output fiber	MMF diameter $100\mu\text{m}$, NA=0.29
Flat detector	$100\mu\text{m}$ square
Refractive index Truemode TM core	1.5563
Refractive index Truemode TM cladding	1.5266

**Figure 3.34:** Alignment tolerance curve for a misalignment of the bottom waveguide with respect to the top waveguide in a two layer optical structure in Truemode material.

whereas the beam that is coupled out at the top mirror only has to propagate through the top cladding layer. During the propagation, the light beam will diverge according to the NA meaning that the light beam coupled out at the bottom mirror will have spread more than the one coupled out at the top mirror. The alignment tolerance range for the bottom waveguide will therefore give the most stringent alignment accuracy requirement.

3.8.2 Experimental results

The patterning of multimode waveguides in a two layer optical structure can be done photolithographically for the dry Truemode and Epocore/Epoclad material because of the fact that the UV-exposure is done in contact mode. The achievable alignment accuracy is in this case determined by the alignment accuracy of the used mask aligner, which is typically $\leq 5\mu\text{m}$, and also depends on the homogeneity of the optical layer. In case laser ablation is used, the waveguides, that have a cross-section of $50\mu\text{m} \times 50\mu\text{m}$ on pitch $125\mu\text{m}$, are patterned into each optical layer separately with the same process parameters as the waveguides in the single layer optical structure. Alignment features are evaporated onto the FR4 substrate or the lower cladding layer. During

Table 3.4: Misalignment and corresponding excess loss for the two layer waveguide structure in Truemode. The alignment tolerance ranges are identical for both the MMF detector and the flat detector with $100\ \mu\text{m}$ diameter.

Excess loss	alignment tolerance range
0.2 dB	$[-5\ \mu\text{m} ; 5\ \mu\text{m}]$
0.5 dB	$[-8\ \mu\text{m} ; 8\ \mu\text{m}]$
0.7 dB	$[-10\ \mu\text{m} ; 10\ \mu\text{m}]$
1 dB	$[-12\ \mu\text{m} ; 12\ \mu\text{m}]$

the evaporation, the sample is covered with a mask that contains the desired alignment features. The alignment features are used to arrange the alignment between the waveguides in top and bottom layer.

The camera on the set-up is tilted under an angle, meaning that there will be a small shift in X-direction over the surface of the sample when focus is moved from the alignment crosses to the top surface. This shift causes a misalignment between the waveguides in top and bottom layer because of the height difference between the plane of the alignment crosses and the top surface. The misalignment however is limited to the X-direction and can therefore be corrected with the use of an alignment pulse. The principle is schematically shown in Fig. 3.35. In a first step, the alignment pulse is ablated using the same mask as the one used for the ablation of the waveguides. The alignment pulses are ablated for each waveguide array separately to compensate for possible tilt of the substrate and are ablated at a given distance from the corresponding alignment cross. The distance is typically $500\ \mu\text{m}$ up to $1\ \text{mm}$ away from the reference point in order to avoid misalignments caused by the tilt of the FR4 substrate. Next, the sample is rotated over 90° and aligned with help of the alignment crosses. If we put the focus onto the top surface, the alignment pulse, which is rotated over 90° , will also be in focus. The left or right wall of the alignment pulse, which did not suffer from the shift when moving focus, is used as a reference point for the ablation of the waveguides. In this way, the horizontal shift over the surface of the sample is corrected. In order to obtain a high alignment accuracy, we have to make sure that the same reference point is used for both layers. For this reason, the alignment marks are evaporated on a planarized surface. In the first tests, a $50\ \mu\text{m}$ thick SU-8 layer, which has excellent planarization properties, was spincoated onto the FR4 substrate. The alignment features were evaporated on the SU8 layer, which is during the evaporation covered with a suitable mask. In order to avoid possible compatibility problems, such as delamination, between the Truemode and SU-8 material in a later stage of processing, we aimed at eliminating the SU-8 layer. This was done by applying the alignment marks directly onto the lower cladding layer, keeping in mind the edge bead that occurs at the edges of the sample. The achievable alignment accuracy is in both cases $\leq 5\ \mu\text{m}$, which is within the alignment tolerance range obtained from the numerical study. A cross-section of a two layer waveguide structure is given in Fig. 3.36. In Fig. 3.36(a) the alignment features are evaporated onto an SU-8 layer; in (b) the alignment features are evaporated directly onto the lower cladding layer.

Loss measurements have been carried out on demonstrator boards that contain a two

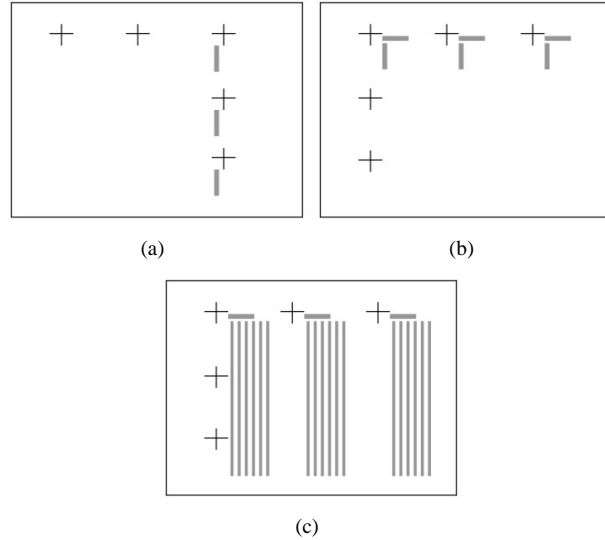
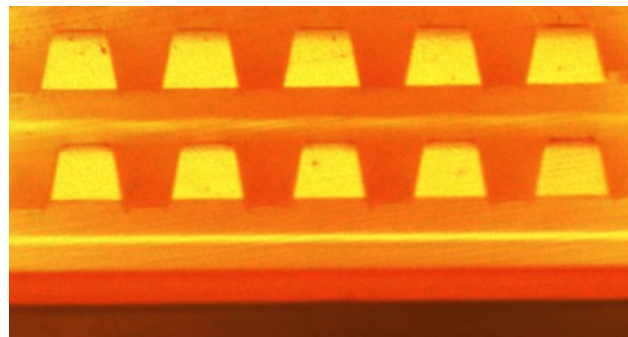
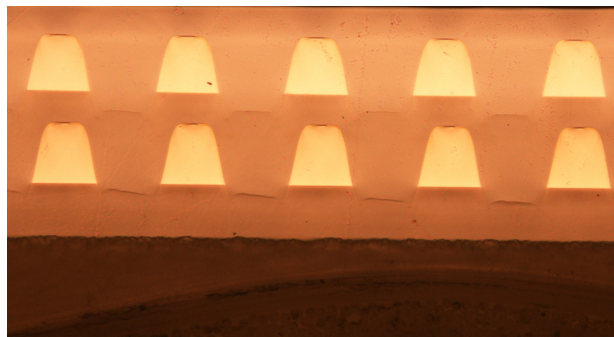


Figure 3.35: Alignment procedure used to align the waveguides in top and bottom layer in a multilayer structure: (a) ablation of alignment pulse; (b) rotation of sample over 90° and aligning; (c) use of right or left wall of 90° rotated alignment pulse as reference point for the ablation.

layer ablated waveguide structure, applied onto an FR4 substrate. The input and output facet of the waveguides are polished manually, which can give some spreading on the measured results. Because of the manual polishing, it is difficult to polish the facets under an exact vertical angle. The surface roughness of the facets can also vary a bit from one place to the other. This explains the small spreading that is experienced during the measurements. The measured link loss includes the incoupling of an 850 nm light signal at the waveguide input facet with a GI optical fiber with core diameter $50 \mu\text{m}$ and NA 0.2, the propagation in the 4.5 cm long ablated Truemode waveguide with cross-section $50 \mu\text{m} \times 50 \mu\text{m}$ and NA 0.3, the outcoupling at the waveguide output facet and the capturing of the outcoupled light spot with a GI optical fiber with core diameter $100 \mu\text{m}$ and NA 0.29. The propagation loss of the waveguides in an array in top and bottom optical layer, located in the centre of the sample, is in good correspondance as can be seen from the diagram in Fig. 3.37(a). The waveguides in the array in the bottom optical layer have an average link efficiency of 75.7% with a standard deviation of 1.7%. The waveguides in the array in the top optical layer have an average link efficiency of 76.4% with a standard deviation of 2.9%. The good reproducibility is not only valid for arrays in the centre of the board but also near the edges of the board, as is shown in the diagram in Fig. 3.37(b). The waveguides in the array in the bottom optical layer have an average link efficiency of 67.6% with a standard deviation of 1.9%. The waveguides in the array in the top optical layer have an average link efficiency of 70% with a standard deviation of 2.5%. The link efficiency is in this case a bit lower than the link efficiency measured on the waveguides in the centre of the sample. This is mainly caused by the variation in layer thickness that becomes apparent near the edges



(a)



(b)

Figure 3.36: Cross-section of a two layer waveguide structure of which the waveguides have a cross-section of $50\ \mu\text{m} \times 50\ \mu\text{m}$ on pitch $125\ \mu\text{m}$: (a) the alignment marks are evaporated on an SU8 layer; (b) the alignment marks are evaporated onto the lower cladding layer.

of the sample because of the edge bead. A plot of a light spot that is coupled out at a waveguide in the top layer and the corresponding waveguide in the bottom layer is shown in Fig. 3.38.

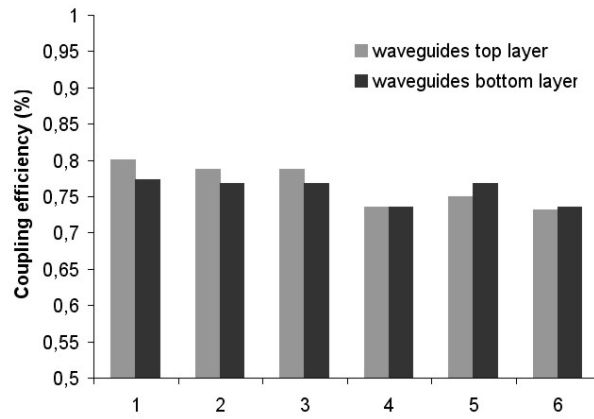
The reproducibility of the thickness of the core and cladding layers in top and bottom layer determines the homogeneity between the waveguides in top and bottom layer. The waveguides in both layers are ablated with the same ablation parameters, which are determined for the ideal case that all layers have the desired thickness of $50\ \mu\text{m}$. The thickness of the layers in the top optical layer can be higher than the desired value near the edges of the sample because of the accumulation of material near the edge, caused by the edge bead resulting from the spincoating of the bottom layer. The edge bead that occurs during the spincoating of the bottom optical layer, will become more apparent after the spincoating of the top optical layer. This problem can be solved by removing the edge bead from the sample after each spincoating step, or by not ablating the waveguides near the edge of the sample, limiting the processable part of the sample. In fig. 3.39 the inhomogeneity problems that are experienced with the truemode material at the edges of the sample are shown.

The smaller core waveguides can also be ablated in a two layer waveguide structure. The required alignment accuracy will in this case however be more stringent than for the $50\ \mu\text{m} \times 50\ \mu\text{m}$ waveguides. The reproducibility of the ablation process will for certain applications not be sufficient in this case. In Fig. 3.40, a cross-section is shown of a two layer waveguide structure, in which the waveguide cores have a cross-section of $\approx 15\ \mu\text{m} \times 15\ \mu\text{m}$.

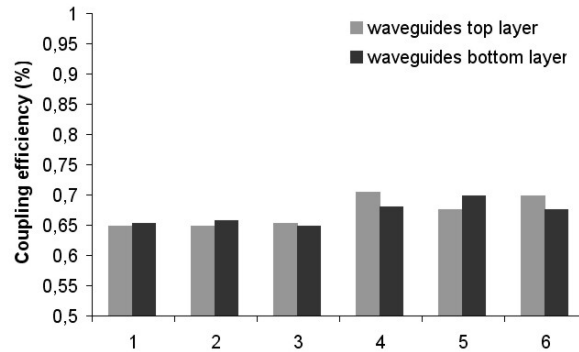
3.9 Conclusions

Multimode optical waveguides with a cross-section of $50\ \mu\text{m} \times 50\ \mu\text{m}$ on pitch $125\ \mu\text{m}$ can be ablated into the Truemode optical layer with KrF excimer laser (248 nm). The waveguides have an average propagation loss of 0.13dB/cm at $850\ \text{nm}$, which is acceptable for short interconnection lengths. The ablation process is serial, which means that the waveguide cores are structured one by one, and mask-less, which makes it an ideal technology for fast prototyping. Laser ablation is compatible with standard PCB manufacturing processes and is already used for the drilling of microvias in high-density electrical boards.

The width of the waveguide core can be changed by using a mask with the appropriate cross-sectional dimension; the pitch between the waveguides in an array by shifting the laser beam over the suitable distance during the ablation. Waveguides with a cross-section of $35\ \mu\text{m} \times 35\ \mu\text{m}$ on a pitch of $62.5\ \mu\text{m}$ have been successfully demonstrated. The cross-sectional diameter of the waveguides can be decreased to $15\ \mu\text{m} \times 15\ \mu\text{m}$, which makes them compatible with with high-speed systems. This can be interesting in case the interconnection density is to be increased. Another way to increase the interconnection density is the use of a multilayer optical structure. A two layer optical structure containing arrays of ablated Truemode waveguides has been presented. The alignment between the waveguides in top and bottom optical layer is done with the help of alignment marks, placed on the lower cladding layer, and the use of an alignment pulse, used to compensate for the tilted position of the camera on the set-up. The achievable alignment accuracy is $\leq 5\ \mu\text{m}$, which is within the 0.2dB excess loss range

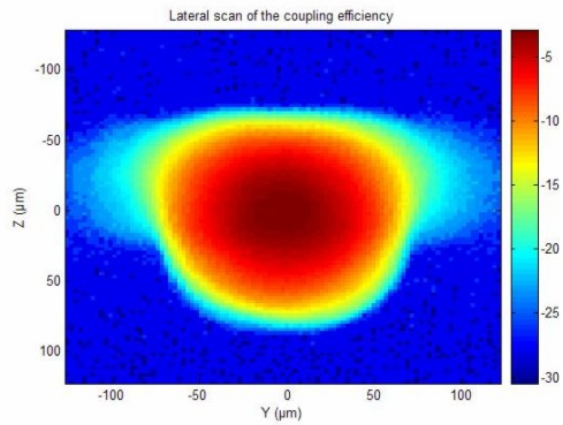


(a)

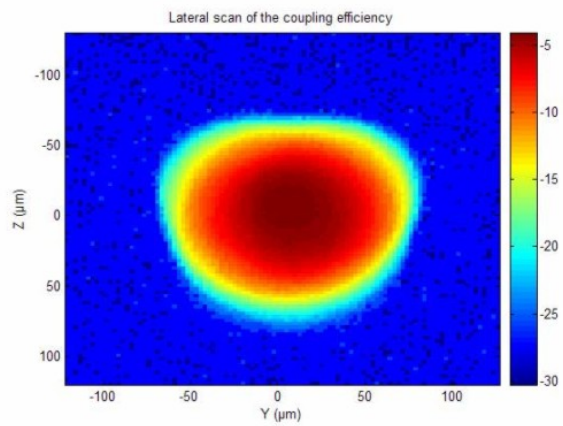


(b)

Figure 3.37: (a) Coupling efficiency of the bottom and corresponding top waveguide of a two layer waveguide array measured on an array on the centre of the sample (b) coupling efficiency of the bottom and corresponding top waveguide measured on an array near the edge of the sample.



(a)



(b)

Figure 3.38: (a) Plot of the light spot that is coupled out at the output facet of a waveguide in the top optical layer; (b) plot of the light spot that is coupled out at the output facet of a waveguide in the bottom optical layer.

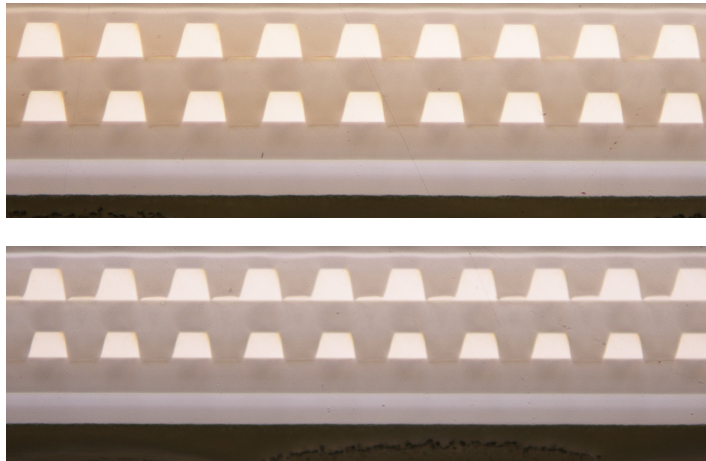


Figure 3.39: (a) Cross-section of a two layer waveguide structure in which the waveguides in top optical layer have a slightly larger cross-section than the waveguides in the bottom optical layer; (b) cross-section of two layer waveguide structure at the edge of the sample, the core layer in the top optical layer is thicker than the one in the bottom optical layer causing the waveguides in the top optical layer not be completely decoupled.



Figure 3.40: Cross-section of a two layer waveguide structure in which the waveguides have a cross-section of $\approx 15 \mu\text{m} \times 15 \mu\text{m}$.

resulting from a numerical study.

All four studied optical polymers are UV-sensitive, which means that they can be directly patterned with use of UV-lithography. Photolithographic waveguides have been patterned into Truemode dry film formulation, Ormocer and Epocore/clad. The lowest propagation loss is obtained for the dry Truemode waveguides (0.05dB/cm at 850 nm). UV-lithography is a parallel process, which means that multiple waveguides or arrays of waveguides can be patterned in the same processing step according to the mask design. The parallel process allows a higher throughput and lower processing time. This makes them interesting for practical applications. The expansion to multiple layers can be done with the use of the mask aligner and a substrate that contains alignment marks that correspond to the alignment marks on the mask.

Bibliography

- [1] L. Eldada, "Polymer integrated optics: promise vs. practicality," *Proc. SPIE*, Vol. 6185 618501, 2006
- [2] H. Ma, A. K. Y. Jen, L. R. Dalton, "Polymer-based optical waveguides: materials, processing, and devices," *Advanced materials*, Vol. 14, No. 19, 2002
- [3] K. Okamoto, "Fundamentals of optical waveguides," *Academic Press*, Second edition, 2006
- [4] M. L. Moynihan, B. Sicard, T. Ho, L. Little, N. Pugliano, J. G. Shelnut, H. B. Zheng, P. Knudsen, D. Lundy, N. Chiarotto, C. Lustig, C. Allen, "Progress towards board level optical interconnect technology," *Proc. SPIE*, Vol. 5731, pp. 50-62, 2005
- [5] X. Wang, R. T. Chen, "Fully embedded board level optical interconnects - From point-to-point interconnection to optical bus architecture," *Proc. SPIE*, Vol. 6899, 689903, 2008
- [6] H. Schröder, J. Bauer, F. Ebling, M. Franke, A. Beier, P. Demmer, W. Süllaud, J. Kostelnik, R. Mödinger, K. Pfeiffer, U. Ostrzinski, E. Griese, "Waveguide and packaging technology for optical backplanes and hybrid electrical-optical circuit boards," *Proc. SPIE*, Vol. 6124, 612407, 2006
- [7] C. G. Choi, S. P. Han, M. H. Jeong, "Fabrication of large-core 1×16 optical power splitters in polymer using hot-embossing process," *IEEE Photonics Technology Letters*, Vol. 15, pp. 825-827, 2003
- [8] G. L. Bona, B. J. Offrein, U. Bapst, C. Berger, R. Beyeler, R. Budd, R. Dangel, L. Dellmann, F. Horst, "Characterization of parallel optical-interconnect waveguides integrated on a printed circuit board," *Proc. SPIE*, Vol. 5453, 2004
- [9] A. L. Glebov, M. G. Lee, K. Yokouchi, "10+ Gb/s Board-Level Optical Interconnects: Fabrication, Assembly, and Testing," *Proc. SPIE*, Vol. 6185, 618501-1, 2006

- [10] W. W. Duley, "UV-lasers: effects and applications in materials science," *Cambridge University Press*, ISBN 0-521-46498-6, 1996
- [11] D. Basting, G. Marowsky, "Excimer laser technology," *Springer-Verlag Berlin Heidelberg*, ISBN-10 3-540-20056-8 2005
- [12] G. Van Steenberge *et al.*, "Laser Ablation of Parallel Optical Interconnect Waveguides," *IEEE Photon. Technol. Lett.*, vol. 18, no. 9, pp. 1106–1108, 2006.
- [13] G. Van Steenberge, "Parallel Optical Interconnections Integrated on a Printed Circuit Board," *PhD Thesis*, Ghent University, 2006
- [14] S. Uhlig, M. Robertsson, "Limitations to and Solutions for Optical Loss in Optical Backplanes," *IEEE Journal of lightwave technology*, Vol. 24, No. 4 , pp. 1710-1724, 2006
- [15] U. Streppel, P. Dannberg, C. Wächter, A. Bräuer, L. Fröhlich, R. Houbertz, M. Popall, "New wafer-scale fabrication method for stacked optical waveguide interconnects and 3D micro-optic structures using photoresponsive (inorganic-organic hybrid) polymers," *Optical materials*, Vol. 21, pp. 475-483, 2002
- [16] M. Karppinen *et al.*, "Embedded optical interconnect between ceramic BGA packages on FR4 board using embedded waveguides and passive optical alignments," *Proc. 56th Electronic Components and Technology Conference*, pp. 799-805 , 2006
- [17] H. Schröder, J. Bauer, F. Ebling, M. Franke, A. Beier, P. Demmer, W. Süllau, J. Kostelnik, R. Mödinger, K. Pfeiffer, U. Ostrzinski, E. Griese "Waveguide and packaging technology for optical backplanes and hybrid electrical-optical circuit boards", *Proceedings SPIE*, Vol. 6124, 612407-1, 2006
- [18] F. E. Doany, C. L. Schow, J. A. Kash, C. Baks, R. Budd, D. M. Kuchta, P. Pospeljugoski, F. Libsch, R. Dangel, F. Horst, B. J. Offrein, "Waveguide-coupled parallel optical transceiver technology for Tb/s-class chip-to-chip data transmission," *Proc. SPIE*, Vol. 6899, 68990V, (2008)
- [19] A. Glebov, M. G. Lee, S. Aoki, D. Kudzuma, J. Roman, M. Peters, L. Huang, D. S. Zhou, K. Yokouchi, "Integrated waveguide microoptic elements for 3D routing in board-level optical interconnects," *Proc. SPIE* Vol. 6126, 2006
- [20] L. Eldada, "Advances in polymer integrated optics," *Journal of selected topics in quantum electronics*, Vol. 6, No. 1, 2000

Chapter 4

Integrated coupling structures

4.1 Introduction

In the previous chapter, we have discussed the fabrication of polymer multimode waveguides, which can be used to transfer optical signals on-board, covering distances of a couple of centimeters up to one meter. These waveguides are used to route light signals in the plane of the optical layer from a source to a destination position. It is clear that with the current wide availability of cheap and reliable vertical emitting and receiving opto-electronic devices at 850nm, these are the premier choice to be used in optical interconnects. However, coupling structures that deflect the light beam over 90° are required to couple the light signals in and out of the plane of the optical layer. The challenge lies in making these coupling structures low-cost and compatible with the existing PCB manufacturing processes.

In this chapter, two different integrated 90° beam deflecting configurations are discussed. The first coupling approach consists of the use of a metalized micro-mirror; the second one of a total internal reflection (TIR) mirror. For both mirror configurations, the 90° beam deflection is realized with the use of a 45° micro-mirror. 45° micro-mirrors have the advantage of being wavelength independent, highly reproducible and can be fabricated with a large variety of technologies such as micro-dicing [1], V-shaped diamond blade [2], reactive ion etching [3], [4] and X-ray lithography [5]. This makes them advantageous over other coupling approaches such as for instance the use of grating couplers [6], which are highly wavelength dependent and require more complicated fabrication processes, not always compatible with the PCB manufacturing and soldering processes.

As was discussed in the previous chapter, waveguide cores with low surface roughness can be ablated into polymer materials which efficiently absorb the wavelength emitted by the laser source. The encouraging results that are obtained for the Truemode material, encourage us to investigate the use of KrF excimer laser ablation as an alternative micro-structuring technology for the patterning of 45° micro-mirrors into the optical layer. The ablated micro-mirrors are directly integrated with the waveguides, which allows high achievable alignment accuracies. The micro-mirrors are used to couple light signals from the optical waveguides toward a photo-detector array or a fiber ribbon and from a VCSEL or fiber ribbon toward the optical waveguides.

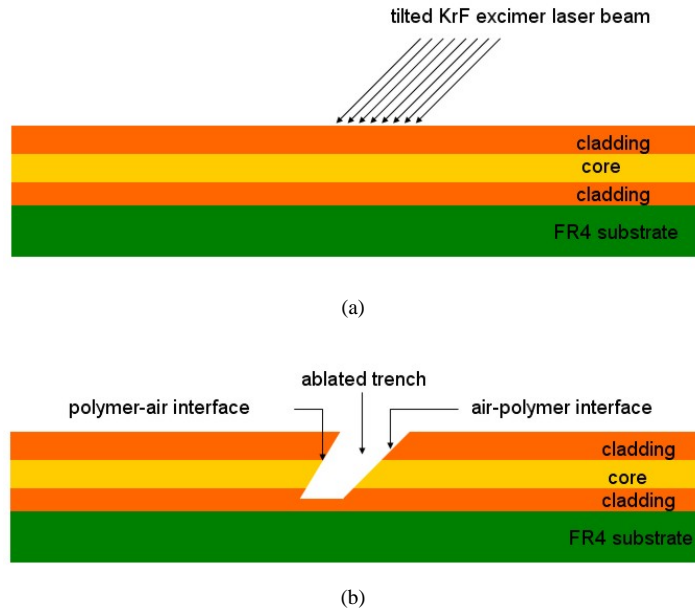


Figure 4.1: (a) Ablation of angled trench into the optical layer with a KrF excimer laser beam placed in a tilted position with respect to the sample; (b) both angled interfaces of the ablated trench can be used for 90° deflection in a different mirror configuration. The polymer-air interface can be used as a total internal reflection mirror; the air-polymer interface can be used for 90° beam deflection after the Au-coating of the mirror facet and the filling of the ablated trench with cladding material.

The KrF excimer laser beam is tilted with respect to the sample for the ablation of the 45° micro-mirrors, which implies that the sample can during the processing be placed horizontally on the translation stage. This approach is also discussed in [7]. This in contrast to the more common approach to do the ablation with the laser beam perpendicular to the translation stage and the sample fixed on a holder in a tilted position on the translation stage, which is used in [8]. An alternative approach is to tilt the sample with respect to the laser beam or the use of a fixed and moving mask. In this way, it is possible to continuously expand the laser irradiated area, and to set the laser irradiated position precisely. This approach is discussed in [9].

During the ablation, a trench is created into the optical layer as is depicted in the scheme in Fig. 4.1. The ablated trench contains two angled interfaces which can both be used for the 90° beam deflection in a different mirror configuration: the polymer-air interface can be used as a TIR mirror; the air-polymer interface can be used for 90° beam deflection after the Au-coating of the mirror facet and the filling of the ablated trench with cladding material.

There is always a certain degree of tapering during the ablation which is responsible for the fact that the angle of both interfaces will differ from each other and from the tilt angle of the laser beam. As can be seen in Fig. 4.1(b), the slope of the polymer-air interface is steeper than the slope of the air-polymer interface. The degree of tapering

depends on the wavelength and fluence of the laser source and the material that is patterned. The tapering angle, or natural ablation angle, can be measured experimentally and the tilt angle can be corrected with the tapering angle in order to obtain a facet with the desired 45° angle. If the laser beam is tilted under the desired 45° angle plus the tapering angle, measured with respect to the vertical axis, a 45° polymer-air interface is obtained which can be used as a TIR mirror. In the case the tapering angle is subtracted two times, the air-polymer interface will show a 45° angle. This facet can be used as a metalized mirror after the metalization of the mirror facet and the filling of the ablated trench with cladding material. Both mirror configurations and are discussed in more detail in the next sections. First, the mirror configurations are studied numerically in order to determine the tolerance range on the fabrication of the component itself and the alignment tolerance range in case the mirror is used in an optical interconnection. Next, the fabrication and characterization of both mirror configurations are presented. These results are then compared to the results from the numerical study in order to be able to determine whether or not laser ablation is a suitable technology for the patterning of the micro-mirrors into the optical layer.

4.2 Metalized 45° micro-mirror

The 45° air-polymer interface can be used to deflect a light beam over 90°, out of the plane of the optical waveguide, on the condition that the 45° facet is metalized and the air gap between the polymer-air interface and the mirror facet filled with cladding material. A cross-section of the ablated trench with the 45° air-polymer interface, and the typical dimensions of the layers and the width of the ablated trench are shown in Fig. 4.2(a). A cross-section of the micro-mirror after the metalization of the mirror facet and the filling of the ablated trench with cladding material is shown in Fig. 4.2(b). The mirror is embedded into the optical layer and is in this way protected from external influence such as moist and dust intrusion. It can be used in a multilayer optical structure for out-of-plane and inter-plane coupling, depending on the orientation of the mirrors with respect to each other.

Numerical simulations have been carried out to evaluate the performance and alignment tolerance range of the metalized 45° micro-mirror in both a single layer and two layer optical waveguide structure. The experimental results are in a next step compared to the results from the numerical study.

4.2.1 Numerical simulations

Single layer optical structure

Non sequential ray-tracing was used for the simulations, as was the case for the the simulations carried out on the two layer waveguide structure discussed in the previous chapter. Considering the patterning of the micro-mirror into the optical layer, an important issue is the required angle accuracy of the mirror facet of the metalized micro-mirror. This can be investigated using the configuration shown in Fig. 4.3. The core and cladding layers have a thickness of 50 μm , as is the case for the fill cladding layer that is used for the filling of the ablated trench. This means that the optical layer has

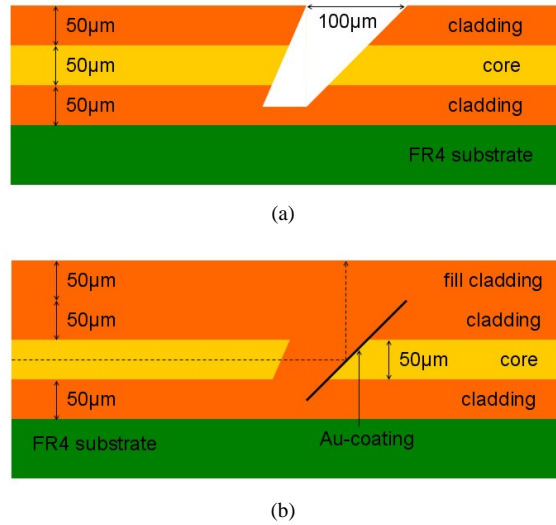


Figure 4.2: (a) Cross-section of the ablated trench with the 45° air-polymer interface, and the typical dimensions; (b) cross-section of the micro-mirror after the metalization of the mirror facet and the filling of the ablated trench with cladding material.

a thickness of $200\mu\text{m}$, instead of the standard thickness of $150\mu\text{m}$, because of the extra cladding layer used for the filling of the ablated trench. Experiments will have to point out the required minimum thickness of the fill cladding layer in order to get a homogeneous filling of the ablated trench. But it is clear that a thinner fill cladding layer is preferable in order to limit the propagation distance from the mirror facet to the detector because of the loss that is associated with the diffraction of the deflected light beam.

The link efficiency of the system depends on the angle β of the mirror facet and the angle α of the core-cladding interface. In the simulations, the angle β of the mirror facet is varied between 40° and 50° for facet angles α ranging from 0° , corresponding to a vertical wall, up to 45° , which would mean that both interfaces are parallel and is not possible in practical cases because of the tapering that occurs during the ablation. The angle α has a very limited influence on the link efficiency because of the small index contrast that exists between the cladding and core material. For the simulations, the thickness of the Au-coating on the mirror facet is assumed to be 500 nm . This is more than eight times thicker than the penetration depth of Au, which is 61.5 nm at 850 nm [10].

An 850 nm light signal is coupled in horizontally with a multimode optical fiber (MMF) with core diameter $50\mu\text{m}$ and NA 0.2 into a Truemode multimode waveguide, which has a cross-section of $50\mu\text{m} \times 50\mu\text{m}$ on a pitch of $125\mu\text{m}$ and NA 0.3. A waveguide propagation loss of 0.04 dB/cm is used in the simulations, according to the value given in the datasheet for UV-defined waveguides. The light propagating in the waveguide is deflected at the metalized mirror facet. The outcoupled light signal is detected with different detector types: a MMF with core diameter $100\mu\text{m}$ and NA 0.29, a round flat detector with diameter $70\mu\text{m}$ and a square flat detector with side $200\mu\text{m}$. The $70\mu\text{m}$

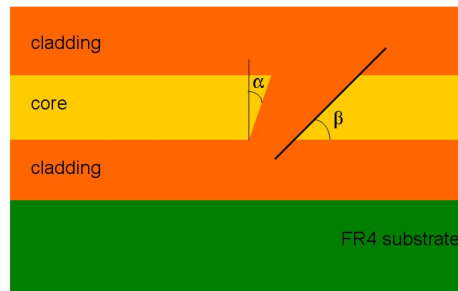


Figure 4.3: Configuration used for the simulations on the metalized micro-mirror. Both the angles α and β have an influence on the link efficiency of the integrated structure.

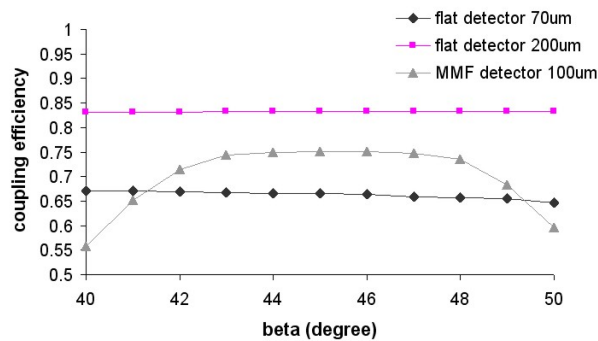


Figure 4.4: Influence of a deviation of 45° of the angle β of the metalized mirror facet on the coupling efficiency of the entire simulated system, and not only of the mirror. The angle α of the opposite interface of the ablated trench is in this case 25°, in accordance with the experimental results discussed in the next section.

diameter round detector has been chosen in correspondence with the size of current high-speed detectors. The 200 μm square detector is used to get an idea of the amount of light that is not captured by the smaller detector because of the diffraction that the deflected light beam experiences. The flat detectors are isotropic, meaning that no NA has been assigned to them. The amount of light that is captured with the MMF detector is mainly determined by its NA, which determines the acceptance angle, and its size. The air gap between the input fiber and the input facet of the waveguides and between the output facet of the waveguides and the detector fiber is set to 10 μm . The detector is fixed at its theoretically ideal position, where the center of the mirror facet and the center of the detector are perfectly aligned.

The resulting tolerance plot for a deviation of the 45° angle of the mirror facet for the different detector types is given in Fig. 4.4. The link efficiency is in this case the one obtained for the entire system which includes incoupling at the waveguide input facet, propagation in the 10 cm long Truemode waveguide, deflection at the metalized mirror, outcoupling at the cladding-air interface and the detection. From this graph, we can see that for the flat detector case the angle of the mirror facet has a limited influence on the link efficiency because of the presence of the Au-coating, which guarantees a high

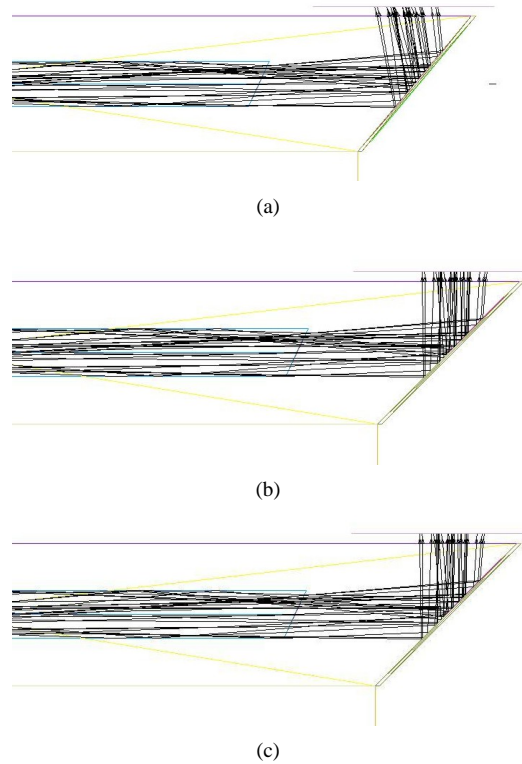


Figure 4.5: (a) Ray trace plot for a mirror facet angle of 40° ; (b) ray trace plot for a mirror facet angle of 45° ; (c) Ray trace plot for a mirror facet angle of 50° . There is a deviation on the angle of the outcoupled spot for the case $\beta \neq 45^\circ$. The light rays will however be forced to deflect at the mirror facet because of the presence of the Au-coating.

reflectivity. The $200\mu\text{m}$ square flat detector captures the entire light spot that is coupled out at the metalized mirror. The deflected light spot will diffract during its propagation through the cladding layer. For this reason, only part of the outcoupled light spot will be captured by the $70\mu\text{m}$ round detector, causing a considerable decrease in the link efficiency. The spreading is mainly due to the large NA of the Truemode waveguides. A ray trace plot for the case of a mirror facet angle of 40° , 45° and 50° is shown in Fig. 4.5.

For the $100\mu\text{m}$ core diameter optical fiber detector, the part of the outcoupled light spot that is captured is mainly determined by the NA of the detector fiber, which determines the acceptance angle and thus the amount of light that will be detected. A light spot that is coupled out at a mirror facet with an angle differing from 45° will not be coupled out vertically but will be coupled out slightly deviating from the vertical axis, as can be seen in the raytrace plots in Fig. 4.5. A deviation of $\pm 2^\circ$ on the 45° angle of the mirror facet has a very limited influence on the link efficiency. For larger deviations, the outcoupled light spot will not be captured entirely by the detector fiber because of its limited acceptance angle and consequently the link efficiency will drop.

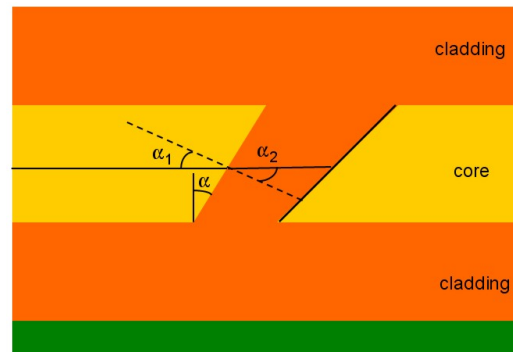


Figure 4.6: Refraction of the central ray that strikes the core-cladding interface. The ray enters under an angle α_1 ; the refracted ray propagates under an angle α_2 , measured with respect to the axis perpendicular to the core-cladding interface. The angle α_2 will be slightly bigger than α_1 because of the slightly lower refractive index of the cladding material with respect to the core material.

The influence of the angle α of the core-cladding interface is rather limited, because of the small index contrast that exists between the core ($n=1.5562$) and cladding ($n=1.5462$) material. The light rays that hit this interface will be refracted according to Snell's law of refraction, as is schematically shown in Fig. 4.6 for the central ray that strikes the core-cladding interface. The angle α_2 of the refracted ray is slightly bigger than the angle α_1 of the entering beam because of the small refractive index difference between the core and cladding material. For the extreme cases $\alpha = 45^\circ$ and $\alpha = 0^\circ$, we get the following situation:

- $\alpha=45^\circ$: this will in practice never be the case because of the tapering that occurs during the ablation. By applying Snell's law, for $\alpha_1=45^\circ$ we get $\alpha_2=46.12^\circ$.
- $\alpha=0^\circ$: the cladding-core interface is in this case at an angle of 90° , which implies that the light spot is coupled out vertically.

The direction of outcoupled light spot will deviate from the vertical direction for $\alpha \neq 0^\circ$ but this deviation will in practical cases be $\leq 1^\circ$.

Multilayer out-of-plane coupling

The metalized micro-mirrors can be used in a multilayer optical structure for out-of-plane and inter-plane coupling. We will first study out-of-plane coupling in a two layer optical structure, in which two optical layers containing multimode waveguides are stacked on top of each other. The studied configuration is shown in Fig. 4.7. The pitch between the outcoupled spots is $250\mu\text{m}$, in accordance with the pitch of the used opto-electronic elements.

The alignment between the mirrors in the bottom and top layer is crucial for the performance of the out-of-plane coupling structure. The tolerance for a misalignment of either the top or bottom mirror with respect to the bottom or top mirror has been simulated by shifting the top/bottom mirror along the Z-axis. In this way, the pitch between

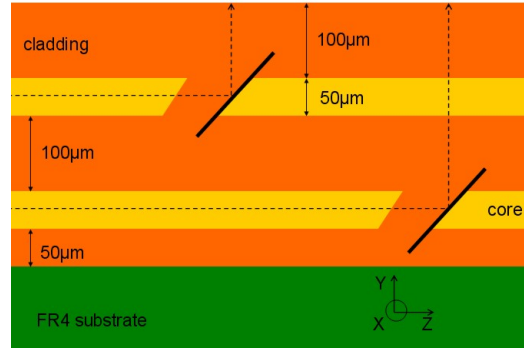


Figure 4.7: Two layer out-of-plane coupling configuration used to simulate the effect of a misalignment along the Z-axis of the top respectively bottom mirror with respect to the bottom respectively top mirror, causing a deviation on the $250\mu\text{m}$ pitch of the detector.

the two outcoupled spots will no longer be in correspondance with the pitch of the opto-electronic elements used. The simulations are carried out under the following conditions:

- input fiber: multimode optical fiber with core diameter $50\mu\text{m}$ and NA 0.2
- Truemode waveguides: cross-section of $50\mu\text{m} \times 50\mu\text{m}$, NA 0.3 and a propagation loss of 0.04 dB/cm at 850 nm
- detector 1: square flat detector with side $100\mu\text{m}$
- detector 2: multimode optical fiber with core diameter $100\mu\text{m}$ and NA 0.29

An 850nm light signal is coupled in horizontally into the Truemode multimode waveguide from the input fiber. The light signal then propagates in the multimode waveguide until it is deflected out-of-plane at the metalized mirror facet. The outcoupled light spot is captured with the detector.

In Fig. 4.8 the alignment tolerance plot is shown of a two layer out-of-plane coupling structure with metalized mirrors for the case where a $100\mu\text{m}$ square flat detector. The center of the detector is aligned with respect to the center of the mirror facet, which is the theoretically ideal position. The detector is fixed at this position, whereas the mirror facet is shifted around the ideal position in Z-direction. The maximum detected power is 80.4% (-0.95dB) for the bottom mirror and 89.4% (-0.49dB) for the top mirror. The alignment tolerance range for an excess loss of 1dB is $[-35\mu\text{m}, 35\mu\text{m}]$ for the top mirror and $[-30\mu\text{m}, 35\mu\text{m}]$ for the bottom mirror. The alignment tolerance range for an excess loss of 0.5dB respectively 0.1dB is $[-30\mu\text{m}, 30\mu\text{m}]$ respectively $[-15\mu\text{m}, 15\mu\text{m}]$ for the top mirror and $[-20\mu\text{m}, 25\mu\text{m}]$ respectively $[-10\mu\text{m}, 15\mu\text{m}]$ for the bottom mirror. These results are summerized in Table 4.1.

The tolerance curve for the bottom mirror is slightly asymmetrical, because of the build-up of the mirror. The detected power reaches its maximal value for for a misalignment of $+5\mu\text{m}$ along the Z-direction. This can be explained in the following way: the rays propagating in the waveguide are first refracted at the core-cladding interface

	BOTTOM MIRROR	TOP MIRROR
1dB excess loss	$[-30\mu\text{m}, 35\mu\text{m}]$	$[-35\mu\text{m}, 35\mu\text{m}]$
0.5dB excess loss	$[-20\mu\text{m}, 25\mu\text{m}]$	$[-25\mu\text{m}, 25\mu\text{m}]$
0.1dB excess loss	$[-10\mu\text{m}, 15\mu\text{m}]$	$[-15\mu\text{m}, 15\mu\text{m}]$

Table 4.1: Alignment tolerance ranges corresponding to an excess loss of 1dB, 0.5dB and 0.1dB for the case where a $100\mu\text{m}$ square flat detector is used.

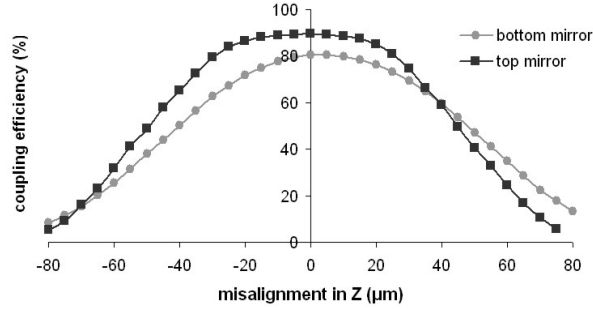


Figure 4.8: Alignment tolerance curve of a two layer out-of-plane coupling structure with metalized mirrors for the case where a $100\mu\text{m}$ square flat detector is used. The center of the detector is aligned with the center of the mirror facet, which is the theoretically ideal position. The detector is fixed at this position, whereas the mirror facet is shifted around the ideal position in Z-direction.

and then propagate through the cladding filled cavity. As was already mentioned, the angle of refraction is $\leq 1^\circ$ because of the small index contrast that exists between the core and cladding material. However, the rays that are deflected at the mirror facet are not coupled out vertically but deviate slightly from the vertical direction, in correspondence with the angle of refraction. The deflected light signal has to propagate through the $100\mu\text{m}$ thick top cladding and fill cladding layer of the bottom optical layer and through the $200\mu\text{m}$ thick top optical layer, with the associated diffraction of the light beam caused by the large NA of the waveguides. For this reason, the maximum link efficiency is not detected at the theoretically ideal position, but $5\mu\text{m}$ away from this position. The tolerance curve for the top mirror is symmetrical around the theoretically ideal position, because of the fact that the deflected light spot only has to propagate through the $100\mu\text{m}$ thick top cladding and fill cladding layer of the top optical layer, with the associated lower degree of spreading.

The alignment tolerance plot for a misalignment of the top mirror around the theoretically position, where the center of the mirror facet is aligned with the center of the detector, along the Z-axis for both the flat and the MMF detector is shown in Fig. 4.9. The maximum link efficiency for the MMF detector is 72.6% (-1.39dB), which is lower than the maximum power detectable with the flat detector. This is again the consequence of the NA of the MMF detector, which determines the acceptance angle and thus the detected power whereas for the flat detector, the detected power is determined by the overlap between the outcoupled light spot and the photo-sensitive area.

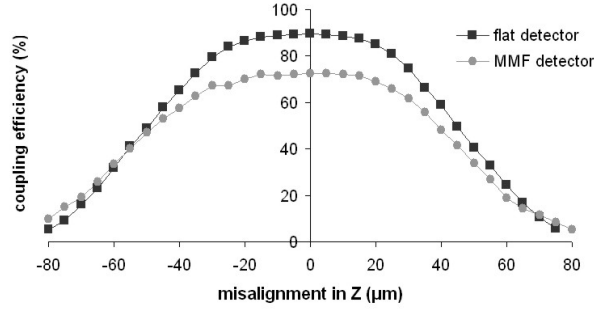


Figure 4.9: Alignment tolerance curve for a misalignment of the top mirror along Z around the theoretically ideal position, where the center of the detector is aligned with the center of the mirror facet, for both the $100\mu\text{m}$ square flat detector and the $100\mu\text{m}$ core diameter multimode optical fiber (MMF).

	BOTTOM MIRROR	TOP MIRROR
1dB excess loss	$[-20\mu\text{m}, 20\mu\text{m}]$	$[-40\mu\text{m}, 40\mu\text{m}]$
0.5dB excess loss	$[-15\mu\text{m}, 15\mu\text{m}]$	$[-30\mu\text{m}, 30\mu\text{m}]$
0.1dB excess loss	$[-5\mu\text{m}, 5\mu\text{m}]$	$[-15\mu\text{m}, 15\mu\text{m}]$

Table 4.2: Alignment tolerance ranges corresponding to an excess loss of 1dB, 0.5dB and 0.1dB for a mechanical misalignment of the detector fiber along X-axis for the case where a $100\mu\text{m}$ core diameter MMF detector is used.

Besides the required accuracy between the mirrors in the two layers, it is also interesting to determine the tolerance for a mechanical misalignment of the detector fiber around its theoretically ideal position along the X-axis. This can be done by scanning the $100\mu\text{m}$ core diameter MMF detector and the $100\mu\text{m}$ square flat detector around their theoretically ideal position along the X-axis. The resulting tolerance plots are shown in Fig. 4.10. The curve is symmetrical, which is logical because of the fact that the detector fiber is shifted along the mirror facet. For the MMF detector, the maximum detected power is 68% (-1.7dB) for the bottom mirror and 72.6% for the top mirror. The alignment tolerance range for an excess loss of 1dB is $[-40\mu\text{m}, 40\mu\text{m}]$ for the top mirror and $[-20\mu\text{m}, 20\mu\text{m}]$ for the bottom mirror. The alignment tolerance range for an excess loss of 0.5dB respectively 0.1dB is $[-30\mu\text{m}, 30\mu\text{m}]$ respectively $[-15\mu\text{m}, 15\mu\text{m}]$ for the top mirror and $[-15\mu\text{m}, 15\mu\text{m}]$ respectively $[-5\mu\text{m}, 5\mu\text{m}]$ for the bottom mirror. The results are summarized in Table 4.3.

Multilayer inter-plane coupling

As was already mentioned, the metalized mirrors can also be used for inter-plane coupling, in which case the light signal is coupled from a waveguide in the top/bottom layer to the corresponding waveguide in the bottom/top layer with or without conservation of the propagation direction. Both configurations are schematically depicted in Fig. 5.10. For both configurations, the bottom mirror is used in the discussed metalized mirror

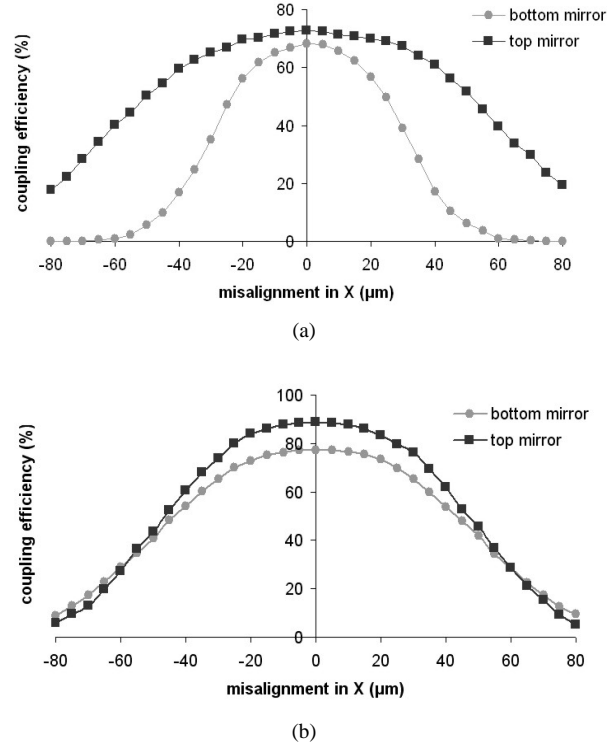
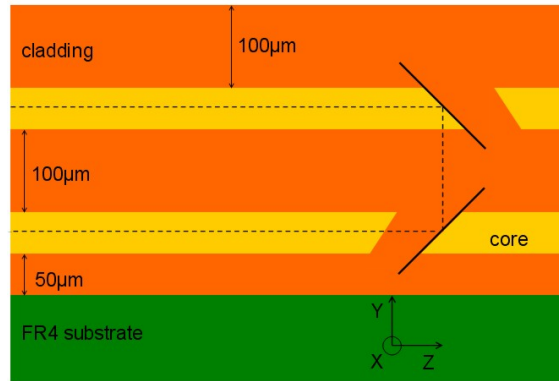


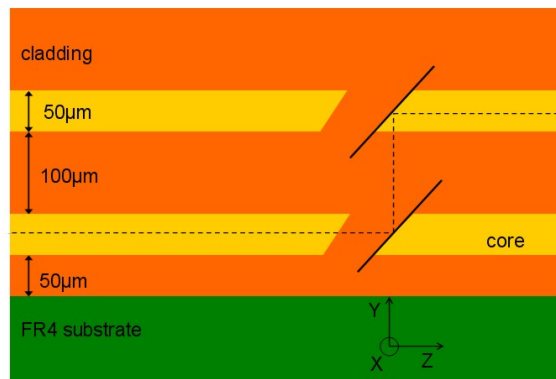
Figure 4.10: (a) Tolerance curve for a mechanical misalignment of the 100 μm core diameter MMF detector around its theoretically ideal position, where the center of the detector is aligned with the center of the mirror facet. The MMF detector is shifted around the ideal position in X-direction; (b) alignment tolerance curve for a mechanical misalignment of the 100 μm square flat detector around the theoretically ideal position along X. The resulting alignment tolerance curves are symmetrical, which is logical because of the fact that the mirror is shifted along the mirror facet.

	BOTTOM MIRROR	TOP MIRROR
1dB excess loss	[-35 μm , 35 μm]	[-35 μm , 35 μm]
0.5dB excess loss	[-25 μm , 25 μm]	[-25 μm , 25 μm]
0.1dB excess loss	[-15 μm , 15 μm]	[-15 μm , 15 μm]

Table 4.3: Alignment tolerance ranges corresponding to an excess loss of 1dB, 0.5dB and 0.1dB for a mechanical misalignment of the detector fiber along X-axis for the case where a 100 μm square flat detector is used.



(a)



(b)

Figure 4.11: (a) Schematic of a two layer waveguide structure with metalized mirrors, where the light signal is coupled from a waveguide in the top/bottom layer to the corresponding waveguide in the bottom/top layer with reversal of the propagation direction; (b) schematic of a two layer waveguide structure with metalized mirrors, where the light signal is coupled from a waveguide in the top/bottom layer to the corresponding waveguide in the bottom/top layer with conservation of the propagation direction.

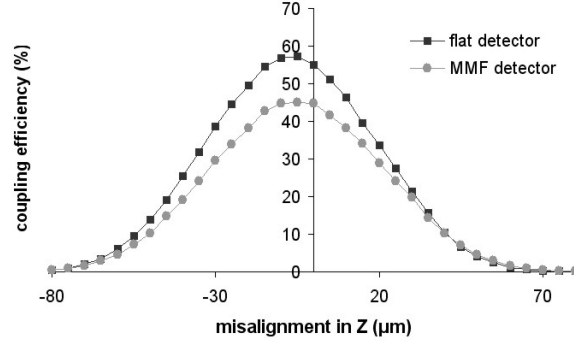


Figure 4.12: Alignment tolerance plot for the inter-plane coupling configuration with reversal of the propagation direction for the case of the flat detector and the MMF detector for a misalignment of the top mirror along the Z-axis around the theoretically ideal position with respect to the bottom mirror.

configuration, in which case the light signal has to pass the filled ablated trench before it reaches the mirror facet, whereas the 90° beam deflection in the top layer is done using a metalized mirror facet, in which case the deflected light beam is directly coupled into the waveguide. The alignment tolerance range of both configurations, with and without conservation of the propagation direction, is studied in a similar way as for the out-of-plane coupling structure. An 850nm light signal is coupled in horizontally in a waveguide in the bottom optical layer with an optical fiber with core diameter 50μm and NA 0.2. The light propagating in the waveguide is deflected a first time as it hits the metalized mirror facet of the bottom mirror. The deflected light spot then propagates through the cladding layers between the two core layers until it is deflected over 90° a second time at the mirror facet in the top optical layer. The light signal then propagates in the waveguide in the top layer until it is coupled out horizontally at the output facet of the waveguides and detected by a 100μm square flat detector or by a 100μm core diameter multimode optical fiber with NA 0.29.

For the determination of the alignment tolerance range, the top mirror is shifted along the Z-axis around the theoretically ideal position, in which case the center of both mirror facets are perfectly aligned. The alignment tolerance plot for the case where the propagation direction is reversed, is shown in Fig. 4.12 for both detector types. The light spot is in this case coupled from a waveguide in the bottom layer to the corresponding waveguide in the top layer with a 180° change in propagation direction, meaning that the deflected light spot is coupled back towards the source. The maximum link efficiency is 57.24% (-2.43dB) for the flat detector and 44.74% (-3.5dB) for the MMF detector, and is reached for a misalignment $Z = -5 \mu\text{m}$. This in contrast to the two layer out-of-plane coupling structure, where the maximum efficiency is obtained for $Z = 5 \mu\text{m}$. Reason for this is the fact that the bottom mirror is shifted along its ideal position in this case whereas the top mirror is shifted in this case. The alignment tolerance range is $[-25\mu\text{m}, 10\mu\text{m}]$ for an excess loss of 1dB, $[-10\mu\text{m}, 0\mu\text{m}]$ for an excess loss of 0.1dB and $[-15\mu\text{m}, 5\mu\text{m}]$ for an excess loss of 0.5dB and this for both the flat and the MMF detector. The results are summarized in Table 4.4.

The tolerance for a mechanical misalignment of the detector along the X-axis is sym-

1dB excess loss	$[-25\mu\text{m}, 10\mu\text{m}]$
0.5dB excess loss	$[-15\mu\text{m}, 5\mu\text{m}]$
0.1dB excess loss	$[-10\mu\text{m}, 0\mu\text{m}]$

Table 4.4: Alignment tolerance ranges corresponding to an excess loss of 1dB, 0.5dB and 0.1dB for a misalignment of the top mirror around its ideal position along the Z-axis. The resulting alignment tolerance ranges are valid for both the flat and the MMF detector.

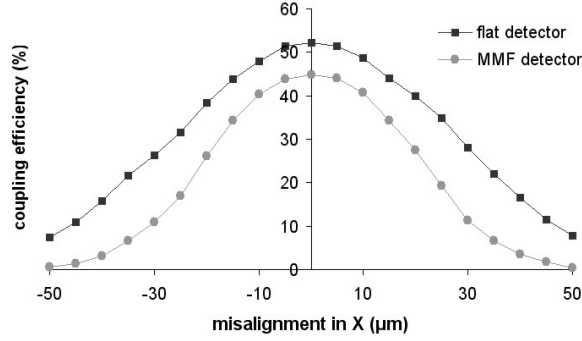


Figure 4.13: Alignment tolerance plot for mechanical misalignment of the detector along the X-axis for the inter-plane coupling configuration with reversal of the propagation direction. The flat detector and the MMF detector are shifted along the X-axis around the theoretically ideal position where the center of the detector is aligned with the center of the waveguide.

metrical around the theoretically ideal position, as can be seen in Fig. 4.13, which is logical since the detector is moved along the mirror facet. The alignment tolerance range is $[-15\mu\text{m}, 15\mu\text{m}]$ for an excess loss of 1dB, $[-5\mu\text{m}, 5\mu\text{m}]$ for an excess loss of 0.1dB and $[-10\mu\text{m}, 10\mu\text{m}]$ for an excess loss of 0.5dB and this for both detector types. The results are summarized in Table 4.5.

A ray trace plot of the studied configuration is shown in Fig. 4.14. From this plot, it is clear that a considerable amount of rays is no longer guides in the waveguide core after the coupling from one layer to the other because of the diffraction of the light beam that occurs during the propagation from the mirror in the bottom layer to the mirror in the top layer.

The link efficiency drops as the width w of the ablated trench increases, caused by

1dB excess loss	$[-15\mu\text{m}, 15\mu\text{m}]$
0.5dB excess loss	$[-10\mu\text{m}, 10\mu\text{m}]$
0.1dB excess loss	$[-5\mu\text{m}, 5\mu\text{m}]$

Table 4.5: Alignment tolerance ranges corresponding to an excess loss of 1dB, 0.5dB and 0.1dB for a mechanical misalignment of the detector along the X-axis. The resulting alignment tolerance ranges are valid for both the flat and the MMF detector.

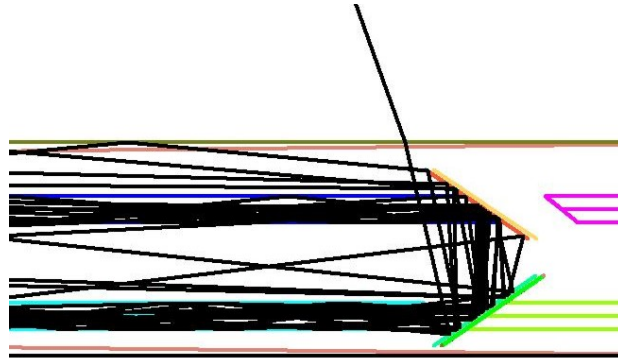


Figure 4.14: Ray trace plot of the inter-plane coupling configuration with reversal of the propagation direction. The plot clearly shows that a considerable amount of rays are no longer guides in the waveguide core after the coupling of light signal from bottom layer to the top layer. This is mainly due to the diffraction that the light beam experiences during the propagation from one mirror to the other.

the larger degree of beam spreading because of the increased propagation length in the fill cladding material prior to reaching the metalized mirror facet. For the case of the MMF detector the link efficiency drops from 46.3% for $w = 100\mu\text{m}$ to 42.5% for $w = 150\mu\text{m}$. The width of the ablated trench is determined by the width of the mask that is used for the ablation, and will be discussed in the next section, which deals with the experimental results.

The second inter-plane coupling configuration is the case where the light signal undergoes a double 90° with conservation of the propagation direction. The alignment tolerance plot for a misalignment of the top mirror along the Z-axis with respect to the theoretically ideal position, in which case the center of the mirror facet and the center of the detector are perfectly aligned with respect to each other, is shown in Fig. 4.15. The alignment tolerance plot is in this case symmetrical around the theoretically ideal position, and has a maximum link efficiency of 54.5% (-2.64dB) for the flat detector and 23.6% (-6.27dB) for the MMF detector. A ray-trace plot of the considered structure is shown in Fig. 4.16. From this plot, it is clear that a considerable amount of rays is no longer guides in the waveguide core after the coupling from one layer to the other because of the diffraction that the light beam experiences during the propagation from one mirror facet to the other. The alignment tolerance range is $[-20\mu\text{m}, 00\mu\text{m}]$ for the flat and $[-15\mu\text{m}, 15\mu\text{m}]$ for the MMF detector for an excess loss of 1dB; $[-10\mu\text{m}, 10\mu\text{m}]$ for the flat and $[-3\mu\text{m}, 3\mu\text{m}]$ for the MMF detector for an excess loss of 0.1dB and $[-15\mu\text{m}, 15\mu\text{m}]$ for the flat and $[-15\mu\text{m}, 15\mu\text{m}]$ for the MMF detector for an excess loss of 0.5dB. These results are summarized in Table 4.6.

4.2.2 Experimental results

The patterning of the metalized 45° micro-mirror requires three processing steps, schematically shown in Fig. 4.17:

- ablation of the trench with a 45° air-polymer interface with the excimer laser

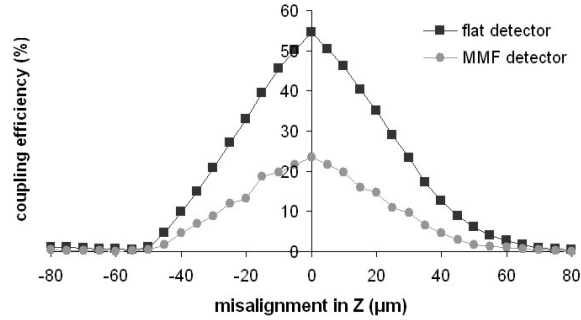


Figure 4.15: Alignment tolerance plot for a mechanical misalignment of the top mirror around its theoretically ideal position along the Z-axis in the inter-plane coupling configuration with conservation of the propagation direction for the case of the flat detector and the MMF detector.

	FLAT DETECTOR	MMF DETECTOR
1dB excess loss	$[-20 \mu\text{m}, 20 \mu\text{m}]$	$[-15 \mu\text{m}, 15 \mu\text{m}]$
0.5dB excess loss	$[-15 \mu\text{m}, 15 \mu\text{m}]$	$[-5 \mu\text{m}, 5 \mu\text{m}]$
0.1dB excess loss	$[-10 \mu\text{m}, 10 \mu\text{m}]$	$[-3 \mu\text{m}, 3 \mu\text{m}]$

Table 4.6: Alignment tolerance ranges corresponding to an excess loss of 1dB, 0.5dB and 0.1dB for a misalignment of the top mirror along the Z-axis in a two layer inter-plane coupling configuration with conservation of propagation direction.

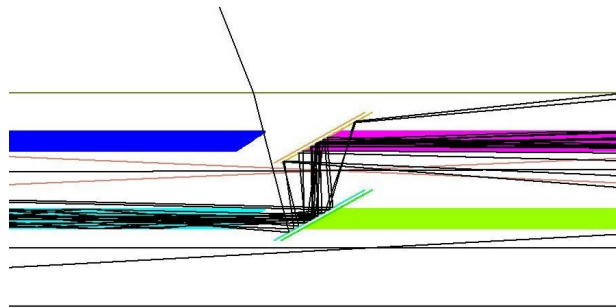
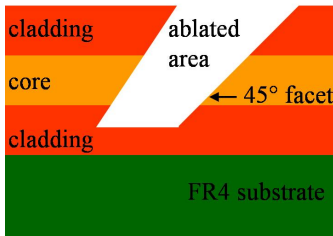
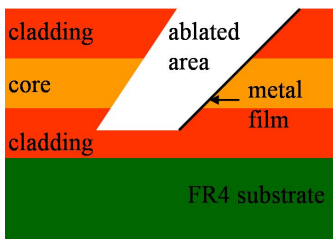


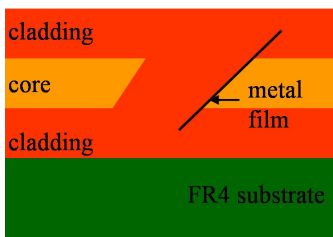
Figure 4.16: Ray trace plot of the inter-plane coupling configuration with conservation of the propagation direction. The plot clearly shows that a considerable amount of rays is no longer guided in the waveguide core after the coupling from one layer to the other. This is mainly due to the spreading of the light beam during the propagation from one mirror to the other.



(a)



(b)



(c)

Figure 4.17: (a) Ablation of a trench with a 45° mirror facet; (b) Au-coating of the mirror facet; (c) filling of the ablated trench with cladding material.

beam in a tilted position with respect to the translation stage and the sample placed horizontally on the translation stage.

- Au-coating of the mirror facet by covering the sample with a suitable mask and placing it into the vacuum chamber of the evaporating unit.
- filling of the ablated trench with cladding material using a spincoating step, giving a planarized top surface.

The optical layer consists of a stack lower cladding/core/top cladding material, each layer having a thickness of 50 μm . The mirror facet has to be ablated through the optical layer, into the lower cladding layer, without ablation of the FR4 substrate because of the high degree of debris deposition this causes. A couple of questions have to be answered in order to be able to ablate high-quality mirrors into the optical layer:

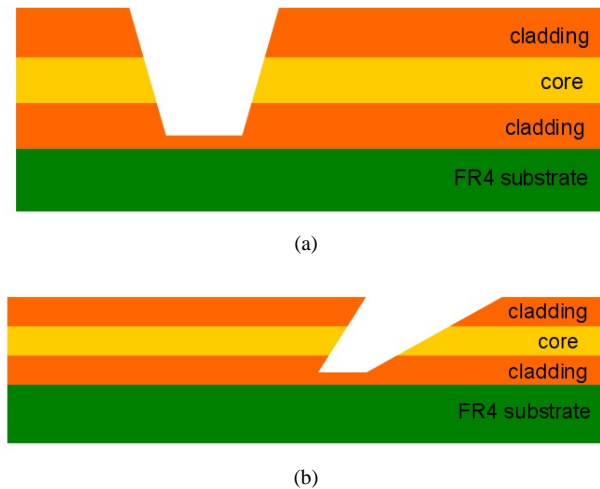


Figure 4.18: (a) Trench that is obtained after ablation with the laser beam perpendicular to the sample; (b) trench that is obtained when the ablation is done with the laser beam in a tilted position.

- what is the required tilt angle of the laser beam in order to obtain a 45° air-polymer interface?
- what is the optimal pulse energy for the ablation of the mirror, delivering a mirror facet with minimum surface roughness?
- what is the optimal mask size?
- what is the best way to deposit the Au-coating on the mirror facet, without Au-deposition on the other interface of the ablated trench?

Optimization of the tilt angle of the laser beam

In the case that the ablation is done with the laser beam perpendicular to the sample, the angle of the sidewalls of the ablated trench are determined by the tapering that occurs during the ablation. The excimer laser beam can be tilted with respect to the sample, allowing the ablation of angled features with the sample in a horizontal position on the translation stage. Because of the tilted position of the laser beam and the tapering that occurs during the ablation, only one of the two interfaces can be ablated at an angle of 45° angle, depending on the tilt angle of the laser beam. If the laser beam is tilted at an angle of 45° , one of the sidewalls of the ablated trench will be at an angle of 45° increased with the tapering angle that occurs during vertical ablation and the tapering angle that occurs during the ablation with the tilted laser beam, as is schematically shown in Fig. 4.18. The tilt angle of the laser beam has to be corrected with these tapering angles in order to obtain a 45° mirror facet.

In order to determine the required tilt angle, mirrors have been ablated at various tilt angles ranging from 45° to 25° . The angle of the mirror facet has in a next step been

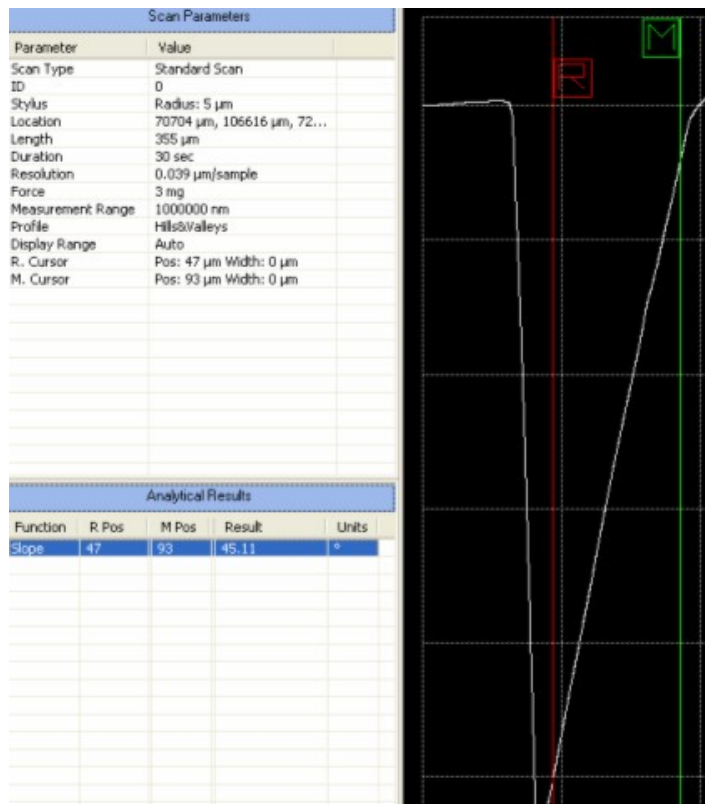


Figure 4.19: Angle of the mirror facet, measured with a stylus profiler (Dektak), showing an angle of 45.11° .

controlled with stylus profiler measurements (Dektak 8, Veeco). A tilt angle of 26° provides a mirror facet with an angle close to 45° , as is shown in the measurement result in Fig. 4.19. The laser beam is tilted manually with the help of a microscrew, which means that small angle variations are possible. Stylus profiler measurements on multiple mirror samples indicate that the average angle of the mirror facet is $45.1^\circ \pm 0.45^\circ$. This is within the tolerance range resulting from the numerical analysis, which was $\pm 2^\circ$ (4.2.1).

Optimization of the pulse energy

The pulse energy that is used for the ablation of the mirror into the optical layer has to be optimized in order to obtain a mirror facet with minimum surface roughness (RMS surface roughness $\leq \lambda/10$ is a good guideline in order to minimize the scattering loss). A good starting point is the pulse energy that is used for the ablation of the waveguides. The laser beam is tilted under a 26° angle, sent through a mask with dimension $800 \mu\text{m} \times 3000 \mu\text{m}$ and projected onto the sample with demagnification. The surface roughness of the mirror facet can be measured with the available optical profiler by attaching the sample on a 45° holder. In this way, the mirror facet is in a horizontal position

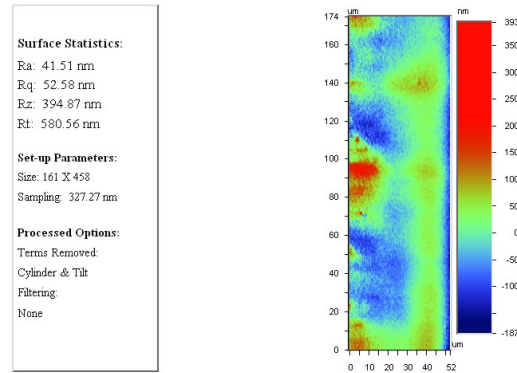


Figure 4.20: Surface roughness plot of a 45° mirror facet, ablated with energy intensity of $7.6\text{mJ}/\text{mm}^2$.

and the surface roughness can be measured with a non-contact optical profiler (Wyko NT3300). The measurements show that the mirror facet is not completely planar, but has a slightly cylindrical shape. This shape is an inherent consequence of the nature of the ablation process. The tilt of the FR4 substrate will also influence the planarity of the mirror.

The surface roughness of the mirror facet depends strongly on the energy of the laser beam. If the laser pulse energy is chosen too low, there will be a large amount of debris deposited on and near the ablated area because of the high number of pulses, and consequently low ablation speed, that are required to ablate the mirror up to the desired depth. If the pulse energy is chosen too high, there will be a considerable amount of thermal ablation with the associated burning and melting. In some cases local delamination can occur between the core and cladding layer, meaning that the adhesion between both layers is gone, because of the high stress that is build-up between the two layers during the ablation.

Mirrors have been ablated with excimer pulse energy set to 3 mJ, 6 mJ and 12 mJ, these pulse energies being the setting values on the ablation set-up itself. The best results are obtained with the pulse energy of 6 mJ, which corresponds to an laser fluence of $7.6\text{mJ}/\text{mm}^2$, measured on the translation stage with an energy meter. The mirror facet has an average RMS surface roughness of $61.53\text{ nm} \pm 6.46\text{ nm}$, measured on a scan area of $52\text{ }\mu\text{m} \times 174\text{ }\mu\text{m}$. An example of a surface roughness plot is given in Fig. 4.20. The roughness of the mirror facet increases considerably in case imperfections such as air bubbles and contaminants such as small particles are present in the layer. Therefore, the application of the optical layer onto the FR4 substrate should be carried out in cleanroom environment.

The mirror facets that are ablated with a pulse energy of 3 mJ have an average RMS surface roughness of $110\text{ nm} \pm 6.2\text{ nm}$, measured on a scan area of $52\text{ }\mu\text{m} \times 174\text{ }\mu\text{m}$. The mirror surface is much rougher than the mirrors ablated with a pulse energy of 6mJ, mainly because of the higher amount of debris that is deposited on the mirror facet. This is due to the high number of pulses, and consequently low ablation speed, that is required for the ablation of the mirror. An example of a surface roughness plot

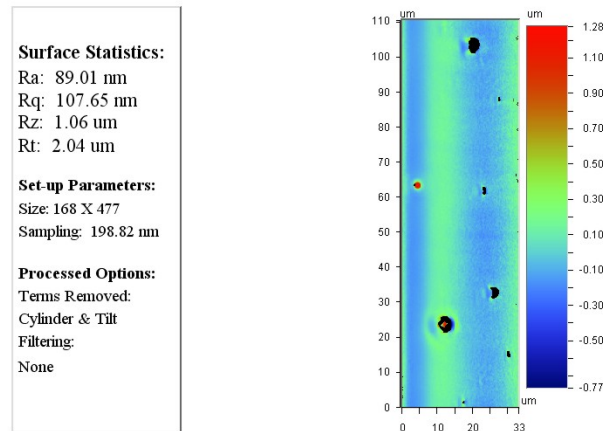


Figure 4.21: Surface roughness plot of a mirror facet ablated with a pulse energy of 3 mJ.

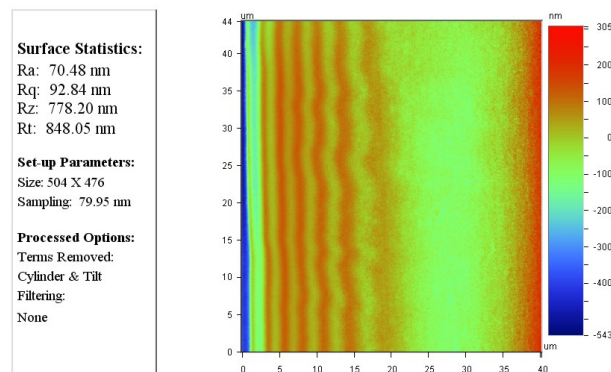


Figure 4.22: Surface roughness plot of a mirror facet ablated with a pulse energy of 12 mJ.

is given in Fig. 4.21. An SEM image of the top view of a mirror facet ablated with a pulse energy of 3 mJ is shown in Fig. 4.23(a).

The mirror facets that are ablated with a pulse energy of 12 mJ have an average RMS surface roughness of $109.4 \text{ nm} \pm 5.6 \text{ nm}$, measured on a scan area of $52 \mu\text{m} \times 174 \mu\text{m}$. The surface roughness is much higher than for the mirrors that are ablated with a pulse energy of 6 mJ because of the melting that occurs during the ablation. Together with this melting a considerable degree of burning also occurs with the associated black decoloration of the ablated areas, which is not desirable for optical applications. An example of a surface roughness plot is given in Fig. 4.21. An SEM image of a 45° mirror facet ablated with a pulse energy of 12 mJ is shown in Fig. 4.23(b).

The ablation parameters have been optimized for the ablation of an $\approx 125 \mu\text{m}$ deep mirror facet. This is done by ablating mirrors at various ablation speeds and measuring the associated ablation depth. The 45° mirror facet is ablated with the following parameters:

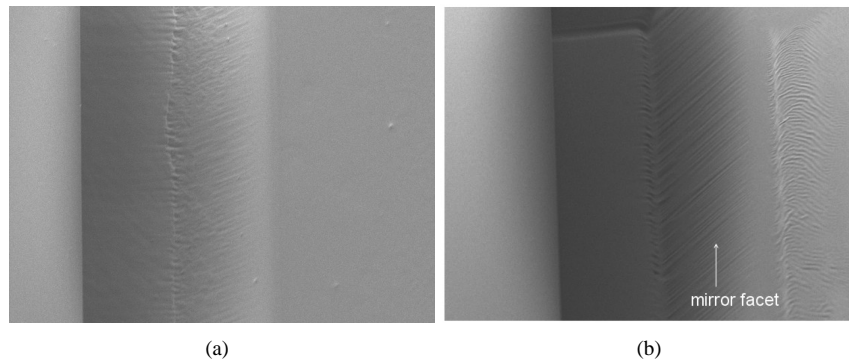


Figure 4.23: (a) SEM image of a 45° mirror facet ablated with a pulse energy of 3mJ; (b) SEM image of a 45° mirror facet ablated with a pulse energy of 12mJ.

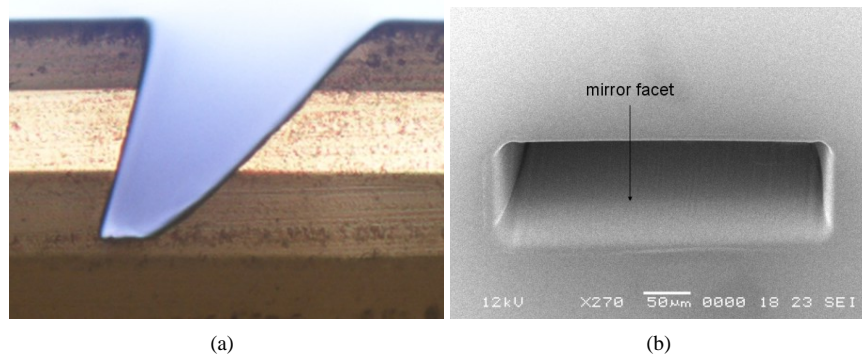


Figure 4.24: (a) Cross-section of an ablated trench with a 45° air-polymer interface; (b) SEM image of the top view of the ablated trench.

- KrF excimer laser beam tilted at an angle of 26°
- mask with dimensions $800 \mu\text{m} \times 3000 \mu\text{m}$, before demagnification
- laser fluence: $7.6 \text{ mJ}/\text{mm}^2$, measured on the translation stage with an energy meter
- ablation speed: $200 \mu\text{m}/\text{s}$

A cross-section of the ablated trench with the 45° air-polymer interface is shown in Fig. 4.24(a). From this picture, it is clear that the core-air interface is much steeper than the mirror facet which justifies the use of the angle $\alpha = 25^\circ$ for the simulations. In Fig. 4.24(b), an SEM image can be seen from the top view of the ablated trench. The mirror is in this case ablated statically in order to have a clear view on the ablated trench. In practice, the mirror is ablated dynamically because of the fact that the mirror is ablated into an array of waveguides which is impossible to do statically because of the fact that the width of the waveguide array exceeds the width of the projection of the mask onto the sample. The dynamic ablation means that the translation stage is moved

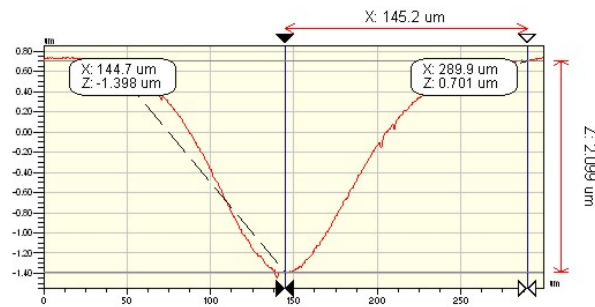


Figure 4.25: (Surface corrugation of the top cladding layer, after the filling of the ablated trench with cladding material.

with respect to the laser beam at a predefined speeds, which determines the number of pulses that is deposited on each location. The surface roughness of the mirror facet is identical for both the static and the dynamic ablation process.

In Fig. 4.24(b), the projection of the rectangular shape of the mask is clearly visible, and is rotated over 90° with respect to the cross-section given in Fig. 4.24(a) in order to have a better view on the mirror facet. The mirror facet and the opposite interface are tilted because of the tilted position of the laser beam. The surface corrugation of the top cladding layer, after the filling of the ablated trench with cladding material, is approximately $2 \mu\text{m}$, as is shown in Fig. 4.25. The tilt angle of the top surface is below 1° , meaning that the planarity of top surface allows the mounting of opto-electronic elements on top the optical layer.

Metalization of the mirror facet

The metalization of the mirror facet is not as straightforward as one would assume. Au is chosen in view of its high reflectivity at 850nm and the availability at the lab. An alternative metal that has a slightly lower reflectivity at 850nm but in general shows a better adhesion to most substrates is Al. The use of Al has however not been evaluated because of the non availability. The deposition of the Au-coating should be strictly limited to the mirror facet, where a high reflectivity is desired, and should not be deposited onto the opposite interface of the ablated trench. The reason for this is the fact that after the filling of the ablated trench with cladding material, the light propagating in the waveguides has to pass this core-cladding interface before it reaches the mirror facet. The deposition of Au onto the opposite interface of the mirror facet will deteriorate the performance of the mirror because, depending on the thickness of the deposited Au-film, part of the light signal or the entire light signal will be reflected at this interface instead of at the mirror facet and will be coupled out in a direction deviating from the vertical direction. The sample is to be covered with a mask during the Au-coating step, in order to have a selective Au-deposition in the area of the mirror facet but not on the remaining part of the ablated trench.

Several tests have been carried out with both Au-evaporation and Au-sputtering as deposition techniques. In the first tests, the ablation of the mirror facet was done through a standard Scotch tape, attached to the top surface of the optical layer prior to the ab-

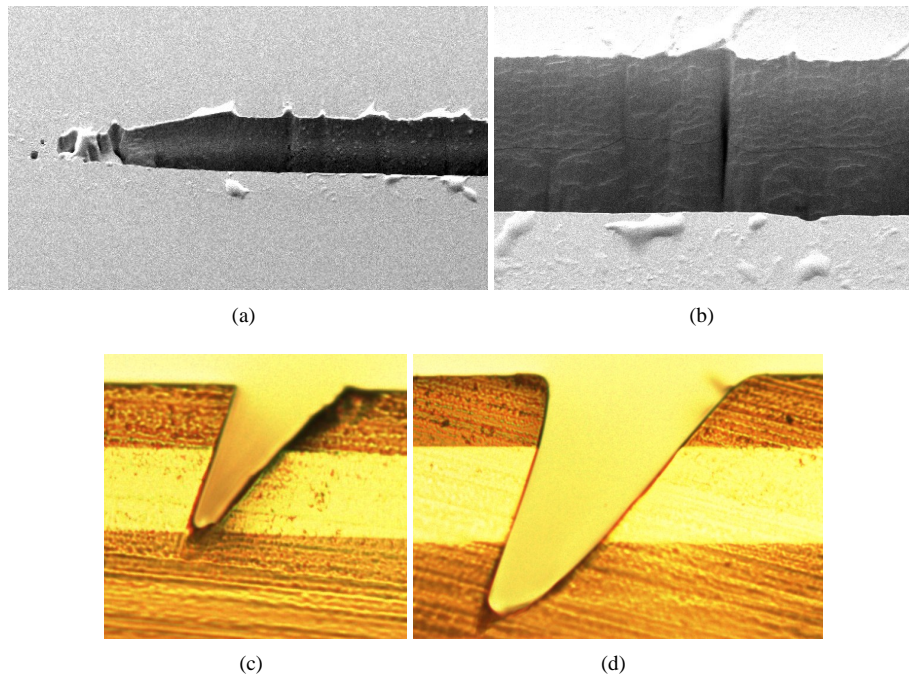


Figure 4.26: (a) SEM image of the top view of the starting point of a mirror that is ablated through a mask that is taped on the surface of the sample; (b) close-up showing the high roughness and uneven surface of the mirror facet ; (c) cross-section of a mirror that is ablated through a mask that is taped on the surface of the sample; (d) cross-section of a mirror that is ablated directly into the optical layer.

lation. In this way, the mask is opened in the places where the mirrors are ablated and it is perfectly aligned with the mirror opening. However, the surface roughness of the ablated mirrors increases more than ten times in this way, making it an unattractive masking solution. When the mirrors are ablated, the mask taped on top of the sample is ablated first. The ablation of the tape creates a rectangular opening with rough edges, because of the bad ablation behaviour of the tape, and a high amount of debris deposition into and next to the ablated area. The roughness of the edges of the rectangular opening in the tape are transferred to the sidewalls of the ablated trench, creating a mirror facet with a very high surface roughness. An SEM image of the ablated mirror trench through the tape is shown in Fig. 4.26(a) and (b). The high surface roughness and the appearance of craters onto the mirror facet are clearly visible in the pictures. A cross-section of a mirror ablated through a mask that is taped on the surface of the optical layer versus the cross-section of a mirror that is directly ablated into the optical layer is given in Fig. 4.26(c) and (d). The angle of the "taped" mirror facet deviates about 2° to 3° from the desired 45° angle. The ablation depth is also considerably lower than for the ablation without the tape, and this for the same ablation parameters. This is of course caused by the fact that the tape is ablated before the mirror facet. It is therefore better to cover the sample after the ablation of the mirror, even though this requires an extra alignment step of the mask with respect to the mirror. Different



Figure 4.27: Schematic showing the alignment of the tape with respect to the ablated trench. The sidewall of the opening in the mask is aligned with the polymer-air interface of the ablated mirror in order to avoid the deposition of Au onto that interface.

types of masks have been studied ranging from scotch tape over polycarbon film to a low adhesion type of tape. The mask is opened with the excimer laser before it is placed on the surface of the sample, and is aligned with respect to the mirror facet with the help of an optical microscope. The scotch tape is not very practical: it has a very good adhesion to the polymer layer which makes the alignment of the tape with respect to the mirror facet more difficult. In addition, the tape releases a thin layer of adhesive on the top surface of the optical layer which can not be removed very easily.

The polycarbon tape does not adhere to the optical layer, leaving a small air gap between the top surface of the optical layer and the mask, making it even more difficult to avoid Au-deposition on the opposite interface of the mirror facet. Tests indicate that it is practically impossible to limit the Au-deposition to the mirror facet, which makes this method not very interesting.

The best results are obtained using a low adhesion tape, which is also used as a protective cover layer for semiconductor wafers. The tape is opened with KrF excimer laser, forming rectangular openings with a width of $\approx 300\mu\text{m}$ in the areas where the mirrors are to be ablated. The ablated trench has a width w of $\approx 120\mu\text{m}$, measured at the top of the top cladding layer. This leaves enough margin for the alignment of the mask with respect to the mirror facet. The tape is placed as close as possible to the intersection of the interface opposite to the mirror facet with the top surface of the optical layer. The principle is schematically shown in Fig. 4.27. From this schematic, it is clear that there will be some Au-deposition on the top surface of the optical layer, next to the mirror facet. This is no problem because the light spot is coupled out at the mirror facet, and will thus not be influenced by this Au-layer. The zone of the top surface that is Au-coated can be limited by using a mask with a smaller opening, but this also makes the alignment of the mask with respect to the ablated trench more difficult.

After the covering of the sample with the mask, leaving only the areas with the ablated mirrors uncovered, it is fixed on a holder that is placed in the vacuum chamber of the evaporating unit (Univex 450, Leybold-Heraeus). The sample is fixed on the holder in a tilted position, in order to avoid the deposition of Au onto the opposite interface of the mirror facet. Mirrors have been Au-coated in the Univex evaporating unit with the sample fixed at tilt angles ranging from 0° (perpendicular to the source) to 45° . The samples that are placed under tilt angle 0° , schematically shown in Fig. 4.28(a), have Au-deposited in the entire cavity, also on the opposite interface of the mirror facet, which will limit the performance of the mirror. This because of the fact that the light

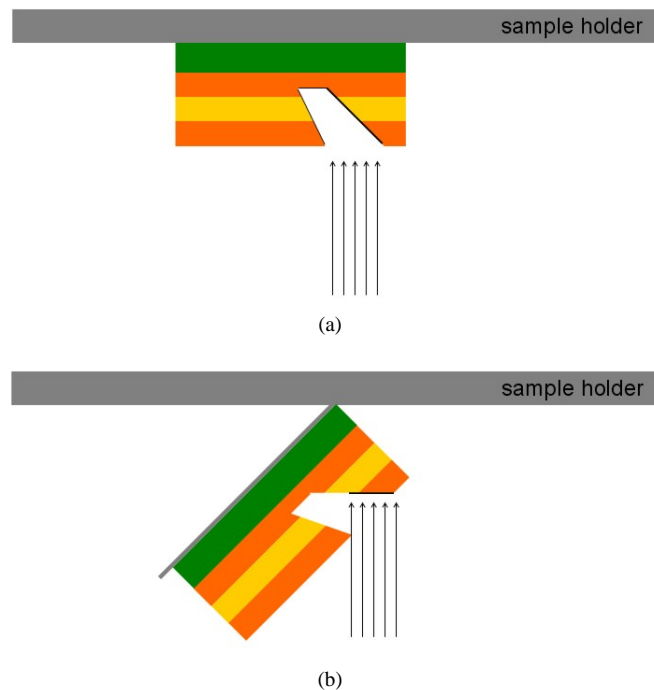


Figure 4.28: (a) Schematic showing the Au-deposition in the ablated trench in case the sample is placed horizontally on the sample holder. The mirror facet is Au-coated but a thin layer of Au is also deposited on the opposite facet because of non directional Au-deposition and scattering in the ablated trench; (b) schematic showing the Au-deposition in the ablated trench in case the sample is tilted under a 45° angle on the holder. The mirror facet is not fully covered because of the shadow effect caused by the opposite interface. The depth up to which the Au is deposited depends not only on the tilt angle but also on the orientation and position of the sample with respect to the Au-source.

spot first has to pass the interface opposite to the mirror facet prior to the 90° beam deflection at the mirror facet. Microscope pictures of the mirror cross-section show that the samples that are tilted under a 45° angle, schematically shown in Fig. 4.28(b), do not suffer from Au-deposition on the opposite interface. Problem here is the fact that the deposition on the mirror facet is complicated by the shadow of the opposite interface and that the mirror facet will consequently not be covered over the entire length of the mirror facet and in this way will limit the performance.

The best results are obtained for a tilt angle of $\approx 15^\circ$, which is in between the two previous values. Microscope pictures of the mirror cross-section show a good coverage of the mirror facet and show no apparent Au-deposition on the opposite interface. However, the position and orientation of the sample with respect to the Au source is important, as is depicted in Fig. 4.29. The samples that are aligned with respect to the Au-source, corresponding to position B in Fig. 4.29, suffer from Au-deposition onto the opposite interface because of the scattering of Au-particles during the evaporation

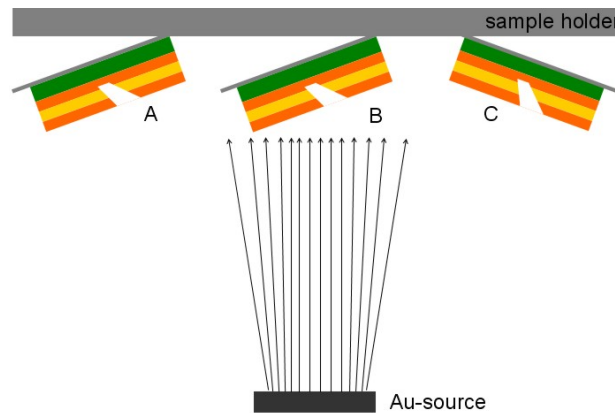


Figure 4.29: The deposition of the Au-coating on the mirror facet depends on the position of the sample on the holder used to position it in the evaporating unit. The three possible positions are marked in the picture by A, B and C. In position B, the sample is aligned with respect to the Au-source. In position A and C, the sample is placed in a eccentric position.

process. This in contrast to the samples that are placed in position C, in which case the scattering can be avoided, at least at first sight, and the Au-layer is only deposited onto the mirror facet. The samples that are placed in position A get more deposition on the opposite interface than on the mirror facet and therefore this position should be avoided. Cross-sections of experimental results are shown in Fig. 4.30.

For the preparation of the cross-sections, the samples are cut with a diamond saw and polished manually after encapsulating them in mecaprex-material, which has been developed for this purpose. The encapsulating step makes the samples unusable for further use because of the encapsulated condition. However, in case the samples are polished manually after the cutting adhesion problems between the Truemode material and the Au-film are frequently experienced. A cross-section of a metalized mirror, where the deposition of the Au-layer is limited to the mirror facet, is shown in Fig. 4.31. The manual polishing step puts a certain amount of pressure on the polished edge of the sample, creating adhesion problems between the Au-coating and the Truemode material, as can be seen in the picture. The loss of adhesion is limited to the zone where the Au-layer is deposited. In real applications, the mirrors will normally not be cut, but the loss of adhesion after the polishing step does show that the adhesion between Truemode and Au is not very good. The evaporation of a thin Ti-film underneath the Au-film, to improve the adhesion to the polymer material, does not offer a solution because cladding material is also applied on top of the metalized mirror facet.

Alternative approaches

Even with the use of mentioned aids, the tilted position of the sample and the orientation and position on the holder, the reproducibility of the Au-coating of the entire mirror facet is poor, necessitating the use of a different deposition technology or a change in mirror design. The first option, the use of a different deposition technology, does

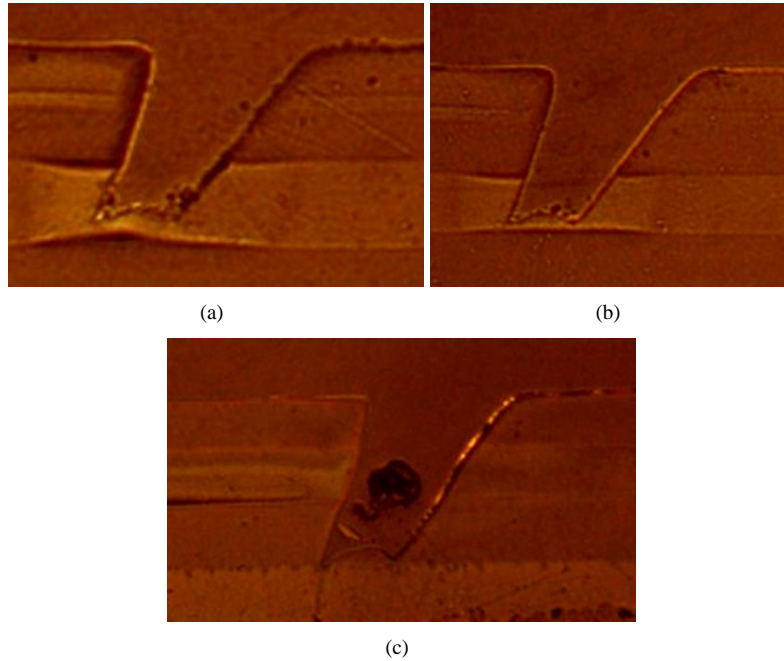


Figure 4.30: (a) Cross-section of a metalized mirror facet placed in position A on the holder. The Au is deposited onto the opposite mirror interface. (b) Cross-section of a metalized mirror facet placed in position B on the holder. The Au is deposited onto mirror facet and the opposite interface. (c) Cross-section of a metalized mirror facet placed in position C on the holder. The Au is deposited onto the mirror facet.

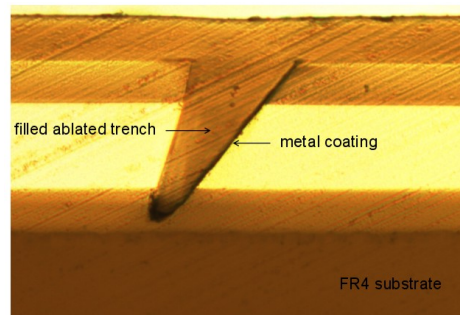


Figure 4.31: Cross-section of a metalized mirror. The Au-deposition is limited to the mirror facet, in accordance with the mirror design. The adhesion between the Au-layer and the Truemode material is lost during the manual polishing step, which puts too much pressure on the edge of the sample. The filling of the ablated trench with cladding material is good, except for the Au-coated area as a consequence of the polishing process.

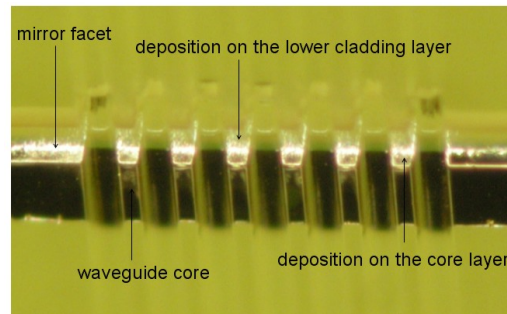


Figure 4.32: Picture of a Au-coated mirror that is ablated directly into the patterned core layer. The top part of the mirror, corresponding to the core layer, has a good Au-coverage and the lower part, corresponding to the lower cladding layer, has a lower coverage.

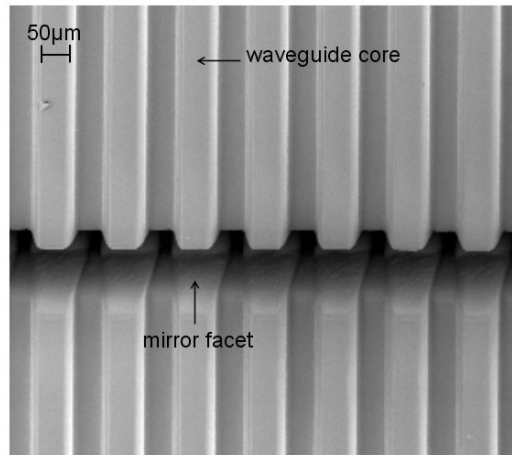
not really offer a solution. At the laboratory, two different Au-deposition technologies are available: evaporation, discussed in the previous paragraphs, and sputtering. The evaporation process has the highest degree of directivity [11], which is a fundamental requirement in order to limit the deposition to the mirror facet. The sputtering process has a low directivity and is typically used to get a homogeneous deposition on an uneven sample.

This leaves the second option, a change in the mirror design, keeping in mind the limitations of the laser ablation process. A first option is to ablate the mirrors directly into the patterned core layer. In this way, the required ablation depth is only $75\ \mu\text{m}$ instead of the $125\ \mu\text{m}$ depth required for the mirrors that are ablated into the optical layer in which case the waveguide cores are covered with cladding material. The top part of the mirror is ablated into the core layer, allowing the full coverage of the core layer during the Au-coating step. It should be noticed that the efficiency of the mirror will slightly drop because the Au-coating is limited to the core layer and potentially also a part of the lower cladding layer.

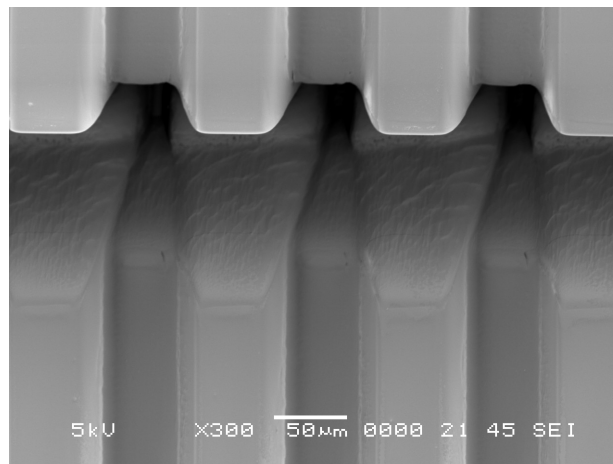
A picture of a Au-coated mirror facet is shown in Fig. 4.32. In this picture, it can be seen that the top part of the mirror, corresponding to the core layer, has a good Au-coverage and the lower part, corresponding to the lower cladding layer, has a lower coverage.

Surface roughness measurements have been carried out with a non-contact profiler, giving an average RMS surface roughness of $162\ \text{nm} \pm 30.5\ \text{nm}$ measured on a scan area of $42\ \mu\text{m} \times 50\ \mu\text{m}$, which is much higher than the roughness measured on the mirrors that are ablated into the planarized optical layer after the application of the top cladding layer. SEM images of a mirror ablated into the patterned core layer are shown in Fig. 4.33. Typically, a surface roughness $\leq \lambda/10$ is given as a guideline for good optical performance with minimal scattering loss. The surface roughness of the mirrors ablated in the core layer is much higher than this limit value, and will have a high scattering loss.

An alternative to the ablation of the mirrors with the tilted KrF excimer laser beam is the use of a triangular mask, which is schematically shown in Fig. 4.34. The laser beam, which is perpendicular to the sample, is in this case sent through a triangular mask with a width w of $800\ \mu\text{m}$ and a length l of $3000\ \mu\text{m}$, which are the mask dimensions before



(a)



(b)

Figure 4.33: (a) SEM image of a mirror ablated directly into the patterned core layer; (b) close-up SEM image of the mirror facet, which confirms the high surface roughness measured with the non-contact optical profiler.

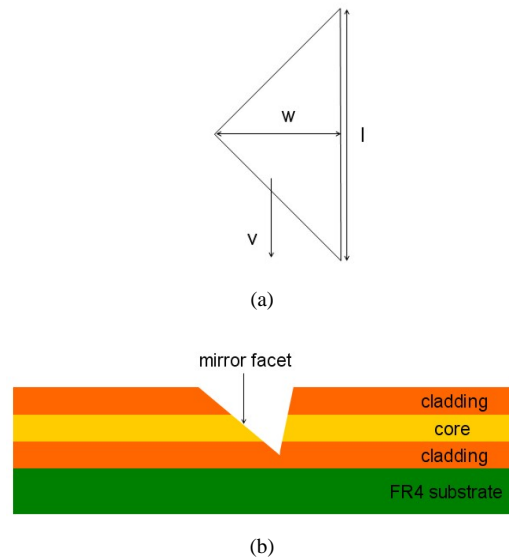


Figure 4.34: (a) Triangular mask that is used for the ablation of the 45° mirror facet. The mask has a length l , a width w and is moved across the sample with a propagation speed v ; (b) trench that is formed into the optical layer after the ablation with the use of the triangular mask. The angle of the mirror facet depends on the ablation depth and the mask dimensions.

the demagnification with factor 10 onto the translation stage. The laser beam is moved along the indicated propagation direction with an ablation speed v . The ablation speed v and the width w of the mask, determine the angle of the mirror facet as it is indicated in Fig. 4.34.

A cross-section of two mirrors that are ablated into the optical layer with the triangular mask at different ablation speed is shown in Fig. 4.35. From these pictures, it is clear that the angle of the potential mirror facet depends on the ablation depth and the mask dimensions. The relation between the ablation speed and the corresponding facet angle, for a laser fluence of 7.6mJ/mm^2 , is shown in Fig. 4.36. From this graph, it can be seen that for the given laser fluence, an ablation speed of $280\ \mu\text{m/s}$ delivers the desired 45° facet, which can be used as a mirror after metalization and filling of the ablated trench. The mirror has a depth of $80\ \mu\text{m}$ and a top width of $95\ \mu\text{m}$. Stylus profiler measurements have been carried out to evaluate the reproducibility of the facet angle. These measurements show that the mirror facet has an angle of $45.03^\circ \pm 0.37^\circ$, measured with respect to the horizontal axis.

The ablated 45° mirror facets have an average RMS surface roughness of $52.46\ \text{nm} \pm 5.52\ \text{nm}$ on a scan area of $110\ \mu\text{m} \times 50\ \mu\text{m}$, which is comparable to the surface roughness of the mirror facets that are ablated with the tilted excimer laser beam. An SEM image of the top view of the projection of the triangular mask onto the optical layer and the top view of a 45° mirror facet ablated with the triangular mask are shown in Fig. 4.37. From these pictures, it can be seen that the mirror has a smooth surface. This in contrast to the surface of the opposite interface, which has a very high roughness.

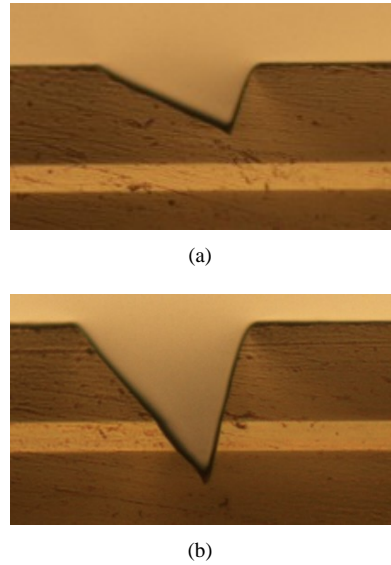


Figure 4.35: (a) Cross-section of a mirror facet ablated with the triangular mask at low ablation speed; (b) cross-section of a mirror facet ablated with the triangular mask at higher ablation speed. From these pictures, it is clear that the mirror facet becomes steeper with increasing ablation depth.

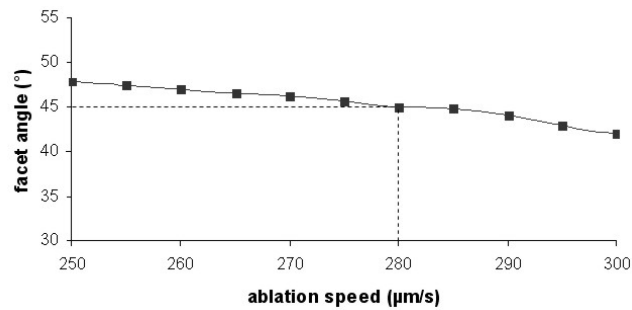
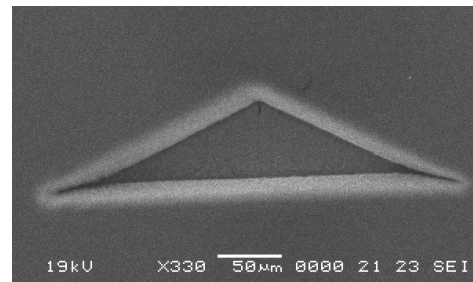
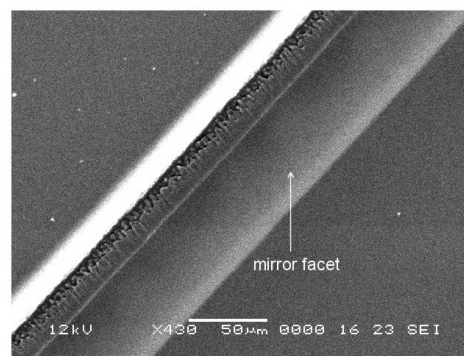


Figure 4.36: Graph of the relation between the ablation speed and the corresponding facet angle, with respect to the horizontal axis, for a laser fluence of 7.6mJ/mm^2 .



(a) a



(b) b

Figure 4.37: (a) SEM image of the top view of the projection of the triangular mask onto the optical layer; (b) SEM image of the top view of a 45° mirror facet ablated with the triangular mask.

This is mainly caused by shape of the triangular mask, which arranges the distributed energy deposition to the optical layer but on the other hand also transfers the roughness of the sidewalls to the mirror facet. This high roughness might be improved with the use of a high quality mask, instead of the kapton masks that are used at the moment and into which the openings are ablated with KrF excimer laser.

The advantage of this configuration is the fact that the opposite mirror facet is not covered, as is the case for the mirrors ablated with the tilted laser beam. This facilitates the control of Au-deposition onto the opposite mirror interface. However, it turns out to be practically impossible to avoid the deposition of Au onto the opposite mirror interface. The Au-coating problems that are experienced imply that the mirror design has to be changed more drastically. In the next section, the use of the opposite mirror interface as out-of-plane coupling mirror is discussed. This interface can be used as a total internal reflection mirror, limiting the use of this mirror configuration to one optical layer.

Despite the problems that are experienced with the selective deposition of Au on the mirror facet, experiments have been carried out to ablate mirrors in a two layer mirror structure. The main aim is to determine whether or not the achievable alignment accuracy with the use of KrF excimer laser ablation is in accordance with the alignment

tolerance range resulting from the numerical study. The ablation of the mirrors into a two layer optical structure is done in the same way as for the two layer waveguide structure, which was discussed in the previous chapter (7.2.1). The achievable alignment accuracy is independent from the fact whether or not a metal coating has been applied. For this reason, the Au-coating step is skipped in these experiments.

The mirrors are ablated into each optical layer separately and are aligned with respect to each other with the use of Au alignment marks, evaporated on the lower cladding layer of the bottom optical layer with a suitable mask, and an alignment pulse, used to compensate for the horizontal shift that occurs when the focus is changed from the alignment marks, applied on the lower cladding layer, to the top surface, where the mirrors are ablated, as was explained in the previous chapter. The alignment accuracy between the mirror in the top optical layer and the mirror in the bottom optical layer has to be within the alignment tolerance range resulting from the numerical study on the different inter-plane and out-of-plane coupling configurations.

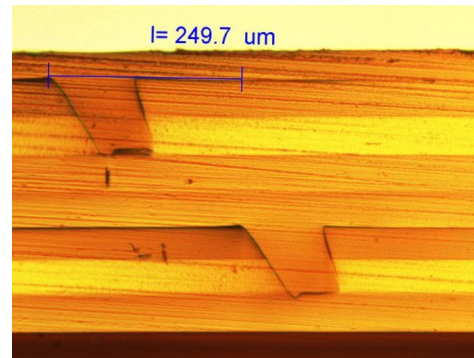
The ablation of the mirrors into a two layer optical structure is done in a very similar way for the out-of-plane coupling configuration and inter-plane coupling configuration with conservation of the propagation direction. In the two layer out-of-plane coupling structure, the distance between the centre of the mirror in the top and bottom optical layer corresponds to the pitch between the outcoupled spots and is consequently in accordance with the pitch of the opto-electronic elements used. A cross-section of a two layer out-of-plane coupling structure is shown in Fig. 4.38(a). The achievable alignment accuracy is $\leq 5\mu\text{m}$, in accordance with the achievable alignment accuracy of the two layer waveguide structure (7.2.1).

The centre of the top and bottom mirror in the inter-plane coupling structure with conservation of the propagation direction are aligned with respect to each other. A cross-section is shown in Fig. 4.38(b). The alignment procedure is identical to the one used for the two layer waveguide and the two layer out-of-plane coupling structure. This means that for both the out-of-plane coupling structure and the inter-plane coupling structure with conservation of propagation direction, the achievable alignment accuracy is $\leq 5\mu\text{m}$, which is within the alignment tolerance range for a 0.1dB excess loss according to the simulation results given in 4.2.1.

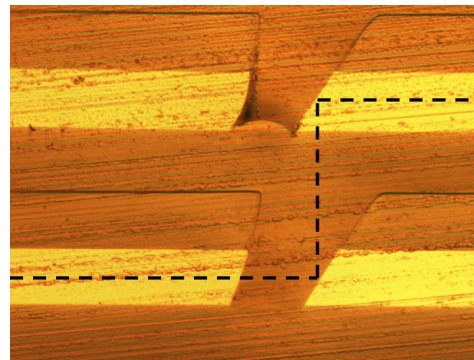
For the inter-plane coupling structure with conservation of the propagation direction, the achievable alignment accuracy $\leq 5\mu\text{m}$, is within the 0.1dB excess loss range for the flat and the 0.5dB excess loss range for the MMF detector. In view of the relatively low link efficiency of the complete system, these excess losses are only acceptable in case a limited number of double 90° bends are required to route the light signal from source to destination.

The ablation of the mirrors for the inter-plane coupling configuration with reversal of the propagation direction is more complicated. The sample has to be rotated over 180° for the ablation of the mirrors in the top layer with respect to the sample position for the ablation of the mirrors in the bottom layer, because the orientation of the top mirror is opposite to the orientation of the bottom mirror. The alignment accuracy between the centre of both mirror facets has to be within the alignment tolerance range resulting from the numerical study. The camera of the ablation set-up is not perpendicular to the translation stage, making the use of an alignment pulse in addition to the alignment marks necessary.

The camera, which is already in a tilted position, is rotated over 26° , together with the



(a)



(b)

Figure 4.38: (a) Cross-section of a two layer out-of-plane coupling structure. The distance between the centre of the mirror in the top and bottom optical layer corresponds to the pitch between the outcoupled spots, which is in this case $250 \text{ } \mu\text{m}$, in correspondence with most commercially available photo-detector and VCSEL arrays; (b) cross-section of an inter-plane coupling structure with conservation of the propagation direction. The centre of the mirror in the top and bottom layer are aligned with respect to each other.

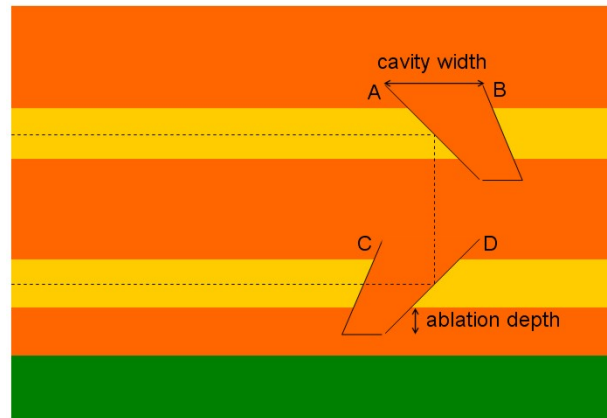


Figure 4.39: Schematic of the two layer inter-plane coupling structure with reversal of the propagation direction, with the main parameters that influence the alignment between the mirrors.

excimer laser beam, for the ablation of the 45° mirror facet. As a result, the edge of the 45° mirror facet is not clearly visible in the projection of the mask on the sample. In contrast, the opposite interface of the 45° mirror facet can be seen clearly in this projection making this edge the reference point that is used to align the center of both mirror facets with respect to each other. The bottom mirror is ablated at a predefined distance from the alignment marks, with the use of the alignment pulse. The distance from the alignment marks that is required to align the center of the mirror in the top layer with respect to the center of the bottom mirror is determined by a number of factors, as can be seen in the sketch in Fig. 4.39.

The predefined distance from the alignment mark that is used for the ablation of the bottom mirror has to be corrected with the distance between point B and C for the ablation of the top mirror. The distances AB and CD correspond to the cavity width w and are determined by the width of the mask that is used for the ablation of the mirrors and the ablation depth. The distance AD corresponds to twice the thickness of the top cladding layer of the top and bottom layer increased with the thickness of the core layer, in case the mirror facet is under an angle of 45° . The distance BC is determined by the following parameters:

- thickness of the core and cladding layers: there is always a certain variation on the layer thickness, especially for the Truemode material, which is spincoated at low speed (typically 200-250rpm for a $50\ \mu\text{m}$ thick layer). The cladding and core layers have a thickness of $50\ \mu\text{m} \pm 5\ \mu\text{m}$ in case the edges of the sample are not taken into account. The achievable accuracy on the layer thickness is relatively low, and can be better for materials with a higher viscosity, which are spincoated at a higher speed. This is the case for for instance Ormocer and Epocore/clad but on the other hand the ablation in these materials gives structures with a higher surface roughness and thus higher scattering loss.
- angle of the mirror facet: the ablation of the mirror facet has a high reproducibility in case the same ablation parameters are used. The mirror facet has an angle

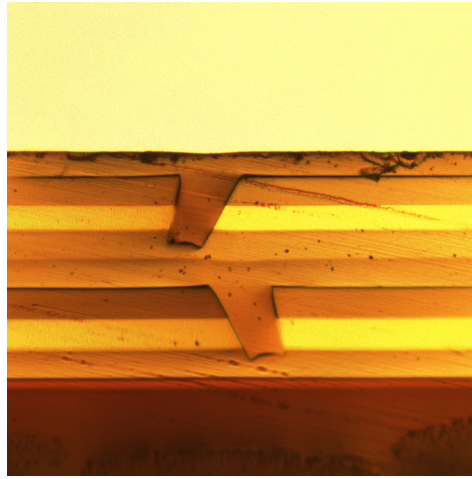


Figure 4.40: Cross-section of a two layer inter-plane coupling structure with reversal of the propagation direction.

of $45^\circ \pm 0.6^\circ$, which should be sufficient in order to obtain a good alignment between the two mirror facets.

- cavity width: the cavity width is determined by the width of the mask that is used for the ablation of the mirrors, and also by the depth of the ablation. The cavity width has a high reproducibility in case the mirrors are always ablated with the same ablation parameters.
- ablation depth: the ablation depth is the depth to which the trench is ablated into the lower cladding layer, and is determined by the ablation parameters and by the thickness of the cladding and core layers. If the top cladding layer and the core layer are thicker than the targeted value, in some cases the ablation of the mirror facet will not be sufficiently deep into the lower cladding layer which deteriorate the performance of the mirror.

From this discussion, it is clear that the achievable alignment accuracy is in this case lower than the achievable alignment accuracy for the other two discussed two layer mirror configurations. The energy of the excimer laser is monitored with an energy meter which allows a high reproducibility on the ablation parameters. The tilt angle of the excimer laser beam is tuned manually with the help of a microscrew to the desired value manually and can be done in a highly reproducible way. The main uncertainty on the alignment accuracy is the thickness of the cladding and core layers, which can only be improved by spincoating the layers at a higher spinspeed. The experimentally achievable alignment accuracy is $\leq 10\mu\text{m}$, which is within the alignment tolerance range for an excess loss of 1dB, resulting from the simulations in 4.2.1. A cross-section is shown in Fig. 4.40. As for the inter-plane coupling configuration with conservation of the propagation direction, this will only be acceptable for a limited number of crossings, especially in view of the relatively low maximum link efficiency.

4.2.3 Characterization

Loss measurements have been carried out on the different discussed metalized mirror configurations. These measurements confirm the conclusions that were drawn in the previous section. The best measurement results are obtained for the metalized mirror that was ablated into the optical layer with the excimer laser beam under a tilt angle of 26° . The mirror facet was metalized by placing the sample under a 15° angle on the holder of the evaporating unit, and was coated with a 100nm thick Au-layer. After the metalization step, the mirror was covered with cladding material.

For the loss measurements, an 850nm light signal is coupled in horizontally with a GI optical fiber with core diameter $50\ \mu\text{m}$ and NA 0.2. The light then propagates in the 4.5 cm long ablated Truemode waveguide, with cross-section $50\ \mu\text{m} \times 50\ \mu\text{m}$ and NA 0.3, until it is deflected over 90° at the metalized mirror facet. The vertically outcoupled light signal is detected with a GI optical fiber with core diameter $100\ \mu\text{m}$ and NA 0.29. The overall link loss is 19dB, of which roughly 0.6dB can be attributed to the waveguide propagation loss and 2dB for the incoupling and outcoupling. This still leaves 16.4dB for the excess loss of the micro-mirror, which an unacceptably high value. This is probably due to the deposition of a thin au-layer onto the opposite mirror interface. Part of the light signal is in this case deflected at this interface instead of the mirror interface and is coupled out under a non vertical angle. This part of the light signal is not detected by the detector fiber because of its limited acceptance angle. The use of a red light source confirms the existance of two seperate light spots, coupled out under a different angle.

The problems with the reproducibility of the selective deposition of the Au-coating on the mirror facet are very obvious during the measurement on different samples, prepared under the same conditions. In most cases, when sending red light through the waveguides, two deflected light spots are seen. This indicates that there is also Au-deposition on the opposite mirror facet. The low reproducibility, associated with the high coupling loss, makes it impossible to use this mirror configuration in practical applications. For this reason, in the next section the use of the opposite mirror interface as a total internal reflection mirror is discussed.

4.3 Total internal reflection mirror

The 45° polymer-air interface of the ablated trench can be used as a total internal reflection (TIR) mirror. The 90° beam deflection relies on the TIR that occurs at the polymer-air interface. One single processing step is sufficient for the patterning of the TIR mirror into the optical layer, making it an interesting candidate for out-of-plane coupling. The main reason why this mirror configuration was not the first choice is the fact that the mirror facet is uncovered and thus not protected from external influence such as dust and moist intrusion which could severely impair the mirror performance. In addition, because of the uncovered nature of the mirror facet, it can not be used in a multilayer structure. These problems can be solved by applying a Au-coating on the mirror facet and the filling of the ablated trench with cladding material, similar to the processing used for the patterning of the metalized micro-mirror, except that in this case the opposite interface of the ablated trench is used as a mirror.

Numerical simulations have been carried out to evaluate the performance and alignment

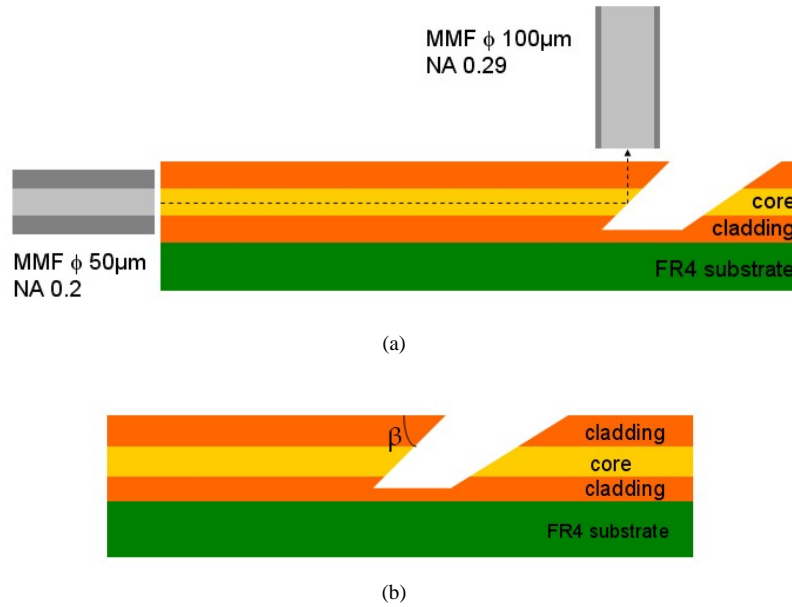


Figure 4.41: (a) Schematic of the considered configuration used for the simulations on the total internal reflection mirror; (b) the angle β of the mirror facet is varied between 40° and 50° in the simulations to determine the tolerance that can be accepted on the mirror facet angle.

tolerance range of the TIR mirror. The experimental results are in a next step compared to the results resulting from the numerical study.

4.3.1 Numerical simulations

An important issue that has to be addressed, is the influence of a deviation of the 45° angle of the mirror facet on the link efficiency. The configuration that is used for the simulations is shown in Fig. 4.41. It consists of an FR4 substrate onto which an optical layer is integrated containing an array of ablated multimode waveguides and a TIR mirror, used to deflect the light beam propagating in the waveguide over 90° . The mirror facet angle β is varied between 40° and 50° .

An 850 nm light signal is coupled in horizontally into the multimode waveguides with an optical fiber with core diameter $50\mu\text{m}$ and NA 0.2. The light beam then propagates in the 10 cm long waveguide and is deflected at the TIR mirror. The out-of-plane coupled light signal is detected with either a round flat detector having diameter $70\mu\text{m}$ or $200\mu\text{m}$, or with an optical fiber with core diameter $100\mu\text{m}$ and NA 0.29. The Truemode waveguides have a cross-section of $50\mu\text{m} \times 50\mu\text{m}$ on pitch $125\mu\text{m}$, NA 0.3 and a propagation loss of 0.13dB/cm at 850 nm. The core layer and top and lower cladding layer have a thickness of $50\mu\text{m}$ each. The distance between the input fiber and the input facet of the waveguides and between the detector and the top surface of the optical layer is set to $10\mu\text{m}$.

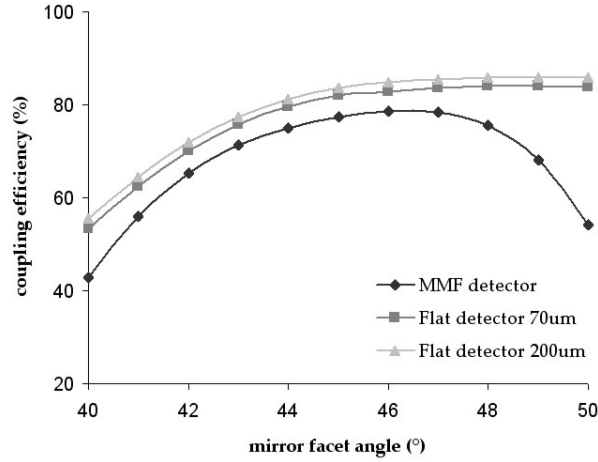


Figure 4.42: Influence of a deviation of the 45° angle of the TIR mirror facet on the link efficiency.

The mirror facet angle β is varied between 40° and 50° . The detector is fixed at the theoretically ideal position, where the centre of the mirror facet is aligned with the centre of the detector. The influence of an angle deviation from 45° on the link efficiency is given in Fig. 4.42. A ray trace plot for a mirror facet angle of respectively 40° , 45° and 50° is given in Fig. 4.43. From these plots, it is clear that in case the mirror facet angle β equals 40° , a considerable amount of rays are lost because they no longer satisfy the condition for total internal reflection. The amount of rays that is lost for this reason is much smaller for mirror facet angles β between 45° and 50° .

We can conclude that the link efficiency decreases with the angle β of the mirror facet, in which case the mirror facet becomes steeper. As was explained in 3.1, the critical angle for TIR is:

- $\theta_c = 39.98^\circ$ for a Truemode core - air interface
- $\theta_c = 78.79^\circ$ for a Truemode core - cladding interface

with θ the angle between the ray and the axis perpendicular to the mirror facet. It is clear that as the facet angle decreases, the number of rays that satisfies the TIR condition $\theta \leq \theta_c$ also decreases and consequently the link efficiency drops. In practice, for the flat detector, this implicates that in case the angle of the mirror facet is within the range $[45^\circ; 50^\circ]$, there is a limited influence on the link efficiency ($\leq 2\%$). The maximum link efficiency of the link is 85.9% in the case that the $200 \mu\text{m}$ square detector is used and 83.8% in the case that the $70 \mu\text{m}$ round detector is used. This maximum link efficiency is obtained for a facet angle of 50° , because of the fact that a maximum amount of rays satisfy the TIR condition in this case and the fact that no NA has been attributed to the flat detectors. For the MMF detector, the situation is slightly different because of the limited acceptance angle, determined by the NA. The maximum link efficiency of the entire link is 78.52% and is obtained for a facet angle of 46° . The tolerance on the mirror facet angle is in this case limited to the range $[45^\circ; 47^\circ]$.

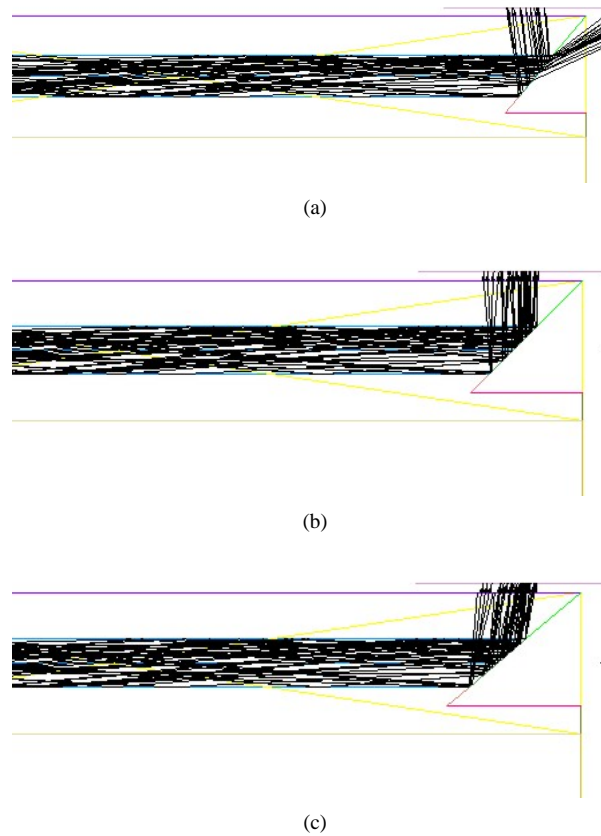


Figure 4.43: (a) Ray trace plot for a mirror facet angle β of 40° . A large amount of rays are lost for not satisfying the TIR condition; (b) ray trace plot for a mirror facet angle β of 45° ; (c) ray trace plot for a mirror facet angle β of 50° .

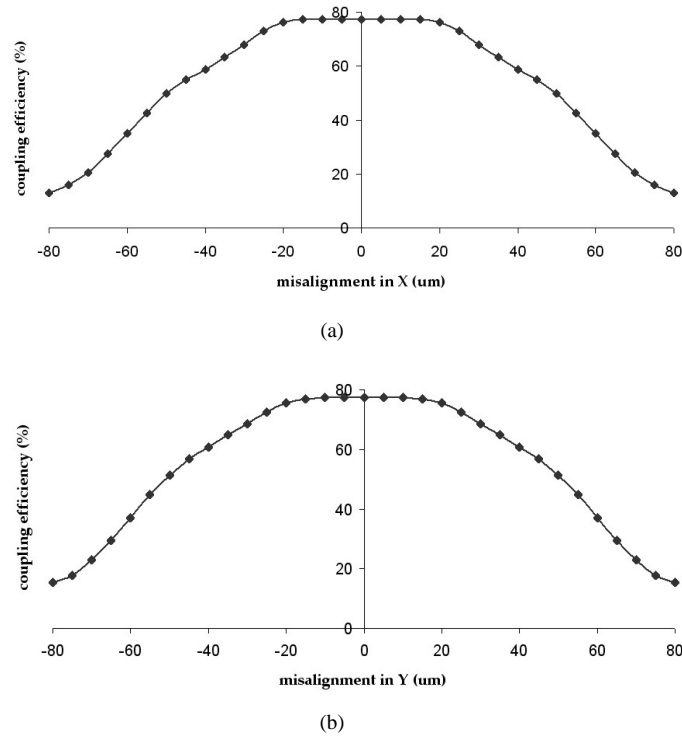


Figure 4.44: (a) Alignment tolerance curve for a mechanical misalignment of the detector fiber in X-direction; (b) alignment tolerance curve for a mechanical misalignment of the detector fiber in Y-direction.

The tolerance for a mechanical misalignment of the MMF detector has been evaluated by shifting the MMF detector around its theoretically ideal position, where the centre of the detector and the centre of the mirror are aligned. The resulting alignment tolerance plot is shown in Fig. 4.7. The shift in X-direction is along the mirror facet, the shift along Y is perpendicular to the mirror facet. The misalignment of the detector fiber in X and Y and the corresponding excess loss are given in Table 4.7. Both alignment tolerance plots are symmetrical around the origin, which is logical because of the build-up of the mirror.

4.3.2 Experimental results

As was the case for the metalized micro-mirrors, the TIR mirrors are ablated into the Truemode optical layer with a tilted KrF excimer laser beam. The tilt angle of the laser beam has to be optimized in order to get a 45° TIR mirror facet. The tapering that occurs during the ablation depends on the laser fluence, the material type, and also on the ablation depth. The tapering angle tends to decrease with increasing ablation depth, making it rather difficult to reproduce the angle of the mirror facet in a very accurate way. In order to increase the angle reproducibility, the mirrors are ablated into

Misalignment in X	excess loss
0.05 dB	$[-20\mu\text{m} ; 20\mu\text{m}]$
0.2 dB	$[-25\mu\text{m} ; 25\mu\text{m}]$
0.5 dB	$[-30\mu\text{m} ; 30\mu\text{m}]$
0.7 dB	$[-35\mu\text{m} ; 35\mu\text{m}]$
1 dB	$[-37\mu\text{m} ; 37\mu\text{m}]$
Misalignment in Y	excess loss
0.1 dB	$[-20\mu\text{m} ; 20\mu\text{m}]$
0.2 dB	$[-25\mu\text{m} ; 25\mu\text{m}]$
0.5 dB	$[-30\mu\text{m} ; 30\mu\text{m}]$
0.7 dB	$[-35\mu\text{m} ; 35\mu\text{m}]$
1 dB	$[-37\mu\text{m} ; 37\mu\text{m}]$

Table 4.7: Misalignment of the detector in X and Y direction around the ideal position and the corresponding excess loss.

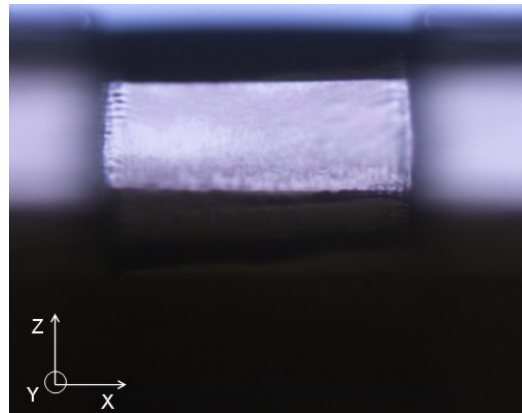
the optical layer with always the same laser parameters and mask dimension. The laser fluence is monitored with an energy meter. The laser fluence and mask size used for the ablation of the TIR mirrors corresponds to the values used for the metalized mirrors. The only parameter that needs to be optimized is the required tilt angle of the excimer laser beam for the ablation of the TIR mirror facet.

It is impossible to measure the surface roughness and angle of the mirror facet with the available equipment because of the build-up of the mirror, which is hidden in the ablated trench. Because the TIR mirrors are ablated with the same laser fluence as the metalized mirror facets, we assume that the surface roughness is comparable. It is very difficult to get an image of the TIR mirror facet. An image of the front view of the TIR mirror facet is shown in Fig. 4.45(a). This picture is taken by ablating the mirror facet at the polished edge of the sample, in such a way that the opposite interface of the ablated trench is over the edge, meaning that the TIR mirror facet is open and can be inspected by putting the sample under a tilted position under the microscope. Since there is no means to measure the mirror facet angle, the tilt angle of the laser beam can only be optimized by carrying out loss measurements on TIR mirrors that are ablated at various tilt angles for given process parameters. The results from these measurements are discussed in the next section. The tilt angle of the laser beam is arranged manually, with the help of a microscrew for fine-tuning, allowing an angle accuracy better than 1° . A picture of the cross-section of an ablated TIR mirror is shown in Fig. 4.45(b).

4.3.3 Characterization

Loss measurements have been carried out on mirrors that were ablated with different tilt angles in an attempt to determine the optimal tilt angle for the ablation of the TIR mirrors. The measurements are carried out on a PI F-206 Hexapod six-axis parallel kinematics robot with a repeatability $0.3 \mu\text{m}$. A picture of the set-up used for the measurements is shown in Fig. 4.46.

The detected output power is very low for mirror facet angles that differ too much from 45° , because of the limited acceptance angle of the detector fiber and also because of



(a)



(b)

Figure 4.45: (a) Front view of a TIR mirror facet, ablated into the Truemode optical layer at the polished edge of a sample; (b) cross-section of a TIR mirror ablated in the Truemode optical layer.

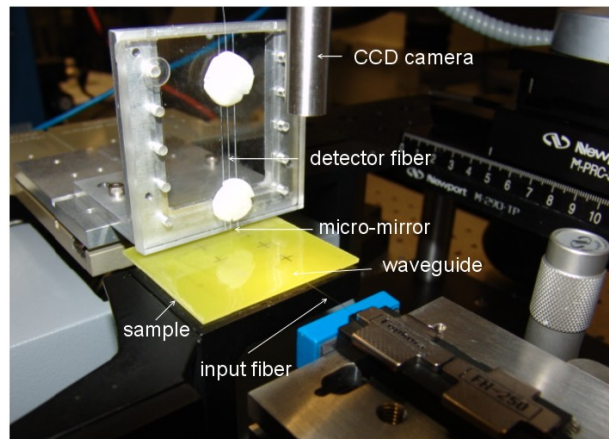


Figure 4.46: Picture of the measurement set-up used for the measurements on the ablated TIR mirrors.

the relatively large amount of light rays that are lost for not satisfying the total internal reflection condition. The tilt angle of the excimer laser beam was gradually increased until the optimum in the detected power was found.

The maximum detected output power has been obtained for the following process parameters:

- excimer laser beam at a tilt angle of 53° ,
- laser fluence of $7.6\text{J}/\text{mm}^2$, measured on the translation stage with an energy meter,
- mask dimension of $800\ \mu\text{m} \times 3000\ \mu\text{m}$, before demagnification
- ablation speed of $125\ \mu\text{m}/\text{s}$, which is lower than the ablation speed used for the ablation of the 45° metalized mirror facet because of the more tilted position of the laser beam.

The performance of the mirror has been evaluated in both a receiver and transmitter configuration. In the receiver configuration, schematically depicted in Fig. 4.47, an 850nm light signal is coupled in horizontally with a GI optical fiber with core diameter $50\ \mu\text{m}$ and NA 0.2 into the multimode waveguide. It then propagates in the $50\ \mu\text{m} \times 50\ \mu\text{m}$ Truemode ablated waveguide with NA 0.3 until it is deflected over 90° at the TIR mirror. The outcoupled light spot is detected with a GI optical fiber with core diameter $100\ \mu\text{m}$ and NA 0.29. The distance between the input fiber and the input facet of the waveguides and between the output facet and the detector fiber is arranged manually with the use of a CCD camera. The optimum measured overall link loss is -2.55dB , corresponding to a link efficiency of 55.6% with a standard deviation of 2.8%. The link loss includes the incoupling at the waveguide input facet, propagation in the 2.5cm long waveguide, 90° beam deflection at the TIR mirror, outcoupling at the output facet and detection with the detector fiber. No in-plane reference measurement was carried out prior to the ablation of the mirror, which makes it difficult to put an exact number on

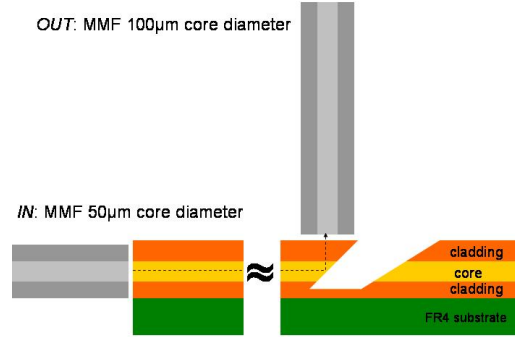


Figure 4.47: Evaluation of the propagation loss of a TIR mirror in a receiver scheme. Light is coupled in horizontally with a $50\mu\text{m}$ core diameter optical fiber with NA 0.2 and is detected vertically with a $100\mu\text{m}$ core diameter optical fiber with NA 0.3.

the mirror coupling loss. If we compare the link loss to the link loss of an ablated waveguide with the same link length, we can assume the mirror coupling loss to be $\leq 1\text{dB}$. This value is better than the results reported in [8], in which case the waveguides have a cross-section of $70\mu\text{m} \times 70\mu\text{m}$ and the outcoupled light detected with a large area detector. In [7], the mirror coupling loss is 0.6dB but no specifications are given on the measurement set-up. In [9], a mirror coupling loss of 0.5dB has been reported. This value is obtained by submitting the ablated mirror to a smoothing step using CO_2 laser. Again no specifications on the measurement set-up are given and the measurements are carried out at a wavelength of 670nm .

The tolerance curve for a mechanical misalignment of the detector fiber is given in Fig. 4.48. The plot is obtained by scanning the detector fiber around its theoretically ideal position, where the detected power reaches a maximum. The plot clearly shows the shape of the light spot that is deflected over 90° at the TIR mirror facet, which is not perfectly circular because of the TIR used for the out-of-plane coupling.

The performance of the TIR mirror in a transmitter scheme has been evaluated on the same demonstrator board by coupling an 850nm light signal in vertically at the TIR mirror facet with a single mode optical fiber SMF-28, which has a core diameter of $8.2\mu\text{m}$ and an NA 0.14. The incoupled light signal is deflected over 90° at the TIR mirror and is coupled into the ablated Truemode waveguide. The light spot that is coupled out horizontally at the output facet of the waveguide is detected with an optical fiber with core diameter $100\mu\text{m}$ and NA 0.29. The optimum measured link efficiency is -1.16dB , which is much lower than the link loss measured in the receiver scheme. This is logical because of the fact that the detected power in the receiver scheme is limited by the spreading of the deflected light beam, caused by the large NA of the Truemode waveguides.

As was already mentioned, the mirror is vulnerable to external influence such as moist and dust intrusion and can not be used in a multilayer scheme because this would require the filling of the ablated trench with cladding material, which would deteriorate the mirror function. The application of a Au-coating onto the TIR mirror facet can solve these problems. In the previous section on the metalized mirror, we have seen

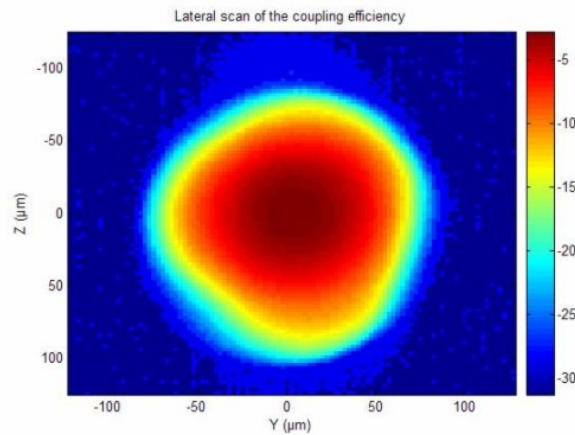


Figure 4.48: (Tolerance for a mechanical misalignment of the detector fiber for the TIR mirror.

that it is possible to get a certain degree of Au-deposition on the TIR mirror facet. However, the TIR mirror is hidden in the ablated trench more than for the metalized mirror configuration because of the 45° angle of the TIR mirror facet. This makes it difficult to get a homogeneous Au-deposition onto the TIR mirror facet.

Loss measurement have been carried out on TIR mirrors ablated into the Truemode optical layer with the above mentioned set-up; the link efficiency was measured in a receiver scheme. After this measurement, a Au-coating was evaporated on the mirror facet by placing the sample in the evaporating unit, covered with a suitable mask. In this mirror configuration, it is very important to avoid the deposition of Au near the output of the deflected light spot. For this reason the alignment of the mask with respect to the TIR mirror interface should be done under a microscope. The link loss was measured again in the same set-up after the evaporation of the Au-coating and remained unchanged with respect to the value measured before the application of the coating. From this we can conclude that there is no or not a sufficiently thick layer of Au deposited onto the TIR mirror facet.

At the laboratory, two different Au-deposition techniques are available: evaporation and sputtering. Au-sputtering should give better coating results because of the lower degree of directivity of the Au-particles. The sample onto which a Au-coating was evaporated is again covered with a mask and this time placed in the sputtering unit. A picture of the Au-coated mirror, after removal of the covering mask, is shown in Fig. 4.49. The sample was measured a third time on the set-up, this time with a sputtered Au-coating on the mirror facet. The measured overall link loss was in this case more than 6dB higher than the value measured before the sputtering step. The spot that was captured by the detector fiber is shown in Fig. 4.50. The plot is obtained by scanning the detector fiber around the position where the link efficiency is maximal. SEM inspection of the mirror facet shows that a periodical micro-structure is formed on the mirror facet during the ablation step, and might explain the enormous loss increase after the Au-coating step. This phenomenon was also described in [9] and might be solved by using a smoothing step with CO_2 laser. SEM images of this micro-structure are shown in Fig. 4.52.

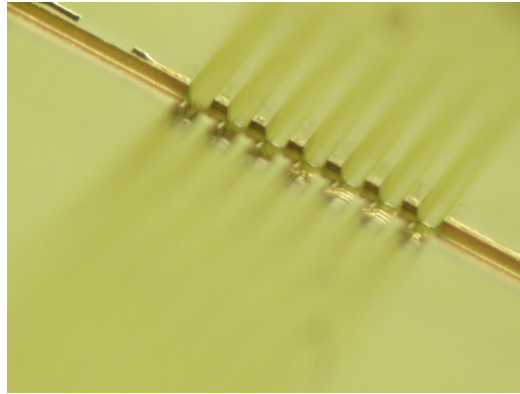


Figure 4.49: (Picture of the Au-coated TIR mirror ablated in Truemode material, after the removal of the mask that is used to cover the sample during the sputtering step.

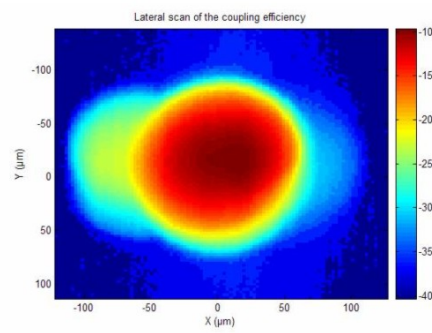


Figure 4.50: Light spot that is deflected over 90° at the metalized TIR mirror facet, captured by the detector fiber.

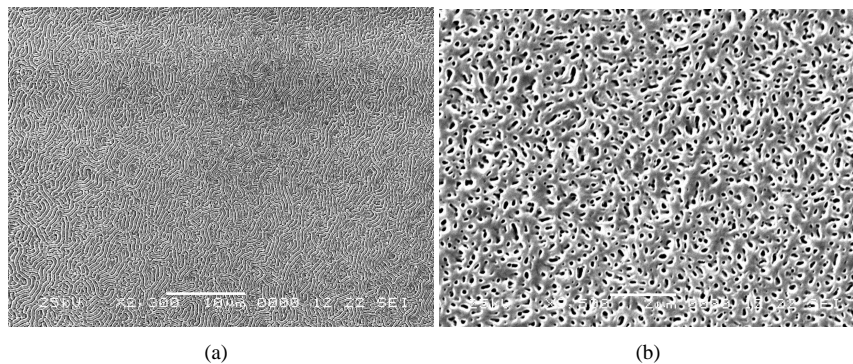


Figure 4.51: (a) SEM image of the micro-structure that is formed in the ablated areas in Truemode material after static ablation; (b) SEM image of the micro-structure that is formed in the ablated area in Truemode material after dynamical ablation.

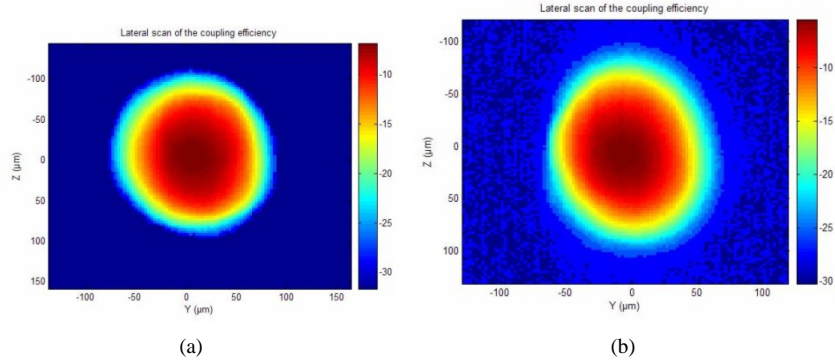


Figure 4.52: (a) Light spot that is detected by the detector fiber after the 90° beam deflection at the TIR mirror in Ormocer material; (b) light spot that is detected by the detector fiber after the 90° beam deflection at the Au-coated TIR mirror in Ormocer material.

The appearance of this micro-structure is only experienced for the Truemode material. The same experiment has been done with mirror ablated into an Ormocer optical layer, containing an array of photolithographically defined waveguides with cross-section $50\mu\text{m} \times 50\mu\text{m}$ and NA 0.27. The surface roughness of the mirrors ablated into the Ormocer material is typically more than the double of the surface roughness measured on mirrors in Truemode material. However, the appearance of a micro-structure is not experienced after the ablation step. The tilt angle of the laser beam has to be slightly adapted in order to get a 45° TIR mirror facet. The mirrors are ablated into the Ormocer layer with a laser fluence of $7.6\text{mJ}/\text{mm}^2$ with the same mask as the one used for the ablation of the TIR mirrors into the Truemode material, but the laser beam is this time tilted under a 51° angle. The tilt angle of the laser beam was again optimized with the use of loss measurements.

The loss measurements have been carried out on the same measurement set-up described before in a receiver scheme. The overall link loss that has been measured before the Au-coating of the mirror facet is -6.61dB . An in-plane reference measurement was carried out prior to the ablation of the TIR mirror. Comparison between the link efficiency measured before and after the ablation of the TIR mirror learns that the mirror coupling loss is 3.1dB . The coupling loss of the TIR mirrors in Ormocer material is much higher than the coupling loss of the TIR mirrors in Truemode material, mainly because of the scattering loss caused by the higher surface roughness. The overall link loss was measured again after the Au-coating of the TIR mirror facet using sputtering. The overall link loss after the Au-coating of the mirror facet is -5.3dB , meaning that the link efficiency of the mirror improved about 1.3dB . However, this still gives a 2.7dB coupling loss per mirror, which is too high for practical applications.

The ablation of TIR mirror in a two layer optical structure can be done in one step, even though the angle of the bottom mirror facet slightly differs from the top facet because of the loss of focus as the ablation depth increases. But again, the susceptibility to dust and moist intrusion can give reliability problems.

4.4 Conclusion

We have discussed the use of KrF excimer laser ablation for the patterning of 45° micro-mirrors into the Truemode optical layer. Two different mirror configurations have been considered: a metalized micro-mirror and a total internal reflection (TIR) mirror. For both configurations, the mirror is directly integrated with the waveguides, which allows high achievable alignment accuracies. The metalized micro-mirror is embedded into the optical layer and in this way protected from external influence such as moist and dust. They can be used in a multilayer optical structure for out-of-plane and inter-plane coupling. The use of KrF excimer laser ablation allows the patterning of mirror facets with a low surface roughness (average of 61 nm RMS on a scan area of $52\ \mu\text{m} \times 174\ \mu\text{m}$). The selective metalization of the mirror facet, without deposition onto the opposite interface, turns out to be a hurdle that can not be overcome.

For this reason, the TIR mirror was studied in more detail. The 90° beam deflection is in this case based on the TIR that occurs at the polymer-air interface. The mirror coupling loss is estimated to be $\leq 1\text{dB}$ and might be improved by submitting the ablated mirror to an additional smoothing step with use of CO₂ laser. Because of the uncovered nature of the mirror facet, this mirror is susceptible to external influence such as moist and dust. In addition, it can not be used in a multilayer structure. These problems can be solved by applying a Au-coating on the mirror facet and the filling of the ablated trench with cladding material. The performance of the mirror after the metalization of the mirror facet is much higher than before. The metalization of the TIR mirror facet is again the limiting step. It turns out to be impossible to get a homogeneous coating on the mirror facet. SEM inspection of the mirror facet shows that a periodical micro-structure is formed on the mirror facet during the ablation step, and might explain the enormous loss increase after the Au-coating step. A smoothing step with use of CO₂ laser might again solve this problem.

Bibliography

- [1] A. L. Glebov, J. Roman, M. G. Lee, K. Yokouchi, "Optical Interconnect Modules With Fully Integrated Reflector Mirrors," *IEEE Phot. Techn. Letters*, Vol. 17, No. 7, pp. 1540-1542, 2005
- [2] Y. Ishii, S. Koike, Y. Arai, Y. Ando, "SMT-compatible optical I/O chip packaging for chip-level optical interconnects," *Proc. ECTC*, 2001
- [3] M. Kagami, A. Kawasaki, H. Ito, "A Polymer Optical Waveguide With Out-of-Plane Branching Mirrors for Surface-Normal Optical Interconnections," *IEEE Journal of Lightwave Technology*, Vol. 19, No. 12, pp. 1949-1955, 2001
- [4] J.-H. Kim, R. T. Chen, "A Collimation Mirror in Polymeric Planar Waveguide Formed by Reactive Ion Etching," *IEEE Phot. Techn. Letters*, Vol. 15, No. 3, pp. 422-424, 2003
- [5] J.-S. Kim, J.-J. Kim, "Fabrication of multimode polymeric waveguides and micromirrors using deep X-ray lithography," *IEEE Phot. Techn. Lett.*, Vol. 16, No. 3, pp. 798-800, 2004

- [6] N. Destouches, D. Blanc, J. Franc, S. Tonchev, N. Hendrickx, P. Van Daele, and O. Parriaux, "Efficient and tolerant resonant grating coupler for multimode optical interconnections," *Optics Express*, Vol. 15, No. 25, pp. 16870-16879
- [7] T. G. Lim *et al.*, "Demonstration of high frequency data link on FR4 printed circuit board using optical waveguides," *Proc. ECTC*, pp. 1268-1274, 2007
- [8] J. Trehella, M. M. Oprysko, "Total internal reflection mirrors fabricated in polymeric optical waveguides via excimer laser ablation," *Proc. SPIE*, Vol. 1377, pp. 66-72, 1990
- [9] T. Matsushima *et al.*, "Development of micro-mirrors in optical-electrical printed wiring boards using excimer laser," *Proc. SPIE*, Vol. 6459, 64590A-1, 2007
- [10] M. Born, E. Wolf, "Principles of optics," *Cambridge University Press*, 1999
- [11] C. A. Harper, "Electronic packaging and interconnection handbook," *McGraw-Hill handbooks*, fourth edition, ISBN 0-07-143048-2
- [12] C. Debaes *et al.*, "Deep proton writing: a rapid prototyping polymer micro-fabrication tool for micro-optical modules," *New Journal of Physics*, Vol. 8, No. 11, 270, 2006.
- [13] J. Van Erps, "Interfacing micro-components for optical interconnections from the FTTH-level to the PCB-level," *PhD thesis*, Vrije Universiteit Brussel, 2008.

Chapter 5

Discrete coupling structures

5.1 Introduction

In the previous chapter, we have discussed the use of ablated micro-mirrors, which are directly integrated into the optical waveguides. The metallization of the mirror facet however turned out to be the most difficult step and the limiting factor on the mirror performance. Since coupling structures are crucial for the adoption of optical interconnections at the board-level, alternatives are sought-after. One alternative is that instead of integrating the micro-mirror directly with the optical waveguides, discrete coupling elements, which are inserted into a micro-cavity in the optical layer in a separate step, can be used. We will look at both a pluggable approach, in which case the discrete coupler is plugged into a micro-cavity in the optical layer, and an embedded approach, in which case the discrete coupler is embedded in the optical layer after insertion into a cavity in the optical layer.

The pluggable couplers contain a 45° micro-mirror that is used for the 90° beam deflection and are patterned into a poly methyl metacrylate (PMMA) plate using Deep Proton Writing (DPW) [1] [2]. The patterned components have a very low surface roughness, which makes them interesting for optical applications because of the limited amount of scattering at the interfaces. Main drawback is the low glass transition temperature T_g of about 100° , which limits the temperature range into which the optical and mechanical properties of the material are guaranteed. The DPW inserts can be replicated in a high-quality plastic with a higher thermal stability using a micro-injection moulding or hot embossing step [3], in this way circumventing the temperature restraint of PMMA. It should be pointed out that these discrete coupling elements can also be patterned with use of other fabrication technologies and in other types of materials, such as the grinding and polishing process that can be used for the fabrication of glass 45° mirror inserts [4], which exhibit superior thermal and mechanical behaviour than PMMA. Main reason for using the DPW-inserts is the availability of these components through close collaborations with the department of photonics and applied optics (FIRW-TONA) at Vrije Universiteit Brussel.

In the following sections, we will first look at the use of pluggable couplers that can be used for both out-of-plane and inter-plane coupling. The fabrication of the demonstrator boards and the insertion process are discussed and the performance of the pluggable

couplers is evaluated with loss measurements. Next, we will discuss the use of an embedded mirror. The embedding process is discussed in detail and the discrete coupler characterized. The performance of the embedded mirror is evaluated with loss measurement and compared to the results obtained for the pluggable coupler.

5.2 Pluggable couplers

The pluggable couplers are inserted into a micro-cavity in the optical layer and can be used in a single layer or multilayer optical structure for inter-plane and out-of-plane coupling. In the following sections, we will first discuss the use of an out-of-plane coupler, which can be used in a single layer and multilayer structure. The performance of the out-of-plane coupler in a single layer structure is evaluated with loss measurements. Next, we will look at the use of inter-plane couplers, used to couple a light signal from the bottom/top layer to the top/bottom layer in a two layer optical structure. We will not go into detail on the fabrication of the components, but put the focus on their practical use and evaluate their performance. We refer to [5] for details on the optimization of the design and the patterning of the components.

5.2.1 Out-of-plane coupler

The considered out-of-plane coupling configuration is schematically shown in Fig. 5.1. The light beam that propagates in the optical waveguide is deflected over 90° , out of the plane of the optical layer, at the 45° micro-mirror, based on the TIR that occurs at the PMMA-air interface. The deflected light spot then propagates in the PMMA until it reaches the flat top exit facet of the coupler and is captured with a detector, this being the receiver configuration. It is of course also possible to couple a light signal in vertically at the flat top with an optical fiber or VCSEL and deflect the light beam over 90° towards the multimode waveguides, which is the transmitter configuration.

The DPW coupler contains a 45° micro-mirror with a height and width of $140 \mu\text{m}$. It has a fixed thickness of $500 \mu\text{m}$, in the direction perpendicular to the optical waveguides, in correspondance with the thickness of the used PMMA substrates. The thickness of the PMMA on top of the mirror, the distance between the top of the mirror facet and the flat top, is preferably as small as possible, in order to limit the diffraction of the light spot during the propagation in the PMMA. On the other hand, the coupler is intended to be plugged into a micro-cavity in the optical layer, which implies that the component has to be mechanically stable in order not to break during the plugging step. For this reason, the central region of the PMMA layer is thinner than at the edges, in this way guaranteeing the mechanical stability. The edges are used to position the component on top of the optical layer, with the mirror into the cavity. The main dimensions of the pluggable coupler are given in Fig. 5.2(a). A picture of a prototyped version of the pluggable coupler is shown in Fig. 5.2(b).

The coupler has been designed for out-of-plane coupling in a demonstrator board that contains a Truemode optical layer containing multimode waveguides with cross-section $50 \mu\text{m} \times 50 \mu\text{m}$ on pitch $125 \mu\text{m}$ and NA 0.3. The large NA of the waveguides causes a considerable amount of spreading of the light spot during the propagation in the PMMA from the mirror facet to the flat top and limits the TIR performance. The increasing spot size can become a problem at the detector side. The use of micro-lenses to collimate or

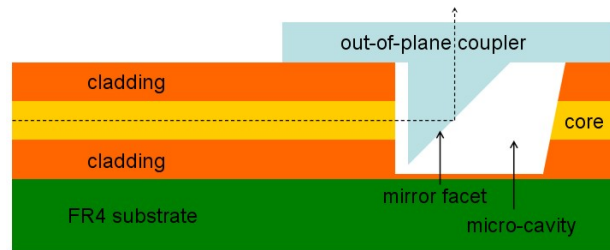


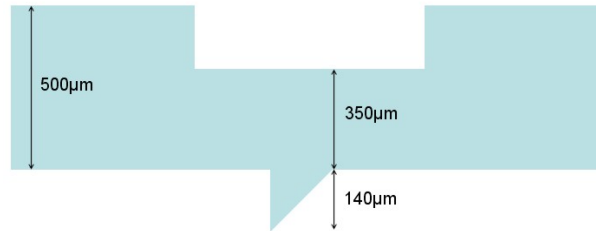
Figure 5.1: Schematic of a DPW out-of-plane coupler which is inserted into an ablated micro-cavity in the optical layer for 90° beam deflection, out of the plane of the optical layer.

focus the beam can ease the coupling of the deflected light signal into for instance an optical fiber or surface-mounted opto-electronic device. Micro-lenses can be directly integrated in the coupler [6], allowing the use of a compact coupling element with a high coupling efficiency. In Fig. 5.3, a picture is shown of an out-of-plane coupler with an integrated cylindrical micro-lens.

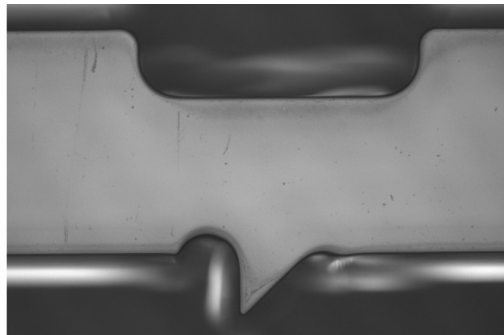
Surface roughness measurements have been carried out on the mirror facet and the flat top exit facet of the coupler with a non-contact optical profiler. The mirror facet has an average RMS surface roughness of $13.4\text{nm} \pm 2.6\text{nm}$; the exit facet has an average RMS surface roughness of $12.5\text{nm} \pm 3.2\text{nm}$, both measured on a scan area of $58\ \mu\text{m} \times 46\ \mu\text{m}$. This is about four times lower than the optimal value obtained for the laser ablated mirror facets in Truemode material and explains the interest in these discrete couplers. A micro-cavity is ablated into the Truemode optical layer with KrF excimer laser to accommodate the pluggable coupler. If the ablation is done with the excimer laser beam perpendicular to the sample, the walls of the micro-cavity are typically at a facet angle of 10° - 15° , in accordance with the tapering that occurs during the ablation. Light rays propagating in the optical waveguide that hit the polymer-air interface are refracted at this interface, according to Snell's law of refraction. The graphical relation between the angle of the entering ray α_1 and the angle of the refracted ray α_2 is depicted in the graph in Fig. 5.4(a). From this graph, the importance of the vertical output facet of the waveguides becomes obvious, mainly because of the large refractive index difference between the polymer material and air. The tapering angle is typically in the range 10° - 15° . From the graph, we can see that for these angles α the refracted central ray will propagate at an angle of 15° - 23° with respect to axis perpendicular to the polymer-air interface, as is schematically shown in Fig. 5.4(b). In addition, the use of a vertical cavity wall allows minimization of the distance between the coupler and the output facet of the waveguides.

The micro-cavity is ablated into the optical layer with the following parameters:

- pulse intensity: $7.6\text{mJ}/\text{mm}^2$, measured on the translation stage with an energy meter
- mask $3000\ \mu\text{m} \times 3000\ \mu\text{m}$, before demagnification
- ablation speed: $230\ \mu\text{m}/\text{s}$, providing a cavity with a depth of $170\ \mu\text{m}$



(a)



(b)

Figure 5.2: (a) Dimensions of the prototyped out-of-plane coupler. The thickness of the PMMA on top of the mirror is in the central zone, where the light spot is coupled out or in, thinner than at the edges. This is done to minimize the propagation distance between the mirror facet and the flat top exit facet without affecting the mechanical stability of the coupler; (b) optical microscope image of a prototyped out-of-plane coupler.

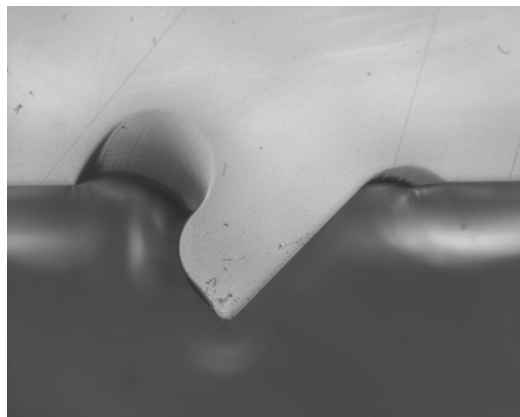


Figure 5.3: Picture of an out-of-plane coupler with an integrated cylindrical micro-lens.

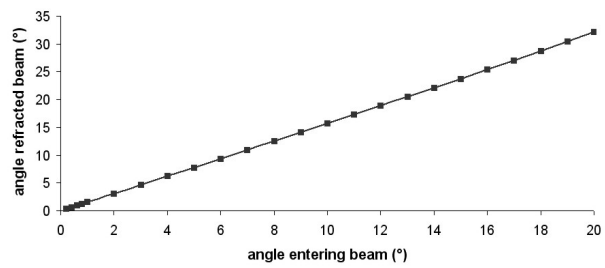
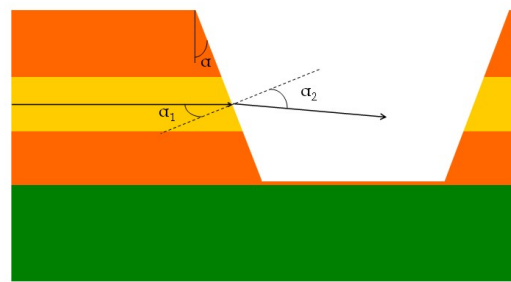


Figure 5.4: (a) Schematic of a micro-cavity ablated with the laser beam perpendicular to the laser source; (b) graphical relation between the angle α_1 of the entering ray and the angle α_2 of the refracted ray.

The excimer laser beam is tilted at an angle of 12° in order to obtain a vertical cavity wall, used as waveguide output facet. The optimization of the tilt angle of the laser beam has been done by ablating cavities at different tapering angles ranging from 5° to 15° at the edge of a sample with polished end facets, and measuring the facet angle with an optical microscope. The vertical angle can not be controlled with stylus profiler measurements because of the physical size of the needle tip. The $170\ \mu\text{m}$ depth of the ablated cavity is larger than the thickness of the $150\ \mu\text{m}$ thick optical layer. An extra lower cladding layer is applied to give some extra vertical distance between the bottom of the mirror facet and the cavity bottom when inserting the component into the cavity. The tilted position of the laser beam implies that the cavity bottom is not flat but also tilted. The $170\ \mu\text{m}$ thickness is measured at the side of the vertical wall, where the cavity depth is the lowest.

The pluggable coupler is inserted manually in the laser ablated micro-cavity by means of a tweezer. The manual insertion process is used here because of the fact that we are making demonstrator boards that serve as a prototype. It is clear that in real applications, pick-and-place equipment can be used to insert the component in the micro-cavity in an accurate way. The position of the coupler in the cavity is optimized with a CCD camera, positioned on the set-up perpendicular to the sample. The air gap that exists between the vertical output facet of the waveguides and the input facet of the coupler should be minimized by pushing the coupler as close as possible to the vertical wall in order to optimize the coupling efficiency between the waveguide and the coupler. A small air gap will however remain, even after optimization of the position of the coupler. This can be solved with the use of index matching gel, which can be used to fill up the air gap between the vertical wall and the coupler. The filling of the ablated cavity or the deposition of gel onto the mirror facet should be avoided since this will affect the mirror performance, except for the case in which a metal coating is applied on the mirror facet.

Because of the tilted laser beam position during the ablation, the cavity bottom is not flat but slightly angled, in accordance with the tilt angle of the laser beam. The cavity depth is the lowest at the side of the vertical wall and the depth increases as we move further away from the vertical wall. This is however not a problem if the cavity is ablated deep enough. The initial alignment of the coupler with respect to the waveguide output facet however has to be done with the necessary caution in order not to damage the mirror facet when touching the cavity bottom. In the experiments, this problem has been solved with the use of an extra lower cladding layer, meaning that the cavity can be ablated deeper into the optical layer, allowing to move the coupler across the cavity without damaging the mirror facet.

The coupler rests on the top surface of the optical layer after the plugging step, meaning that planarity of the optical layer is required in order not to induce an angular misalignment. Measurements show that the tilt angle of the top surface is $\leq 1^\circ$ in the zone next to the ablated cavity, that supports the coupler. This should be sufficient for good coupling performance and will be controlled in the next paragraph with loss measurements.

Coupling efficiency measurements

Loss measurements have been carried out to evaluate the performance of the pluggable out-of-plane coupler. The component is first characterized in a fiber-to-fiber scheme.

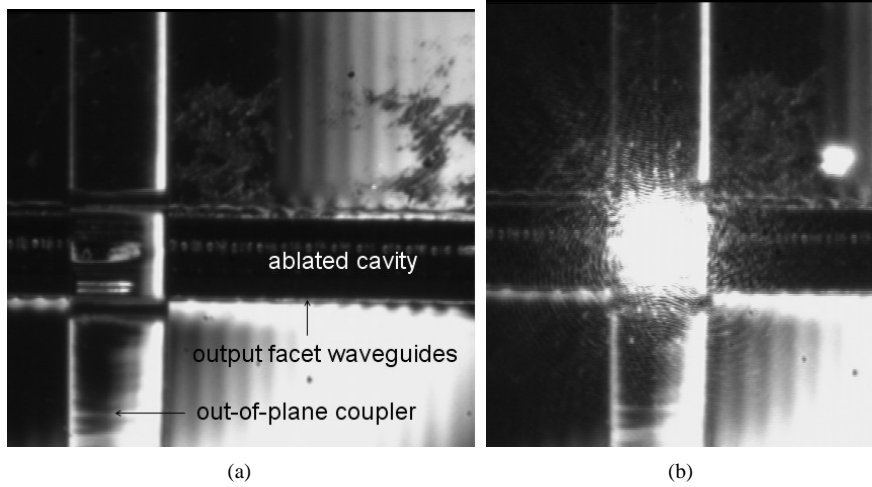


Figure 5.5: (a) Picture of the top view of the out-of-plane coupler, plugged into the laser ablated cavity; (b) picture of the light spot coupled out-of-plane at the mirror facet.

A $50\ \mu\text{m}$ core diameter optical fiber with NA 0.2 is used as input fiber; a $100\ \mu\text{m}$ core diameter optical fiber with NA 0.29 is used as detector fiber. A hexapod 6-axis motion robot is used for the measurements, allowing the positioning of the detector fiber with an accuracy of 300 nm and to perform two-axis scans to measure the tolerance for mechanical misalignments of the detector fiber. The position of the input fiber is optimized manually with the help of a red light source. The input fiber is butt-coupled at the input of the 45° mirror; the detector fiber is placed vertically at the flat top exit facet of the coupler to capture the light spot that is deflected at the mirror facet. Coupling efficiencies as high as 83.7% have been measured, corresponding to a coupling loss of 0.77dB. The tolerance for a mechanical misalignment of the detector fiber is measured to be $\pm 26\ \mu\text{m}$ for a 1dB excess loss. The low coupling loss confirms the excellent optical quality of the out-of-plane coupler.

The pluggable coupler is in next step inserted into a micro-cavity in the optical layer of a demonstrator board consisting of an FR4 substrate onto which a Truemode optical layer is integrated that contains arrays of multimode waveguides with cross-section $50\ \mu\text{m} \times 50\ \mu\text{m}$ on pitch $125\ \mu\text{m}$ and NA 0.3. The lower cladding layer has a thickness of $100\ \mu\text{m}$, in order to be able ablate the cavity up to a depth of $170\ \mu\text{m}$ without ablation of the FR4 substrate. Moreover, in this way we have about $30\ \mu\text{m}$ margin between the bottom of the mirror and the bottom of the cavity when inserting the coupler. The out-of-plane coupler is plugged into the cavity manually by means of a tweezer. A picture of the top view of the out-of-plane coupler, plugged into the laser ablated cavity is shown in Fig. 5.5 for the case where the light source is turned off respectively on.

An 850nm light signal is coupled in horizontally into the waveguide with a $50\ \mu\text{m}$ core optical fiber with NA 0.2, propagates in the 5 cm long ablated Truemode waveguides and is deflected over 90° at the mirror facet. The vertically outcoupled light spot is detected with an optical fiber with core diameter $100\ \mu\text{m}$ and NA 0.29. The air gap between the output facet and the detector fiber is optimized with use of a CCD camera

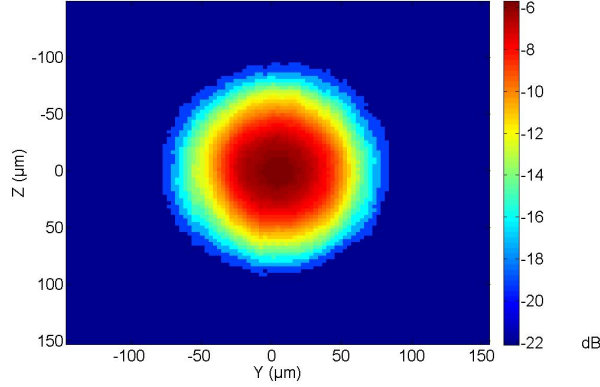


Figure 5.6: Plot of the light spot that is coupled out at the out-of-plane coupler in a receiver configuration, using the demonstrator board with the ablated Truemode waveguides and the ablated micro-cavity for the insertion of the pluggable coupler.

and is assumed to be a couple of tens of microns maximum. The measured coupling efficiency over the entire link is -5.69dB , corresponding to a coupling efficiency of 27.1%. This includes the in-plane butt-coupling from the input fiber to the PCB integrated waveguides, propagation in the 5 cm long waveguides, coupling towards the out-of-plane coupler, 90° beam deflection at the TIR mirror facet of the pluggable coupler, and outcoupling towards the detector fiber. The light spot that is captured with the detector fiber is shown in Fig. 5.6. The tolerance for a mechanical misalignment of the detector fiber for an excess loss of 1dB is $\pm 26 \mu\text{m}$.

The overall coupling efficiency is lower than expected, viewing the excellent coupling efficiency of the pluggable coupler in a fiber-to-fiber scheme. We should however take into account that the input fiber in the latter has NA 0.2 as opposed to NA 0.3 of the Truemode waveguides. The high NA of the Truemode waveguides is responsible for the relatively large portion of the incoupled light signal that is not deflected at the mirror facet because of not satisfying the condition for total internal reflection and the large degree of spreading during the propagation in the PMMA prior to reaching the exit facet. This is confirmed by carrying out loss measurements in a transmitter configuration. An 850nm light signal is coupled in vertically at the out-of-plane coupler with a standard single mode optical fiber SMF-28. The deflected light signal propagates in the multimode waveguide until it is coupled out at the output facet of the waveguides (corresponding to the input facet in the receiver configuration). The outcoupled light spot is captured with an optical fiber with core diameter $100 \mu\text{m}$ and NA 0.29. The overall link efficiency is in this case 3dB, corresponding to a coupling efficiency of 50%. The tolerance for a mechanical misalignment of the SMF-source for an excess loss of 1dB is $\pm 16 \mu\text{m}$.

The coupling efficiency in the receiver configuration can be improved by applying a sufficiently thick Au-coating on the mirror facet, this way forcing the 90° beam deflection at the mirror facet, or with the use of a curved mirror [7] [8] instead of a straight mirror facet. The curved mirror can collimate the beam upon reflection, and hence limit the spreading of the light spot that is coupled out of the waveguide. The main drawback

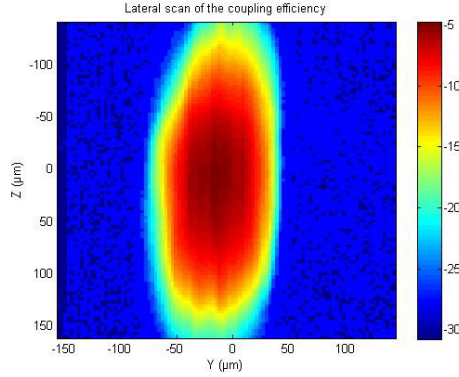


Figure 5.7: Plot of the light spot that is coupled out at the enhanced out-of-plane coupler. From this plot it is clear that the cylindrical micro-lens collimates the light beam in one direction.

of the use of the curved mirror is the fact that the centre of the waveguide core and the focal point of the curved mirror have to be aligned with respect to each other. As was already discussed, there is always an uncertainty of $\pm 5 \mu\text{m}$ on the layer thickness of the Truemode layers because of the low spinspeed that is used for the application of the layers. This limits the achievable accuracy and thus coupling efficiency. Measurements have been carried out with an enhanced out-of-plane coupler, which contains a curved micro-mirror and an integrated cylindrical micro-lens at the exit facet. We refer to [8] for more details on the enhanced pluggable coupler.

The enhanced coupler is plugged into the same demonstrator board than the one used for the measurements on the standard component. The measured overall link loss is in this case -4.7dB , corresponding to a coupling efficiency of 33.9%. This is about 1dB better than the value obtained with the standard coupler, but can probably be improved even more in case the curved mirror design is adapted to the actual layer thickness of the core and cladding layer. A cylindrical micro-lens at the top or exit facet of the coupler can focus the light spot that is coupled out at the exit facet in one direction, as can be clearly seen in the plot of the light spot that is captured with the detector fiber, shown in Fig. 5.7. The tolerance for a mechanical misalignment of the detector fiber is $\pm 20 \mu\text{m}$ in the direction where the light is collimated and $\pm 40 \mu\text{m}$ in the opposite direction. This measurement demonstrates the potential of adapting the mirror design for a targetted application. The measurement results are summarized in Table 5.1.

A flat cavity bottom can in some cases be desirable, and can be achieved by applying a thin Cu-layer underneath the optical layer onto the substrate. The Cu layer is not ablated by the excimer laser in contrast to the optical layer and as such serves as a selective ablation stop layer, delivering a flat cavity bottom. The main constraint is the fact that the Cu layer thickness should be at least $4 \mu\text{m}$ to serve as an ablation stop layer. The cavity can in this case be ablated through the entire optical layer, without ablation of the FR4 substrate, with the associated debris deposition. In addition, the initial alignment of the coupler with respect to the waveguides will not be as critical as is the case for the tilted cavity bottom since the mirror facet can be damaged when touching the cavity bottom.

fiber-to-fiber scheme 83.7%	0.77dB
Demonstrator board in receiver scheme 27.1%	5.69dB
Demonstrator board in transmitter scheme 50%	3dB
Demonstrator board in receiver scheme with enhanced coupler 33.9%	4.7dB

Table 5.1: Overview of the measurement result obtained for the pluggable out-of-plane coupler.

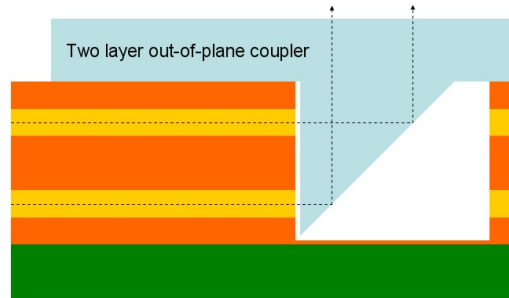


Figure 5.8: Schematic showing the insertion of an out-of-plane coupler in a two layer optical structure. The right wall of the cavity is in this drawing vertical, whereas experimentally it is in a tilted position, in correspondance with the tilt angle of the laser beam.

The out-of-plane coupler can be used in a multilayer optical structure without much change to the original mirror design. The main change is the mirror length and width, which have to be increased to cover the different optical layers. It is clear however that as the number of layers increases, the propagation distance in the PMMA also increases. This means that the light spot will spread even more than for the single layer out-of-plane coupler. The principle of the insertion of an out-of-plane coupler in a two layer optical structure is schematically shown in Fig. 5.8.

A picture of a first prototyped two layer out-of-plane coupler is shown in Fig. 5.9. In view of the increased path length in comparison to the single layer out-of-plane coupler and to avoid cross-talk between the upper and lower channel, cylindrical micro-lenses with a radius of curvature of $50 \mu\text{m}$ are integrated at the input of the coupler to ensure collimation, in one direction, of the beam emitted by each waveguide layer. The mirror has a length of $300 \mu\text{m}$, the pitch between the upper and lower channel is $175 \mu\text{m}$. Measurements were carried out in a fiber-to-fiber scheme, similar to the measurements on the single layer out-of-plane coupler, indicate coupling losses of 1.63dB for the upper channel and 1.24dB for the lower channel. Cross-talk between the upper and lower channel was measured to be smaller than -30dB. The component has not yet been characterized in a demonstrator board, as has been done for the single layer out-of-plane coupler.

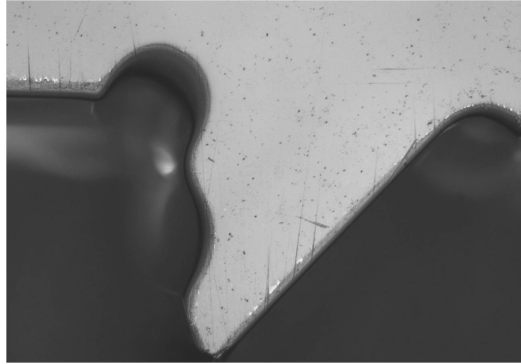


Figure 5.9: Picture of a first prototyped two layer out-of-plane coupler with integrated cylindrical micro-lenses to collimate, in one direction, the light beam emitted by the upper and lower channel and to avoid cross-talk between the two channels.

5.2.2 Inter-plane coupler

In a multilayer optical structure, besides out-of-plane coupling, inter-plane coupling is required to efficiently route the light signals across the board. We study a two layer optical structure, where each optical layer contains arrays of multimode waveguides. Two inter-plane coupling configurations can be considered, as schematically shown in Fig. 5.10. The inter-plane coupling requires a double 90° bend, which can be done using two 45° micro-mirrors. The 90° beam deflection relies on the TIR at occurs at the PMMA-air interface. The orientation of the two mirrors with respect to each other determines whether or not the propagation direction is maintained or shifted over 180° . In Fig. 5.10(a) the light beam is coupled from a waveguide in the bottom layer to the corresponding waveguide in the top layer or vice versa from the top to the bottom layer, with conservation of the propagation direction. The centre of both 45° mirrors are aligned with respect to each other and are oriented in the same way. In Fig. 5.10(b) the propagation direction is turned over 180° . The centre of the mirror facets of the two 45° micro-mirrors are aligned with respect to each other and are oriented in the opposite way, meaning that the mirror of the top layer is rotated over 90° with respect to the mirror in the top layer.

Pictures of the first prototyped inter-plane couplers are shown in Fig. 5.11. The prototyped couplers have been designed for insertion in a two layer optical structure where the spacing between the two core layers is $165 \mu\text{m}$. The propagation length in the PMMA is preferably as low as possible in view of the large NA of the Truemode waveguides. The achievable spacing between both layers is mainly determined by the size of the proton beam that is used for the patterning of the component. Loss measurements have been carried out at 850nm on the inter-plane coupler with conservation of the propagation direction in a fiber-to-fiber scheme. A multimode optical fiber with core diameter $50 \mu\text{m}$ and NA 0.2 was used at the input and a $100 \mu\text{m}$ core diameter optical fiber with NA 0.3 at the output. A coupling loss of 1.6dB has been measured, corresponding to a coupling efficiency of 70%. This can probably be improved by applying a Au-coating on the mirror facet, even though the application of the Au onto the vertical mirror facet will not be very straightforward, if not impossible, and by de-

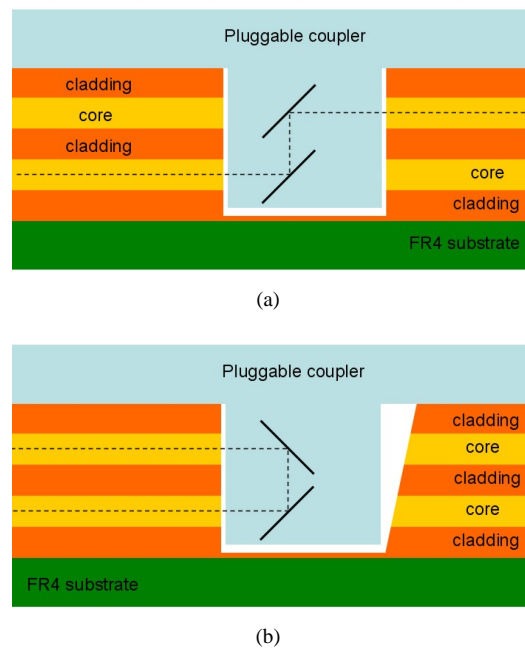
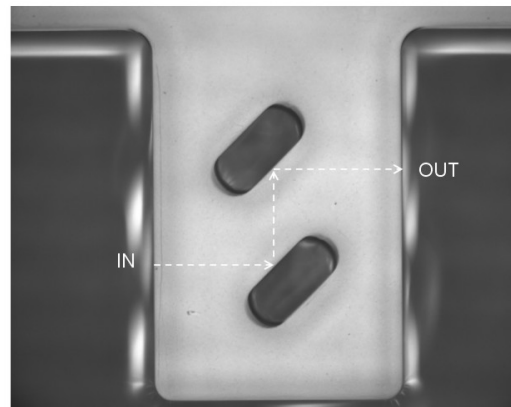
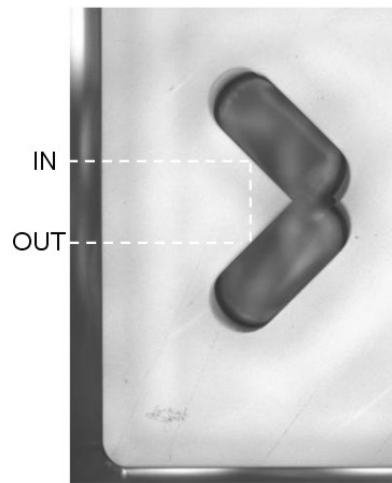


Figure 5.10: (a) Schematic principle of the inter-plane coupler that can be used to couple a light signal from a waveguide in the top layer to the corresponding waveguide in the bottom layer and vice versa with conservation of the propagation direction; (b) schematical principle of the inter-plane coupler that can be used to couple a light signal from a waveguide in the top layer to the corresponding waveguide in the bottom layer and vice versa with a 180° shift in propagation direction.



(a)



(b)

Figure 5.11: (a) Picture of a prototyped inter-plane coupler that can be used to couple a light signal from a waveguide in the top layer to the corresponding waveguide in the bottom layer and vice versa with conservation of the propagation direction; (b) picture of a prototyped inter-plane coupler that can be used to couple a light signal from a waveguide in the top layer to the corresponding waveguide in the bottom layer and vice versa with a 180° shift in propagation direction.

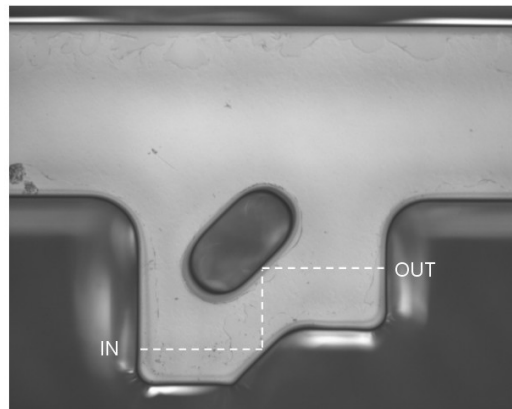


Figure 5.12: Picture of the enhanced inter-plane coupler with conservation of the propagation direction. This mirror design makes it easier to insert the coupler into the micro-cavity without damaging the component because of the increased margin between the bottom of the cavity and the bottom of the mirror.

creasing the spacing between the two core layers. The tolerance for an excess loss of 1dB for a mechanical misalignment of the detector fiber is $\pm 25 \mu\text{m}$.

The inter-plane coupler can be plugged into a laser ablated cavity in the optical layer. For the inter-plane coupler with conservation of the propagation direction, the cavity should contain two vertical walls. One vertical wall is used as waveguide output facet, the other one as waveguide input facet for the light spot that is outcoupled at the output facet of the coupler. The width of the cavity should be in correspondance with the width of the coupler, in order to minimize the propagation in air. The cavity has to be ablated in two steps: in a first step one vertical wall is ablated with the tilted excimer laser beam; in a second step, the sample is rotated over 180° for the ablation of the second vertical wall. The best approach here is to foresee a Cu-layer on the FR4 substrate in the area where the cavity will be ablated. In this way, the ablation can be done down to the Cu-layer, providing a cavity with a flat bottom. The pluggable coupler design has been optimized for insertion into the optical layer, as is shown in the picture in Fig. 5.12. This mirror design makes it easier to insert the coupler into the micro-cavity without damaging the component because of the increased margin between the bottom of the cavity and the bottom of the mirror.

For the inter-plane coupler with reversal of the propagation direction the cavity has to contain only one vertical wall, in view of the fact that the vertical wall is both used as waveguide input and output facet. Loss measurements have not been carried out on this inter-plane coupler because of the fact that it is physically impossible to position the input and output fiber at the same side of the component with the current design because of the vertical channel spacing.

The inter-plane couplers have so far not been evaluated in a demonstrator board but these tests are planned in the near future. It has however been demonstrated that the components can be used for inter-plane coupling.

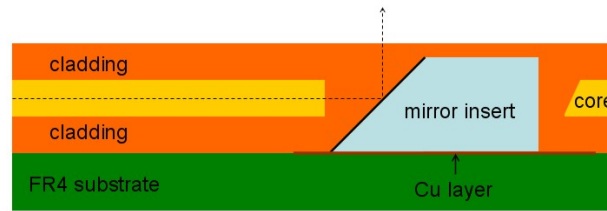


Figure 5.13: Operation principle of a mirror insert embedded into a cavity in the PCB: the light propagating in the optical waveguide is coupled out of the plane of the optical layer by means of a 90° deflection on the Au-coated micro-mirror or vice versa, as illustrated by the dashed arrow.

5.3 Embedded micro-mirror

In the previous section, the use of pluggable coupling structures was discussed. These discrete coupling elements have an excellent optical quality and a low coupling loss. The most important advantage is the fact that its pluggable character allows an easy replacement of the component after failure. The main drawback however is the relatively high excess loss caused after the plugging of the component into the micro-cavity because of the crossing of the different interfaces, with the associated Fresnel loss, the propagation through the relatively thick PMMA layer that is required for the mechanical stability of the coupler and the fact that the top surface of the sample is no longer planarized.

The advantages of the integrated coupling structure, i.e. the high achievable alignment accuracy discussed in the previous chapter, and the discrete coupling structure, i.e. excellent optical quality of the mirror facet, can be combined using a hybrid approach, in which a discrete micro-mirror is embedded into a micro-cavity in the optical layer, which contains an array of multimode waveguides. The principle is schematically shown in Fig. 5.13. A light signal that is coupled into the waveguide, will propagate in the multimode waveguide until it is deflected over 90° at the metallized mirror facet, out of the plane of the optical layer.

The embedded approach has the advantage that the mirror can be embedded in a late stage of processing, making the compatibility with the entire fabrication process unnecessary. This can in some cases be an advantage, especially if the fabrication process requires lamination or soldering steps with the associated high temperature and/or pressure. Because of its embedded character, the mirror is protected from external influence such as moist and dust intrusion. The top surface of the optical layer remains planarized after the embedding of the mirror, allowing the lamination of additional layers, which makes it possible to integrate the optical layer into the PCB.

Simulations have not been carried out on this mirror configuration, in view of the resemblance to the metallized mirror approach. In contrast to the metallized mirror, which is directly integrated in the waveguide, the Au-coating is evaporated onto the mirror facet in a separate step prior to the insertion of the component into the micro-cavity. This has the advantage that the Au-coating on the mirror facet can be controlled before the insertion into the optical layer and that Au-deposition on the waveguide output facet can be avoided. The main limiting factor for the performance of the in-

tegrated metallized micro-mirrors, presented in the previous chapter, can be circumvented in this way. In the next sections, the experimental results are discussed and the characterization of the embedded mirror is presented.

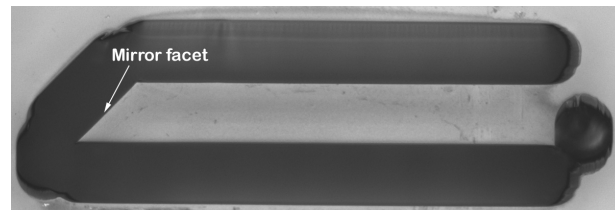
5.3.1 Experimental results

The embedding of the micro-mirror requires three processing steps:

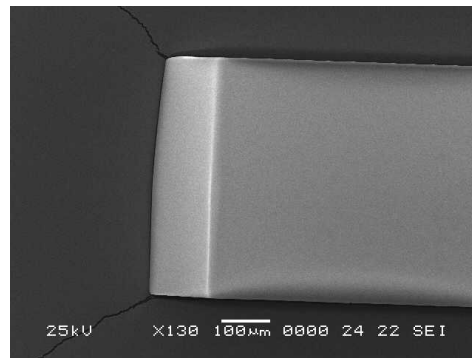
- ablation of a micro-cavity into the optical layer for the insertion of the Au-coated micro-mirror. A flat cavity bottom is required for optimal performance. For this reason, a Cu-island is foreseen on the substrate in the area where the mirrors will be embedded. The Cu-island serves as an ablation stop layer and guarantees the flatness of the cavity bottom.
- deposition of a small amount of adhesive onto the cavity bottom surface for the fixation of the micro-mirror insert into the cavity. The mirror insert is aligned with respect to the output facet of the waveguides, which corresponds to the vertical cavity sidewall.
- filling of the micro-cavity with cladding material using a spincoating step. This way, the air gap between the output facet of the waveguides and the Au-coated mirror facet and the remaining part of the cavity are filled with cladding material. The top surface is planarized, allowing for instance the placement of optoelectronic elements onto the surface of the optical layer or the lamination of additional layers to get a fully integrated structure.

As was the case for the pluggable couplers, presented in the previous section, the micro-mirror insert is patterned with deep proton writing (DPW) into a $500\mu\text{m}$ thick PMMA substrate. The discrete micro-mirror has a length of 1.0 mm , a height of $130\mu\text{m}$ and a width of $500\mu\text{m}$. If desired, the height and length can be adjusted, keeping in mind however the manageability and mechanical stability of the insert. The width is determined by the thickness of the used PMMA substrate and consequently fixed to $500\mu\text{m}$. It is clear that, because of its small dimensions, the handling of the component has to be done with the necessary caution in order not to damage the mirror facet. The pressure that is practised on the top of the component should be limited to an absolute minimum in order to avoid breaking of the component.

In Fig. 5.14(a), an optical microscope picture is shown of the sideview of the mirror insert after the etching step, before it is detached from the PMMA plate. The mirror is attached to the PMMA substrate at only one point and can be removed from the PMMA substrate by pushing the component out of the plate by means of a tweezer. Before fixation of the micro-mirror insert into the laser ablated micro-cavity, a 100-nm thick Au-coating is evaporated onto the mirror facet. In most cases, a thin layer of Ti is evaporated underneath the Au-film to improve the adhesion of the Au-film to the component. Scotch tape tests however indicate that the adhesion of the Au-coating onto the mirror facet is sufficiently good, meaning that the use of a thin layer of Ti underneath the Au-film is not required. The mirror is during the evaporation attached on a low adhesion tape, in order to be able to remove it from the tape after the evaporation step without damaging the mirror facet. The main limitation in the current approach is the $500\mu\text{m}$ width of the micro-mirror, meaning that for arrays with more



(a)



(b)

Figure 5.14: (a) Side view of the mirror insert, before it is detached from the patterned PMMA plate. The mirror is attached to the plate on one single position and can be removed from the PMMA substrate by pushing the back of the insert with a tweezer ; (b) SEM image of the DPW micro-mirror insert confirming the smoothness of mirror facet, as was verified with surface roughness measurements. The cracks that can be seen near the edges of the component are present in the double-sided tape onto which the component is attached.

than 4 waveguides on pitch $125\mu\text{m}$ multiple mirrors have to be placed and aligned next to each other.

The surface roughness of the micro-mirror facet has been measured with a non-contact optical profiler (Wyko NT3300), showing an average RMS surface roughness of $13.4\text{nm} \pm 2.6\text{nm}$, when averaging 5 measurements of an area of $60\mu\text{m} \times 48\mu\text{m}$ at random locations. Fig. 5.14(b) shows a Scanning Electron Microscope (SEM) image of the prototyped 45° micro-mirror insert, confirming the smooth mirror surface. The 45° angle of the mirror has been controlled with stylus profiler measurements, showing an average angle of $44.8^\circ \pm 0.2^\circ$.

The micro-mirror is inserted into a micro-cavity, ablated into the optical layer with a KrF excimer laser. When the micro-cavity is ablated with the excimer laser beam perpendicular with respect to the translation stage and thus the sample, the two interfaces of the ablated cavity are at the tapering angle. It is preferred to have a micro-cavity with a vertical wall at the side of the output facet of the waveguides, corresponding to the side of the cavity where the mirror insert is fixed. In this way, the distance between the output facet of the waveguides and the mirror facet can be minimized, limiting the spreading of the light spot during the propagation in the cladding filled gap.

Because of the tapering that occurs during the ablation, the excimer laser beam has to be tilted under the tapering angle, which is energy and material dependent, in order to obtain a vertical waveguide output facet. In this way, one of the interfaces is under a vertical angle and the other wall under the double tapering angle. The micro-cavity is ablated with the following parameters:

- mask with cross-sectional dimensions of $3050\mu\text{m} \times 3050\mu\text{m}$, before the demagnification.
- excimer laser beam tilted at an angle 12° with respect to the sample, placed horizontally on the translation stage.
- laser fluence: 0.76 J/cm^2 , measured on the translation stage with an energy meter.

A flat cavity bottom is required for optimal performance of the embedded mirror. Planarity of the bottom surface is required to preserve the 45° of the mirror facet: angular misalignment would induce a non-perpendicular out-of-plane coupling and consequently a reduction in coupling efficiency. The angle of the mirror will deviate from 45° for an angled cavity bottom. Since the cavity is ablated with the KrF excimer laser beam under a tilt angle of 12° , the cavity bottom will not be flat if no precautions are taken. For this reason, a $5\mu\text{m}$ to $9\mu\text{m}$ thick Cu-layer is foreseen on the FR4 substrate in the area where the mirrors will be embedded. For thicknesses above $4\mu\text{m}$, the Cu-layer serves as an ablation stop layer for the KrF excimer laser, meaning that the ablation is selectively stopped on the Cu-surface. In this case, the flatness of the cavity bottom corresponds to the flatness of the FR4 substrate. It is clear that the Cu-layer should not be too thick in order not to disturb the light path of the waveguides. Experiments indicate that the waveguide performance is not affected for Cu layer thicknesses below $10\mu\text{m}$. The FR4 substrate suffers from twist and bow, especially if thermal steps are required in the processing. In view of the small dimensions of the mirror insert, this will probably not cause problems. The bottom of the ablated cavity has an average RMS surface roughness of 781nm on a scan area of $0.92\text{mm} \times 1.2\text{mm}$, measured with

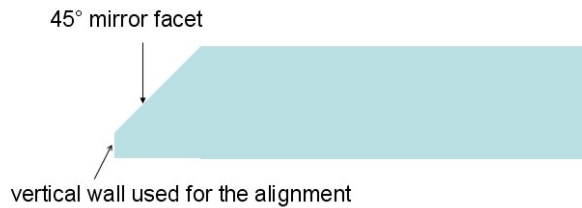


Figure 5.15: Drawing of a mirror insert where part of the mirror facet is vertical, in order to be able to push the insert against the vertical output facet of the waveguides, hereby minimizing the distance between the output of the waveguides and the mirror facet, without damaging the mirror facet.

an optical profiler (Wyko NT3300). The tilt of the bottom of the cavity is $\leq 1^\circ$, which is sufficiently low to guarantee the good performance of the mirror. We refer to 4.2.1 of the previous chapter due to the similar built-up, where simulations indicate that a deviation of $\pm 2^\circ$ on the 45° angle of the mirror facet has a limited influence on its performance.

The insert is attached to the Cu bottom surface of the laser ablated cavity using a drop of thermally curing glue, which is applied onto the Cu-surface by means of a syringe with a fine needle in order to be able to control the amount of glue that is deposited. The glue is spread out away from the vertical waveguide output facet in order to avoid contamination of the output of the waveguides and also of the mirror facet. Pressure is applied on top of the mirror insert with a tweezer in order to push the excess glue away toward the back of the mirror insert. A glue layer with a thickness of typically $5 \mu\text{m}$ to $10 \mu\text{m}$ is left, and is cured subsequently in a convection oven at 150° for 5 minutes.

The alignment between the mirror and the output facet of the waveguides is arranged manually without the use of mechanical alignment features. However, mechanical alignment features and/or fine-placement equipment could be used to increase the alignment accuracy and speed up the assembly process. The distance between the mirror facet and the output of the waveguides is minimized by pushing the mirror insert as close as possible to the vertical wall. One possibility to improve the alignment between the mirror and the output facet of the waveguides is the use of a mirror insert as is depicted in Fig. 5.15. In this case, the mirror facet is protected by the presence of a short vertical part, which can be used to press the insert against the vertical output facet of the waveguides without damaging the mirror facet.

In Fig. 5.16, a top view is shown of a DPW micro-mirror insert glued onto the Cu bottom surface of the cavity after the thermal curing step. The reflection of the waveguide cores can be seen on the Au-coated mirror facet. The mirror insert is made of PMMA material, which has T_g around $\approx 100^\circ\text{C}$, well below the 150°C required for the thermal curing step of the glue. However, no visual damage is observed after the thermal curing step which indicates that the Au-coating probably protects the PMMA insert from this high temperature, maintaining the mirror geometry. It should also be emphasized that the curing step only takes five minutes.

After the glueing of the DPW micro-mirror insert onto the Cu surface of the cavity bottom, the ablated trench is filled with Truemode cladding material in a spincoating step. The Truemode cladding layer is then UV-exposed in a nitrogen environment

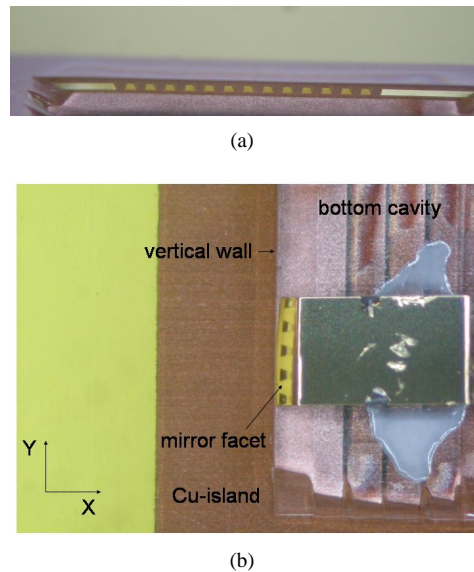


Figure 5.16: (a) Image of the output facet of the waveguides, taken with an optical microscope with the sample in a tilted position; (b) Top view of a mirror insert, glued onto the Cu-surface of the cavity bottom. As can be seen in the picture, the glue is applied towards the back of the insert to avoid contamination of the mirror facet and the output facet of the waveguides. The reflection of the waveguide cores can be clearly observed on the mirror facet.

without use of a mask and in a next step cured in a convection oven at 120°C for one hour. The mirror insert is during the curing step covered by the cladding material, which has excellent thermal properties, protecting the mirror insert from the relatively high curing time and temperature, at least on a PMMA temperature scale. A $10\mu\text{m}$ to $20\mu\text{m}$ thick cladding layer is sufficient for the homogeneous filling of the cavity, which typically has a size of $1\text{mm}\times 1.2\text{mm}$. The planarity of the optical layer is maintained after the embedding of the mirror.

The picture in Fig. 5.17 shows what happens when the mirror insert is glued onto the Cu surface of the cavity bottom using an excess amount of glue. During the curing step, the glue starts to flow and is attracted towards the small air gap between the output facet and the mirror facet by a capillary effect. The mirror facet and output facet of the waveguides are partially contaminated with glue, giving a decrease in the coupling efficiency of the embedded mirror. This problem can be avoided by controlling the amount of glue that is deposited with the use of a syringe and by making sure that the glue is deposited towards the back of the insert, opposite to the output facet of the waveguides. A small drop of glue is sufficient since the mirror insert is covered with cladding material in a next step, fixing its position.

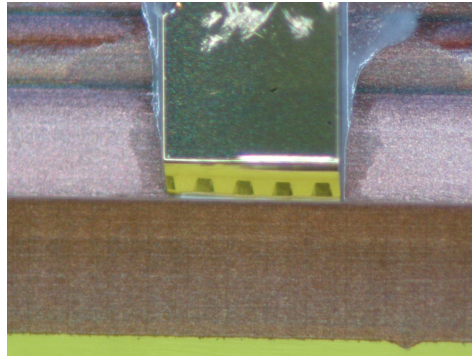


Figure 5.17: Top view of a mirror insert which is glued onto the Cu surface of the cavity bottom using an excess amount of glue, which is applied to close to the mirror facet. The mirror facet and output facet of the waveguides is partially contaminated with the glue.

5.4 Characterization

Loss measurements have been carried out to evaluate the the performance of the embedded mirror at the targetted wavelength of 850 nm. The measurements have been carried out in a receiver (Rx) scheme. An in-plane reference measurement was first carried out on a demonstrator board that consists of an FR4 substrate with an integrated Truemode optical layer, containing an array of ablated multimode waveguides with cross-section $50\mu\text{m}\times 50\mu\text{m}$ on pitch $125\mu\text{m}$ with NA 0.3. The substrate contains a Cu-island with dimensions $5\text{ mm}\times 5\text{ mm}$ in the area where the mirror will be embedded into the optical layer. The Cu-layer has a thickness ranging from $2\mu\text{m}$, in case the Cu-layer is sputtered on the FR4 substrate, covered with a suitable rectangular mask during the sputtering, up to $9\mu\text{m}$ or $18\mu\text{m}$ in case precoated FR4 substrates are used, and the Cu-island etched away with the use of a suitable mask, which is in this case the inverse of the mask used for the sputtering process.

For the in-plane reference measurement, schematically depicted in Fig. 5.18(a), an 850 nm light signal is coupled into the waveguide with a multimode optical fiber (MMF) with core diameter $50\mu\text{m}$ and NA 0.2. The light signal then propagated in the 4.5 cm long waveguide, is coupled out horizontally at the waveguide output facet and the outcoupled light signal is detected with a MMF with core diameter $100\mu\text{m}$ and NA 0.29. The distance between the input fiber and the input facet of the waveguide and between the output facet of the waveguide and the detector fiber is optimized with use of a CCD camera and is typically a couple of tens of microns. The measured overall in-plane efficiency of the link is -1.3dB.

Then, a micro-cavity is ablated into the optical layer and the mirror inserted into the cavity and covered with cladding material. The Cu-island is situated at the edge of the sample, which justifies the comparison between the in-plane reference measurement and the measurement with the embedded mirror. For the second measurement, again an 850 nm light is coupled in horizontally with a MMF with core diameter $50\mu\text{m}$ and NA 0.2. The light then propagates in the Truemode waveguide, with NA 0.3. The propagating light spot is coupled out of the plane of the optical layer at the Au-coated

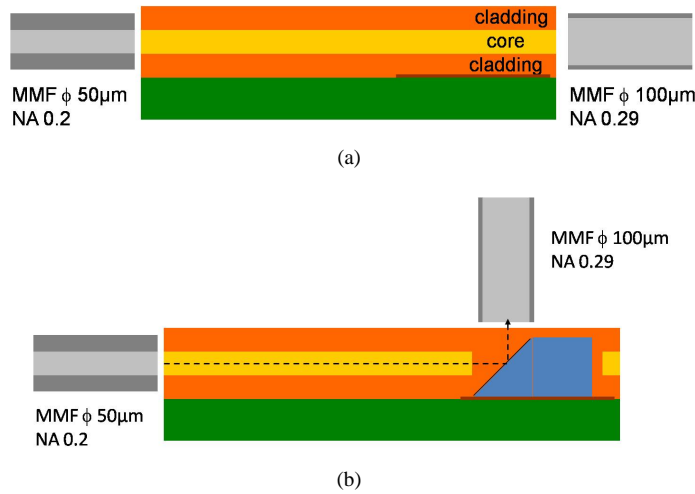


Figure 5.18: (a) Set-up used to carry out the in-plane reference measurement: an 850 nm light signal is coupled in horizontally into the waveguide with an optical fiber with core diameter $50 \mu\text{m}$ and NA 0.2, then propagates in the waveguide until it is coupled out at the output facet of the waveguide and is detected with an optical fiber with core diameter $100 \mu\text{m}$ and NA 0.29; (b) set-up used to measure the link efficiency at the receiver side: an 850 nm light signal is coupled in horizontally into the waveguide with an optical fiber with core diameter $50 \mu\text{m}$ and NA 0.2, then propagates in the waveguide until it is coupled out of the plane of the optical layer at the Au-coated mirror facet and is detected with an optical fiber with core diameter $100 \mu\text{m}$ and NA 0.29.

mirror facet and is detected with a MMF with core diameter $100 \mu\text{m}$ and NA 0.29, this time placed in a vertical position as is shown in Fig. 5.18(b). As can be seen in Fig. 5.18, the length of the Truemode waveguide in the embedded mirror configuration is $\leq 5 \text{ mm}$ shorter than for the reference measurement because of the fact that the cavity has to be ablated in the zone of the Cu-island, which is located near the edge of the demonstrator board. The overall measured link efficiency is -1.65 dB . Correcting for the 5 mm shorter waveguide, with the associated 0.06 dB loss, we can conclude that the embedding of the mirror causes an excess loss of approximately 0.3 dB , which can be attributed as the coupling loss of the embedded mirror, corresponding to a coupling efficiency of 93%.

The tolerance for misalignment of the detector fiber has been evaluated by scanning the detector fiber around its theoretically ideal position, where the centre of the mirror and the detector are perfectly aligned. The alignment tolerance plot, shown in Fig. 5.19, shows that the -1 dB tolerance range is $\pm 24 \mu\text{m}$. The light spot that is deflected over 90° at the mirror facet and is detected by the MMF detector has a nice circular shape. A rough estimation of the performance of the embedded mirror at the transmitter (Tx) side has been performed by coupling an 850 nm light signal in vertically at the mirror position with a single mode fiber (SMF-28), which has core diameter $8.2 \mu\text{m}$ and NA 0.14, and measuring the amount of light that is coupled out horizontally at the output facet of the waveguides (for the Rx measurements this is the input facet) of the wave-

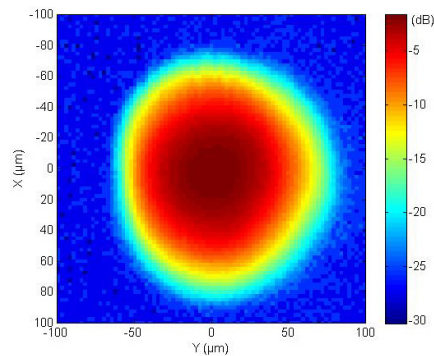


Figure 5.19: The alignment tolerance plot of the coupling efficiency clearly shows the circularity of the outcoupled spot. The measured 1dB tolerance range is $\pm 24 \mu\text{m}$.

guides with a MMF with core diameter $100\mu\text{m}$ and NA 0.29. No in-plane reference measurement was carried out prior to the embedding of the micro-mirror in this case. It is therefore not possible to give an exact number for the excess loss caused by the embedding of the mirror insert. The average overall efficiency of the link is dB, which is comparable or even better than the total link efficiency measured at the Rx-side.

5.5 Conclusion

In this chapter two different approaches have been presented that can be followed when discrete coupling elements are used to deflect the light beam over 90° , out of the plane of the optical layer. The first approach consists of a pluggable coupler, which is inserted into a micro-cavity in the optical layer. The pluggable coupler can be used in an out-of-plane as well as in an inter-plane coupling configuration. The out-of-plane coupler contains a 45° micro-mirror with excellent optical quality and has a coupling efficiency of 83.7% in a fiber-to-fiber scheme. However, the coupling efficiency decreases considerably when the coupler is inserted into the micro-cavity in the Truemode optical layer of a demonstrator board. This is mainly because of the large NA of the Truemode waveguides, which is responsible for a high TIR loss and the large amount of spreading during the propagation in the PMMA material from the mirror facet to the flat top exit facet. A second source of loss is the air gap that exists between the output facet of the waveguides and the input facet of the coupler, and which can only be eliminated by locally applying index matching gel. In addition, the top surface of the optical layer is no longer planarized, which can give problems with the surface mounting of optoelectronic elements or the lamination of additional layers. The inter-plane couplers have a good coupling efficiency, 70% for the one with conservation of the propagation direction, but have not been tested yet in a demonstrator board.

A drawback of the pluggable couplers is the fact that their mirror facet is not protected from external influence such as moist and dust intrusion, which could severely impede their TIR performance. The measured coupling efficiency of the components in a fiber-to-fiber configuration is good but the loss that is measured after insertion in a demonstrator board is rather high for the out-of-plane coupler, and assumably also for

the inter-plane couplers.

A better approach is the use of an embedded micro-mirror, which actually means that the discrete micro-mirror is covered with cladding material after the application of a Au-coating and the insertion into the micro-cavity. The top surface of the optical layer is in this case planarized, allowing the surface mounting of opto-electronic elements or the lamination of additional layers. The distance between the output facet of the waveguide and the mirror facet can be minimized by pushing the mirror insert the closest possible to the vertical wall of the ablated cavity. The cavity is in a next step filled with cladding material, which means that the light spot that is coupled out of the waveguide propagates in the cladding material before it reaches the mirror facet and also after the 90° beam deflection. The distance between the centre of the mirror facet and the top of the optical layer is typically 85 μm to 95 μm, which is much smaller than the propagation distance that has to be covered in the case of the pluggable coupler. The embedded mirror has a coupling efficiency of 93% in a receiver configuration, and the outcoupled light spot has a nice circular shape.

We can conclude that the performance of the embedded micro-mirror by far exceeds the performance of the pluggable micro-mirror because of the fact that TIR loss is avoided because of the presence of the Au-coating on the mirror facet. The mirror is embedded into the optical layer and is in this way protected from external influence.

Bibliography

- [1] B. Volckaerts, "Deep lithography with ions: a journey from ion interaction phenomena to high-precision fiber connector components," *PhD Thesis*, Vrije Universiteit Brussel, 2004
- [2] C. Debaes *et al.*, "Deep proton writing: a rapid prototyping polymer micro-fabrication tool for micro-optical molecules," *New J. of Phys.*, Vol. 8, No. 11, 270, 2006
- [3] J. Van Erps *et al.*, "Hot embossing of micro-optical components prototyped by deep proton writing," *IEEE Phot. Techn. Lett.*, Vol. 20, No. 18, pp. 1539-1541, 2008
- [4] N. Hendrickx, J. Van Erps, T. Alajoki, N. Destouches, D. Blanc, J. Franc, P. Karioja, H. Thienpont, P. Van Daele, "Towards Low Cost Coupling Structures for Short-Distance Optical Interconnections," *Proc. EMPC 2007 conference*, pp. 247-252
- [5] J. Van Erps, "Interfacing micro-components for optical interconnections from the FTTH-level to the PCB-level," *PhD thesis*, Vrije Universiteit Brussel, 2008
- [6] H. Ottevaere *et al.*, "Two-dimensional plastic microlens arrays by Deep Lithography with Protons: fabrication and characterization," *J. Opt. A: Pure Appl. Opt.*, Vol. 4, pp. 22-28, 2002
- [7] J.-H. Kim, R. T. Chen, "A Collimation Mirror in Polymeric Planar Waveguide Formed by Reactive Ion Etching," *IEEE Phot. Techn. Letters*, Vol. 15, No. 3, pp. 422-424, 2003

- [8] J. Van Erps, S. Heyvaert, C. Debaes, B. Van Giel, N. Hendrickx, P. Van Daele, H. Thienpont, "Enhanced pluggable out-of-plane coupling components for printed circuit board-level optical interconnections," *Proc. SPIE, Micro-optics*, Vol. 6992, 699227, 2008

Chapter 6

Reliability and stability

6.1 Introduction

Optical interconnections are slowly finding their way towards practical applications in many different areas. Standardisation is required in order to get a broad acceptance of the optical interconnect technology and is not yet existing. One of the main problem that currently exist are the different methods that are used to evaluate the performance of optical waveguides and coupling structures. This can go from differences in the way the optical loss of the elements is measured (difference in the operating wavelength (for instance 850 nm versus 980 nm), different incoupling and/or detection conditions (fibers with different core diameter and/or numerical aperture)). Currently, there is no general approach, even though initiatives are being taken in this direction [1], [2]. The aim should be to come to set of standards focused on optical interconnections, in the same way as this has been done for telecom applications. Optical interconnections will only be adopted by industry once they have proven their potential, not only on a short term but also on a longer term and this for various environments, which can vary from an office environment to an outside environment, dependent on the targeted application. End-users in several application areas are rather reluctant when it comes the adoption of polymer materials in their fabrication process, mainly because of the fact that their long-term reliability and stability has not yet been proven.

An important characteristic for practical applications is the thermal stability of the optical and mechanical properties of the used polymer materials. Reason for this is the fact that they are subject to yellowing, meaning that the colour of the sample progressively becomes yellow upon thermal aging. Typically, such aging results from the formation of partially conjugated molecular groups characterized by broad ultraviolet absorption bands, which tail off in intensity through the visible spectrum [3]. These tails can stretch up to a wavelength of 800-900 nm, and influence the absorption in this wavelength range. The absorption in the blue wavelength region (470 nm) increases at a faster rate compared to the red wavelength region (650 nm). As a result, the sample absorbs more blue light and starts to appear yellow [4]. The yellowing is strongly influenced by the chemical structure of the original polymer and increases with higher aging times and temperatures, as is shown in the graphs in Fig. 6.1 for a siloxane-type material. The chemical structure of the various backbone segments in the optical

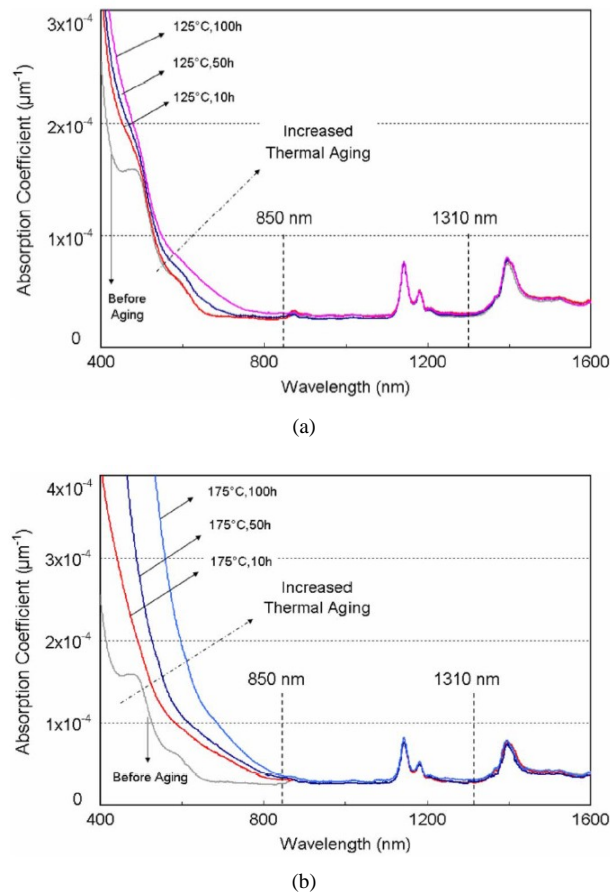


Figure 6.1: (a) Influence of thermal aging at a temperature of 125°C on the absorption spectrum for different aging times [4]; (b) influence of thermal aging at a temperature of 175°C on the absorption spectrum for different aging times [4].

polymer can vary substantially from a simple aliphatic to aromatic, and linkages can vary from ether to ester or urethane [5]. The choice of these linkages and monomers or oligomers ultimately determines to a significant degree the characteristics of the resulting polymer, including surface energy, hardness, toughness, elasticity modulus, water uptake, and stability towards aging. In fully halogenated materials, yellowing becomes almost negligible because the absence of hydrogen prohibits the formation of H-halogen products that will result in carbon double bonds. These unsaturated double bonds are the major cause of yellowing when they are slowly oxidized under long-term thermal aging [3].

Different optical polymer materials have been developed over the last few years, which have excellent optical and thermal properties [5]. Next to the influence of environmental stress such as for instance heat and moist, another important question is what happens to the material properties when they are submitted to a lamination cycle or a

solder reflow step, which are typical processes associated with PCB manufacturing. A lamination process typically requires temperatures around 180°C and a pressure of 15 bar whereas the reflow step requires temperatures as high as 260°C over a short period of time, usually a couple of tens of seconds.

In this chapter, we will first have a look at the reproducibility of the Truemode ablated waveguides, which is of course crucial for practical applications. Next, the influence of two accelerated aging tests and a lamination and solder step on the insertion loss will be discussed. Telcordia environmental reliability standards for passive optical components (GR-1209-CORE and GR-1221-CORE) have been used as a reference. Telcordia GR-1209-CORE (generic requirements for passive optical components) contains criteria that are used to verify the device's performance under various conditions and to demonstrate its ability to perform over its expected lifetime. The environmental and mechanical tests that are specified are used to demonstrate the short term operational performance of the components. Telcordia GR-1221-CORE (generic requirements assurance requirements for passive optical components) addresses the long-term reliability of passive optical components. Two accelerated aging tests have been carried out: an accelerated temperature-humidity aging test (85°C and 85% relative humidity) and a thermal cycling test. These tests have been chosen because of the availability of suitable equipment.

Of particular concern for polymers are extreme temperatures and humidity, as well as the broad range of temperatures that may bracket either the T_g or the sub- T_g relaxations of the polymer. Polymers that stand up to 85°C and 85% relative humidity conditions have been demonstrated, and some polymers have already passed the telcordia GR1209 and GR1221 environmental tests [5]. Extensive materials research has yielded polymers that are highly reliable, to the extent that they are no longer the limiting factor in component lifetime.

The link loss of FR4 substrates containing an integrated optical layer with ablated Truemode waveguides, with a cross-section of $50\ \mu\text{m} \times 50\ \mu\text{m}$ on pitch $125\ \mu\text{m}$ and NA 0.3, is evaluated before and after submitting them to the proposed tests. The link loss is measured in a fiber-to-fiber scheme in the plane of the optical waveguides, as is schematically shown in Fig. 6.2. An 850 nm light signal is coupled in horizontally with a graded index optical fiber with core diameter $50\ \mu\text{m}$ and NA 0.2 into the Truemode waveguide, which has NA 0.3. The light signal that is coupled out at the waveguide output facet is detected with an optical fiber with core diameter $100\ \mu\text{m}$ and NA 0.29. In the next sections, we will discuss the influence of the different environmental tests and processing conditions on the link loss of the waveguide samples. The pass criterium, in accordance with the telcordia tests, is a $\pm 0.5\text{dB}$ change on the insertion loss. According to the specifications in the datasheet, telcordia 1209 tests undertaken on waveguides have resulted in no changes in the optical properties of the waveguides [7].

6.2 Reproducibility

The first question we have to ask ourselves when we want to use ablated Truemode waveguides in practical applications, is the reproducibility of the propagation loss of waveguides that are located in the same array, in different arrays on the same board and in arrays on different boards. This is done by measuring the link efficiency in the

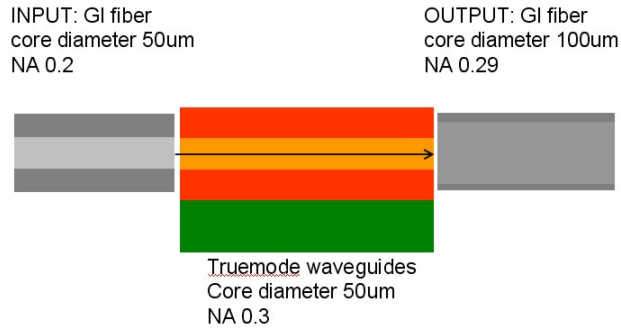


Figure 6.2: Schematic representation of the set-up used to evaluate the performance of the Truemode waveguide after submitting them to the different reliability and stability tests explained in this chapter.

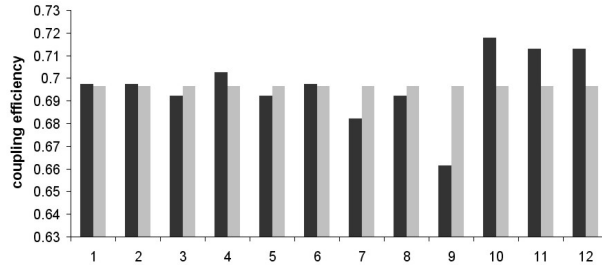


Figure 6.3: Link efficiency of 4 cm long Truemode ablated waveguides located in the same array on a demonstrator board. The light gray bars indicate the average link efficiency. The reproducibility is better than 5%.

described fiber-to-fiber scheme.

The reproducibility of the link efficiency of waveguides in the same array on a demonstrator board is better than 5%, as can be seen in Fig. 6.3. The waveguides have a length of 4 cm and show an average link loss of 1.57dB, corresponding to a link efficiency of 69.6% with a standard deviation of 1%. The same holds for waveguides in different arrays on the same board, at least in the case that the thickness of the optical layer is the same at the different measured locations. This is the case if neither of them are situated in the edge bead zone, where the layer thickness is locally thicker than on the rest of the sample, and which is located near the edge of the sample. The reproducibility of the link efficiency of waveguides on different boards, with the same link length, is again better than 5%, as is shown in Fig. 6.4. The waveguides on both boards have a length of 5.1 cm. The waveguides have an average link loss of 1.71dB on board 1, corresponding to a link efficiency of 67.2% with standard deviation 0.5%, and of 1.7dB for board 2, corresponding to a link efficiency of 67.6% with a standard deviation of 1%. The small variations on the link efficiency around the average value can be attributed to the uncertainty on the measurement result and the manual polishing process of the waveguide end facets.

Loss measurements have been carried out on more than 50 demonstrator boards with

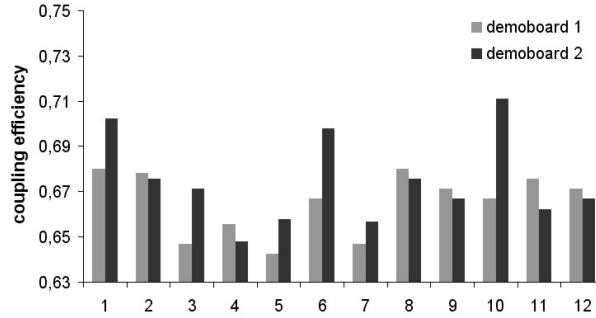


Figure 6.4: Link efficiency of 5.1 cm long Truemode ablated waveguides located in an array on two different demonstrator boards. The reproducibility is again better than 5%.

	link efficiency (link loss)
waveguides in the same array link length 4 cm	69.6% \pm 1% (1.57dB)
waveguides in different arrays on the same board link length 4 cm	69.6% \pm 1% (1.57dB)
waveguides on different boards with the same link length link length 5.1 cm	67.1% \pm 0.5% (1.71dB) (board 1) 67.6% \pm 1% (1.7dB) (board 2)

Table 6.1: Link efficiency (link loss) of waveguides in the same array, in different arrays on the same board and on different boards.

various waveguide lengths, giving results that are very similar to the above listed ones. From these measurements, we can conclude that the reproducibility of the ablated Truemode waveguides with a cross-section of $50 \mu\text{m} \times 50 \mu\text{m}$ on pitch $125 \mu\text{m}$ is better than 5%, and this for both waveguides in the same array and also different arrays on the same demonstrator board and for waveguides on different demonstrator boards but with the same link length. The results are summarized in Table 6.1.

It should be noticed that these results are obtained for samples containing waveguides with a length of 3 cm up to 9 cm. It is clear that for these short waveguide lengths, it is difficult to say with certainty whether or not the waveguide is in a steady-state condition. The measured values however, are in accordance with the results coming from cut-back measurements. As was already mentioned in chapter 3, the optical loss of any waveguide material can be described as the sum of intrinsic and extrinsic loss. Absorbance effects due to vibrational overtones of aliphatic groups or hydroxy groups are typical drivers for intrinsic loss, while surface roughness, defects and processing variables can cause extrinsic loss. Creating low-loss meter-long waveguides is a significant challenge because any type of defect resulting from trapped air bubbles, debris or coating imperfections can have a substantial impact on the loss characteristics of the waveguide [8]. For the tested waveguide lengths, it is possible to pattern waveguides with a low amount of defects incorporated. It is clear however, that the risk of incorporating defects will increase with the waveguide length. Longer waveguide lengths have not been evaluated because no suitable equipment is available for the fabrication of the

samples.

6.3 Accelerated aging tests

Two accelerated aging tests have been carried out: an accelerated temperature-humidity aging test (85/85 test) and a thermal cycling test. The influence of both tests on the link efficiency of the waveguide samples is given in the following sections. The tests are carried out according to the specifications given in Telcordia GR-1209. Telcordia GR-1221 requires longer cycle times, which was in our case impossible in view of the fact that the equipment has to stay available to other users.

6.3.1 85/85 test (85°C/85% relative humidity)

During the 85/85 test, the waveguide sample is placed in a climate cabinet for 168 hours (one week) submitted to a temperature of 85°C and 85% relative humidity. The sample contains an array of ablated waveguides with a length of 3.5 cm. The average link loss of the waveguides was measured to be 1.57dB before the 85/85 test, corresponding to a link efficiency of 69.6% with a standard deviation of 1.5%. The measurements were done over again after submitting the sample to the proposed test. No mechanical failure such as cracking or delamination occurs after this step, despite the CTE mismatch that exists between the polymer and the FR4 substrate. An average link loss of 2.68dB is measured after the stay in the climate cabinet, corresponding to a link efficiency of 54% with a standard deviation of 1.5%. The increased link loss is a consequence of the deposition of a thin layer on the end facets during the stay in the climate cabinet, which degrades the quality of the waveguide input and output facet. Optical microscope inspection does however not reveal the presence of this layer. This effect has also been observed and described in [10]. This thin layer can be removed by polishing the end facets of the sample again. Two polishing steps, using the two polishing plates with the lowest surface roughness, are sufficient to restore the quality of the waveguide input and output facet. The sample is measured again after the polishing step. The waveguides now have an average propagation loss of 1.46dB, corresponding to a coupling efficiency of 71.3% with a standard deviation of 0.6%. The average propagation loss of the waveguides is after the polishing step 0.1dB lower than before the submission to the 85/85 test, which is within the uncertainty on the measurement. The measurement result on the sample before the 85/85 test, after the 85/85 test without polishing and after the 85/85 test with the additional polishing step are shown in Fig. 6.5. The results are summarized in Table 6.2.

More than 5 samples have been submitted to the 85/85 test, and evaluated in a next step. The measurement results confirm the results present above. The fact that humidity has very little effect on Truemode is a consequence of the highly cross-linked nature, resulting in a tightly bound network with a low level of voids, leaving little space for water to be absorbed. The temperature of 85°C is within the thermal stability range of the material. We can conclude that the performance of the ablated Truemode waveguides remains intact after this accelerated aging test in case the waveguide input and output facet are protected or encapsulated. It would however also be interesting to investigate the influence on the link efficiency of an increase in the number of test hours and of subsequent stays in the climate cabinet.

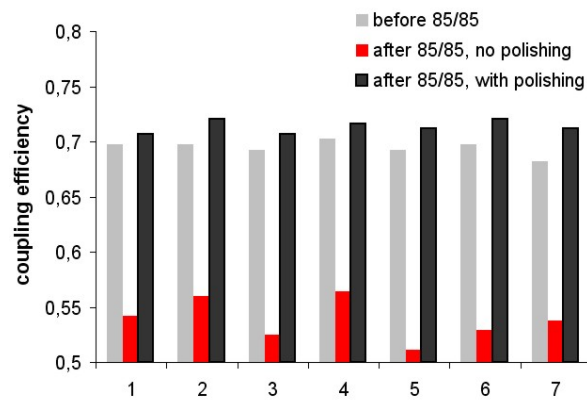


Figure 6.5: Link efficiency of the waveguides measured on the sample before the 85/85 test, after the 85/85 test without polishing and after the 85/85 test with the additional polishing step.

	link efficiency (link loss)
before 85/85 test	69.6% \pm 1% (1.57dB)
after 85/85 test without polishing of waveguide end facets	54% \pm 1.5% (2.68dB)
after 85/85 test with polishing of waveguide end facets	71.3% \pm 0.6% (1.46dB)

Table 6.2: Link efficiency (link loss) of waveguide sample before and after submitting it to the 85/85 test for 168 hours, with and without the polishing of the waveguide end facets after the test.

Minimum temperature	0°
Maximum temperature	85°
Dwell time at extremes	15 minutes
Temperature slope	1°/minute
Number of cycli	20

Table 6.3: Parameters used for thermal cycling test 1.

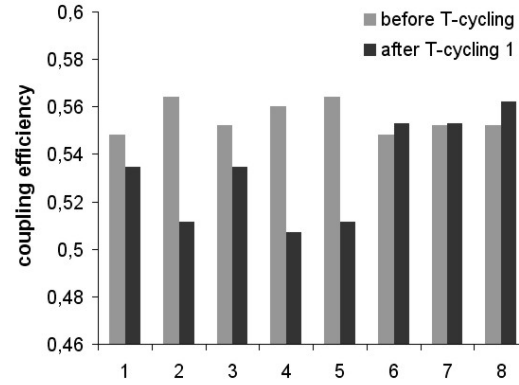


Figure 6.6: Link efficiency of the waveguides measured on the sample before and after the thermal cycling test 1.

6.3.2 Thermal cycling

The influence of thermal stress induced by temperature differences has been tested by submitting two sample to two different tests. The first sample contains an array of ablated Truemode waveguides with a length of 7.5 cm and is submitted to the first thermal cycling test of which the parameters are specified in Table 6.3. The waveguides on the sample have an average link loss of 2.55dB, corresponding to a link efficiency of 55.5% with standard deviation 0.6%. The waveguide end facets are manually polished after submitting it to the test, as was the case for the samples submitted to the 85/85 test. After the thermal cycling test 1, the measured average link loss is 2.72dB, corresponding to a link efficiency of 53.3% with standard deviation 2%. No delamination, cracking or decoloration can be observed after the test. The measurement results are schematically represented in Fig. 6.6.

The second sample contains an array of ablated Truemode waveguides with a length of 5.5 cm and an ablated total internal reflection (TIR) mirror. The sample is submitted to thermal cycling test 2, of which the parameteres are specified in Table 6.4. The link loss is in this case measured by sending an 850 nm light signal in horizontally with an optical fiber with core diameter 50 μm and NA 0.2 and by capturing the light spot that is coupled out vertically at the TIR mirror with an optical fiber with core diameter 100 μm and NA 0.29. An average link loss of 5.3dB has been measured prior to the thermal cycling test, corresponding to a link efficiency of 29.5% with standard deviation 1.2%. After the thermal cycling test 2, the measured average link loss is 5.2dB, corresponding

Lowest temperature	-40°C
Highest temperature	85°C
Dwell time at extremes	15 minutes
temperature slope	1°/minute
number of cycli	20

Table 6.4: Parameters used for thermal cycling test 2.

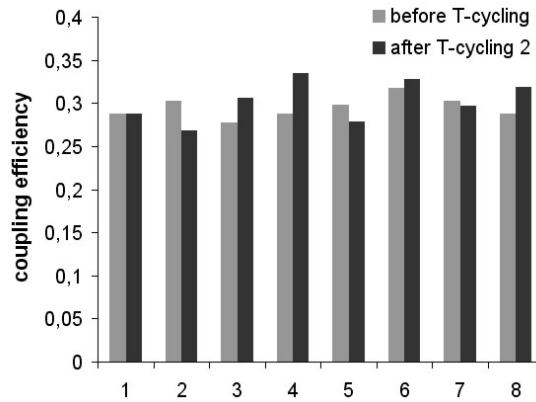


Figure 6.7: Link efficiency of the sample containing an array of ablated waveguides and a TIR mirror measured on the sample before and after the thermal cycling test 2.

to a link efficiency of 30.3% with standard deviation 2.3%. Again, no delamination, cracking or decoloration can be observed after this test. The measurement results are schematically represented in Fig. 6.7. The results of both thermal cycling tests are summarized in Table 6.5.

For the thermal cycling test, it is very important to avoid the presence of small mechanical defects such as small particles or air bubbles into the optical layer. These defects can act as an initiation site for crack propagation and delamination, eventually leading to device failure. Tests were carried out on waveguide sample in which the top cladding layer was partially delaminated from the core layer, came out of the climate cabinet completely cracked and delaminated. For this reason, it is very important to deposit the layers in a cleanroom environment and to avoid abrupt temperature changes during and right after the curing of the layers.

	thermal cycling test 1	thermal cycling test 2
before the test	55.5% \pm 0.6% (2.55dB)	29.5% \pm 1.2% (5.3dB)
after the test	53.3% \pm 2% (2.72dB)	30.3% \pm 2.3% (5.2dB)

Table 6.5: Link efficiency (link loss) of two waveguide samples before and after submitting them to the two different thermal cycling tests.

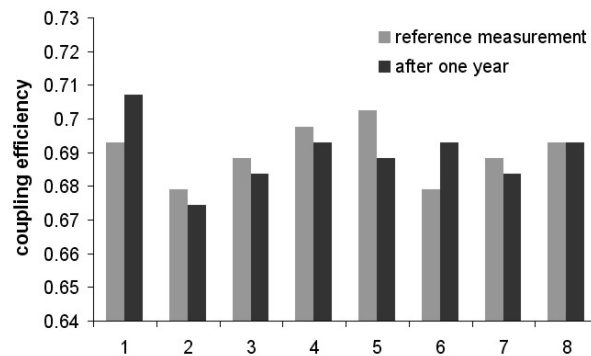


Figure 6.8: Link efficiency of the waveguides measured on the sample right after the fabrication and after a one year stay in an office environment.

6.4 Thermal stability

Five samples with ablated Truemode waveguides were conserved in an office environment, exposed to natural and artificial light and changing temperature, for a period of one year. No visual changes can be observed with an optical microscope after one year. The insertion loss of the waveguides is maintained after the year in the office environment, as is schematically shown in Fig. 6.8.

6.5 PCB manufacturing

One of the main requirements on the proposed solution to integrate optical interconnections to the board-level, is the compatibility with the existing PCB manufacturing and soldering processes. The two main processes are a lamination step and a solder reflow step. The influence of both processes on the insertion loss of the ablated Truemode waveguides is discussed in the following two sections.

6.5.1 Lamination

It is very likely that the first applications utilizing optical interconnect technology will require hybrid boards that have both optical and electrical interconnects [8]. Copper technology will continue to be used to provide the majority of links while optical technology will be used to satisfy the high-speed links. As a result, any new waveguide material will need to be able to withstand traditional PCB manufacturing processes, including metallization, drilling and lamination. Embedding waveguide layers within a hybrid board provides maximum flexibility with respect to system design and interconnect density. Although challenges remain with light turning and coupling, the first step is to demonstrate the ability to embed low-loss waveguides using conventional lamination processing [8].

The embedded optical layer is protected from external influence such as dust and moist and has a higher resistance against certain subsequent processing steps such as soldering compared to an optical layer that is integrated on top of the PCB. The accessibility

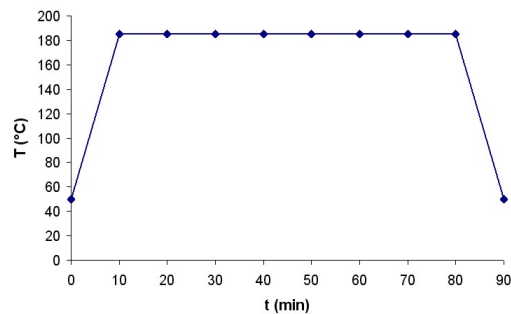


Figure 6.9: Progress of temperature in time during the lamination cycle.

of the optical layer is an important issue, because the requirement to be able to couple light signals in and out of the optical layer. For this reason, RCC (Resin Coated Cu) sheets (Isofoil 160i), which were developed for micro-via applications, were chosen as a suitable laminate material. The RCC sheets consist of a resin carrier with a Cu-layer on top, and are available in various thicknesses. The sheets used for the lamination tests have a top Cu-layer with a thickness of $9 \mu\text{m}$ and a resin layer with a thickness of $90 \mu\text{m}$. The sheet is cut in the same dimensions as the waveguide sample and laminated onto it. The best results are obtained in case the same stack of layers is laminated on both sides of the waveguide sample. The lamination of the RCC sheet on the waveguide sample is done in a vacuum laminator (Lauffer); the progress of the temperature T during the 90 minute long lamination cycle is given in Fig. 6.9. The pressure is 17 bar during the entire cycle; the vacuum pressure is 2 mbar.

A picture of the cross-section of an array of waveguides after the lamination is shown in Fig. 6.10. No mechanical damage is observed on the waveguide cores with an optical microscope. The waveguide shape remains intact after the lamination step, no flowing or flattening of the waveguide cores is observed.

Loss measurements have been carried out before and after the lamination step in order to be able to evaluate the influence on the propagation loss of the waveguides. Before the lamination, the waveguides had a length of 3.5 cm and an average link loss of 1.57dB, corresponding to a link efficiency of 69%, with a standard deviation of 1%. After the lamination of the isofoil sheet onto the sample, the input and output facet of the waveguides have to be polished again because of the fact that the resin starts to flow during the lamination and leaves a thin layer on the edges of the sample. The polishing of the waveguide input and output facet is done manually, in the same way as before the lamination. After the polishing step, the sample has a remaining length of 2.4 cm. The measured average overall link loss is 1.44dB, corresponding to a link efficiency of 71% with a standard deviation of 0.9%. The apparent 0.13dB gain after the lamination step can be attributed to the 1.1 cm shorter waveguide. If the coupling efficiency is corrected for the shorter waveguide length, the average coupling efficiency is 69% with a standard deviation of 0.9%, which is in very good correspondence with the results before the lamination. In Fig. 6.11, the effect of the lamination step on the coupling efficiency is shown. The coupling efficiency after the lamination step has in the graph been corrected for the shorter waveguide length. From this graph, we can conclude

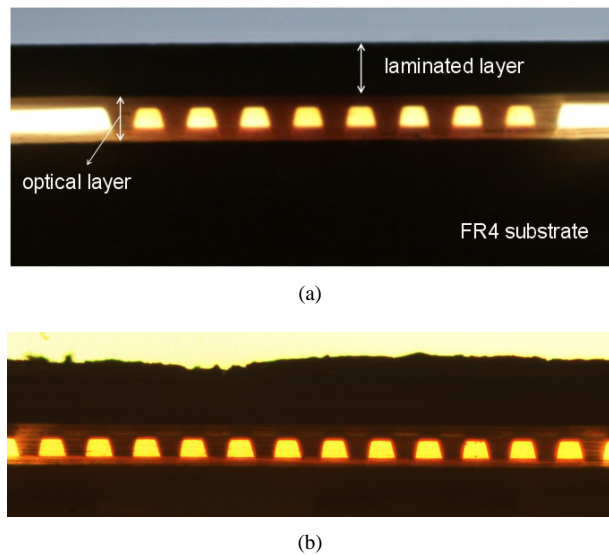


Figure 6.10: (a) Cross-section of an array of ablated Truemode waveguides after the lamination of the Isofoil sheet; (b) the waveguides shape is maintained after the lamination step. The Cu-layer is at the top of the laminated sample, the wavy shape is a consequence of the manual polishing process.

	link efficiency (link loss)
before lamination link length 3.5 cm	$69\% \pm 1\%$
after lamination link length 2.4 cm	$71\% \pm 0.9\%$ (1.44dB)

Table 6.6: Link efficiency (link loss) of the waveguide sample before and after submitting it to the lamination cycle.

that the propagation loss of the optical waveguides is almost not affected by the lamination process. These measurement results have been repeated on multiple samples. We can conclude that the propagation loss of the ablated Truemode waveguides is not affected by the lamination step and remains within 0.025dB/cm from the original value of 0.13dB/cm. The measurement results are summarized in Table 6.6.

It should be noticed that the cross-linking of the optical layer has to be completed in order to be able to repeat these results. Lamination tests were also carried out on samples where the optical layer was cured in the convection oven at a temperature of 90°C for about 3 hours, instead of 1 hour at 120°C as is specified in the datasheet. These curing tests were carried out in an attempt to avoid the cracking of the top cladding layer that was experienced on some samples after the curing step in the oven, probably because of stress built-up between the layers. The curing at lower temperature avoided the cracking but also provided waveguides with an increased propagation loss. The propagation loss was almost tripled in this case after the lamination step, even though

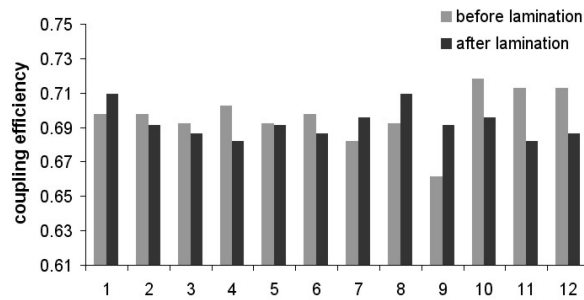


Figure 6.11: Link efficiency of the ablated Truemode waveguides, measured on the same demoboard before and after the lamination step. The link efficiency measured after the lamination step has been corrected for the shorter waveguide length.

no visual damage was observed in the cross-section of the waveguides.

DSC (differential scanning calorimetry) measurements confirm that the Truemode material is not completely cross-linked after the curing step in the convection oven at 90°C for about 3 hours. An unstable base line with a large exothermal peak is observed during the first heating step to 150°C. This exothermal peak is not observed when the sample is cooled down, which indicates that an irreversible chemical reaction took place during the first heating phase such as a curing step. The instability that is observed in the first heating step disappears during the second and third heating step, showing only the glass transition. The DSC curve measured on the non fully cured Truemode core material is given in Fig. 6.12. TGA measurements indicate that the fully cured Truemode material is thermally stable up to a temperature above 150°C, as can be seen in TGA curve measured on the fully cured Truemode core material in Fig. 6.13. From this, it can be concluded that the layers have to be cured at a temperature of 120°C for one hour in a convection oven in order to be able to use the material in a reliable way.

6.6 Solder reflow

Cost reduction is critical to accelerate the market growth of opto-electronic modules and systems. To reduce the cost, it is necessary to connect and maintain hundreds of optical precision alignments through a batch assembly process that is compatible with the existing manufacturing technology. Soldering is the technology of choice for this assembly process. It can be used to couple optical fibers or waveguides to devices such as VCSELs and photodetectors. The alignment can vary from sub-micron to micron levels for single- respectively multimode applications. In addition to providing electrical connections, solder is useful in the formation of passive, precision alignments for opto-electronic packaging [11].

At our research lab, the solder reflow is done in a vapour phase reflow oven. The progress of the temperature during the reflow step is shown in Fig. 6.14. This reflow cycle gives excellent results for soldering with SAC solder (mixture of 96.5% Sn, 3% Ag and 0.5% Cu) and SnAg solder. A waveguide sample is submitted to the same

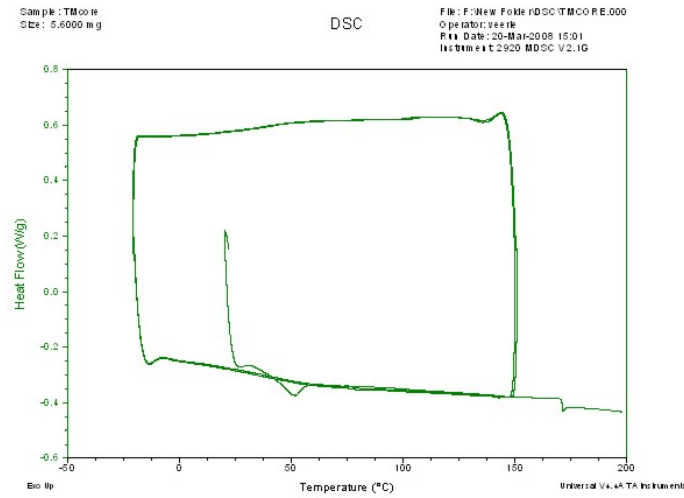


Figure 6.12: Curve resulting from the DSC analysis carried out on the non fully cured Truemode core material.

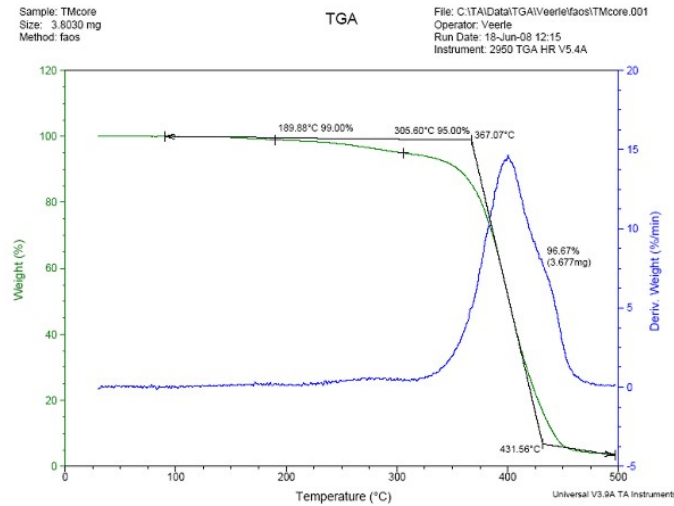


Figure 6.13: Curve resulting from TGA analysis carried out on the fully cured Truemode core material.

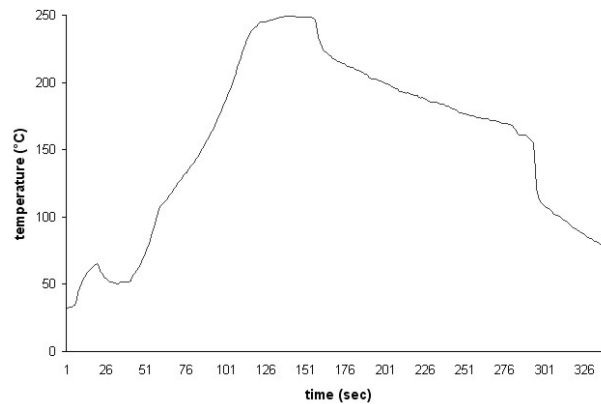


Figure 6.14: Progress of temperature during the solder reflow cycle.

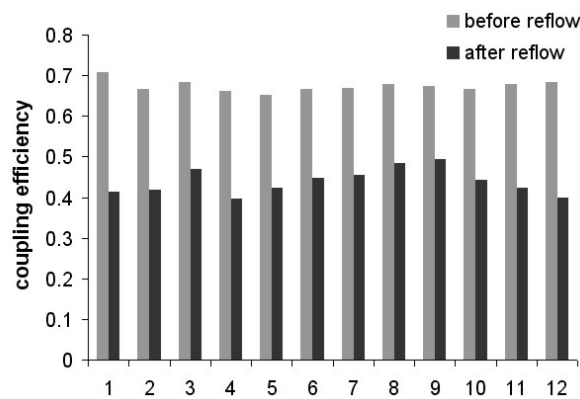


Figure 6.15: Coupling efficiency of the waveguides measured on the sample before and after the solder reflow cycle.

reflow cycle as the one given in Fig. 6.14 to study the influence of a solder reflow step. The highest temperature of 240°C is only reached during a period of approximately 5 seconds, but the temperature does stay over 200°C for over 30 seconds.

The waveguide sample contains an array of ablated Truemode waveguides with a length of 4.5 cm. The measured average overall link loss was 1.77dB before the solder reflow step, corresponding to a coupling efficiency of 67.3% with a standard deviation of 1.4%. The sample is in a next step submitted to a solder reflow cycle by placing it in a reflow oven according to the above given temperature profile. The average link loss after the solder reflow step is 3.57dB, corresponding to coupling efficiency of 43.8% with a standard deviation of 3.1%. The measurement result are graphically represented in Fig. 6.15. The waveguide end facets were polished after the reflow step, to remove the thin layer of material that is deposited during the reflow step.

The sample has a darker appearance after the reflow step, caused by a certain degree

of "burning" of the FR4 substrate. The glass transition temperature T_g of the FR4 substrate is typically 125-135°C [9], which is over 100°C lower than the 240°C to which the sample is exposed. When the T_g is reached, the resin changes from its glasslike state to its rubberlike state which causes changes in the laminate's properties. The T_g is not a measure of the resin's melting point, but rather a point at which molecular bonds begin to weaken enough to cause a change in physical properties such as the dimensional stability and the flexural strength. TGA measurements indicate that Truemode cladding material is thermally stable up to 285.5°C and the core material up to °C. The increased waveguide propagation loss that is experienced after the reflow step can to a certain extent be attributed to the deformation of the FR4 substrate that occurs during the exposure to the high temperature.

6.7 Conclusion

Samples with ablated Truemode waveguides have been submitted to environmental tests to evaluate the performance after aging. The samples have also been submitted to lamination step and reflow step. The reproducibility of the ablated Truemode waveguides is better than 5% and this for both waveguides on the same sample and on different samples. The propagation loss of the waveguides is not affected by an accelerated aging test which is tested by submitting the sample to 85°C and 85% relative humidity for one week. Thermal cycling between -40°C and 85°C has been carried out on waveguide samples and has no influence on the propagation loss. The Truemode waveguides can be laminated in a PCB-stack, without affecting the performance. It must however be noticed that the optical layer has to be completely cross-linked in order to be able to reproduce these results. The waveguide samples have also been submitted to a solder reflow step. The propagation loss increases about 1.8dB, and this for the same waveguide length. The increased propagation loss is most probably a consequence of the deformation of the FR4 substrate during the reflow step.

Bibliography

- [1] Microphotonics Center Consortium, Communication Technology Roadmap, <http://www.mpc-web.mit.edu>
- [2] National Institute of Advanced Industrial Science and Technology (AIST), <http://www.aist.jp>
- [3] L. Eldada, "Telcordia qualification and beyond: reliability of today's polymer photonic components," *Proc. SPIE*, Vol. 5724, pp. 96-106, 2005
- [4] S. G. Hegde, S. K. Sitaraman, "Thermal aging reliability of package-level polymer optical waveguides," *IEEE Transactions on advanced packaging*, Vol. 31, no. 2, 2008
- [5] L. Eldada, "Polymer integrated optics: promise vs. practicality," *Proc. SPIE*, Vol. 6185 618501, 2006

- [6] H. Ma, A. K. Y. Jen, L. R. Dalton, "Polymer-based optical waveguides: materials, processing, and devices," *Advanced materials*, Vol. 14, No. 19, 2002
- [7] Exxelis Ltd. (UK), <http://www.exxelis.com>
- [8] M. L. Moynihan, B. Sicard, T. Ho, L. Little, N. Pugliano, J. G. Shelnut, H. B. Zheng, P. Knudsen, D. Lundy, N. Chiarotto, C. Lustig, C. Allen, "Progress towards board level optical interconnect technology," *Proc. SPIE*, Vol. 5731, pp. 50-62, 2005
- [9] C. A. Harper, "Electronic packaging and interconnection handbook," *McGraw-Hill Handbooks*, 4th edition, ISBN 0-07-143048-2
- [10] M. Immonen, M. Karppinen, J. K. Kivilahti, "Investigation of environmental reliability of optical polymer waveguides embedded on printed circuit boards," *Circuit World*, Vol. 33, no. 4, pp. 9-19, 2007
- [11] Q. Tan, Y. C. Lee, "Soldering technology for optoelectronic packaging," *Proc. ECTC*, pp. 26-36, 1996

Chapter 7

Demonstration of on-board optical interconnects

7.1 Introduction

A lot of the work that has been described in the previous chapters of this PhD thesis has been applied and carried out within the framework of the network of excellence on micro-optics (NEMO), supported by the European Commission through the sixth framework programme (FP6). Within NEMO different university laboratories and research institutes collaborate in the aim to combine the competences of the different partners and in this way create added value. Our research group was mainly involved in workpackage 9 (WP9), which deals with micro-optics for PCB and MCM interconnects, and workpackage 4 (WP4), which is the centre for packaging and integration. The two main achievements within the network are the design and fabrication of an active demonstrator board, which is based on an existing demonstrator board, and the design and fabrication of an in-plane fiber-to-waveguide connector. Both tasks were carried out within the framework of the Optoboard project, which was a collaboration between VTT Research Centre in Finland (VTT), Vrije Universiteit Brussel (VUB), and Universiteit Gent (UGent). The network has allowed and stimulated the combination of the capabilities of the different partners to improve the performance of the existing prototype and this on a short time-scale. In the following sections, we will first present the achievements made in the area of the active demonstrator board and then discuss the design and fabrication of the in-plane connector.

7.2 Active demonstrator

The first task within the optoboard project is the improvement of the performance of an existing active demonstrator board that was fabricated at VTT research centre in Finland [1]. It consists of a 4×10 Gb/s optical interconnect demonstrator, shown in the picture in Fig. 7.1. The optical link demonstrator consists of a 4-channel ball grid array (BGA)-mounted transmitter and receiver module built on LTCC (low temperature co-fired ceramics) substrates as well as four parallel multimode optical waveguides with a

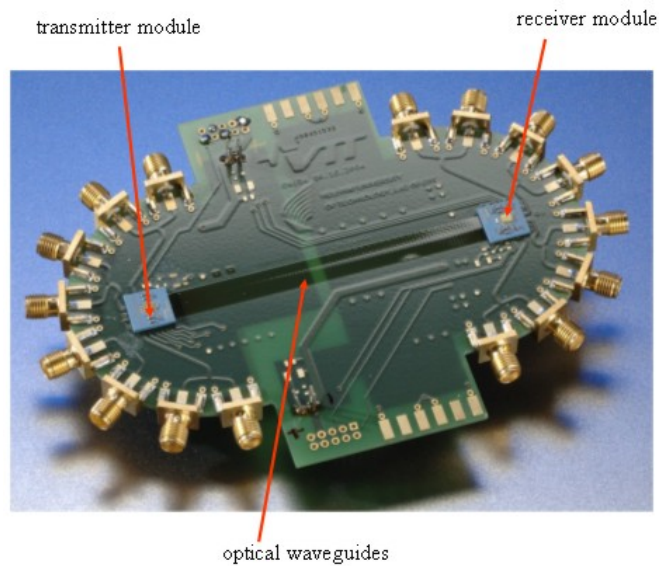


Figure 7.1: Picture of a 4×10 Gb/s optical interconnect demonstrator that was fabricated at VTT [1]. The optical link demonstrator consists of a 4-channel BGA-mounted transmitter and receiver modules built on LTCC substrates as well as four parallel multimode optical waveguides with a length of 85 mm, fabricated on the PCB (courtesy of VTT).

cross-section of $50 \mu\text{m} \times 50 \mu\text{m}$ on a pitch of $250 \mu\text{m}$ and a length of 85 mm, fabricated on the PCB. In the original board, the waveguide cores are patterned into a $50 \mu\text{m}$ thick SU8 layer with standard UV-lithography; the surrounding cladding material is mr-L6050XP. The waveguides have a propagation loss of 0.55dB/cm at 850 nm [1].

The schematic structure of the transmitter and receiver modules as well as the optical coupling is illustrated in Fig. 7.2. The coupling between the opto-electronic module and the PCB is done with the help of two micro-lens arrays, of which one is mounted on the side of the module and the other on the side of the PCB, and a discrete Al-coated glass micro-mirror. This coupling scheme is referred to as an expanded beam concept. The expanded beam concept between the opto-electronic module and the PCB relaxes the alignment requirements, enabling surface mount technology (SMT) assembly. The micro-mirror is fabricated by grinding and polishing one edge of a $100 \mu\text{m}$ thick glass substrate in such a way that a 45° bevel is formed. Several substrates are grinded by stacking them into a jig which makes it possible to mount them in a 45° angle precision lapping and polishing machine. After polishing, the substrates are diced with a dicing saw. An Al-coating is evaporated on the glass surfaces for high reflectivity. A picture of the top view of a glass micro-mirror, placed at the output facet of the waveguides, is shown in Fig. 7.3. The transmitter is based on a 4-channel VCSEL emitter chip and a 4-channel driver IC chip. The receiver module is based on a 4-channel PIN detector chip and a 4-channel amplifier IC chip. All chips are bare dies. A picture of the transmitter/receiver module, which both have a similar build-up, BGA-mounted on the PCB is shown in Fig. 7.4.

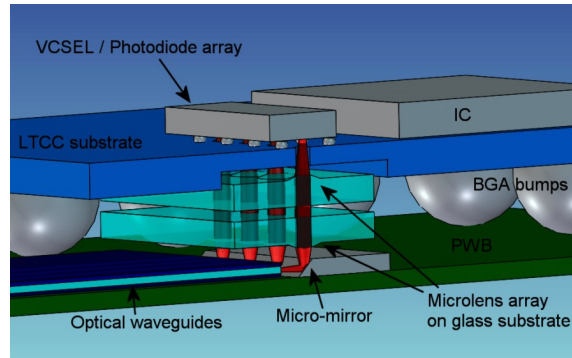


Figure 7.2: Schematic structure of the transmitter and receiver modules and the optical coupling [1]. The expanded beam concept between the opto-electronic module and the PCB loosens the alignment requirements, enabling SMT assembly (courtesy of VTT).

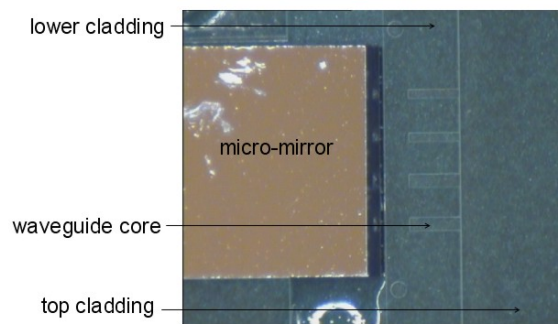


Figure 7.3: Picture of the top view of the micro-mirror placed at the output facet of the waveguides.

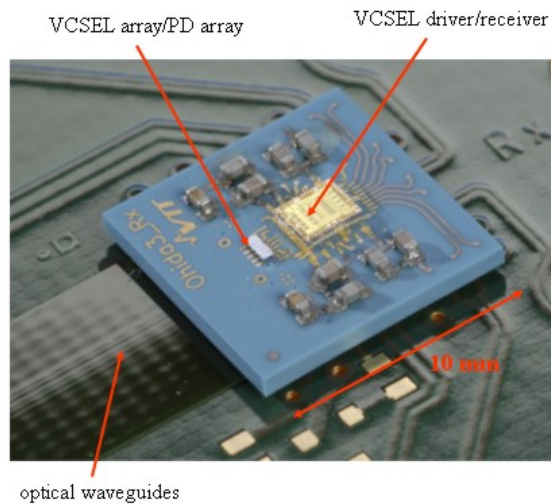


Figure 7.4: Picture of a transmitter/receiver module, which both have the same build-up, BGA-mounted on the PCB.

The transmitter and receiver module are mounted on the circuit board using BGAs. In the original demonstrator board, the opto-electronic components are mounted on top of the LTCC substrate. The LTCC substrate is opened locally in the area where the components are mounted in order to allow light signals to be sent and received. As was already mentioned, the coupling between the VCSEL/PD array and the waveguide array is based on two micro-lens arrays and a micro-mirror. One lens array is mounted into a cavity on the BGA side of the LTCC substrate, whereas the other micro-lens array and the micro-mirror are mounted on the PCB. With this design, an expanded and collimated beam is obtained between the module and the board, relaxing the sensitivity to potential misalignments resulting from the BGA board assembly. The total link loss in this configuration was estimated to be 19dB; the characterized transversal tolerances, in the plane of the optical waveguides, with 1dB loss margin were ± 40 to $60 \mu\text{m}$. Loss measurements indicate that the micro-mirror causes an average coupling loss of 5.1dB, which is higher than the other coupling approaches that were studied within the project [2].

Within WP9, it was decided that we would try to improve the performance of the optical link by using a different coupling approach and to reduce the number of optical components in the original VTT demonstrator board. The assembly of the discrete micro-lens arrays that collimates the VCSEL beam requires high accuracy mounting and is thus costly. For this reason, it is preferable to eliminate this assembly step. The Centre Suisse d'Electronique et de Microtechnique (CSEM), one of the partners within the network, has developed a wafer-scale replication process, which combines UV-casting and lithography, to realise micro-lenses directly on top of the VCSEL wafer [3]. These i-VCSELs can reduce the farfield full width half maximum (FWHM) divergence to an angle of around 6° and a $1/e^2$ farfield divergence of 11° for 1mW optical power. Instead of mounting the opto-electronic components on top of the LTCC substrate, as was the case for the original demonstrator board, it was decided to mount the components

on the bottom of a cavity in the LTCC substrate. A picture of a 4-channel i-VCSEL array chip with $250\ \mu\text{m}$ pitch, wire-bonded onto the bottom of a cavity in the LTCC substrate is shown in Fig. 7.6(a).

Two different NEMO demonstrator boards have been developed: the first one (first generation) is a basic demonstrator board that combines the competences of the different partners involved in the workpackage and was fabricated at the beginning of the project. The second one (second generation) is an improved version that was fabricated in the last year of the project after obtaining encouraging results with the embedded mirror configuration. Both demonstrator boards are discussed on the next sections. The substrates are diced into in a transmitter part and a receiver part, allowing us to evaluate both sides separately. The demonstrator boards have up to now been evaluated in a transmitter configuration.

7.2.1 First generation active demonstrator

The first NEMO demonstrator board contains the following parts:

- improved transmitter and receiver module on LTCC substrate, connected to the FR4 circuit board with BGAs (VTT),
- i-VCSEL array, which is a VCSEL array with integrated micro-lenses (CSEM),
- DPW pluggable out-of-plane coupler (VUB),
- array of four Truemode waveguides and a micro-cavity for the insertion of the pluggable coupler, both patterned into the optical layer using KrF excimer laser ablation (UGent).

The LTCC technology offers the possibility to implement precision structures for optical alignment directly onto the electronics packaging substrate. The 4-channel i-VCSEL array is wire-bonded on the bottom a cavity in the LTCC substrate, this in contrast to the previous design where the active components were mounted on top of the LTCC substrate. The cavity enables to adjust the separation between the VCSEL and the printed circuit board so that the optical components can fit in between, as is schematically shown in Fig. 7.5. The transmitter module is mounted on the printed circuit board with BGA solder balls. Pictures of the i-VCSEL and driver chip wire-bonded on the cavity on the LTCC substrate and of the LTCC module BGA-mounted on the printed circuit board are shown in Fig. 7.6.

The contribution of our group to this demonstrator is focused on the following tasks:

- application of a Truemode optical layer on the PCB. Truemode is chosen instead of SU-8, which was used for the original demonstrator, because of the lower propagation loss and the possibility to pattern the layer with use of KrF excimer laser ablation,
- patterning of an array of four waveguides with a cross-section of $50\ \mu\text{m} \times 50\ \mu\text{m}$ on a pitch of $250\ \mu\text{m}$ into the Truemode optical layer with use of KrF excimer laser ablation,
- patterning of a micro-cavity into the optical layer to accommodate the pluggable coupler,

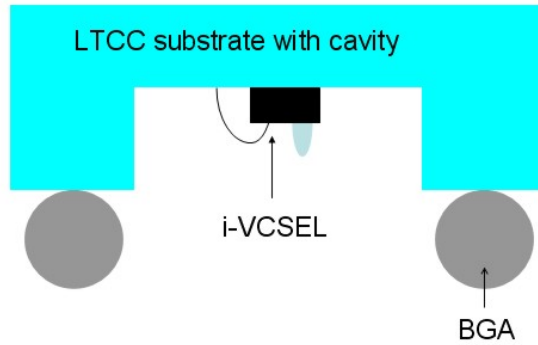
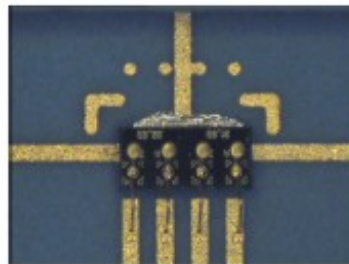
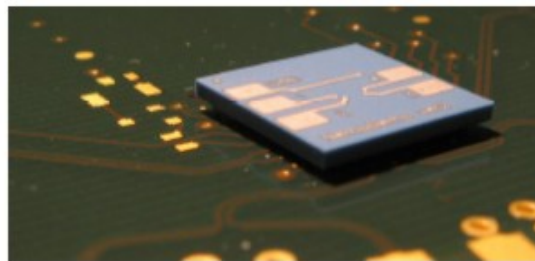


Figure 7.5: Schematic of the LTCC module: the i-VCSEL is wire-bonded in the cavity in the LTCC module. The cavity enables to adjust the separation between the VCSEL and the printed circuit board so that the optical components can fit in between.



(a)



(b)

Figure 7.6: (a) Picture of the i-VCSEL array wire bonded on the cavity in the LTCC module [4]; (b) picture of the LTCC module BGA mounted on the printed circuit board [4].

and are a direct application of the results from the PhD work described in the previous chapters.

Application of the optical layer

The Truemode optical layer is applied onto the PCB using spincoating. The optical material should only be deposited in the designated waveguide area, limited to the central region, in this way leaving the bond pads and electrical contacts free, as is schematically shown in Fig. 7.7. Therefore, the material should be removed from the remaining areas. The most convenient way to do this is the use of a photo-sensitive material, which can be patterned using standard UV-lithography through a suitable photo-mask. However, Truemode has to be UV-exposed in proximity mode in a nitrogen environment which excludes the use of the mask aligner that is available at our cleanroom facilities. Other photo-sensitive materials that can be UV-exposed in standard environment exist, but usually show a higher propagation loss and are not always favorable to the use of laser ablation. An example of such as material is Epocore/clad, of which the propagation is more than 5 times higher than Truemode and which is not have good ablation properties. In order to be able to use a Truemode optical layer, an alternative application method has to be found.

Different tests have been carried out in order to efficiently remove the excess material. In the first tests, the sample was covered with tape prior to the spincoating step, leaving only the waveguide region uncovered. The tape is removed after the spincoating of the layer. Problem with this approach is the accumulation of material near the edge of the tape, similar to the edge bead that occurs near the edge of the sample when layers are spincoated at low spinspeed. The accumulation of material increases with the number of layers that are applied, because of the relatively high thickness of the tape compared to the 50 μm thickness of the cladding and core layer, which makes it very difficult to control the thickness of the layers. The best results were obtained for the case where the polymer is deposited over the entire board and the excess material removed with a cleanroom wipe after the deposition step. A relaxation step, during which the sample rests on a bench for about 30 minutes, is required between the removal of the excess material and the UV-exposure step. In this way, the excess optical material that is pushed to the center during the removal step, can flow back to its original position. After the relaxation step there is still a small amount of excess material near the center of the optical layer, creating an optical layer with a slightly cylindrical cross-section. The homogeneity of the layer thickness is sufficiently high in order to be able to pattern the waveguides without any problems. The application and cross-linking of the Truemode optical layer is done with the parameters specified in 2.3.1.

Ablation of the waveguides

After the deposition of the two lower cladding layers and core layer, the waveguide core features are ablated into the core layer according to the procedure described in 3.4. The use of two lower cladding layer, with a total thickness of 100 μm , allows us to have a higher tolerance on the depth of the micro-cavity, which is ablated in the next step. It is clear that the alignment of the waveguides with respect to the position where the active components are mounted on the board is very important for the performance of the link. The alignment of the waveguides is done with the help of the alignment marks

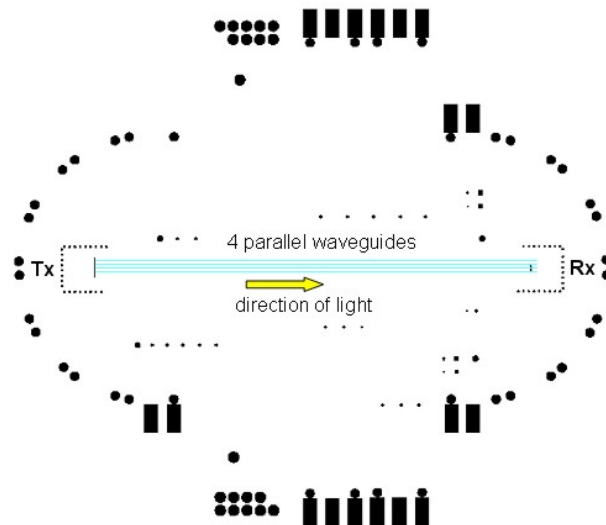


Figure 7.7: Schematic of the demonstrator board with an indication of the position of the array of four parallel waveguides, applied in the central region of the sample. The alignment of the waveguides on the board is done with the help of the alignment marks present on the substrate and the use of an alignment pulse.

that are present on the board, and the use of an alignment pulse, which was described in , and which is used to compensate for the shift in the direction perpendicular to the waveguides when the focus is moved from the alignment marks to the top surface of the core layer. After the ablation of the four waveguide cores with a cross-section of $\approx 50 \mu\text{m} \times 50 \mu\text{m}$ on a pitch of $250 \mu\text{m}$, the top cladding layer is spincoated, UV-exposed and cured in a convection oven.

Ablation of the micro-cavity

The next step is the ablation of the micro-cavity into the optical layer that is used to accommodate the DPW out-of-plane coupler. The cavity is ablated with the same parameters as were described in 5.3. The cavity has a depth of $170 \mu\text{m}$, allowing to optimize the position of the component along the cavity without damaging the mirror facet. The pluggable coupler contains a 45° micro-mirror that is used to deflect the light beam over 90° , based on the TIR that occurs at the PMMA-air interface. A more detailed description of the use of the pluggable coupler is given in chapter 5.

Characterization

Optical loss measurements were carried out on the demonstrator board to evaluate the performance of the current configuration. A first evaluation of the embedded mirror demonstrator was done in collaboration with VUB in a fiber-to-fiber scheme both in receiver and transmitter configuration, as is schematically shown in Fig. 7.8. The demonstrator board has first been measured in a receiver configuration. An 850nm light signal is coupled in horizontally into the waveguide with an optical fiber with

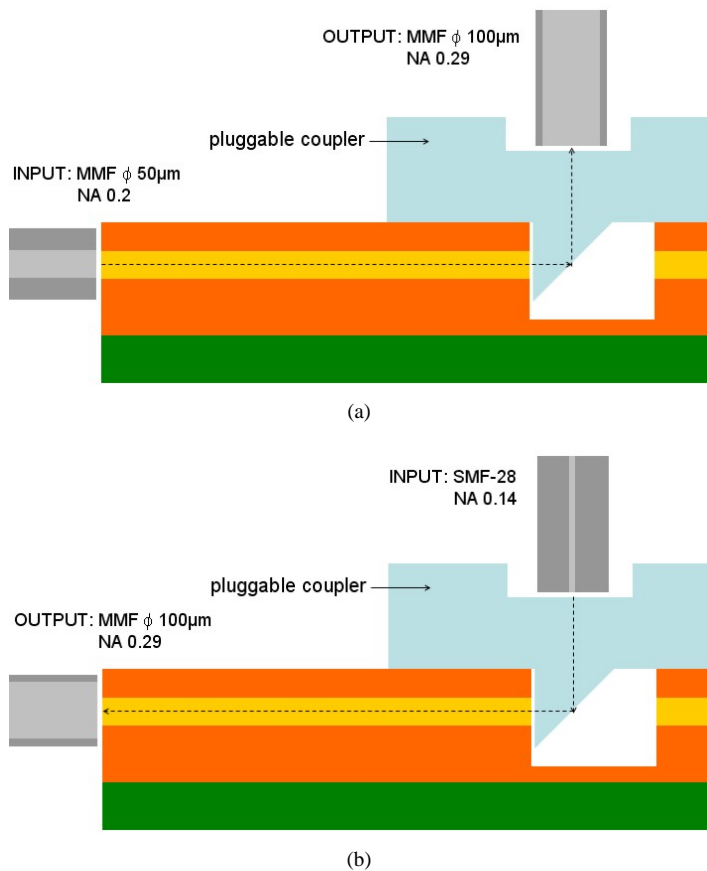


Figure 7.8: (a) Set-up used to measure the first generation demonstrator board in a fiber-to-fiber scheme in a receiver configuration; (b) set-up used to measure the first generation demonstrator board in a fiber-to-fiber scheme in a transmitter configuration.

core diameter 50 μ m and NA 0.2. The light signal then propagates in the 4.5 cm long waveguide Truemode waveguide, which has a cross-section of 50 μ m \times 50 μ m and NA 0.3, until it is deflected over 90 $^\circ$ at the TIR mirror of the pluggable coupler. The out-coupled light spot is captured with an optical fiber with core diameter 100 μ m and NA 0.29. The measured overall link loss is 5.6dB, corresponding to a link efficiency of 27.5%. A plot of the light spot that is coupled out at the pluggable coupler is shown in Fig. 7.9.

The board is in a next step measured in a fiber-to-fiber scheme in transmitter configuration, schematically shown in Fig. 7.8(b). An 850nm light spot is in this case coupled in vertically at the pluggable coupler with an SMF-28 fiber, which has a core diameter of 9.3 μ m and NA 0.13. The light spot is deflected over 90 $^\circ$ at the TIR mirror facet and coupled into the Truemode waveguide. The light spot that is coupled out at the waveguide output facet is detected with an optical fiber with core diameter 100 μ m and NA 0.29. The measured overall link efficiency is -3dB, corresponding to a link

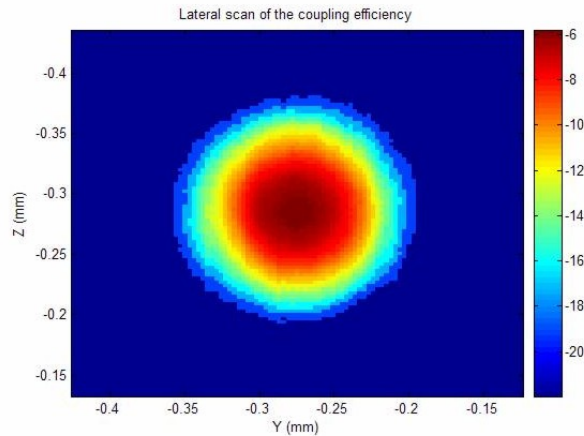


Figure 7.9: Plot of the light spot that is coupled out at the pluggable coupler (courtesy of VTT).

efficiency of 50%. The link efficiency is in this case much higher than the one in the receiver configuration, mainly because of the larger amount of rays that satisfy the TIR condition.

The final evaluation of the performance of the board is done at VTT [4]. Loss measurements have been carried out in a transmitter scheme, with use of the transmitter module. An 850nm light signal is coupled in vertically using an i-VCSEL, which is mounted on the bottom of a cavity in the LTCC module. The light spot is deflected over 90° at the TIR mirror of the pluggable coupler and coupled into the Truemode waveguide. The light then propagates in the 4.5 cm long waveguide until it is coupled out at the waveguide output facet and detected with an optical fiber with core diameter $200 \mu\text{m}$ and NA 0.22. The measured overall link loss is 10.4dB, which is higher than the link loss measured on the board in the fiber-to-fiber scheme in transmitter configuration. This is mainly because of the relatively big distance between the i-VCSEL and the mirror facet, which is on the order of $100 \mu\text{m}$ to $200 \mu\text{m}$.

Alignment tolerance measurements were carried out, before the BGA assembly, by attaching the transmitter on a moving stage (Newport AutoAlignment Station 8100) and by measuring the outcoupled optical power as a function of the misalignment in lateral direction. The alignment tolerance for an excess loss of 1dB is $\pm 16 \mu\text{m}$ along the mirror facet and $\pm 10 \mu\text{m}$ in the direction perpendicular to the mirror facet.

When compared to the original demonstrator board that was designed by VTT, this design requires higher alignment accuracies, because it does not provide the expanded beam concept. However, the optical link contains less components, which makes the assembly process simpler and potentially more cost-effective. We assume that the link loss of this demonstrator board is higher than the one measured on the original demonstrator board. A link loss of 19dB was measured on the original demonstrator board, in which case the evaluation is done over the entire link, from the transmitter to the receiver side. This in contrast to the 10.4dB link loss measured on this demonstrator board, in which case the transmitter part is evaluated separately.

The coupling efficiency can be increased by using an enhanced pluggable coupler,

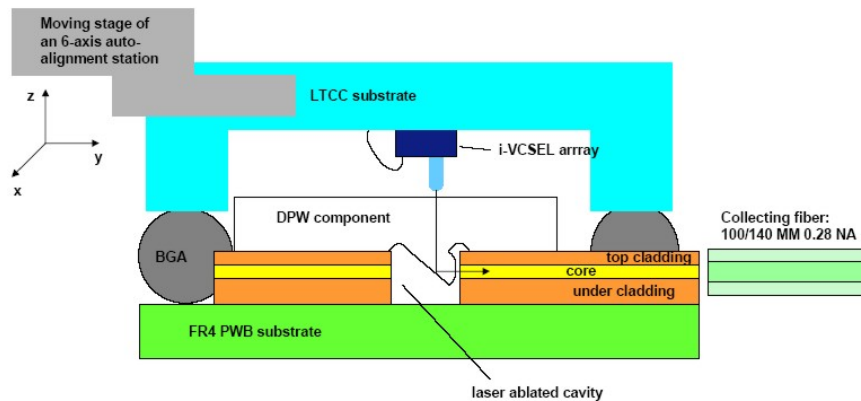


Figure 7.10: Schematic of the built-up of the first active demonstrator board with the use of the lensed DPW insert.

as was reported in [5], which contains an integrated micro-lens and has a reduced thickness between the top of the mirror and the flat top. Loss measurements were carried out at VTT using the measurement set-up that is schematically shown in Fig. 7.10. The DPW insert contains an integrated micro-lens at the vertical wall of the pluggable coupler, to collimate the light spot that is coupled in into the Truemode waveguides at the vertical cavity wall. The mirror facet has a height and width of $140 \mu\text{m}$, the thickness of the PMMA between the top of the mirror and the flat top exit facet is $\approx 300 \mu\text{m}$. The measured overall link loss is in this case 7.9dB, which is 2.5dB better than the results obtained with the standard pluggable coupler. We do have to notice that the detector fiber is in this case a MMF with core diameter $100 \mu\text{m}$ and NA 0.28. The alignment tolerance range for an excess loss of 1dB is identical to the results obtained with the standard pluggable coupler, mainly because of the position where the micro-lens is integrated.

7.2.2 Second generation demonstrator board

After the encouraging results obtained with the embedded mirror insert configuration, which was described in 5.3, it was decided to fabricate a second generation demonstrator board, which contains an embedded mirror insert instead of a pluggable out-of-plane coupler. The dry film formulation of the Truemode core material became available around the same time and was preferred over the wet film formulation because of the possibility to use UV-lithography in contact mode in standard environment for the patterning of the waveguide cores into the optical layer. In this way, not only the throughput but also the achievable alignment accuracy is increased. There is currently no dry film formulation available for the Truemode cladding material, meaning that the wet film formulation has to be used which is UV-exposed in proximity mode in nitrogen environment. The lower and top cladding layer are spincoated over the entire board, allowing a better uniformity in the layer thickness across the board. The bondpads however have to stay opened for the assembly of the active opto-electronic components. This can be done using the CO_2 laser for the opening of the optical layer up to

the bondpads. A couple of KrF excimer laser pulses are used to remove the last bits of optical material from the bondpad, allowing a good electrical contact. The opening of the electrical contacts and bondpads is done in a final phase of processing, after the embedding of the mirror insert. The embedded mirror insert and the remaining part of the waveguide array is during this step covered with a low adhesion tape to avoid the deposition of debris in this area.

The tasks carried out by our group are the following:

- application of the dry Truemode optical layer.
- patterning of the waveguide cores into the optical layer with use of UV-lithography in standard environment through a mask that is placed in contact mode. The mask contains an array of four waveguides with a cross-section of $\approx 50 \mu\text{m} \times 50 \mu\text{m}$ on a pitch of $250 \mu\text{m}$ and the same alignment marks as the ones that can be found on the PCB substrate.
- ablation of a micro-cavity containing a vertical wall, which is used as the waveguide output facet, for the insertion of the discrete mirror.
- glueing of the mirror insert on the copper bottom of the cavity.
- filling of the ablated cavity with cladding material.
- opening of the bondpads with use of CO_2 and KrF excimer laser ablation.
- manual polishing of the waveguide input facet.

The mirror is embedded into the optical layer according to the procedure described in 5.3. In order to obtain an optimal coupling efficiency, the center of the mirror facet has to be aligned with the center of the i-VCSEL. The mirror insert is pushed as close as possible to the vertical wall of the cavity, which corresponds to the waveguide output facet, in order to minimize the distance between the waveguide output facet and the mirror facet. This means that the position of the mirror insert is determined by the position of the vertical wall. The vertical wall has to be ablated at a distance of $65 \mu\text{m}$, corresponding half the length of the mirror facet, from the ideal position of the mirror insert, where the center of the mirror facet is aligned with the i-VCSEL. A good alignment is possible if the mirror is pushed close enough to the vertical wall. After the insertion of the mirror in the micro-cavity and the fixation to the cavity bottom with a drop of thermally curable glue, the cavity is filled with cladding material.

Characterization

A first evaluation of the embedded mirror demonstrator was done in collaboration with VUB in a fiber-to-fiber scheme in both a receiver and a transmitter configuration. The demonstrator board has first been measured in a receiver configuration, as is schematically shown in Fig. 7.11(a). An 850nm light signal is coupled in horizontally into the waveguide with an optical fiber with core diameter $50 \mu\text{m}$ and NA 0.2. The light signal then propagates in the 4.5 cm long Truemode waveguide, which has a cross-section of $50 \mu\text{m} \times 50 \mu\text{m}$ and NA 0.3, until it is deflected at the metallized mirror facet. The outcoupled light spot is captured with an optical fiber with core diameter $100 \mu\text{m}$ and

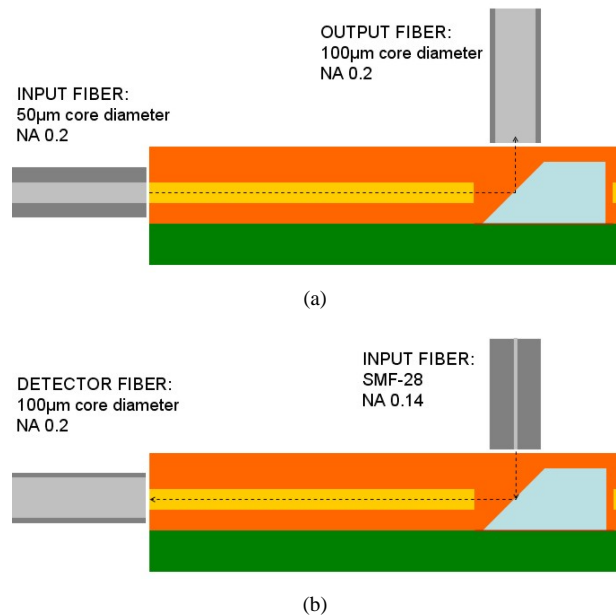


Figure 7.11: (a) Set-up used to measure the second generation demonstrator board in a fiber-to-fiber scheme in a receiver configuration; (b) set-up used to measure the second generation demonstrator board in a fiber-to-fiber scheme in a transmitter configuration..

NA 0.29. The measured overall link loss is 2.5dB, corresponding to a link efficiency of 56%, which is more than 3dB better than the measurement results obtained with the pluggable out-of-plane coupler. A picture of the demonstrator board with the embedded mirror on the measurement set-up in the fiber to fiber scheme in a receiver configuration is shown in Fig. 7.12. A red light source is in this case used to show the 90° fiber-to-fiber light pad.

The board is in a next step measured in a fiber-to-fiber scheme in a transmitter configuration, as is schematically shown in Fig. 7.11(b). In this case, an 850nm light spot is coupled in vertically at the embedded mirror with an SMF-28 fiber, which has a core diameter of 8.2 μm and NA 0.14. The light spot is deflected at the metallized mirror facet and coupled into the Truemode waveguide. The light spot that is coupled out at the waveguide output facet is detected with an optical fiber with core diameter 100 μm and NA 0.29. The measured overall link efficiency is -3.23dB, which is slightly lower than the efficiency measured in the receiver scheme. This is probably a consequence of the build-up of the mirror which forces the incoupled light spot to propagate in the cladding material after the deflection at the mirror facet prior to reaching the waveguide input facet.

The board has then been evaluated at VTT research institute. The board is measured in a transmitter scheme, with this time the LTCC module with the i-VCSEL at the input side and an optical fiber with core diameter 100 μm and NA 0.29 as detector fiber. The transmitter module can be mounted on the PCB with BGAs by using a flip-chip

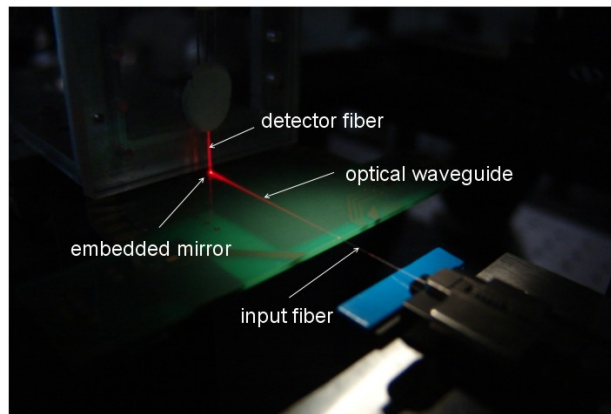


Figure 7.12: Picture of the demonstrator board with the embedded mirror on the measurement set-up in a fiber to fiber scheme in a receiver configuration.

bonder, or alternatively, it might be assembled with a high precision SMT pick-and-place machine. The distance between the output of the i-VCSEL and the top surface of the optical layer is $100\ \mu\text{m}$ to $200\ \mu\text{m}$. Alignment tolerance measurements were done before the BGA assembly by attaching the transmitter module onto a moving stage (Newport AutoAlignment Station 8100) and measuring the outcoupled optical power as a function of misalignments in the lateral direction. The overall efficiency of the optical link with the embedded mirror is -4.5dB . This value can probably be improved by minimizing the distance between the i-VCSEL and the optical layer, in this way minimizing the diffraction of the outcoupled light spot. The alignment tolerance for an excess loss of 1dB is $\pm 20\ \mu\text{m}$ along the mirror facet and $\pm 16\ \mu\text{m}$ perpendicular to the mirror facet, which is a bit more relaxed than the results obtained for the first generation demoboard.

7.2.3 Conclusion

Two different active demonstrator boards have been designed and evaluated, based on a $4 \times 10\text{Gb/s}$ optical interconnect demonstrator that was fabricated at VTT. The performance of the boards has first been evaluated in a fiber-to-fiber scheme in collaboration with VUB. The results are summarized in Table 7.1. The boards have then been evaluated by VTT in a transmitter scheme, this time using the LTCC module with the integrated i-VCSEL at the input side. The results of these measurements are summarized in Table 7.2. From these results, we can conclude that we succeeded in improving the performance of the first generation demonstrator board. Based on the characterization results, we assume that the performance of the second generation demonstrator board is better than the one of the original demonstratorboard that was fabricated at VTT, even though we did not carry out loss measurements over a complete link, from transmitter to receiver side.

The first generation boards were very useful to more acquainted with the technologies of the different partners and to get familiar with the design of the demonstrator. However, the performance of the board was not as good as expected and we were not able to

demonstrator board	first generation	second generation
coupling component	pluggable coupler	embedded mirror
receiver configuration	5.6dB (27.5%)	2.5dB (56%)
transmitter configuration	3dB (50%)	3.23dB (47.5%)

Table 7.1: Link loss (link efficiency) of the first and second generation demonstrator boards, carried out in collaboration with VUB in a fiber-to-fiber scheme in a receiver respectively transmitter configuration.

demonstrator board	first generation	second generation
coupling component	pluggable coupler	embedded mirror
detector fiber	MMF ϕ 200 μm , NA 0.22	MMF ϕ 100 μm , NA 0.29
link loss	10.4dB (9%)	4.5dB (35.5%)

Table 7.2: Link loss (link efficiency) of the first and second generation demonstrator boards, carried out at VTT in a transmitter scheme using the LTCC module with the integrated i-VCSEL.

improve the performance of the original VTT demonstrator board. The performance of the second generation demonstrator board exceeds by far the performance of the first generation board. This is mainly because of the high coupling efficiencies that can be obtained with the use of the embedded mirror insert. This again confirms the potential of the embedded mirror for the 90° beam deflection in board-level optical interconnects. The performance of the board could be improved by optimizing the distance between the i-VCSEL and the top of the optical layer. In the end, we can conclude that it is possible to get a good result on a relatively short time-scale by combining the competences and technologies of different partners, which was exactly the aim of the network of excellence on micro-optics. The Truemode waveguides, the ablated waveguides in the wet film formulation as well as the UV-defined waveguides in the dry film formulation, are valuable for the in-plane light propagation. The embedded mirror approach is very useful for the coupling of the light in and out of the optical layer. This means that the building blocks that were discussed in the previous chapters, can be used in functional demonstrator boards.

7.3 In-plane connector

In contrast to the active demonstrator, where light is coupled in and out vertically, it is in some cases necessary to couple the light signal in and/or out horizontally, directly in the plane of the optical layer without first deflecting the light signal over 90° . For this purpose, VUB and UGent designed an in-plane connector, the design of which is given in Fig. 7.13. The details on the design and the fabrication of the connector are given in the following paragraphs. The in-plane connector is intended to be mounted on an optical PCB that contains an array multimode waveguides with cross-section 50

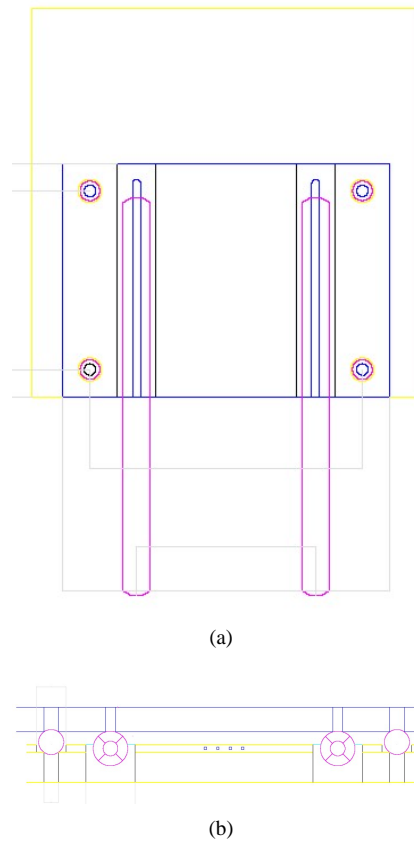


Figure 7.13: (a) CAD drawing of the top view of the in-plane connector; (b) CAD drawing of the side view of the in-plane connector (courtesy of VUB).

$\mu\text{m} \times 50 \mu\text{m}$ on pitch $250 \mu\text{m}$. The array contains four UV-defined waveguides in our case. The reason for this is the availability of the mask that was used for the patterning of the waveguides on the active demonstrator. The alignment between the waveguides that are integrated on the PCB and the array of fibers that are positioned in the connector is done passively.

7.3.1 Connector design

The connector design is based on the design of an MT (mechanically transferable) connector, which is used to couple light between two fiber ribbons, schematically shown in Fig. 7.14. The connector ferrule, the part of the connector that is used for fiber alignment, contains fiber capillaries on a pitch of $250 \mu\text{m}$ into which typically 8 to 12 fibers with an outer diameter of $125 \mu\text{m}$ are positioned. Guiding pins on either end of the fiber row help to align the connector ferrules during mating. These precise steel guiding pins, which have a diameter of $699 \mu\text{m} \pm 0.5 \mu\text{m}$ are located in very precise pin holes. The distance between the centre of both MT guiding pins is 4.6 mm. The

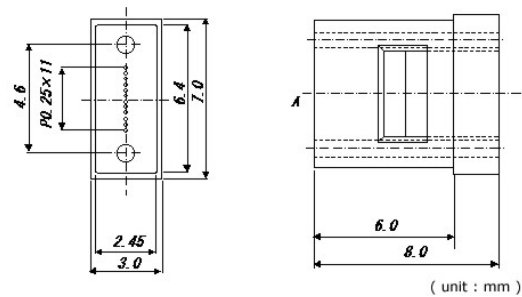


Figure 7.14: Schematic of an MT connector. The connector ferrule contains fiber capillaries on a pitch of $250\ \mu\text{m}$ into which typically 8 to 12 fibers with an outer diameter of $125\ \mu\text{m}$ are positioned. The MT guiding pins are positioned at a distance of 4.6 mm from each other, and are used to help align the ferrules during mating [7].

dimensional tolerances on these aligning features are within $1\ \mu\text{m}$. The pre-alignment of the ferrules is guaranteed by the surrounding connector housing (MPO (multifiber pull off) or MTP (mechanical transfer pull off)). The mating between the connectors is realized by a simple push-pull mechanism.

The in-plane connector that is discussed here is used to couple light signals from an array of polymer multimode waveguides to an array of optical fibers and vice versa in an efficient way. This in contrast to a standard MT connector, that is used to couple light between two optical fiber arrays. What we mainly want to copy from the MT connector is the user-friendly approach. The polymer waveguides have a cross-section of $50\ \mu\text{m} \times 50\ \mu\text{m}$ on a pitch of $250\ \mu\text{m}$ and are integrated on top of the PCB. The array of optical fibers is positioned in the connector in an alignment plate on a pitch of $250\ \mu\text{m}$. The alignment principle is schematically shown in Fig. 7.15, and in more detail in Fig. 7.16.

The main requirements on the connector are a good lateral and vertical alignment between the optical fibers and the polished end facet of the polymer multimode waveguides. The connector consists of two separate parts that are put together, perpendicular with respect to each other:

- the base plate contains two predefined rectangular trenches, used to glue the MT guiding pins to the base plate, and four predefined circular alignment features, used to connect the base plate to the PCB, parallel to the optical waveguides, by placing it on the micro-spheres that are glued on the PCB into circular openings. The predefined features that are used for the positioning of the MT guiding pins and for the connection of the base plate onto the PCB are patterned in the same processing step, in this way allowing a high achievable alignment accuracy.
- the alignment plate contains micro-holes into which the optical fibers are inserted and two circular openings with a diameter of $700\ \mu\text{m}$. This plate is used to position the optical fibers in the correct way with respect to the polymer waveguides. The alignment plate is slid over the MT guiding pins. The fiber alignment plate is in this way connected to the base plate. The capillaries and the two circular openings are patterned in the same processing step.

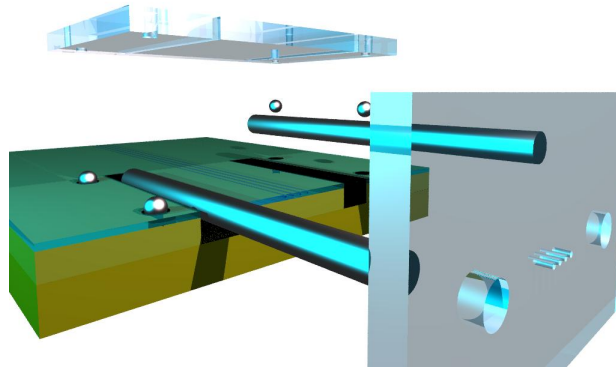
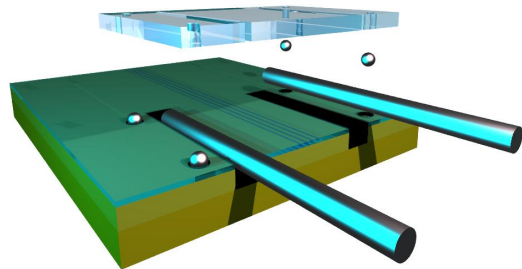


Figure 7.15: Schematical representation of the alignment principle of the in-plane connector. The microspheres are used to arrange the vertical and lateral alignment, the MT guiding pins are used to arrange the alignment between the array of optical fibers and the polymer waveguides with the help of a fiber alignment plate that can be slid over the MT pins (courtesy of VUB).

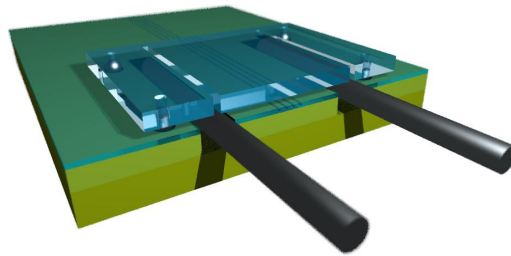
The alignment is arranged in two steps in the following way:

- the microspheres are used to arrange the alignment in lateral and vertical direction. They have a diameter of $508 \mu\text{m}$ and are glued into circular openings with a diameter of $300 \mu\text{m}$ in the PCB, as is schematically shown in Fig. 7.17(a), with the associated dimensions. As can be seen in the figure, the depth of the circular opening is not very critical. The base plate is placed on the PCB, parallel to the optical layer, by fixing it to the microspheres. The sphere sticks out of the PCB over $450 \mu\text{m}$, determined by the $300 \mu\text{m}$ diameter of the circular opening, and in this way defines the vertical position of the base plate. The lateral position of the base plate is defined by the position of the micro-spheres on the PCB. The base plate contains circular cavities with a depth of $110 \mu\text{m}$ and a width of $418 \mu\text{m}$ in order to be able to position it onto the microspheres in a stable way.
- the MT guiding pins are glued onto the base plate in predefined trenches with a width of $200 \mu\text{m}$. They rest in the rectangular openings in the PCB after the connection of the base plate, without touching the bottom of the opening because this would disturb the vertical position of the base plate, as is shown in Fig. 7.17(b).
- the fiber alignment plate is slid over the MT guiding pins to arrange the alignment between the fibers and the polymer waveguides.

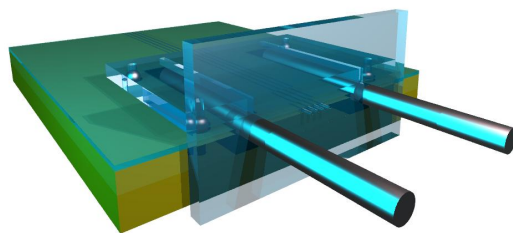
Different processing steps are required for the fabrication of the in-plane connector such as: patterning of the alignment features in the PCB, application of the optical layer and patterning of the waveguide array, mounting of the microspheres onto the PCB, glueing of the MT guiding pins to the base plate and putting together the different parts



(a)



(b)



(c)

Figure 7.16: (a) The PCB contains rectangular openings to accommodate the MT guiding pins, which are glued to the base plate. It also contains circular openings into which the microspheres are glued; (b) the base plate is positioned on the PCB, parallel to the optical layer, with the help of the microspheres; (c) the fiber alignment plate is slid over the MT guiding pins with the help of predefined circular openings. In this way, the alignment between the optical fibers and the polymer waveguides is arranged (courtesy of VUB).

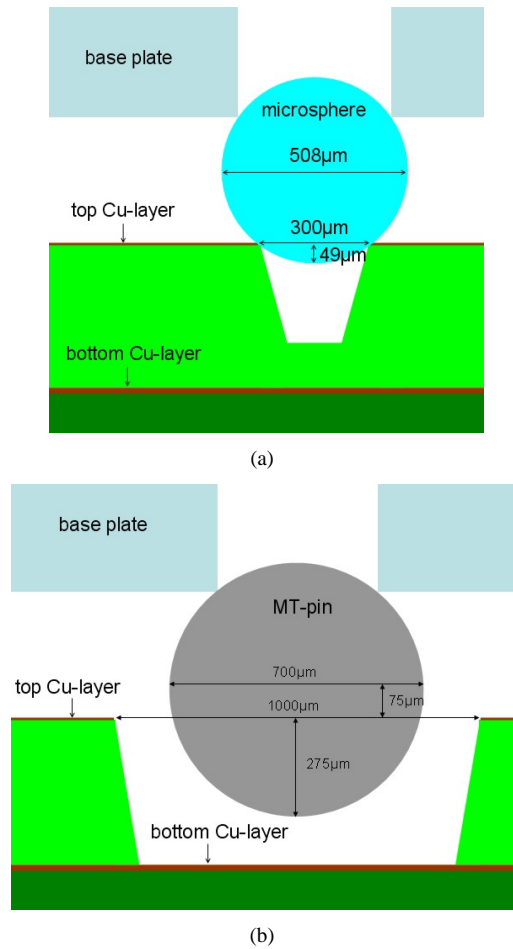


Figure 7.17: (a) Schematic view of the base plate that is attached to the PCB with microspheres, which are glued into circular openings on the PCB; (b) schematic view of the MT guiding pins, which are glued to the base plate and float in the rectangular opening in the PCB.

of the connector. The different steps are discussed in more detail in the remaining part of this section. The aim is to make a prototype of an in-plane connector by combining the capabilities of different partners, who have the following contributions:

- the base plate and the fiber alignment plate are patterned into PMMA using DPW (VUB),
- the patterning of the alignment features in the PCB is done using laser ablation (UGent),
- the application of the optical layer, which is integrated on the PCB, and the patterning of the waveguide array (UGent),
- the mounting of the different connector parts and of the fibers into the fiber alignment plate (VUB and VTT).

7.3.2 Processing of the PCB substrate

The first step in the process flow is the fabrication of a suitable PCB substrate. As was already mentioned, the PCB contains following alignment features:

- two rectangular openings with a width of 1 mm and a length of 1 cm, patterned in the substrate using laser ablation. They are not used for alignment purposes but to accommodate the MT guiding pins, which have a diameter of $699\mu\text{m} \pm 5\mu\text{m}$. The depth of the openings has to be $\geq 360\mu\text{m}$, to make sure that the MT-pins do not touch the bottom of the ablated trench.
- circular openings are ablated into the PCB for the positioning of the microspheres onto which the base plate is fixed. The microspheres are used to arrange the alignment in lateral and vertical direction. The diameter and position of the openings have to be very accurate for this reason, because they determine the accuracy with which the base plate is mounted onto the PCB.

The MT guiding pins are glued onto the base plate and float in the rectangular openings after the positioning of the base plate on the micro-spheres. The available FR4 substrates typically have a thickness ranging from 1 mm up to 1.6 mm. CO₂ laser ablation can be used to selectively remove the FR4 material in the designated areas. The ablation of the FR4 material is accompanied with a considerable amount of debris deposition and burning because of the thermal nature of the ablation process. In addition, it is difficult to accurately control the ablation depth. A solution to this problem is the use of a Cu-coating, that can serve as an ablation stop layer for the CO₂ laser ablation. In case an extra layer is laminated on the Cu-coated FR4 substrate, it is possible to control the ablation depth by ablating up to the underlying Cu-layer.

The laminated layer has to be compatible with the FR4 substrate and has to be laser patternable. The most obvious choice for the lamination are the following:

- prepreg sheets (Duraver), which are a high T_g base material of the same epoxy system type like FR4. The sheets can be patterned with use of CO₂ laser ablation. The ablation is accompanied with a considerable amount of debris deposition caused by the ablation of the glass fibers that are incorporated in the sheets for mechanical and thermal stability.

- resin sheets, which are RCC (Resin Coated Cu) foils (Isofoil 160i), designed for microvia board fabrication. They can be easily patterned using CO₂ laser ablation, with clean ablated features and a low deposition of debris.

For an optimal result it is best to laminate the same stack of layers on both sides of the Cu-coated FR4 substrate. Two different stacks are considered and evaluated:

- for the first type of substrate, schematically shown in Fig. 7.18(a), a stack of two prepreg sheets with a thickness of 180 μm and a sheet of RCC with 35 μm resin and 5 μm Cu are laminated on both sides of the Cu-coated FR4 substrate. The resulting substrate is very similar to the original FR4 substrate, except for the two integrated Cu-layers. The Cu-coating on the FR4 substrate has a thickness of 18 μm and is used as an ablation stop layer. The Cu-layer at the top surface of the substrate after the lamination step has a thickness of 5 μm and is used as a mask for the ablation of the alignment features with the CO₂ laser. The laminated layer has a total thickness of 395 μm , not counting the Cu-layers. A cross-section of the laminated substrate is shown in Fig. 7.19.
- in the second substrate type, two openings with a width of 2 mm and a length of 1 cm at a distance of 5.6 mm from each other are ablated into the prepreg sheets before the lamination. The openings are located in the area where the rectangular and circular openings have to be ablated. The same stack is laminated as was the case for the first type of substrate, except that in this case the prepreg sheets contain two openings, which have to be appropriately aligned with respect to each other before the lamination step. During the lamination, the resin starts to flow and fills up the opened zones in the prepreg sheets. The resin sheets does not have glass fibers incorporated in them, allowing a clean ablation in this region with a low deposition of debris and limited amount of burning. A surface roughness plot and surface corrugation measurement of the laminated stack are shown in Fig. 7.20. The only problem is the height difference between the filled openings and the remaining part of the substrate, which is approximately 13 μm . This height difference has to be taken into account in the design of the connector in order not to disturb the vertical alignment of the base plate. Special attention also has to be given to the height difference between the area where the optical layer is deposited and the remaining part of the substrate. From the surface corrugation plot, it can be seen that this value differs from the height difference between the filled opening and the unopened substrate part.

The same lamination cycle is used for the two substrate types. The progress of temperature and pressure during the lamination cycle is shown in Fig. 7.21. The top Cu-layer can be used as a mask for the ablation of the rectangular and circular openings in the laminated stack, hence improving the quality of the ablated structures. The openings in the top Cu-layer are made with use of the frequency tripled Nd-YAG laser (355nm), which selectively ablates the Cu-material without ablation of the prepreg and resin. The movement of the laser beam is computer-controlled, allowing a high achievable alignment accuracy between the rectangular and circular openings. After the patterning of the top Cu layer with Nd-YAG laser, the openings in the laminated stack are ablated with the CO₂ laser. The top and side view of the circular and rectangular openings are schematically shown in Fig. 7.22. As was already mentioned, the rectangular openings

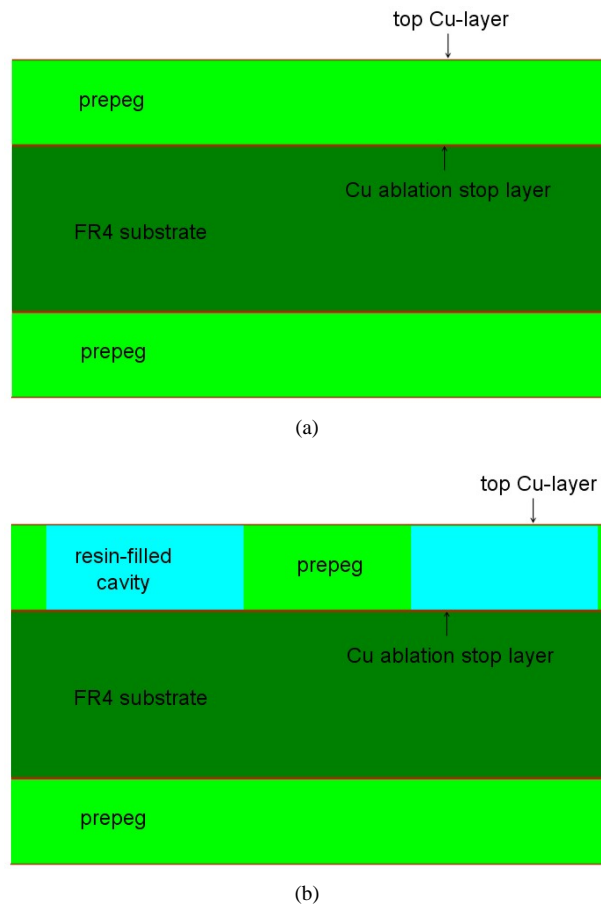


Figure 7.18: (a) Cross-section of the first substrate type in which case two prepreg layers and an RCC layer are laminated on both sides of the FR4 substrate; (b) cross-section of the second substrate type in which case openings are made into the prepreg sheets in the areas where the openings are to be ablated. The openings are during the lamination filled with resin.

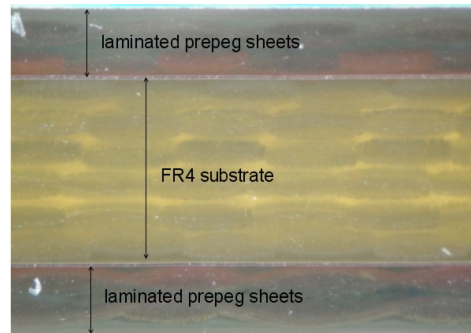


Figure 7.19: Cross-section of the Cu-coated FR4 substrate onto which two prepeg layers and an RCC layer are laminated on each side.

are ablated up to the underlying Cu-layer whereas an ablation depth a bit higher than $50\ \mu\text{m}$ is sufficient for the circular openings.

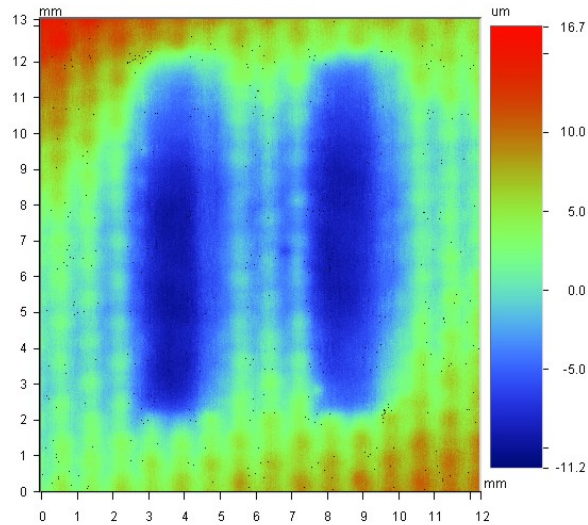
7.3.3 Application of the optical layer

There are no alignment features present in the top Cu-layer, which are required to properly align the mask with respect to the sample. It also turns out to be impossible to ablate them into the top Cu-layer with the required accuracy using a frequency tripled Nd-YAG laser. The alignment features could be etched into the Cu-layer, but this requires the fabrication of a new mask which is at this moment not interesting in view of the fact that the fabricated connector is a first prototype and not yet an improved version. In addition, there is only a small range of coloring between the Cu and the underlying prepeg material, which makes the alignment step a time-consuming task.

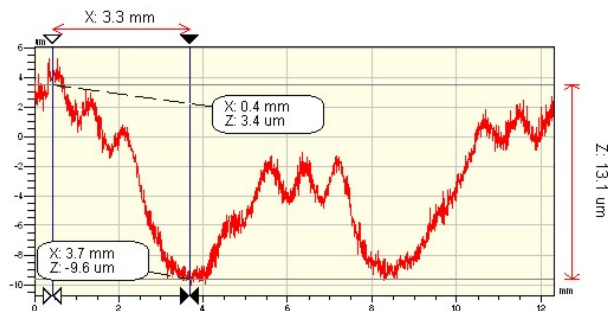
A possible solution is to first apply the lower cladding and patterned core layer. The waveguide cores can then in a next step be used to properly align the ablated rectangular and circular openings with respect to the waveguide cores. Despite the relatively high optical loss at $850\ \text{nm}$, Epocore/clad was chosen for the polymer optical layer, because it can be UV-exposed in contact mode on the mask aligner through the available mask, that was also used for the active demonstrator. The top Cu-layer can be etched open in the zone where the optical layer is to be applied to improve the adhesion between the optical layer and the substrate. The adhesion between the optical material and the Cu-layer was on some boards not sufficient to survive the manual polishing step that is required to prepare the end facets of the optical PCB.

7.3.4 Ablation of the openings in the laminated stack

First, the pattern of rectangular and circular openings is ablated into the top Cu-layer with a Nd-YAG laser in the same ablation step. The alignment between the ablated features and the waveguides is done with the help of the non-coated waveguide cores. The waveguide cores can be clearly seen with the camera on the ablation set-up and are used as a reference point for the ablation of the openings. The circular openings have a diameter of $300\ \mu\text{m}$ and are located at a distance of $7\ \text{mm}$ from each other, in both



(a)



(b)

Figure 7.20: (a) Surface roughness plot of the substrate after the lamination step. The two rectangular openings with a width of 2 mm and a length of 1 cm can be clearly observed; (b) surface corrugation of the substrate in the region with the openings in the prepreg, that are filled with resin during the lamination step. The height difference between the resin-filled openings and the remaining part of the substrate is $\approx 13 \mu\text{m}$. The central zone that is slightly higher than the filled openings is the area where the optical layer is deposited. These height differences have to be taken into account in the connector design for a good performance.

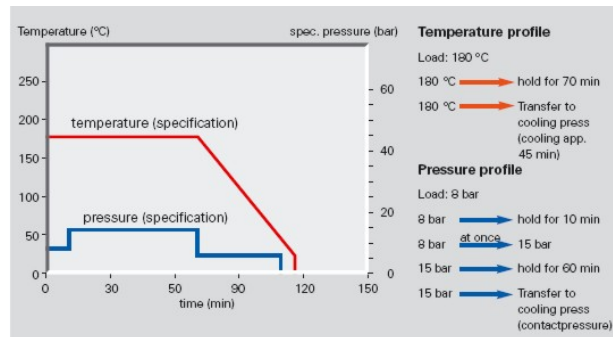
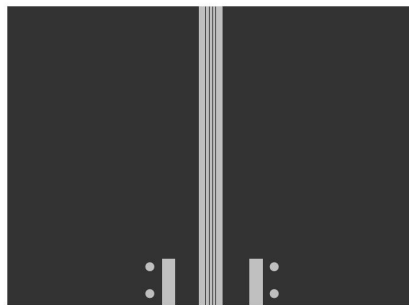
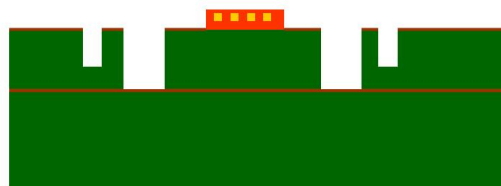


Figure 7.21: Progress of temperature and pressure during the lamination cycle that is used for the fabrication of the PCB substrates [6].



(a)



(b)

Figure 7.22: (a) Top view of the rectangular and circular openings that are ablated into the PCB substrate. The light gray colour indicates the zones where the Cu-layer is opened. The optical layer is deposited in the opened area in the center of the sample; (b) side view of the openings that are ablated into the PCB substrate for the fixation of the MT-alignment pins and the micro-spheres that are used for the fixation of the base plate. The array of four waveguides is positioned in the centre of the sample.

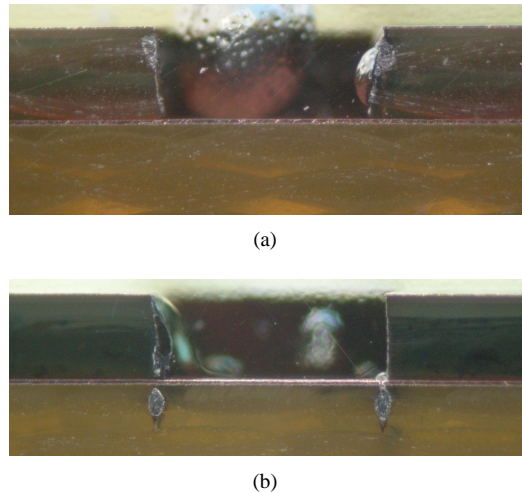


Figure 7.23: (a) Cross-section of a rectangular opening, ablated into prepeg; (b) cross-section of a rectangular opening, ablated into resin-filled openings in the prepeg sheets.

lateral directions. The rectangular openings have a width of 1 mm and a length of 1.5 cm; the center of the openings are located at a distance of 4.6 mm from each other, in correspondance with the distance between the center of the MT guiding pins in an MT connector. For stability reasons, the circular openings are ablated 5 mm away from the edge of the sample.

After the patterning of the top Cu-layer, this layer serves as a mask for the ablation of the underlying prepeg or RCC material. The CO₂ laser selectively ablates the prepeg and RCC without touching the Cu. As was already mentioned, the rectangular openings are ablated up to the underlying Cu-layer. A cross-section of an ablated rectangular opening in prepeg and RCC respectively are shown in Fig. 7.23. From these pictures it is clear that the edges of the opening ablated in RCC are much smoother and less tapered. The bottom of the opening is in this case also cleaner than in the case of the prepeg, mainly because of the fact that the fibers in the prepeg are not ablated very easily. A picture of the top view of the rectangular and circular openings is given in Fig. 7.24.

It is clear that the opening of the top Cu-layer in the central region for the application of the optical layer and next to it for the rectangular and circular openings can be done in one processing step using photolithography. In this case the sample is covered with photoresist and is UV-exposed through a suitable mask. After the development step, the part of the sample where the Cu-layer has to remain is covered with photoresist. The zones where the photoresist is washed off are selectively etched. However, this requires the design and fabrication of a suitable mask and is for that reason better done after the optimization of the connector design. This in contrast to the existing connector, which is intended to serve as a prototype.

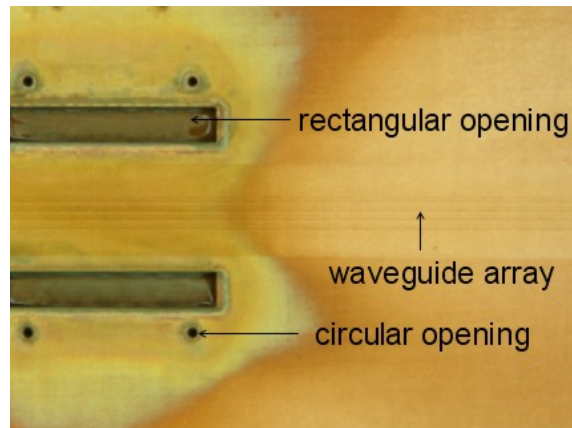


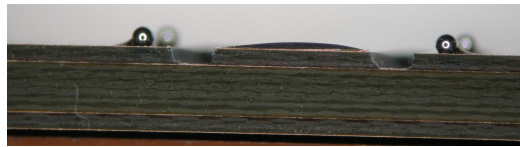
Figure 7.24: Picture of the top view of the circular and rectangular openings, ablated into the optical PCB.

7.3.5 Insertion of the micro-spheres

The micro-spheres have a diameter of $508 \mu\text{m}$ and are inserted into the circular openings in the substrate, which have a diameter of $300 \mu\text{m}$. The diameter of the holes has to be very accurate because it determines the part of the micro-sphere that is stuck in the hole and the part that sticks out. The spheres are glued into the circular holes with a UV-curing adhesive. Shear test measurements have been carried out to determine the strength necessary to push a micro-sphere is fixed into the circular cavity out of its glued position. This test shows that a shear force of 80g is needed to remove the micro-sphere from its original position, meaning that the four microspheres deliver a shear force of 320g. This should be more than sufficient to hold the in-plane connector structure, which consists of the base plate and the alignment plate into which the fibers are fixed. Fig. 7.25 shows a sideview and topview of the micro-spheres glued into the circular openings. This picture is taken of one of the first demonstrator boards, for this reason the distance between the polished end facet and the first circular opening is smaller than the before mentioned 5 mm. The optical waveguides are in this applied directly on the Cu-layer.

7.3.6 Mounting of the base plate and the fiber alignment plate

After the fixation of the microspheres to the optical PCB, the base plate can be mounted by placing it on the microspheres using the predefined trenches that were patterned in the base plate. After the fixation of the base plate on the optical PCB, the fiber alignment plate, with the optical fibers inserted in the fiber capillaries, is slid over the MT guiding pins. The alignment between the polymer waveguides and the optical fibers depends to a large extent on the diameter and the exact position of the circular openings. This processing step is currently ongoing, but no results are available yet.



(a)



(b)

Figure 7.25: (a) Sideview of the microspheres glued into the circular openings in the optical PCB; (b) top view of the microspheres, glued into the circular openings in the optical PCB. The thermal nature of the CO₂ ablation process can be clearly seen in the change of colour of the Cu-layer.

7.3.7 Conclusion

A fiber-to-waveguide in-plane connector has been designed and fabricated. The design is based on a standard MT-connector, which is used to efficiently couple light between two fiber ribbons. The alignment is done passively with the use rectangular and circular openings in the FR4 substrate and an alignment plate for the alignment of the fibers with respect to the waveguides. The circular openings are used to arrange the lateral and vertical alignment of the baseplate. The rectangular openings are used to accommodate the MT-guiding pins, which are used to arrange the alignment between the polished end facet of the waveguides and the array of fibers. A fiber alignment plate, which contains circular openings for the insertion of the fibers and two circular openings to slide it over the MT-pins. The alignment is thus arranged in two separate steps: in a first step with the microspheres and in a second step by sliding the fiber alignment plate over the MT-pins. The position of the microspheres is determined by the diameter of the circular opening and by the accuracy of the glueing process (the position will also deviate from the ideal position in case an excess of glue is present under the microsphere) and also determines the position of the baseplate. In view of the fact that the MT-pins are glued onto the baseplate, it is clear that the position of the MT-pins is also determined by the position of the microspheres. For this reason, special attention has to be paid to the patterning of the circular openings in the top Cu-layer. Measurement will have to point out whether or not Nd-YAG laser ablation can be used for this purpose or whether UV-patterning of the top Cu-layer is required. Laser ablation however is a very valuable technology for this application because of the fact that materials can be selectively ablated by using the appropriate laser source. The first prototype of the in-plane fiber-to-waveguide connector is currently being put together and will be evaluated in the near future.

7.4 Conclusion

Two demonstrator-type of activities have been described in this chapter, carried out within the framework of the network of excellence on micro-optics (NEMO) in collaboration with external partners VUB and VTT. The fabricated demonstrators make a significant contribution towards the demonstration and implementation of optical interconnections to the board-level. The first demonstrator that has been described in this chapter deals with the realization of a complete optical link using the technology described in this thesis in the previous chapters for a high-speed parallel optical interconnection demonstrator. The work done clearly demonstrates the benefit of the technology developed in this thesis, and more specifically regarding the coupling structures and the waveguide fabrication. In collaboration with VUB and VTT, two generations of active demonstrator boards have been fabricated. The demonstrator is based on a prototype that was fabricated at VTT and that makes use of micro-lenses to relax the alignment tolerance for the mounting of the opto-electronic elements. These micro-lenses however first have to be fabricated and then mounted in an accurate way in a separate processing step. We decided to reduce the number of components and assembly steps by not making use of micro-lenses to relax the incoupling and outcoupling conditions.

The first generation board contained an array of ablated Truemode waveguides, a plug-

gable coupler, used for out-of-plane coupling, and a laser ablated cavity to accommodate the pluggable coupler. Loss measurements have been carried out in a transmitter configuration, with the use of the LTCC module with the integrated i-VCSEL at the input side, and indicate that the optical link is properly working. The link loss however is assumed too high and is assumed to be higher than the one measured on the original demonstrator board that was fabricated at VTT. The discrete pluggable coupler is in addition susceptible to dust and moist intrusion because of the fact that it is uncovered. The encouraging results that have been obtained with the use of the embedded mirror insert inspired us to make a second generation demonstrator board based on this coupling approach. The performance of the first generation board has been considerably improved by making use of UV-defined Truemode waveguides, patterned into the dry film formulation of the core material, and the embedded mirror insert for the out-of-plane coupling. Loss measurements were again carried out in a transmitter configuration, with the use of the LTCC module with the integrated i-VCSEL at the input side. The link efficiency increased by more than 25% with respect to the first generation demonstrator board and might be improved even more by optimizing the distance between the i-VCSEL and the optical layer.

The second demonstrator consists of the design and fabrication of a fiber-to-waveguide in-plane connector, which is based on a standard MT-connector. The alignment is done passively with the use of microspheres, MT-pins, and a fiber alignment plate. The microspheres determine the lateral and vertical alignment of the baseplate, which is positioned onto it. MT-guiding pins are glued onto the baseplate and are used to position the fiber alignment plate. The fiber alignment plate contains circular openings for the insertion of the optical fibers and two circular openings to slide the plate over the MT-pins. The alignment is thus arranged in two separate steps: in a first step the microspheres are used to arrange the lateral and vertical alignment; in a second step the fiber alignment plate is slid over the MT-pins to arrange the alignment between the polished waveguide end facets and the fibers.

The microsphere are glued into circular openings in the substrate, which also contains rectangular openings to accommodate the MT-pins. The accuracy on the position of the microspheres is determined by the accuracy on the diameter of the circular openings in the substrate and by the accuracy of the glueing process. Laser ablation is used for the patterning of the circular and rectangular openings in the substrate and turns out to be a very valuable process for this application mainly because of the possibility to selectively ablate materials, dependent on the used laser source, and because of the fact that the design can be changed very easily, which is an advantage when prototyping the connector. The first prototype of the in-plane fiber-to-waveguide connector is currently being put together and will be evaluated in the near future.

Bibliography

- [1] M. Karppinen *et al.*, "Embedded optical interconnect between ceramic BGA packages on FR4 board using embedded waveguides and passive optical alignments," *Proc. 56th Electronic Components and Technology Conference*, pp. 799-805, 2006
- [2] N. Hendrickx, J. Van Erps, T. Alajoki, N. Destouches, D. Blanc, J. Franc, P. Karjoja, H. Thienpont, P. Van Daele, "Towards Low Cost Coupling Structures for

Short-Distance Optical Interconnections, ” *Proc. EMPC 2007 conference*, pp. 247-252

- [3] C. Gimkiewicz *et al.*, ”Wafer-scale replication and testing of micro-optical components for VCSELs, ” *Proc. SPIE*, Vol. 5453, pp. 13-26 , 2004
- [4] T. Alajoki, N. Hendrickx, J. Van Erps, S. Obi, M. Karppinen, Hugo Thienpont, P. Van Daele, P. Karioja, ”Optical Coupling and Optoelectronics Integration Studied on Demonstrator for Optical Interconnects on Board, ” *Proc. EMPC 2007 conference*, pp. 258-261
- [5] J. Van Erps, ”Interfacing micro-components for optical interconnections from the FTTH-level to the PCB-level,” *PhD thesis*, Vrije Universiteit Brussel, 2008
- [6] <http://www.isola-group.com>
- [7] A. Van Hove, ”Termination and interconnection technology for parallel optoelectronic systems,” *PhD thesis*, Universiteit Gent, 2001

Chapter 8

Conclusion

8.1 Placing the work into context

This PhD thesis deals with the integration of optical interconnections to the board-level. A first motivation for this work is the fact that optical interconnections offer a possible solution to the bandwidth problems that will be encountered with the use of electrical interconnections in the near future. However, this is currently not the main driver for the practical use of optical interconnects. Since cost is a major issue for the adoption of optical interconnects, they will only be used in this field when they become cost-advantageous over electrical interconnects, which is not yet the case. Currently, the lower weight, lower space occupancy and lower sensitivity to EMI/EMC problems are the main drivers for using optical channels instead of copper ones, and this in applications like automotive, sensing, data storage, aeronautics, computing,... Another important requirement on the proposed solution is compatibility with the existing PCB manufacturing and soldering processes.

The integration of optical interconnections to the board-level can be done with the use of a polymer optical layer. Polymer materials offer a number of advantages over other alternative waveguide media such as glass sheets and optical fibers such as potentially low cost (for a large enough market), the large variety of potential technologies that can be used to pattern the polymer layers and the ability to tailor the properties such as the refractive index and the mechanical properties. The main requirement on the polymer material are a low optical loss, a high thermal and mechanical stability and compatibility with the existing PCB manufacturing processes. Main focus within this work is on the use of Truemode Backplane™ Polymer, which is UV-patternable, has excellent optical and thermal properties and is compatible with the main PCB manufacturing processes, which restricts the number of possible solutions.

Multimode optical waveguides with a cross-section of $50\mu\text{m} \times 50\mu\text{m}$ on pitch $125\mu\text{m}$ have been successfully ablated into the Truemode optical layer with a KrF excimer laser (248 nm). The waveguides have an average propagation loss of 0.13dB/cm at 850 nm, which is acceptable for short interconnection lengths. Laser ablation has the advantage of being a flexible and maskless technology, making it ideal for fast prototyping, and is fully compatible with standard PCB manufacturing. The waveguide ablation process is serial, which makes the technology less interesting for the patterning of waveguides

on large-area boards although the flexibility in adapting the waveguide pattern, in-situ, might be an advantage over lithography using standard masks. It should be noted that laser ablation, as a serial process, is now frequently used in PCB manufacturing for drilling micro-via's.

A second way to structure waveguides into the optical layer is the use of UV-lithography. Most of the available optical polymers are UV-sensitive, which means that they can be directly patterned. UV-lithography allows a high throughput, making it ideal for practical applications, and is compatible with standard PCB manufacturing. The use of a mask aligner and a high-quality mask allows for an expansion to a multilayer optical structure.

The use of a multilayer optical structure can be interesting for high-density interconnections, where they can ease the routing scheme. A two layer optical structure containing arrays of ablated Truemode waveguides has been presented. The achievable alignment accuracy is $\leq 5 \mu\text{m}$, which is within the 0.2dB excess loss range resulting from a numerical study.

Optical interconnections also require light sources and during the last few years, reliable VCSELs came commercially available. These light sources can be integrated in the optical layers, but the key challenge lies in the coupling of the light between the VCSEL and the waveguide itself or between the waveguide and other external components (detectors, connectors, fibers,...). It is clear that coupling structures are needed in order to be able to couple the light in and out of the optical layer. This can be done with the use of 45° micro-mirrors, used to deflect the light beam over 90° . Several different options and configurations have been studied in this work, but best results were obtained with the use of an embedded micro-mirror insert, which is embedded into the optical layer and in this way protected from external influence. Loss measurements indicate that the mirror induces an average coupling loss $\leq 0.35\text{dB}$ (92%), which is competitive with other results reported by other research groups.

Another important issue that is sometimes forgotten, is the reliability and stability of the proposed solution. Samples with ablated Truemode waveguides have been submitted to environmental tests to evaluate the performance after aging. The samples have also been submitted to lamination step and reflow step. The reproducibility of the ablated Truemode waveguides is better than 5% and this for both waveguides on the same sample and on different samples. The propagation loss of the waveguides is not affected by an accelerated aging test which is tested by submitting the sample to 85°C and 85% relative humidity for one week. Thermal cycling between -40°C and 85°C has been carried out on waveguide samples and has no influence on the propagation loss. The Truemode waveguides can be laminated in a PCB-stack, without affecting the performance. It must however be noticed that the optical layer has to be completely cross-linked in order to be able to reproduce these results. The solder reflow step has a negative influence on the propagation loss which increases considerably. The increased propagation loss is most probably a consequence of the deformation of the FR4 substrate during the reflow step.

Two demonstrator-type of activities have been described, which have been carried out within the framework of the network of excellence on micro-optics (NEMO) in collaboration with external partners VUB and VTT. The fabricated demonstrators make a significant contribution toward the demonstration and implementation of optical interconnections to the board-level. The first demonstrator deals with the realization of

a complete optical link using the technology described in this thesis for a high-speed parallel optical interconnection demonstrator. The work done clearly demonstrates the benefit of the technology developed in this thesis, and more specifically regarding the coupling structures and the waveguide fabrication. In collaboration with VUB and VTT, two generations of active demonstrator boards have been fabricated. The demonstrator is based on a prototype that was fabricated at VTT and that makes use of micro-lenses to relax the alignment tolerance for the mounting of the opto-electronic elements. These micro-lenses however first have to be fabricated and then mounted in an accurate way in a separate processing step. We decided to reduce the number of components and assembly steps by not making use of micro-lenses to relax the incoupling and outcoupling conditions.

The first generation board contained an array of ablated Truemode waveguides, a pluggable coupler, used for out-of-plane coupling, and a laser ablated cavity to accommodate the pluggable coupler. Loss measurements have been carried out in a transmitter configuration, with the use of the LTCC module with the integrated i-VCSEL at the input side, and indicate that the optical link is properly working. The link loss however is assumed too high and is assumed to be higher than the one measured on the original demonstrator board that was fabricated at VTT. The discrete pluggable coupler is in addition susceptible to dust and moist intrusion because of the fact that it is uncovered. The encouraging results that have been obtained with the use of the embedded mirror insert inspired us to make a second generation demonstrator board based on this coupling approach. The performance of the first generation board has been considerably improved by making use of UV-defined Truemode waveguides, patterned into the dry film formulation of the core material, and the embedded mirror insert for the out-of-plane coupling. Loss measurements were again carried out in a transmitter configuration, with the use of the LTCC module with the integrated i-VCSEL at the input side. The link efficiency increased by more than 25% with respect to the first generation demonstrator board and might be improved even more by optimizing the distance between the i-VCSEL and the optical layer.

The second demonstrator consists of the design and fabrication of a fiber-to-waveguide in-plane connector, which is based on a standard MT-connector, and has been made in very close collaboration with VUB. The alignment is done passively with the use of microspheres, MT-pins, and a fiber alignment plate. The microspheres determine the lateral and vertical alignment of the baseplate, which is positioned onto it. MT-guiding pins are glued onto the baseplate and are used to position the fiber alignment plate. The fiber alignment plate contains circular openings for the insertion of the optical fibers and two circular openings to slide the plate over the MT-pins. The alignment is thus arranged in two separate steps: in a first step the microspheres are used to arrange the lateral and vertical alignment; in a second step the fiber alignment plate is slid over the MT-pins to arrange the alignment between the polished waveguide end facets and the fibers.

The microspheres are glued into circular openings in the substrate, which also contains rectangular openings to accommodate the MT-pins. The accuracy on the position of the microspheres is determined by the accuracy on the diameter of the circular openings in the substrate and by the accuracy of the glueing process. Laser ablation is used for the patterning of the circular and rectangular openings in the substrate and turns out to be a very valuable process for this application mainly because of the possibility to

selectively ablate materials, dependent on the used laser source, and because of the fact that the design can be changed very easily, which is an advantage when prototyping the connector. The first prototype of the in-plane fiber-to-waveguide connector is currently being put together and will be evaluated in the near future.

8.2 Future work

Laser ablation has proved to be a valuable technology to micro-structure a large variety of materials ranging from polymer materials to ceramics and metals. It is however not clear whether laser ablation will be the most cost-effective technology to structure large area panels. The technology remains interesting for the patterning of micro-cavities, which can be used to accommodate discrete micro-optical elements, and alignment features. The compatibility with the existing PCB manufacturing processes and high achievable accuracy are big advantages in this field.

The use of multilayer optical structures has to be investigated more profoundly. Numerical simulations indicate that the coupling loss that the light signal experiences when it is coupled from one layer to the other is very high, and in most cases probably unacceptable. Loss measurements have to be carried out on a two layer demonstrator board that contains multimode waveguides and micro-mirrors for the inter-plane coupling.

The reliability of the ablated waveguides has been tested experimentally. For a full working optical link however, the reliability of the combination waveguides and coupling structures is of big importance. The stability and reliability tests that have been carried out on the waveguides should be repeated on a board-level optical link.

It is clear that the performance of the active demonstrator board with the embedded mirror can be improved by optimizing the distance between the i-VCSEL and the mirror facet. More demonstrator boards should be fabricated in order to find other possible ways to improve the performance even more.

Optical interconnections are now on the edge of breakthrough within systems and on boards and they offer solutions to deal with the problems of high-speed and high density data communications. However in the end everything comes back to the cost, not only of the interconnection itself, but of the whole system. Still lots of work has to be done to bring this cost down for the applications in the area of telecommunications as these require in most cases single-mode operation, but, as mentioned above, the advantages in view of density, weight, immunity, ... are at this very moment triggering a breakthrough of optical interconnections in other fields such as sensing, automotive and robotics.

In a few years time, when optical interconnections on board will be well established, common and widely accepted within systems, the technology being used might be very different from what we propose here, but we are convinced that this work and the results presented here will have contributed a lot in achieving this goal or at least triggered a discussion, new ideas and the final breakthroughs.

Publication list of the PhD candidate

Publications in international peer reviewed journals

- [1] N. Hendrickx, J. Van Erps, E. Bosman, C. Debaes, H. Thienpont and P. Van Daele, "Embedded micromirror inserts for optical printed circuit boards," *IEEE Photon. Technol. Lett.*, Vol. 20, no. 20, pp. 1727-1729, 2008
- [2] N. Hendrickx, J. Van Erps, G. Van Steenberge, H. Thienpont and P. Van Daele, "Laser Ablated Micromirrors for Printed Circuit Board Integrated Optical Interconnections," *IEEE Photon. Technol. Lett.*, Vol. 19, no. 11, pp. 822-824, October 2007
- [3] N. Hendrickx, J. Van Erps, G. Van Steenberge, H. Thienpont, P. Van Daele, "Tolerance analysis for multilayer optical interconnections integrated on a printed circuit board," *Journal of Lightwave Technology*, Vol. 25, no. 9, pp. 2395-2401, September 2007
- [4] N. Hendrickx, G. Van Steenberge, P. Geerinck and P. Van Daele, "Laser Ablation as Enabling Technology for the Structuring of Optical Multilayer Structures," *Journal of Physics: conference series*, Vol. 59, pp. 118-121, 2007
- [5] J. Van Erps, N. Hendrickx, C. Debaes, P. Van Daele, H. Thienpont, "Discrete out-of-plane coupling components for Printed Circuit Board-level optical interconnections," *IEEE Photon. Technol. Lett.*, Vol. 19, No. 21, pp. 1753-1755, November 2007
- [6] N. Destouches, D. Blanc, J. Franc, S. Tonchev, N. Hendrickx, P. Van Daele, and O. Parriaux, "Efficient and tolerant resonant grating coupler for multimode optical interconnections," *Optics Express*, Vol. 15, No. 25, pp. 16870-16879
- [7] G. Van Steenberge, N. Hendrickx, E. Bosman, J. Van Erps, H. Thienpont, and P. Van Daele, "Laser Ablation of Parallel Optical Interconnect Waveguides," *Photonics Technology Letters*, Vol. 18, no. 9, May 2006

Publications in international conference proceedings

- [1] N. Hendrickx, J. Van Erps, E. Bosman, C. Debaes, H. Thienpont, P. Van Daele, "Embedded 45° Micro-Mirror for Out-of-Plane Coupling in Optical PCBs," *Proc. 14th MicroOptics Conference (MOC 2008)*, pp. 279, 2008
- [2] N. Hendrickx, J. Van Erps, E. Bosman, H. Thienpont, P. Van Daele, "Coupling structures for out-of-plane coupling in optical PCBs," *Proc. SPIE*, Vol. 6992, 69226, 2008
- [3] N. Hendrickx, J. Van Erps, H. Thienpont, P. Van Daele, "Out-of-plane coupling structures for optical optical printed circuit boards," *Proc. OFC-NFOEC*, Paper No. JThA8, 2008
- [4] N. Hendrickx, J. Van Erps, H. Thienpont, P. Van Daele, "Inter-plane coupling structures for PCB-integrated multilayer optical interconnections," *Proc. EMPC 2007*, pp. 65-69, 2007
- [5] N. Hendrickx, J. Van Erps, T. Alajoki, N. Destouches, D. Blanc, J. Franc, P. Kari-oja, H. Thienpont, P. Van Daele, "Towards low-cost coupling structures for short-distance optical interconnections," *Proc. EMPC 2007*, pp. 247-252, 2007
- [6] N. Hendrickx, J. Van Erps, H. Thienpont, P. Van Daele, "Embedded laser ablated micro-mirrors for intra- and out-of-plane coupling in multilayer optical interconnections," *Proc. IEEE LEOS*, pp. 575-576, 2006
- [7] N. Hendrickx, J. Van Erps, H. Thienpont, P. Van Daele, "Tolerance analysis of PCB-integrated optical interconnections," *Proc. OSA frontiers in optics, silicon and III-V based optoelectronics for optical interconnects I*, FW05, 2006
- [8] N. Hendrickx, J. Van Erps, H. Suyal, M. Taghizadeh, H. Thienpont, P. Van Daele, "Roughness measurements on coupling structures for optical interconnections integrated on a printed circuit board," *Proc. SPIE*, Vol. 6185, 6185E, 2006
- [9] N. Hendrickx, G. Van Steenberge, P. Geerinck, J. Van Erps, H. Suyal, M. Taghizadeh, H. Thienpont, P. Van Daele, "Laser ablated coupling structures for stacked optical interconnections on a printed circuit boards," *Proc. SPIE*, Vol. 6185, 6185E, 2006
- [10] N. Hendrickx, G. Van Steenberge, P. Geerinck, P. Van Daele, "Multilayer optical interconnections integrated on a printed circuit board," *Proceedings of the 10th Annual Symposium of the IEEE/LEOS Benelux Chapter*, pp. 213-216, 2005
- [11] N. Hendrickx, H. Suyal, G. Van Steenberge, A. McCarthy, A. Walker, H. Ottevaere, H. Thienpont, M. R. Taghizadeh, P. Van Daele, "Laser ablation and laser direct writing as enabling technologies for the definition of micro-optical elements," *Proc. SPIE*, Vol. 5956, 2005
- [12] N. Hendrickx, G. Van Steenberge, P. Geerinck, H. Ottevaere, H. Thienpont, P. Van Daele, "Multilayer Optical Interconnections Integrated on a Printed Circuit Board," *Proc. 15th European Microelectronics and Packaging Conference and Exhibition (EMPC2005 - IMAPS 2005)*, pp.329-333, 2005

- [13] C. Debaes, J. Van Erps, N. Hendrickx, T. Alajoki, M. Vervaeke, M. Karppinen, H. Suyal, N. Destouches, J. Franc, O. Parriaux, G. Van Steenberge, M. Taghizadeh, P. Karioja, P. Van Daele, H. Thienpont, "Opto-PCB: Three Demonstrators for Optical Interconnections," *Proc. 14th MicroOptics Conference (MOC 2008)*, pp. 34-35, 2008
- [14] N. Destouches, J.C. Pommier, S. Tonchev, J. Franc, O. Parriaux, N. Hendrickx, P. Van Daele, "Leaky Mode Mediated High Efficiency Grating Excitation of Heavily Multimode Slab Waveguides," *Proc. 14th MicroOptics Conference (MOC 2008)*, pp. 54-55, 2008
- [15] J. Van Erps, S. Heyvaert, C. Debaes, B. Van Giel, N. Hendrickx, P. Van Daele, H. Thienpont "Enhanced pluggable out-of-plane coupling components for printed circuit board-level optical interconnections," *Proc. SPIE*, Vol. 6992, 699227, 2008
- [16] J. Van Erps, N. Hendrickx, Y. Ishii, C. Debaes, P. Van Daele, H. Thienpont "Pluggable coupling components for multilayer interconnections on the printed circuit board-level," *Proc. 13th Micro-Optics conference (MOC)*, D4, pp. 74-75, 2007
- [17] M. Karppinen, T. Alajoki, P. Karioja, N. Hendrickx, G. Van Steenberge, P. Van Daele, J. Van Erps, C. Debaes, H. Thienpont, S. Obi, M. Immonen, J. Kivilahti, A. Glebov, "Integration of optical interconnects on circuit boards," *Proc. 13th Micro-Optics conference (MOC)*, E4, pp. 94-97, 2007
- [18] J. Van Erps, N. Hendrickx, C. Debaes, P. Van Daele, H. Thienpont, "Pluggable inter-plane couplers for multilayer board-level optical interconnections," *Proc. of the 33rd European Conference on Optical Communication (ECOC)*, Vol. 5, P054, 2007
- [19] N. Destouches, D. Blanc, J. Franc, N. Hendrickx, S. Tonchev, J.-C. Pommier, P. Van Daele, O. Parriaux, "Resonant network on multimode waveguide: a coupling efficiency of 78%," *Journées Nationales d'Optique Guidée*,
- [20] J. Van Erps, N. Hendrickx, C. Debaes, P. Van Daele, H. Thienpont, "Prototyping of pluggable out-of-plane coupling components for multilayer optical interconnections," *Proc. EMPC*, pp. 70-75, 2007
- [21] T. Alajoki, N. Hendrickx, J. Van Erps, S. Obi, M. Karppinen, H. Thienpont, P. Van Daele, P. Karioja, "Optical coupling and optoelectronics integration studied on demonstrator for optical interconnects on board," *Proc. EMPC*, pp. 258-261, 2007
- [22] E. Bosman, G. Van Steenberge, N. Hendrickx, P. Geerinck, W. Christiaens, J. Vanfleteren, P. Van Daele, "Multimode optical interconnections embedded in flexible electronics," *Proc. EMPC*, pp. 155-160, 2007
- [23] N. Destouches, D. Blanc, J. Franc, N. Hendrickx, S. Tonchev, J.-C. Pommier, P. Van Daele, O. Parriaux, "Efficient resonant grating coupler for short distance optical interconnections," *NEMO Scientific General Networking Meeting*, 2007
- [24] C. Debaes, J. Van Erps, N. Hendrickx, T. Alajoki, M. Vervaeke, M. Karppinen, H. Suyal, O. Parriaux, G. Van Steenberghe, M. Taghizadeh, P. Karioja, P. Van Daele,

- H. Thienpont, "Opto-PCB project," *NEMO Scientific General Networking Meeting*, 2007
- [25] J. Van Erps, N. Hendrickx, C. Debaes, P. Van Daele, H. Thienpont, "Pluggable coupling structures for multilayer board-level optical interconnections," *NEMO Scientific General Networking Meeting*, 2007
- [26] G. Van Steenberge, N. Hendrickx, E. Bosman, S. Van Put, P. Geerinck, P. Van Daele, "Laser Ablation: a Versatile Micro-Machining Technology," *NEMO Scientific General Networking Meeting*, 2007
- [27] J. Van Erps, , C. Debaes, M. Vervaeke, L. Desmet, N. Hendrickx, G. Van Steenberge, H. Ottevaere, P. Vinck, V. Gomez, S. Van Overmeire, Y. Ishii, P. Van Daele, A. Hermanne, H. Thienpont, "Low-cost micro-optics PCB-level photonic interconnects," *Proc. SPIE*, Vol. 6476, 64760L, 2007
- [28] G. Van Steenberge, N. Hendrickx, P. Geerinck, E. Bosman, S. Van Put, P. Van Daele, "Development of a technology for fabricating low cost parallel optical interconnects," *Proc. SPIE*, Vol. 6185, 2006
- [29] J. Franc, N. Destouches, D. Blanc, J.-C. Pommier, S. Tonchev, G. Van Steenberge, N. Hendrickx, A. Last, O. Parriaux, "High efficiency diffraction grating coupler for low cost optical interconnect," *Proc. SPIE*, Vol. 6185, 2006
- [30] G. Van Steenberge, N. Hendrickx, P. Geerinck, E. Bosman, S. Van Put, J. Van Erps, H. Thienpont, P. Van Daele, "Development of a fabrication technology for integrating low cost optical interconnects on a printed circuit board," *Proc. SPIE*, Vol. 6126, 612603, 2006
- [31] J. Van Erps, , G. Van Steenberge, N. Hendrickx, P. Geerinck, B. Volckaerts, C. Debaes, P. Van Daele, H. Thienpont, "Deep lithography with protons to prototype pluggable micro-optical out-of-plane coupling structures for multimode waveguides," *Proc. SPIE*, Vol. 5956, pp. 52-63, 2005
- [32] G. Van Steenberge, P. Geerinck, S. Van Put, N. Hendrickx, H. Ottevaere, H. Thienpont, P. Van Daele, "45° out-of-plane deflecting mirrors for optical printed circuit boards," *Proc. 15th European Microelectronics and Packaging Conference & Exhibition (EMPC2005 - IMAPS 2005)*, pp. 557-560, 2005
- [33] G. Van Steenberge, S. Van Put, N. Hendrickx, E. Bosman, P. Geerinck, P. Van Daele, H. Suyal, M. Taghizadeh, "Laser patterning," *Workshop on Micro-optics - Benefits for Industry, NEMO - FP6 - Project*, March 2005

Publications in national conference proceedings

- [1] N. Hendrickx, G. Van Steenberge, P. Geerinck, P. Van Daele, "Multilayer optical interconnections integrated on a printed circuit board," *6th FTW PHD Symposium, Interactive poster session*, 2005

- [2] G. Van Steenberge, P. Geerinck, S. Van Put, N. Hendrickx, H. Ottevaere, H. Thienpont, P. Van Daele, "Laser ablated micromirrors for optical printed circuit boards," *5th FTW PHD Symposium, Interactive poster session*, paper no. 127

List of Figures

1.1	Relation between cost and distance for an electrical versus optical link at 10Gb/s (Courtesy of IBM).	2
1.2	Evolution of the FR4 losses as a function of frequency.	4
1.3	The graph shows that the use of low loss tangent dielectric material such as Rogers instead of FR4 has a positive effect on the maximum data rate that can be achieved for a given link length [7].	4
1.4	(a) Typical dimension of a copper channel; (b) number of optical channels that fit the same cross-section as the copper channel (Courtesy of FCI).	5
1.5	Schematic of the developed fiber with small diameter and high refractive index contrast [14].	7
1.6	Double-sided optically functionalized thin glass with waveguide dimensions of approx. $53 \mu\text{m} \times 110 \mu\text{m}$, fabricated by silver-ion exchange using a salt melt [15].	7
1.7	Cross-section of a polymer waveguides with a cross-section of $50 \mu\text{m} \times 50 \mu\text{m}$ (left) and $35 \mu\text{m} \times 35 \mu\text{m}$ (right) [18].	7
1.8	(a) Application and curing of the lower cladding layer; (b) application of the core layer, followed by the patterning of the core layer using UV-exposure through a suitable mask and the development of the UV-exposed layer; (c) after the development step, for the case of a negative resist type polymer, the waveguide cores remain on the sample while the remaining part of the layer is washed off; (d) the waveguide cores are coated with the top cladding layer, and are after this step surrounded by cladding material.	10
1.9	Flip-chip optical interconnection based on the Optobump concept [50].	12
1.10	Schematic of the Terabus board-level optical link. Two optomodules are connected through an array of polymer waveguides in the optocard [52].	14
1.11	Cross-section of a four layer waveguide structure in Ormocer, patterned using UV-lithography [53].	15
1.12	Illustration showing the processing steps used to fabricate the two-dimensional waveguide structure: (a) fabrication of one-dimensional waveguide arrays; (b) stacking of the diced waveguide layers; (c) two-dimensional waveguide structure with integrated mirrors used to couple light to/from the photodetector/VCSEL array [53].	16

1.13	(a) The lower cladding and wedge layers are deposited and the wedge base is patterned; (b) one side of the wedge base is tapered to 45° by micro-dicing and a thin Au film is deposited on the tapered wedge side; (c) the waveguide core layer is deposited and the channel waveguide is patterned with photolithography; (d) the top cladding layer is coated on top of the formed waveguide and mirror structure [55].	17
1.14	Schematic representation of the use of a 45° ended optical fiber that is used to couple the light from transmitter to the waveguides and from the waveguides to the receiver [56].	18
2.1	Classification of polymer by chain structure. We can distinguish between linear polymers, branched polymers, polymer networks and ladder polymers [4].	29
2.2	Schematic representation of the initiation of the monomer [4].	31
2.3	Schematic representation of the reactions that take place during the propagation phase [4].	32
2.4	Schematic representation of the termination phase [4]. In this case the termination is done by combining radicals.	33
2.5	Young's modulus in function if temperature for an amorf polymer material.	34
2.6	Surface roughness of the FR4 substrate, measured with a stylus profiler on 3 different scan lengths. In (a) and (b) the high surface roughness of the FR4 substrate can be clearly observed. In (c) the tilting of the FR4 substrate can be observed.	39
2.7	Patterning of negative versus positive type photoresist. The studied polymer materials behave like a negative photo-resist, which means that the UV-exposed zones will remain after the development step.	40
2.8	Absorption spectrum of the Truemode material [7]. From this graph, we can see that the absorption reaches a minimum around 850 nm, which is the targeted wavelength.	40
2.9	(a) Basic structure of a metacrylate ;(b) basic structure of the photo-initiator Irgacure 651 that is used for the radical polymerization of Truemode. The photo-initiator can be split into two radicals by the UV-induced cleavage of the bond that is marked with the arrow.	41
2.10	(a) The spincurve for the Truemode core material; (b) the spincurve of the Truemode cladding material.	42
2.11	(a) Cross-section of the optical layer in the center of the sample; (b) cross-section of the same sample taken at the edge of the sample, where the edge bead can be very clearly observed. Two approximately 50 μm thick cladding layers are in this case applied onto the core layer in this sample.	43
2.12	Processing steps used for the patterning of the Truemode layers.	44

2.13	(a) TGA curve measured on the Truemode cladding material. From this curve, we can conclude that the Truemode cladding material is thermally stable up to a temperature of 346°C; (b) TGA curve measured on the Truemode core material. From this curve, we can conclude that the Truemode core material is thermally stable up to a temperature of 305°C	46
2.14	(a) DSC curve measured on the Truemode cladding material; (b) DSC curve measured on the Truemode core material.	47
2.15	Absorption spectrum of Ormocer® [12].	49
2.16	Application process for the Ormocer layers.	49
2.17	(a) Spincurve of the Ormoclad material; (b) spincurve of the Ormocore material.	50
2.18	Spincurve of the SU-8 material.	52
2.19	(a) Spincurve of the Epocore material; (b) spincurve of the Epoclad material.	54
3.1	(a) Waveguide cross-section; (b) cross-sectional refractive index profile.	59
3.2	(a) Processing steps that are required for the patterning of the waveguides in the optical layer using direct lithography; (b) processing steps that are required for the patterning of the waveguides in the optical layer using embossing [9].	61
3.3	(a) The photon energy of the laser beam is deposited in the irradiated surface and the near-surface region down to a penetration depth that is characteristic of the laser wavelength and the material; (b) as soon as the photon density inside the material exceeds a certain threshold, the ablation threshold, the photon energy can be used for material decomposition. An ablation plume is formed that expulses the decomposed material away from the surface and leaves an ablated crater; (c) controlled material removal.	64
3.4	Picture of the ablation set-up.	65
3.5	Optical path of the excimer laser beam.	66
3.6	Array of five waveguides.	67
3.7	Ablation of the waveguide core features into the optical layer.	67
3.8	Cross-section of an array of ablated waveguides in Truemode, the waveguides have a cross-section of approximately 50μm×50μm on pitch 125μm and are ablated with a pulse energy of 12mJ. The thermal ablation process is in this case dominant, giving a black appearance to the waveguide cores and the surrounding optical material.	68
3.9	Cross-section of an array of ablated waveguides in Truemode, the waveguides have a cross-section of ≈50μm×50μm on pitch 125μm. The waveguide core has a height of 50 μm and a width of 45 μm at the top of the core layer and 60 μm at the bottom of the core layer.	69
3.10	SEM image of the patterned core layer.	70
3.11	Surface roughness of the top of an ablated waveguide core, prior to the deposition of the top cladding layer, measured with a non-contact optical profiler (Wyko NT3300).	70

3.12	Surface corrugation of a 50 μm top cladding layer, applied on top of an array of ablated waveguides.	71
3.13	Surface corrugation of the top cladding layer, applied on top of an array of ablated waveguides, for a cladding layer thickness of 30 μm	71
3.14	Picture of a sample placed on the measurement set-up in the configuration that is used to evaluate the performance of arrays of multimode waveguides.	72
3.15	Propagation loss of a laser ablated waveguide, obtained with cut-back measurements. The waveguides have a propagation loss of 0.13dB/cm [13].	72
3.16	Lateral scan of the light spot that is detected by the detector fiber.	73
3.17	Surface roughness plot of the top of a waveguide core ablated inOrmocer.	74
3.18	Surface roughness plot of the top of a waveguide core ablated inEpocore.	74
3.19	Surface roughness plot of the top of a waveguide core ablated inSU-8.	74
3.20	(a) Cross-section of an array of waveguides with cross-section $\approx 50 \mu\text{m} \times 50 \mu\text{m}$ on pitch 125 μm ; (b) cross-section of an array of waveguides with cross-section $\approx 50 \mu\text{m} \times 50 \mu\text{m}$ on pitch 250 μm	75
3.21	Surface roughness plot of the top of a photolithographic waveguide in dry Truemode.	76
3.22	Surface corrugation of the top cladding layer applied on top of an array of photolithographic waveguides in dry Truemode.	76
3.23	Cross-section of an array of photolithographic waveguides with a cross-section of 100 $\mu\text{m} \times 50 \mu\text{m}$ on pitch 125 μm in Ormocer.	77
3.24	Surface roughness plot of the top of a photolithographic waveguide in Ormocer.	77
3.25	(a) Cross-section of an array of photolithographic waveguides in SU8, without the use of the UV-filter. The T-topping of the waveguide cores can be clearly observed; (b) cross-section of an array of photolithographic waveguides in SU8 in case the UV-filter is used.	78
3.26	(a) Cross-section of an array of photolithographic waveguides with cross-section 50 $\mu\text{m} \times 50 \mu\text{m}$ on pitch 125 μm in Epocore/clad; (b) cross-section of an array of photolithographic waveguides with cross-section 50 $\mu\text{m} \times 50 \mu\text{m}$ on pitch 250 μm in Epocore/clad.	79
3.27	Surface roughness plot of the top of a photolithographic waveguide in Epocore.	79
3.28	Cross-section of an array of ablated waveguides in Truemode with cross-sectional dimension 25 $\mu\text{m} \times 42 \mu\text{m}$ on pitch 62.5 μm	81
3.29	Surface corrugation of the 50 μm thick top cladding layer, applied on top of an array of ablated waveguides with cross-section 25 $\mu\text{m} \times 42 \mu\text{m}$ on pitch 62.5 μm	81
3.30	(a) Cross-section of an array of ablated small core waveguides in TM; (b) the waveguides have a cross-section of $\approx 15 \mu\text{m} \times 15 \mu\text{m}$ on pitch 125 μm	84
3.31	Interconnection scheme for a board with 4 input Tx channels and 4 output Rx channels.	85
3.32	(a) Input facet of the waveguides; (b) cross-section of the two layer waveguide structure with integrated metallized micro-mirrors.	86

3.33	(a) Cross-section of a trapezoidal waveguide core, with top angle β ; (b) influence of the top angle β on the coupling efficiency.	87
3.34	Alignment tolerance curve for a misalignment of the bottom waveguide with respect to the top waveguide in a two layer optical structure in Truemode material.	88
3.35	Alignment procedure used to align the waveguides in top and bottom layer in a multilayer structure: (a) ablation of alignment pulse; (b) rotation of sample over 90° and aligning; (c) use of right or left wall of 90° rotated alignment pulse as reference point for the ablation.	90
3.36	Cross-section of a two layer waveguide structure of which the waveguides have a cross-section of $50 \mu\text{m} \times 50 \mu\text{m}$ on pitch $125 \mu\text{m}$: (a) the alignment marks are evaporated on an SU8 layer; (b) the alignment marks are evaporated onto the lower cladding layer.	91
3.37	(a) Coupling efficiency of the bottom and corresponding top waveguide of a two layer waveguide array measured on an array on the centre of the sample (b) coupling efficiency of the bottom and corresponding top waveguide measured on an array near the edge of the sample.	93
3.38	(a) Plot of the light spot that is coupled out at the output facet of a waveguide in the top optical layer; (b) plot of the light spot that is coupled out at the output facet of a waveguide in the bottom optical layer.	94
3.39	(a) Cross-section of a two layer waveguide structure in which the waveguides in top optical layer have a slightly larger cross-section than the waveguides in the bottom optical layer; (b) cross-section of two layer waveguide structure at the edge of the sample, the core layer in the top optical layer is thicker than the one in the bottom optical layer causing the waveguides in the top optical layer not be completely decoupled.	95
3.40	Cross-section of a two layer waveguide structure in which the waveguides have a cross-section of $\approx 15 \mu\text{m} \times 15 \mu\text{m}$	95
4.1	(a) Ablation of angled trench into the optical layer with a KrF excimer laser beam placed in a tilted position with respect to the sample; (b) both angled interfaces of the ablated trench can be used for 90° deflection in a different mirror configuration. The polymer-air interface can be used as a total internal reflection mirror; the air-polymer interface can be used for 90° beam deflection after the Au-coating of the mirror facet and the filling of the ablated trench with cladding material.	100
4.2	(a) Cross-section of the ablated trench with the 45° air-polymer interface, and the typical dimensions; (b) cross-section of the micro-mirror after the metalization of the mirror facet and the filling of the ablated trench with cladding material.	102
4.3	Configuration used for the simulations on the metalized micro-mirror. Both the angles α and β have an influence on the link efficiency of the integrated structure.	103

4.4	Influence of a deviation of 45° of the angle β of the metalized mirror facet on the coupling efficiency of the entire simulated system, and not only of the mirror. The angle α of the opposite interface of the ablated trench is in this case 25° , in accordance with the experimental results discussed in the next section.	103
4.5	(a) Ray trace plot for a mirror facet angle of 40° ; (b) ray trace plot for a mirror facet angle of 45° ; (c) Ray trace plot for a mirror facet angle of 50° . There is a deviation on the angle of the outcoupled spot for the case $\beta \neq 45^\circ$. The light rays will however be forced to deflect at the mirror facet because of the presence of the Au-coating.	104
4.6	Refraction of the central ray that strikes the core-cladding interface. The ray enters under an angle α_1 ; the refracted ray propagates under an angle α_2 , measured with respect to the axis perpendicular to the core-cladding interface. The angle α_2 will be slightly bigger than α_1 because of the slightly lower refractive index of the cladding material with respect to the core material.	105
4.7	Two layer out-of-plane coupling configuration used to simulate the effect of a misalignment along the Z-axis of the top respectively bottom mirror with respect to the bottom respectively top mirror, causing a deviation on the $250\mu\text{m}$ pitch of the detector.	106
4.8	Alignment tolerance curve of a two layer out-of-plane coupling structure with metalized mirrors for the case where a $100\mu\text{m}$ square flat detector is used. The center of the detector is aligned with the center of the mirror facet, which is the theoretically ideal position. The detector is fixed at this position, whereas the mirror facet is shifted around the ideal position in Z-direction.	107
4.9	Alignment tolerance curve for a misalignment of the top mirror along Z around the theoretically ideal position, where the center of the detector is aligned with the center of the mirror facet, for both the $100\mu\text{m}$ square flat detector and the $100\mu\text{m}$ core diameter multimode optical fiber (MMF).	108
4.10	(a) Tolerance curve for a mechanical misalignment of the $100\mu\text{m}$ core diameter MMF detector around its theoretically ideal position, where the center of the detector is aligned with the center of the mirror facet. The MMF detector is shifted around the ideal position in X-direction; (b) alignment tolerance curve for a mechanical misalignment of the $100\mu\text{m}$ square flat detector around the theoretically ideal position along X. The resulting alignment tolerance curves are symmetrical, which is logical because of the fact that the mirror is shifted along the mirror facet.	109
4.11	(a) Schematic of a two layer waveguide structure with metalized mirrors, where the light signal is coupled from a waveguide in the top/bottom layer to the corresponding waveguide in the bottom/top layer with reversal of the propagation direction; (b) schematic of a two layer waveguide structure with metalized mirrors, where the light signal is coupled from a waveguide in the top/bottom layer to the corresponding waveguide in the bottom/top layer with conservation of the propagation direction.	110

4.12	Alignment tolerance plot for the inter-plane coupling configuration with reversal of the propagation direction for the case of the flat detector and the MMF detector for a misalignment of the top mirror along the Z-axis around the theoretically ideal position with respect to the bottom mirror.	111
4.13	Alignment tolerance plot for mechanical misalignment of the detector along the X-axis for the inter-plane coupling configuration with reversal of the propagation direction. The flat detector and the MMF detector are shifted along the X-axis around the theoretically ideal position where the center of the detector is aligned with the center of the waveguide.	112
4.14	Ray trace plot of the inter-plane coupling configuration with reversal of the propagation direction. The plot clearly shows that a considerable amount of rays are no longer guides in the waveguide core after the coupling of light signal from bottom layer to the top layer. This is mainly due to the diffraction that the light beam experiences during the propagation from one mirror to the other.	113
4.15	Alignment tolerance plot for a mechanical misalignment of the top mirror around its theoretically ideal position along the Z-axis in the inter-plane coupling configuration with conservation of the propagation direction for the case of the flat detector and the MMF detector.	114
4.16	Ray trace plot of the inter-plane coupling configuration with conservation of the propagation direction. The plot clearly shows that a considerable amount of rays is no longer guided in the waveguide core after the coupling from one layer to the other. This is mainly due to the spreading of the light beam during the propagation from one mirror to the other.	114
4.17	(a) Ablation of a trench with a 45° mirror facet; (b) Au-coating of the mirror facet; (c) filling of the ablated trench with cladding material.	115
4.18	(a) Trench that is obtained after ablation with the laser beam perpendicular to the sample; (b) trench that is obtained when the ablation is done with the laser beam in a tilted position.	116
4.19	Angle of the mirror facet, measured with a stylus profiler (Dektak), showing an angle of 45.11°.	117
4.20	Surface roughness plot of a 45° mirror facet, ablated with energy intensity of 7.6mJ/mm ² .	118
4.21	Surface roughness plot of a mirror facet ablated with a pulse energy of 3 mJ.	119
4.22	Surface roughness plot of a mirror facet ablated with a pulse energy of 12 mJ.	119
4.23	(a) SEM image of a 45° mirror facet ablated with a pulse energy of 3mJ; (b) SEM image of a 45° mirror facet ablated with a pulse energy of 12mJ.	120
4.24	(a) Cross-section of an ablated trench with a 45° air-polymer interface; (b) SEM image of the top view of the ablated trench.	120
4.25	(Surface corrugation of the top cladding layer, after the filling of the ablated trench with cladding material.	121

4.26	(a) SEM image of the top view of the starting point of a mirror that is ablated through a mask that is taped on the surface of the sample; (b) close-up showing the high roughness and uneven surface of the mirror facet ; (c) cross-section of a mirror that is ablated through a mask that is taped on the surface of the sample; (d) cross-section of a mirror that is ablated directly into the optical layer.	122
4.27	Schematic showing the alignment of the tape with respect to the ablated trench. The sidewall of the opening in the mask is aligned with the polymer-air interface of the ablated mirror in order to avoid the deposition of Au onto that interface.	123
4.28	(a) Schematic showing the Au-deposition in the ablated trench in case the sample is placed horizontally on the sample holder. The mirror facet is Au-coated but a thin layer of Au is also deposited on the opposite facet because of non directional Au-deposition and scattering in the ablated trench; (b) schematic showing the Au-deposition in the ablated trench in case the sample is tilted under a 45° angle on the holder. The mirror facet is not fully covered because of the shadow effect caused by the opposite interface. The depth up to which the Au is deposited depends not only on the tilt angle but also on the orientation and position of the sample with respect to the Au-source.	124
4.29	The deposition of the Au-coating on the mirror facet depends on the position of the sample on the holder used to position it in the evaporating unit. The three possible positions are marked in the picture by A, B and C. In position B, the sample is aligned with respect to the Au-source. In position A and C, the sample is placed in a eccentric position.	125
4.30	(a) Cross-section of a metalized mirror facet placed in position A on the holder. The Au is deposited onto the opposite mirror interface. (b) Cross-section of a metalized mirror facet placed in position B on the holder. The Au is deposited onto mirror facet and the opposite interface. (c) Cross-section of a metalized mirror facet placed in position C on the holder. The Au is deposited onto the mirror facet.	126
4.31	Cross-section of a metalized mirror. The Au-deposition is limited to the mirror facet, in accordance with the mirror design. The adhesion between the Au-layer and the Truemode material is lost during the manual polishing step, which puts too much pressure on the edge of the sample. The filling of the ablated trench with cladding material is good, except for the Au-coated area as a consequence of the polishing process.	126
4.32	Picture of a Au-coated mirror that is ablated directly into the patterned core layer. The top part of the mirror, corresponding to the core layer, has a good Au-coverage and the lower part, corresponding to the lower cladding layer, has a lower coverage.	127
4.33	(a) SEM image of a mirror ablated directly into the patterned core layer; (b) close-up SEM image of the mirror facet, which confirms the high surface roughness measured with the non-contact optical profiler.	128

4.34	(a) Triangular mask that is used for the ablation of the 45° mirror facet. The mask has a length l , a width w and is moved across the sample with a propagation speed v ; (b) trench that is formed into the optical layer after the ablation with the use of the triangular mask. The angle of the mirror facet depends on the ablation depth and the mask dimensions.	129
4.35	(a) Cross-section of a mirror facet ablated with the triangular mask at low ablation speed; (b) cross-section of a mirror facet ablated with the triangular mask at higher ablation speed. From these pictures, it is clear that the mirror facet becomes steeper with increasing ablation depth.	130
4.36	Graph of the relation between the ablation speed and the corresponding facet angle, with respect to the horizontal axis, for a laser fluence of 7.6mJ/mm ²	130
4.37	(a) SEM image of the top view of the projection of the triangular mask onto the optical layer; (b) SEM image of the top view of a 45° mirror facet ablated with the triangular mask.	131
4.38	(a) Cross-section of a two layer out-of-plane coupling structure. The distance between the centre of the mirror in the top and bottom optical layer corresponds to the pitch between the outcoupled spots, which is in this case 250 μm , in correspondence with most commercially available photo-detector and VCSEL arrays; (b) cross-section of an inter-plane coupling structure with conservation of the propagation direction. The centre of the mirror in the top and bottom layer are aligned with respect to each other.	133
4.39	Schematic of the two layer inter-plane coupling structure with reversal of the propagation direction, with the main parameters that influence the alignment between the mirrors.	134
4.40	Cross-section of a two layer inter-plane coupling structure with reversal of the propagation direction.	135
4.41	(a) Schematic of the considered configuration used for the simulations on the total internal reflection mirror; (b) the angle β of the mirror facet is varied between 40° and 50° in the simulations to determine the tolerance that can be accepted on the mirror facet angle.	137
4.42	Influence of a deviation of the 45° angle of the TIR mirror facet on the link efficiency.	138
4.43	(a) Ray trace plot for a mirror facet angle β of 40°. A large amount of rays are lost for not satisfying the TIR condition; (b) ray trace plot for a mirror facet angle β of 45°; (c) ray trace plot for a mirror facet angle β of 50°.	139
4.44	(a) Alignment tolerance curve for a mechanical misalignment of the detector fiber in X-direction; (b) alignment tolerance curve for a mechanical misalignment of the detector fiber in Y-direction.	140
4.45	(a) Front view of a TIR mirror facet, ablated into the Truemode optical layer at the polished edge of a sample; (b) cross-section of a TIR mirror ablated in the Truemode optical layer.	142
4.46	Picture of the measurement set-up used for the measurements on the ablated TIR mirrors.	143

4.47	Evaluation of the propagation loss of a TIR mirror in a receiver scheme. Light is coupled in horizontally with a $50\mu\text{m}$ core diameter optical fiber with NA 0.2 and is detected vertically with a $100\mu\text{m}$ core diameter optical fiber with NA 0.3.	144
4.48	(Tolerance for a mechanical misalignment of the detector fiber for the TIR mirror.	145
4.49	(Picture of the Au-coated TIR mirror ablated in Truemode material, after the removal of the mask that is used to cover the sample during the sputtering step.	146
4.50	Light spot that is deflected over 90° at the metalized TIR mirror facet, captured by the detector fiber.	146
4.51	(a) SEM image of the micro-structure that is formed in the ablated areas in Truemode material after statical ablation; (b) SEM image of the micro-structure that is formed in the ablated area in Truemode material after dynamical ablation.	146
4.52	((a) Light spot that is detected by the detector fiber after the 90° beam deflection at the TIR mirror in Ormocer material; (b) light spot that is detected by the detector fiber after the 90° beam deflection at the Au-coated TIR mirror in Ormocer material.	147
5.1	Schematic of a DPW out-of-plane coupler which is inserted into an ablated micro-cavity in the optical layer for 90° beam deflection, out of the plane of the optical layer.	153
5.2	(a) Dimensions of the prototyped out-of-plane coupler. The thickness of the PMMA on top of the mirror is in the central zone, where the light spot is coupled out or in, thinner than at the edges. This is done to minimize the propagation distance between the mirror facet and the flat top exit facet without affecting the mechanical stability of the coupler; (b) optical microscope image of a prototyped out-of-plane coupler. . .	154
5.3	Picture of an out-of-plane coupler with an integrated cylindrical micro-lens.	154
5.4	(a) Schematic of a micro-cavity ablated with the laser beam perpendicular to the laser source; (b) graphical relation between the angle α_1 of the entering ray and the angle α_2 of the refracted ray.	155
5.5	(a) Picture of the top view of the out-of-plane coupler, plugged into the laser ablated cavity; (b) picture of the light spot coupled out-of-plane at the mirror facet.	157
5.6	Plot of the light spot that is coupled out at the out-of-plane coupler in a receiver configuration, using the demonstrator board with the ablated Truemode waveguides and the ablated micro-cavity for the insertion of the pluggable coupler.	158
5.7	Plot of the light spot that is coupled out at the enhanced out-of-plane coupler. From this plot it is clear that the cylindrical micro-lens collimates the light beam in one direction.	159

5.8	Schematic showing the insertion of an out-of-plane coupler in a two layer optical structure. The right wall of the cavity is in this drawing vertical, whereas experimentally it is in a tilted position, in correspondance with the tilt angle of the laser beam.	160
5.9	Picture of a first prototyped two layer out-of-plane coupler with integrated cylindrical micro-lenses to collimate, in one direction, the light beam emitted by the upper and lower channel and to avoid cross-talk between the two channels.	161
5.10	(a) Schematic principle of the inter-plane coupler that can be used to couple a light signal from a waveguide in the top layer to the corresponding waveguide in the bottom layer and vice versa with conservation of the propagation direction; (b) schematical principle of the inter-plane coupler that can be used to couple a light signal from a waveguide in the top layer to the corresponding waveguide in the bottom layer and vice versa with a 180° shift in propagation direction.	162
5.11	(a) Picture of a prototyped inter-plane coupler that can be used to couple a light signal from a waveguide in the top layer to the corresponding waveguide in the bottom layer and vice versa with conservation of the propagation direction; (b) picture of a prototyped inter-plane coupler that can be used to couple a light signal from a waveguide in the top layer to the corresponding waveguide in the bottom layer and vice versa with a 180° shift in propagation direction.	163
5.12	Picture of the enhanced inter-plane coupler with conservation of the propagation direction. This mirror design makes it easier to insert the coupler into the micro-cavity without damaging the component because of the increased margin between the bottom of the cavity and the bottom of the mirror.	164
5.13	Operation principle of a mirror insert embedded into a cavity in the PCB: the light propagating in the optical waveguide is coupled out of the plane of the optical layer by means of a 90° deflection on the Au-coated micro-mirror or vice versa, as illustrated by the dashed arrow. .	165
5.14	(a) Side view of the mirror insert, before it is detached from the patterned PMMA plate. The mirror is attached to the plate on one single position and can be removed from the PMMA substrate by pushing the back of the insert with a tweezer ; (b) SEM image of the DPW micro-mirror insert confirming the smoothness of mirror facet, as was verified with surface roughness measurements. The cracks that can be seen near the edges of the component are present in the double-sided tape onto which the component is attached.	167
5.15	Drawing of a mirror insert where part of the mirror facet is vertical, in order to be able to push the insert against the vertical output facet of the waveguides, hereby minimizing the distance between the output of the waveguides and the mirror facet, without damaging the mirror facet. .	169

5.16	(a) Image of the output facet of the waveguides, taken with an optical microscope with the sample in a tilted position; (b) Top view of a mirror insert, glued onto the Cu-surface of the cavity bottom. As can be seen in the picture, the glue is applied towards the back of the insert to avoid contamination of the mirror facet and the output facet of the waveguides. The reflection of the waveguide cores can be clearly observed on the mirror facet.	170
5.17	Top view of a mirror insert which is glued onto the Cu surface of the cavity bottom using an excess amount of glue, which is applied too close to the mirror facet. The mirror facet and output facet of the waveguides is partially contaminated with the glue.	171
5.18	(a) Set-up used to carry out the in-plane reference measurement: an 850 nm light signal is coupled in horizontally into the waveguide with an optical fiber with core diameter 50 μm and NA 0.2, then propagates in the waveguide until it is coupled out at the output facet of the waveguide and is detected with an optical fiber with core diameter 100 μm and NA 0.29; (b) set-up used to measure the link efficiency at the receiver side: an 850 nm light signal is coupled in horizontally into the waveguide with an optical fiber with core diameter 50 μm and NA 0.2, then propagates in the waveguide until it is coupled out of the plane of the optical layer at the Au-coated mirror facet and is detected with an optical fiber with core diameter 100 μm and NA 0.29.	172
5.19	The alignment tolerance plot of the coupling efficiency clearly shows the circularity of the outcoupled spot. The measured 1dB tolerance range is $\pm 24 \mu\text{m}$	173
6.1	(a) Influence of thermal aging at a temperature of 125°C on the absorption spectrum for different aging times [4]; (b) influence of thermal aging at a temperature of 175°C on the absorption spectrum for different aging times [4].	178
6.2	Schematic representation of the set-up used to evaluate the performance of the Truemode waveguide after submitting them to the different reliability and stability tests explained in this chapter.	180
6.3	Link efficiency of 4 cm long Truemode ablated waveguides located in the same array on a demonstrator board. The light gray bars indicate the average link efficiency. The reproducibility is better than 5%.	180
6.4	Link efficiency of 5.1 cm long Truemode ablated waveguides located in an array on two different demonstrator boards. The reproducibility is again better than 5%.	181
6.5	Link efficiency of the waveguides measured on the sample before the 85/85 test, after the 85/85 test without polishing and after the 85/85 test with the additional polishing step.	183
6.6	Link efficiency of the waveguides measured on the sample before and after the thermal cycling test 1.	184
6.7	Link efficiency of the sample containing an array of ablated waveguides and a TIR mirror measured on the sample before and after the thermal cycling test 2.	185

6.8	Link efficiency of the waveguides measured on the sample right after the fabrication and after a one year stay in an office environment. . . .	186
6.9	Progress of temperature in time during the lamination cycle.	187
6.10	(a) Cross-section of an array of ablated Truemode waveguides after the lamination of the Isofoil sheet; (b) the waveguides shape is maintained after the lamination step. The Cu-layer is at the top of the laminated sample, the wavy shape is a consequence of the manual polishing process.	188
6.11	Link efficiency of the ablated Truemode waveguides, measured on the same demoboard before and after the lamination step. The link efficiency measured after the lamination step has been corrected for the shorter waveguide length.	189
6.12	Curve resulting from the DSC analysis carried out on the non fully cured Truemode core material.	190
6.13	Curve resulting from TGA analysis carried out on the fully cured Truemode core material.	190
6.14	Progress of temperature during the solder reflow cycle.	191
6.15	Coupling efficiency of the waveguides measured on the sample before and after the solder reflow cycle.	191
7.1	Picture of a 4×10Gb/s optical interconnect demonstrator that was fabricated at VTT [1]. The optical link demonstrator consists of a 4-channel BGA-mounted transmitter and receiver modules built on LTCC substrates as well as four parallel multimode optical waveguides with a length of 85 mm, fabricated on the PCB (courtesy of VTT).	196
7.2	Schematic structure of the transmitter and receiver modules and the optical coupling [1]. The expanded beam concept between the optoelectronic module and the PCB loosens the alignment requirements, enabling SMT assembly (courtesy of VTT).	197
7.3	Picture of the top view of the micro-mirror placed at the output facet of the waveguides.	197
7.4	Picture of a transmitter/receiver module, which both have the same build-up, BGA-mounted on the PCB.	198
7.5	Schematic of the LTCC module: the i-VCSEL is wire-bonded in the cavity in the LTCC module. The cavity enables to adjust the separation between the VCSEL and the printed circuit board so that the optical components can fit in between.	200
7.6	(a) Picture of the i-VCSEL array wire bonded on the cavity in the LTCC module [4]; (b) picture of the LTCC module BGA mounted on the printed circuit board [4].	200
7.7	Schematic of the demonstrator board with an indication of the position of the array of four parallel waveguides, applied in the central region of the sample. The alignment of the waveguides on the board is done with the help of the alignment marks present on the substrate and the use of an alignment pulse.	202

7.8	(a) Set-up used to measure the first generation demonstrator board in a fiber-to-fiber scheme in a receiver configuration; (b) set-up used to measure the first generation demonstrator board in a fiber-to-fiber scheme in a transmitter configuration.	203
7.9	Plot of the light spot that is coupled out at the pluggable coupler (courtesy of VTT).	204
7.10	Schematic of the built-up of the first active demonstrator board with the use of the lensed DPW insert.	205
7.11	(a) Set-up used to measure the second generation demonstrator board in a fiber-to-fiber scheme in a receiver configuration; (b) set-up used to measure the second generation demonstrator board in a fiber-to-fiber scheme in a transmitter configuration.. . . .	207
7.12	Picture of the demonstrator board with the embedded mirror on the measurement set-up in a fiber to fiber scheme in a receiver configuration.	208
7.13	(a) CAD drawing of the top view of the in-plane connector; (b) CAD drawing of the side view of the in-plane connector (courtesy of VUB).	210
7.14	Schematic of an MT connector. The connector ferrule contains fiber capillaries on a pitch of 250 μm into which typically 8 to 12 fibers with an outer diameter of 125 μm are positioned. The MT guiding pins are positioned at a distance of 4.6 mm from each other, and are used to help align the ferrules during mating [7].	211
7.15	Schematic representation of the alignment principle of the in-plane connector. The microspheres are used to arrange the vertical and lateral alignment, the MT guiding pins are used to arrange the alignment between the array of optical fibers and the polymer waveguides with the help of a fiber alignment plate that can be slid over the MT pins (courtesy of VUB).	212
7.16	(a) The PCB contains rectangular openings to accommodate the MT guiding pins, which are glued to the base plate. It also contains circular openings into which the microspheres are glued; (b) the base plate is positioned on the PCB, parallel to the optical layer, with the help of the microspheres; (c) the fiber alignment plate is slid over the MT guiding pins with the help of predefined circular openings. In this way, the alignment between the optical fibers and the polymer waveguides is arranged (courtesy of VUB).	213
7.17	(a) Schematic view of the base plate that is attached to the PCB with microspheres, which are glued into circular openings on the PCB; (b) schematic view of the MT guiding pins, which are glued to the base plate and float in the rectangular opening in the PCB.	214
7.18	(a) Cross-section of the the first substrate type in which case two prepreg layers and an RCC layer are laminated on both sides of the FR4 substrate; (b) cross-section of the second substrate type in which case openings are made into the prepreg sheets in the areas where the openings are to be ablated. The openings are during the lamination filled with resin.	217
7.19	Cross-section of the Cu-coated FR4 substrate onto which two prepreg layers and an RCC layer are laminated on each side.	218

7.20	(a) Surface roughness plot of the substrate after the lamination step. The two rectangular openings with a width of 2 mm and a length of 1 cm can be clearly observed; (b) surface corrugation of the substrate in the region with the openings in the prepeg, that are filled with resin during the lamination step. The height difference between the resin-filled openings and the remaining part of the substrate is $\approx 13 \mu\text{m}$. The central zone that is slightly higher than the filled openings is the area where the optical layer is deposited. These height differences have to be taken into account in the connector design for a good performance.	219
7.21	Progress of temperature and pressure during the lamination cycle that is used for the fabrication of the PCB substrates [6].	220
7.22	(a) Top view of the rectangular and circular openings that are ablated into the PCB substrate. The light gray colour indicates the zones where the Cu-layer is opened. The optical layer is deposited in the opened area in the center of the sample; (b) side view of the openings that are ablated into the PCB substrate for the fixation of the MT-alignment pins and the micro-spheres that are used for the fixation of the base plate. The array of four waveguides is positioned in the centre of the sample.	220
7.23	(a) Cross-section of a rectangular opening, ablated into prepeg; (b) cross-section of a rectangular opening, ablated into resin-filled openings in the prepeg sheets.	221
7.24	Picture of the top view of the circular and rectangular openings, ablated into the optical PCB.	222
7.25	(a) Sideview of the microspheres glued into the circular openings in the optical PCB; (b) top view of the microspheres, glued into the circular openings in the optical PCB. The thermal nature of the CO_2 ablation process can be clearly seen in the change of colour of the Cu-layer. . .	223

List of Tables

2.1	Wavelengths and intensities of some important vibrational overtones [5].	36
2.2	Main properties of Truemode Backplane™ Polymer, as they are given in the datasheet [7].	41
2.3	Results of the TGA measurement on Truemode Backplane™ Polymer cladding and core material.	45
2.4	Main properties of used Ormocer material.	49
2.5	Main properties of used Epocore/Epoclad material.	53
3.1	Value of the NA, θ_{max} and ϕ_{max} for Truemode, Ormocer, Epocore/clad.	59
3.2	Main characteristics of KrF excimer laser	66
3.3	Technical parameters used for the simulations.	88
3.4	Misalignment and corresponding excess loss for the two layer waveguide structure in Truemode. The alignment tolerance ranges are identical for both the MMF detector and the flat detector with 100 μm diameter.	89
4.1	Alignment tolerance ranges corresponding to an excess loss of 1dB, 0.5dB and 0.1dB for the case where a 100 μm square flat detector is used.	107
4.2	Alignment tolerance ranges corresponding to an excess loss of 1dB, 0.5dB and 0.1dB for a mechanical misalignment of the detector fiber along X-axis for the case where a 100 μm core diameter MMF detector is used.	108
4.3	Alignment tolerance ranges corresponding to an excess loss of 1dB, 0.5dB and 0.1dB for a mechanical misalignment of the detector fiber along X-axis for the case where a 100 μm square flat detector is used.	109
4.4	Alignment tolerance ranges corresponding to an excess loss of 1dB, 0.5dB and 0.1dB for a misalignment of the top mirror around its ideal position along the Z-axis. The resulting alignment tolerance ranges are valid for both the flat and the MMF detector.	112
4.5	Alignment tolerance ranges corresponding to an excess loss of 1dB, 0.5dB and 0.1dB for a mechanical misalignment of the detector along the X-axis. The resulting alignment tolerance ranges are valid for both the flat and the MMF detector.	112

4.6	Alignment tolerance ranges corresponding to an excess loss of 1dB, 0.5dB and 0.1dB for a misalignment of the top mirror along the Z-axis in a two layer inter-plane coupling configuration with conservation of propagation direction.	114
4.7	Misalignment of the detector in X and Y direction around the ideal position and the corresponding excess loss.	141
5.1	Overview of the measurement result obtained for the pluggable out-of-plane coupler.	160
6.1	Link efficiency (link loss) of waveguides in the same array, in different arrays on the same board and on different boards.	181
6.2	Link efficiency (link loss) of waveguide sample before and after submitting it to the 85/85 test for 168 hours, with and without the polishing of the waveguide end facets after the test.	183
6.3	Parameters used for thermal cycling test 1.	184
6.4	Parameters used for thermal cycling test 2.	185
6.5	Link efficiency (link loss) of two waveguide samples before and after submitting them to the two different thermal cycling tests.	185
6.6	Link efficiency (link loss) of the waveguide sample before and after submitting it to the lamination cycle.	188
7.1	Link loss (link efficiency) of the first and second generation demonstrator boards, carried out in collaboration with VUB in a fiber-to-fiber scheme in a receiver respectively transmitter configuration.	209
7.2	Link loss (link efficiency) of the first and second generation demonstrator boards, carried out at VTT in a transmitter scheme using the LTCC module with the integrated i-VCSEL.	209